INSTITUT LAUE-LANGEVIN

NEUTRON DATA BOOKLET

SECOND EDITION

EDITORS

Albert-José Dianoux
ILL (Grenoble)

Gerry Lander
ITU (Karlsruhe)

**NEUTRONS
FOR SCIENCE**

ocpscience

July 2003

NEUTRON DATA BOOKLET

AFFILIATIONS

H. Börner, J. Brown, C. J. Carlile, R. Cubitt, R. Currat, A. J. Dianoux, B. Farago, A.W. Hewat, J. Kulda, E. Lelièvre-Berna, G.J. McIntyre, S. A. Mason, R. P. May, A. Oed, J. R. Stewart, F. Tasset and J. Tribolet
- *Institut Laue-Langevin, France*

I. Anderson - *Spallation Neutron Source, Oak Ridge, USA*

D. Dubbers - *University of Heidelberg, Germany*

R. S. Eccleston, M. Johnson and C. C. Wilson - *ISIS, Rutherford Appleton Laboratory, Unitied Kingdom*

G. Lander - *Institut für Transuranium Elements, Karlsruhe, Germany*

H. Rauch - *Atominstitut der Österreichischen Universitäten, Austria*

R. B. Von Dreele - *Los Alamos National Laboratory, USA*

W. Waschkowski - *Technische Universität München, Germany*

Secretary: A. Mader

Institut Laue-Langevin
BP 156
38042 Grenoble Cedex 9 FRANCE
E-mail: sco@ill.fr   Web: www.ill.fr

NEUTRONS
FOR SCIENCE

Second Edition, July 2003

Contents

Neutron Data Booklet, Second Edition

To make freely available a small pocketbook that covers the wide field of neutron scattering, is clearly an idea which was timely. The first edition of 5000 copies was absorbed by the growing neutron community worldwide within a few months of being published.

The obvious need for a second edition has allowed certain corrections to be made to the first edition – inevitable given the speed with which it was written and printed – and to rectify some omissions – notably a new chapter on diffraction methods on continuous sources by Alan Hewat and Garry McIntyre.

I want to thank Christian Vettier, ILL's Science Director, who is at the origin of this project and the two editors Gerry Lander from Kalsruhe and José Dianoux from Grenoble who have energetically pursued and implemented the idea, and of course the authors who have once again responded admirably to a tight deadline.

Colin Carlile
ILL Director
16th March 2003

PREFACE FOR NEUTRON DATA BOOKLET

Welcome to the *Neutron Data Booklet*. The success of the X-ray and Nuclear Physics Booklets, and the ever-increasing number of neutron users, has led the ILL in collaboration with Old City Publishing, to compile this "little book of facts."

We are first grateful to Christian Vettier of the ILL who persuaded us to undertake this task and helped in many ways in getting people to cooperate. We thank all those who contributed most sincerely; we realise that this is not a research document, and therefore lacking in real excitement. On the other hand, we hope they (and you the reader) will find it above all "useful" and get to feel that having one in your pocket is part of the dress code for a practicing neutron scatterer. Our thanks to the secretarial help at the ILL, who are listed. They gainfully struggled over tables to format and kept their cool.

Although this document was produced at the ILL, we recognise the importance of spallation neutrons, and we hope you will find all you need about neutrons in general in the pages. The editors would like to be informed of both errors and omissions so that these may be corrected in future editions and for when the information is loaded onto the web. In particular, suggestions for further tables or chapters will be warmly received, especially if they are accompanied by a "volunteer author"!

Finally, thanks to Ian Mellanby and Guy Griffiths of Old City Publishing for following through with this and making such a presentable final product.

Albert-José Dianoux, *ILL, Grenoble, France*
Gerry Lander, *ITU, Karlsruhe, Germany*

Neutron Properties

Neutron Scattering Lengths

H. Rauch and W. Waschkowski

1. Introduction

Free neutrons are ideal tools for a lot of experiments, for instance for the investigation of the atomic and molecular structure and of the dynamics of condensed matter. Fission and spallation processes are used for an effective production of free neutrons. These neutrons can be extracted from the moderator block and are guided to the experimental devices outside the reactor shielding. For most experiments monochromatic neutrons are needed, which have to be filtered out from the thermal spectrum leaving the moderator. When pulsed sources or mechanical choppers are used, the time-of-flight technique can be used to measure the energy and the energy change of neutrons. Absorption, transmission and scattering of neutrons are also used for non-destructive inspection of materials.

The scattering length of the neutron-nucleus system is the basic quantity which describes the strength and character of the interaction of low-energy neutrons with the individual nuclei and atomic structures. The values of scattering lengths vary irregularly from one nucleus to another due to their strong dependence on the details of the individual nuclear interaction. Therefore, low-energy neutrons are an important tool for the investigation of the static and dynamic properties of condensed matter since they distinguish between various elements and isotopes. They can also be used for a detailed study of the interaction of the neutron as an elementary particle with its surroundings. The related scattering lengths are of fundamental interest for structure and dynamics investigations of condensed matter, in nuclear research, for biological systems, and for other disciplines. In most cases accurate and reliable values of scattering lengths for chemical elements and also for separated isotopes are needed as input data for the interpretation of experiments with neutrons.

In the past various tables of scattering lengths have been presented in the literature, sometimes with the aim to collect all experimental results including the references [1-6]. Thermal cross section values have been added because they are

also relevant in scattering experiments when extinction and background effects have to be estimated [2,3,5,7].

2. Properties of the neutron

Neutrons have distinct particle properties, which influence the experimental scattering results. They have nearly no electrical properties: "no" electrical charge, "no" electrical dipole momentum. Neutrons mainly obey nuclear interaction. However, their magnetic moment couples to the local magnetic field of magnetic atoms and ions. Neutrons also exhibit weak interaction which is responsible for neutron decay.

Table 1: Neutron Properties

Mass	m =	**$1.674928(1) \cdot 10^{-27}$ kg**
Spin	s =	$-\hbar/2$
magnetic moment	μ =	$-9.6491783(18) \cdot 10^{-27}$ JT^{-1}
β-decay lifetime	τ =	885.9 ± 0.9 s
confinement radius	R =	0.7 fm
quark structure		udd

3. Scattering lengths

Low-energy neutrons are scattered isotropically within the center-of-mass system, which indicates that no orbital momentum is involved in the scattering process ($l = 0$). This fact is equivalent to the statement that the range of interaction is much smaller than the center-of-mass wavelength, λ, of the neutrons. This enables, within the Born approximation and the ordinary scattering theory, the introduction of a point-like interaction in the form of the Fermi pseudopotential [8]

$$V(\vec{r}) = \frac{2\pi\hbar^2}{m_r} \, a \, \delta(\vec{r}) \tag{1}$$

where $m_r = m_n m_k / (m_n + m_k)$ is the reduced mass of the neutron (m_n) – nucleus system. Here, a is the free scattering length, which is related to the scattering amplitude f_o of the scattered spherical wave by $f_o = -a$. This definition is chosen to get for an infinite repulsive potential the relation $a = R$, where R is the radius of this scattering potential.

Rather well known is the scattering of a plane neutron wave (wave number k) by a single fixed nucleus (spin $I = 0$) which results in a spherical scattered wave: $f(\theta) \exp(ikr)/r$. Within the Born approximation the scattering amplitude does in this case not depend on the scattering angle and one gets

$$f(\theta) = -a \tag{2}$$

More rigorously, for slow neutrons, s-wave scattering dominates and leads to an s-wave phase shift δ_o. The scattering amplitude f_o, is a complex quantity given by

$$f_o = \frac{1}{2ik_o}(e^{-2i\delta_o} - 1), \qquad Re(f_o) = -a \tag{3}$$

This relation shows that the scattering length determines the leading term of how the phase shift depends on the momentum of the interacting particle. Thus, in the low energy limit, the relation holds $a \cong \delta_o/k$.

The total scattering cross section σ_s is given by the imaginary part of the scattering amplitude by the optical theorem.

$$\sigma_s = \frac{4\pi}{k} Im(f_o) \tag{4}$$

The scattering amplitude consists of a potential and a resonance part, which can be determined from resonance parameters.

$$\begin{aligned}
Re(f_o) &= f_p + f_r \\
&= \frac{1}{2k_o}\left\{(1 - \Sigma_2)\sin 2\delta_o - \Sigma_1 \cos 2\delta_o\right\} \\
Im(f_o) &= \frac{1}{2k_o}\left\{1 - (1 - \Sigma_2)\cos 2\delta_o - \Sigma_1 \sin 2\delta_o\right\}
\end{aligned} \tag{5}$$

By Breit-Wigner formalism the sums can be written as

$$\Sigma_1 = \sum_r \frac{k}{k_r} \frac{\Gamma_{nr}(E - E_r)}{(E - E_r)^2 + \frac{\Gamma_r^2}{4}}, \qquad \Sigma_2 = \sum_r \frac{k}{k_r} \frac{\Gamma_{nr}\Gamma_r/2}{(E - E_r)^2 + \frac{\Gamma_r^2}{4}} \tag{6}$$

where the summation must be carried out over all resonances r (all means resolved and unresolved resonances as well as bound levels at negative energies) at the resonance energies E_r. Γ_{nr} stands for the neutron scattering width and Γ_r for the total (scattering and absorption) width.

For nuclei with spin I 0, the s-wave neutron interaction leads to two compound spin states (with $I + 1/2$ and $I - 1/2$). Then the resonance sums must be weighted with the spin statistical factors $g_\pm$.

$$\begin{aligned}
g_+ &= \frac{I+1}{2I+1} \; ; \qquad g_- = \frac{I}{2I+1} \; ; \\
\Sigma_{1,2} &= g_+ \sum\nolimits_{1,2}^+ + g_- \sum\nolimits_{1,2}^- .
\end{aligned} \tag{7}$$

The potential part of the scattering amplitude is the spin independent potential scattering radius R' being of theoretical interest (Fig. 1). Systematic calculations of the neutron-nucleus scattering parameters from experimental data have been reported by Aleksejew et al. [9].

Neutron optical phenomena occur due to the collective interaction with many scattering centers. Therefore, the mean phase shift $<\delta_o>$, or the mean interaction potential , become relevant. In this case the momentum transfer occurs to the whole assembly of particles and therefore, the center of mass system equals the laboratory
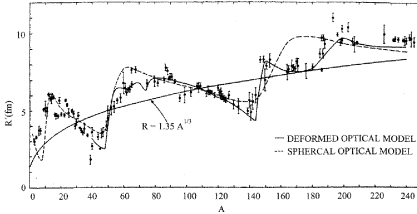
Figure 1: Measured and calculated values of the potential scattering radius [2,3].

system and the bound scattering length b, where $b = a\,(m_n + m_K)/m_K$. Its average value denotes the coherent scattering length b_c.

$$b_c = g_+ b_+ + g_- b_-$$
(8)

and its variance determines the incoherent scattering length b_i

$$b_i^2 = g_+ g_- (b_+ - b_-)^2$$
(9)

The related cross sections are

$$\sigma_c = 4\pi b_c^2 \quad ; \qquad \sigma_i = 4\pi b_i^2$$
(10)

and the total scattering cross becomes

$$\sigma_s = \sigma_c + \sigma_i$$
(11)

With the kinetic neutron energy $E = \hbar^2/2m_n\lambda^2$ the refraction index n - being the ratio of the wave number inside (K) and outside (k) of a mean potential $\overline{V}$ of a nuclei collective with a density N - follows from Eq. (1) and can be expressed as:

$$n^2 - 1 = -\frac{\overline{V}}{E} = -\lambda^2 Nb_c/\pi,$$
(12)

which lead to a refraction index of

$$n = \frac{K}{k} = \sqrt{1 - \frac{\overline{V}}{E}} \cong 1 - \lambda^2 \frac{Nb_c}{2\pi}.$$
(13)

In this simple treatment absorption and magnetic effects are neglected.

When the absorption (reaction) processes are included one obtains a complex index of refraction in the form [10,11]

$$n = 1 - \frac{\lambda^2 N}{2\lambda} \sqrt{b_c^2 - \left(\frac{\sigma_r}{2\lambda}\right)^2} + i\frac{\sigma_r N\lambda}{4\pi}$$
(14)

where $\sigma_r = \sigma_a + \sigma_i$ includes the absorption and incoherent scattering cross section.

4. Methods of measurements

Scattering lengths can be deduced from total cross section measurements, but for this evaluation a lot of corrections are necessary. Therefore, techniques for a more direct determination of coherent scattering lengths have been developed which are based on neutron optical phenomena. A great variety of methods for the determination of coherent scattering lengths exists, because all collective interaction effects are characterized by this quantity. The standard method is based on Bragg diffraction; whereas advanced methods use classical neutron optics, where a more direct relation between the scattering length and the measurable quantities exist [4,11]. That means, less corrections must be performed during the data evaluation and the accuracy of the deduced quantity becomes much higher. The considerable efforts to determine scattering lengths with high accuracy for investigations in fundamental questions lead to techniques of single crystal neutron interferometer [12] and of gravity refractometry [13]. With both techniques a reliability of the order of $\Delta b/b = 10^{-4}$ can be achieved.

Advanced methods for measurements of coherent scattering lengths are total reflection, Christiansen filter technique, and neutron interferometry. The spin dependent scattering lengths, which are of particular interest for theoretical interpretations and for isotopic substitution techniques, can be obtained by polarization techniques of neutrons and nuclei. Incoherent nuclear polarization-dependent cross sections can be determined from a combination of free scattering cross sections with directly measured scattering lengths as well. Free potential scattering radii, which are of fundamental interest for the theory of optical nuclear model, can be deduced from coherent scattering lengths subtracting the resonance contribution. For more information about these techniques we refer to literature [6,11].

5. Data of coherent scattering lengths and of thermal cross sections

This new compilation has the aim to give recommended coherent scattering lengths for elements and if available for isotopes; this will be done including recommended error bars according to the best possible criteria such as check of consistency of the complete nuclear data set (absorption, energy dependence of scattering cross section, incoherence, spin depending scattering lengths). Table 2 shows the recommended values. For the spin dependent scattering length an alternative set of b_+ and b_- values exists because in most cases $(b_+ - b_-)^2$ has been measured. Column 7 of Table 2 indicates whether separate $(b_+ - b_-)$ values are known (+/-) or/and whether a strong energy dependence of the scattering lengths exists (E). The table gives the most probable set. The explanation of the symbols is as follows:

Column

1: ZSymbA   nuclide: charge number Z - element symbol - mass number A
2: p or $T_{1/2}$ abundance (in %) or half-live $T_{1/2}$
3: I   nuclear spin I
4: b_c bound coherent scattering length (in fm)
5: b_+ spin-dependent scattering length for $I+1/2$ (in fm)
6: b_- spin-dependent scattering length for $I-1/2$ (in fm)
7: c   indication whether separate (b_+ - b_-) values are available (+/-)
        and/or a strong energy dependence exists (E)
8: σ_{coh} coherent cross section in barn
9: σ_{inc} incoherent cross section in barn
10: σ_{scatt} total cross section in barn
11: σ_{abs} thermal absorption cross section in barn for 0.0253 eV
*   stands for estimated values

All scattering cross sections follow from known scattering lengths (Eqs. (8)-(11)) but in the table separately measured values are given which results in a certain inconsistency of the values reflecting the fact of conflicting experimental results.

A summary of all measured neutron scattering lengths until 1991 is given in [1] and the references for the values recommended in this summary can be found in [6]. It should be mentioned that there is still a lack of information of scattering lengths of many isotopes and especially of many spin dependent scattering lengths. Any reader is asked to inform the authors about new or unnoticed values. Thank you in advance.

References

[1] Koester, L., Rauch, H., Seymann, E.: Atomic Data and Nucl. Data Tab. **49** (1991) 65.

[2] Mughabghab, S.F., Divadeenam, M., Holden, N.E.: Neutron Cross Sections, Vol. 1, Part A; Academic Press, New York, London (1981).

[3] Mughabghab, S.F.: Neutron Cross Sections, Vol. 1, Part B; Academic Press, New York, London (1984).

[4] Sears, V.F.: Meth. Exp. Phys. **23A** (1986) 521.

[5] Sears, V.F.: Neutron News **3** (1992) 26.

[6] Rauch, H., Waschkowski, W.: Landolt-Boernstein **16A**, Chapt. 6, Springer Berlin (2000).

[7]   CINDA 2000, "Microscopic Neutron Data". IAEA, Vienna 2000, ISSN 1011-2545.

[8]   Fermi, E., Marshall, L.: Phys. Rev. **71** (1947) 666.

[9]   Aleksejev, A., Barkanova, S., Tambergs, J., Krasta, T., Waschkowski, W., Knopf, K.: Z. Naturforschung **53a** (1998) 855.

[10] Goldberger, M.L., Seitz, F.: Phys. Rev. **71** (1947) 294.

[11] Sears, V.F.: Neutron Optics, Oxford University Press (1989).

[12] Rauch, H., Werner, S.A.: Neutron Interferometry, Clarendon Press, Oxford (2000).

[13] Koester, L., in: Neutron Physics (Ed. G. Hoehler); Springer Tracts in Mod. Phys. **80**, Springer Berlin (1977).

Neutron scattering lengths and cross sections

ZSymbA	p or T$_{1/2}$	I	b$_c$	b$_+$	b$_-$	c	σcoh	σ inc	σscatt	σabs
0-N-1	**10.3 MIN**	**1/2**	**-37.0(6)**	**0**	**-37.0(6)**		**43.01(2)**		**43.01(2)**	**0**
1-H			**-3.7409(11)**				**1.7568(10)**	**80.26(6)**	**82.02(6)**	**0.3326(7)**
1-H-1	99.985	1/2	-3.7423(12)	10.817(5)	-47.420(14)	+/-	1.7583(10)	80.27(6)	82.03(6)	0.3326(7)
1-H-2	0.0149	1	6.674(6)	9.53(3)	0.975(60)		5.592(7)	2.05(3)	7.64(3)	0.000519(7)
1-H-3	12.26 Y	1/2	4.792(27)	4.18(15)	6.56(37)		2.89(3)	0.14(4)	3.03(5)	< 6.0E-6
2-He			**3.26(3)**				**1.34(2)**	**0**	**1.34(2)**	**0.00747(1)**
2-He-3	0.00013	1/2	5.74(7)	4.374(70)	9.835(77)	E	4.42(10)	1.532(20)	6.0(4)	5333.0(7.0)
2-He-4	0.99987	0	3.26(3)				1.34(2)	0	1.34(2)	0
3-Li			**-1.90(3)**				**0.454(10)**	**0.92(3)**	**1.37(3)**	**70.5(3)**
3-Li-6	7.5	1	2.0(1)	0.67(14)	4.67(17)	+/-	0.51(5)	0.46(5)	0.97(7)	940.0(4.0)
3-Li-7	92.5	3/2	-2.22(2)	-4.15(6)	1.00(8)	+/-	0.619(11)	0.78(3)	1.40(3)	0.0454(3)
4-Be-9	**100**	**3/2**	**7.79(1)**				**7.63(2)**	**0.0018(9)**	**7.63(2)**	**0.0076(8)**
5-B			**5.30(4)**				**3.54(5)**	**1.70(12)**	**5.24(11)**	**767.0(8.0)**
5-B-10	19.4	3	-0.2(4)	-4.2(4)	5.2(4)		0.144(6)	3.0(4)	3.1(4)	3835.0(9.0)
5-B-11	80.2	3/2	6.65(4)	5.6(3)	8.3(3)		5.56(7)	0.21(7)	5.77(10)	0.0055(33)
6-C			**6.6484(13)**				**5.551(2)**	**0.001(4)**	**5.551(3)**	**0.00350(7)**
6-C-12	98.89	0	6.6535(14)				5.559(3)	0	5.559(3)	0.00353(7)
6-C-13	1.11	1/2	6.19(9)	5.6(5)	6.2(5)	+/-	4.81(14)	0.034(11)	4.84(14)	0.00137(4)
7-N			**9.36(2)**				**11.01(5)**	**0.50(12)**	**11.51(11)**	**1.90(3)**
7-N-14	99.635	1	9.37(2)	10.7(2)	6.2(3)		11.03(5)	0.50(12)	11.53(11)	1.91(3)
7-N-15	0.365	1/2	6.44(3)	6.77(10)	6.21(10)		5.21(5)	0.00005(10)	5.21(5)	0.000024(8)
8-O			**5.805(4)**				**4.232(6)**	**0.000(8)**	**4.232(6)**	**0.00019(2)**
8-O-16	99.75	0	5.805(5)				4.232(6)	0	4.232(6)	0.00010(2)
8-O-17	0.039	5/2	5.6(5)	5.52(20)	5.17(20)		4.20(22)	0.004(3)	4.20(22)	0.236(10)
8-O-18	0.208	0	5.84(7)				4.29(10)	0	4.29(10)	0.00016(1)
9-F-19	**100**	**1/2**	**5.654(12)**	**5.632(10)**	**5.767(10)**	**+/-**	**4.017(14)**	**0.0008(2)**	**4.018(14)**	**0.0096(5)**
10-Ne			**4.566(6)**				**2.620(7)**	**0.008(9)**	**2.628(6)**	**0.039(4)**
10-Ne-20	90.5	0	4.631(6)				2.695(7)	0	2.695(7)	0.036(4)
10-Ne-21	0.27	3/2	6.66(19)				5.6(3)	0.05(2)	5.7(3)	0.67(11)
10-Ne-22	9.2	0	3.87(1)				1.88(1)	0	1.88(1)	0.046(6)
11-Na-23	**100**	**3/2**	**3.63(2)**	**6.42(4)**	**-1.00(6)**	**+/-**	**1.66(2)**	**1.62(3)**	**3.28(4)**	**0.530(5)**
12-Mg			**5.375(4)**				**3.631(5)**	**0.08(6)**	**3.71(4)**	**0.063(3)**
12-Mg-24	78.99	0	5.49(18)				4.03(4)	0	4.03(4)	0.050(5)
12-Mg-25	10	5/2	3.62(14)	4.73(30)	1.76(20)	+/-	1.65(13)	0.28(4)	1.93(14)	0.19(3)

ZSymbA	p or $T_{1/2}$	I	b_c	b_+	b_-	c	σ_{coh}	σ_{inc}	σ_{scatt}	σ_{abs}
12-Mg-26	11	0	4.89(15)							0.0382(8)
13-Al-27	**100**	**5/2**	**3.449(5)**	**3.67(2)**	**3.15(2)**		**1.495(4)**	**0.0082(6)**	**1.503(4)**	**0.231(3)**
14-Si			**4.15071(22)**				**2.1633(10)**	**0.004(8)**	**2.167(8)**	**0.171(3)**
14-Si-28	92.2	0	4.106(6)				2.120(6)		2.120(6)	0.177(3)
14-Si-29	4.7	1/2	4.7(1)	4.50(15)	4.7(4)	+/-	2.78(12)	0.001(2)	2.78(12)	0.101(14)
14-Si-30	3.1	0	4.58(8)				2.64(9)		2.64(9)	0.107(2)
15-P-31	**100**	**1/2**	**5.13(1)**			**+/-**	**3.307(13)**	**0.005(10)**	**3.312(16)**	**0.172(6)**
16-S			**2.847(1)**				**1.0186(7)**	**0.007(5)**	**1.026(5)**	**0.53(1)**
16-S-32	95	0	2.804(2)				0.9880(14)		0.9880(14)	0.54(4)
16-S-33	0.74	3/2	4.74(19)			+/-	2.8(2)	0.3(6)	3.1(6)	0.54(4)
16-S-34	4.2	0	3.48(3)				1.52(3)		1.52(3)	0.227(5)
16-S-36	0.02	0	3.0(1.0)*				1.1(8)		1.1(8)	0.15(3)
17-Cl			**9.5792(8)**				**11.528(2)**	**5.3(5)**	**16.8(5)**	**33.5(3)**
17-Cl-35	75.77	3/2	11.70(9)	16.3(2)	4.0(3)	+/-	17.06(6)	4.7(6)	21.8(6)	44.1(4)
17-Cl-37	24.23	3/2	3.08(6)	3.10(7)	3.05(7)	+/-	1.19(5)	0.001(3)	1.19(5)	0.433(6)
18-Ar			**1.909(6)**				**0.458(3)**	**0.225(5)**	**0.683(4)**	**0.675(9)**
18-Ar-36	0.34	0	24.9(7)				77.9(4)		77.9(4)	5.2(5)
18-Ar-38	0.07	0	3.5(3.5)				1.5(3.1)		1.5(3.1)	0.8(5)
18-Ar-40	99.59	0	1.7				0.421(3)	0	0.421(3)	0.660(9)
19-K			**3.67(2)**				**1.69(2)**	**0.27(11)**	**1.96(11)**	**2.1(1)**
19-K-39	93.3	3/2	3.79(2)	5.15	1.51	+/-	1.76(2)	0.25(11)	2.01(11)	2.1(1)
19-K-40	0.012	4	3.1(1.0)*				1.1(6)	0.5(5)*	1.6(9)	35.0(8.0)
19-K-41	6.7	3/2	2.69(8)				0.91(5)	0.3(6)	1.2(6)	1.46(3)
20-Ca			**4.70(2)**				**2.78(2)**	**0.05(3)**	**2.83(2)**	**0.43(2)**
20-Ca-40	96.94	0	4.78(5)				2.90(2)	0	2.90(2)	0.41(2)
20-Ca-42	0.64	0	3.36(10)				1.42(8)	0	1.42(8)	0.68(7)
20-Ca-43	0.13	7/2	-1.56(9)				0.31(4)	0.5(5)	0.8(5)	6.2(6)
20-Ca-44	2.13	0	1.42(6)				0.25(2)	0	0.25(2)	0.88(5)
20-Ca-46	0.003	0	3.55(21)				1.6(2)	0	1.6(2)	0.74(7)
20-Ca-48	0.18	0	0.39(9)				0.019(9)	0	0.019(9)	1.09(14)
21-Sc-45	**100**	**7/2**	**12.1(1)**	**6.91(22)**	**18.99(28)**	**+/-**	**19.0(3)**	**4.5(3)**	**23.5(6)**	**27.5(2)**
22-Ti			**-3.370(13)**				**1.485(2)**	**2.87(3)**	**4.35(3)**	**6.09(13)**
22-Ti-46	8	0	4.72(5)				3.05(7)	0	3.05(7)	0.59(18)
22-Ti-47	7.5	5/2	3.53(7)	0.46(23)	7.64(13)		1.66(11)	1.5(2)	3.2(2)	1.7(2)
22-Ti-48	73.7	0	-5.86(2)				4.65(3)	0	4.65(3)	7.84(25)
22-Ti-49	5.5	7/2	0.98(5)	2.6(3)	-1.2(4)		0.14(1)	3.3(3)	3.4(3)	2.2(3)
22-Ti-50	5.3	0	5.88(10)				4.80(12)	0	4.80(12)	0.179(3)
23-V			**-0.443(14)**				**0.01838(12)**	**5.08(6)**	**5.10(6)**	**5.08(4)**

ZSymbA	p or T$_{1/2}$	I	b$_c$	b$_+$	b$_-$	c	σ$_{coh}$	σ$_{inc}$	σ$_{scatt}$	σ$_{abs}$
23-V-50	0.25	6	7.6(6)*				7.3(1.1)	0.5(5)*	7.8(1.0)	60.0(40.0)
23-V-51	99.75	7/2	-0.402(2)	4.93(25)	-7.58(28)	+/-	0.0203(2)	5.07(6)	5.09(6)	4.9(1)
24-Cr			**3.635(7)**				**1.660(6)**	**1.83(2)**	**3.49(2)**	**3.05(6)**
24-Cr-50	4.35	0	-4.50(5)				2.54(6)	0	2.54(6)	15.8(2)
24-Cr-52	83.8	0	4.914(15)				3.042(12)	0	3.042(12)	0.76(6)
24-Cr-53	9.59	3/2	-4.20(3)	1.16(10)	-13.0(2)		2.22(3)	5.93(17)	8.15(17)	18.1(1.5)
24-Cr-54	2.36	0	4.55(10)				2.60(11)	0	2.60(11)	0.36(4)
25-Mn-55	100	5/2	**-3.750(18)**	**-4.93(46)**	**-1.46(33)**		**1.75(2)**	**0.40(2)**	**2.15(3)**	**13.3(2)**
26-Fe			**9.45(2)**				**11.22(5)**	**0.40(11)**	**11.62(10)**	**2.56(3)**
26-Fe-54	5.8	0	4.2(1)				2.2(1)	0	2.2(1)	2.25(18)
26-Fe-56	91.7	0	10.1(2)				12.42(7)	0	12.42(7)	2.59(14)
26-Fe-57	2.19	1/2	2.3(1)				0.66(6)	0.3(3)*	1.0(3)	2.48(30)
26-Fe-58	0.28	0	15(7)				28.0(26.0)	0	28.0(26.0)	1.28(5)
27-Co-59	100	7/2	**2.49(2)**	**-9.21(10)**	**3.58(10)**	+/-	**0.779(13)**	**4.8(3)**	**5.6(3)**	**37.18(6)**
28-Ni			**10.3(1)**				**13.3(3)**	**5.2(4)**	**18.5(3)**	**4.49(16)**
28-Ni-58	67.88	0	14.4(1)				26.1(4)	0	26.1(4)	4.6(3)
28-Ni-60	26.23	0	2.8(1)				0.99(7)	0	0.99(7)	2.9(2)
28-Ni-61	1.19	3/2	7.60(6)				7.26(11)	1.9(3)	9.2(3)	2.5(8)
28Ni-62	3.66	0	-8.7(2)				9.5(4)	0	9.5(4)	14.5(3)
28-Ni-64	1.08	0	-0.37(7)				0.017(7)	0	0.017(7)	1.52(3)
29-Cu			**7.718(4)**				**7.485(8)**	**0.55(3)**	**8.03(3)**	**3.78(2)**
29-Cu-63	69.1	3/2	6.477(13)			+/-	5.2(2)	0.006(1)	5.2(2)	4.50(2)
29-Cu-65	30.9	3/2	10.204(20)			+/-	14.1(5)	0.40(4)	14.5(5)	2.17(3)
30-Zn			**5.680(5)**				**4.054(7)**	**0.077(7)**	**4.131(10)**	**1.11(2)**
30-Zn-64	48.9	0	5.23(4)				3.42(5)	0	3.42(5)	0.93(9)
30-Zn-66	27.8	0	5.98(5)				4.48(8)	0	4.48(8)	0.62(6)
30-Zn-67	4.1	5/2	7.58(8)	5.8(5)	10.1(7)	+/-	7.18(15)	0.28(3)	7.46(15)	6.8(8)
30-Zn-68	18.6	0	6.04(3)				4.57(5)	0	4.57(5)	1.1(1)
30-Zn-70	0.62	0	6.9(1.0)*				4.5(1.5)	0	4.5(1.5)	0.092(5)
31-Ga			**7.288(2)**				**6.675(4)**	**0.16(3)**	**6.83(3)**	**2.75(3)**
31-Ga-69	60	3/2	8.043(16)	6.3(2)	10.5(4)	+/-	7.80(4)	0.091(11)	7.89(4)	2.18(5)
31-Ga-71	40	3/2	6.170(11)	5.5(6)	7.8(1)	+/-	5.15(5)	0.084(8)	5.23(5)	3.61(10)
32-Ge			**8.185(20)**				**8.42(4)**	**0.18(7)**	**8.60(6)**	**2.20(4)**
32-Ge-70	20.7	0	10.0(1)				12.6(3)	0	12.6(3)	3.0(2)
32-Ge-72	27.5	0	8.51(10)				9.1(2)	0	9.1(2)	0.8(2)
32-Ge-73	7.7	9/2	5.02(4)	8.1(4)	1.2(4)		3.17(5)	1.5(3)	4.7(3)	15.1(4)
32-Ge-74	36.4	0	7.58(10)				7.2(2)	0	7.2(2)	0.4(2)
32-Ge-76	7.7	0	8.2(1.5)				8.0(3.0)	0	8.0(3.0)	0.16(2)

ZSymbA	p or T$_{1/2}$	I	b$_c$	b$_+$	b$_-$	c	σ$_{coh}$	σ$_{inc}$	σ$_{scatt}$	σ$_{abs}$
33-As-75	100	3/2	6.58(1)	6.04(5)	7.47(8)	+/-	5.44(2)	0.060(10)	5.50(2)	4.5(1)
34-Se			**7.970(9)**				**7.98(2)**	**0.32(6)**	**8.30(6)**	**11.7(2)**
34-Se-74	0.9	0	0.8(3.0)				0.1(6)	0	0.1(6)	51.8(1.2)
34-Se-76	9	0	12.2(1)				18.7(3)	0	18.7(3)	85.0(7.0)
34-Se-77	7.5	0	8.25(8)				8.6(2)	0.05(25)	8.65(16)	42.0(4.0)
34-Se-78	23.5	0	8.24(9)				8.5(2)	0	8.5(2)	0.43(2)
34-Se-80	50	0	7.48(3)				7.03(6)	0	7.03(6)	0.61(5)
34-Se-82	8.84	0	6.34(8)				5.05(13)	0	5.05(13)	0.044(3)
35-Br			**6.79(2)**				**5.80(3)**	**0.10(9)**	**5.90(9)**	**6.9(2)**
35-Br-79	50.49	3/2	6.79(7)			+/-	5.81(2)	0.15(6)	5.96(13)	11.0(7)
35-Br-81	49.31	3/2	6.78(7)			+/-	5.79(12)	0.05(2)	5.84(12)	2.7(2)
36-Kr			**7.81(2)**				**7.67(4)**	**0.01(14)**	**7.68(13)**	**25.0(1.0)**
36-Kr-78	0.35	0						0		6.4(9)
36-Kr-80	2.5	0						0		11.8(5)
36-Kr-82	11.6	0						0		29.0(20.0)
36-Kr-83	11.5	9/2								185.0(30.0)
36-Kr-84	57	0						0	6.6	0.113(15)
36-Kr-86	17.3	0	8.07(26)				8.2(4)	0	8.2(4)	0.003(2)
37-Rb			**7.08(2)**				**6.32(4)**	**0.5(4)**	**6.8(4)**	**0.38(1)**
37-Rb-85	72.17	5/2	7.07(10)				6.2(2)	0.5(5)*	6.7(5)	0.48(1)
37-Rb-87	27.83	3/2	7.27(12)				6.6(2)	0.5(5)*	7.1(5)	0.12(3)
38-Sr			**7.02(2)**				**6.19(4)**	**0.06(11)**	**6.25(10)**	**1.28(6)**
38-Sr-84	0.56	0	5.0(2.0)				6.0(2.0)	0	6.0(2.0)	0.87(7)
38-Sr-86	9.9	0	5.68(5)				4.04(7)	0	4.04(7)	1.04(7)
38-Sr-87	7	9/2	7.41(7)				6.88(13)	0.5(5)*	7.4(5)	16.0(3.0)
38-Sr-88	82.6	0	7.16(6)				6.42(11)	0	6.42(11)	0.058(4)
39-Y-89	100	1/2	**7.75(2)**	8.4(2)	5.8(5)	+/-	**7.55(4)**	**0.15(8)**	**7.70(9)**	**1.28(2)**
40-Zr			**7.16(3)**				**6.44(5)**	**0.02(15)**	**6.46(14)**	**0.185(3)**
40-Zr-90	51.48	0	6.5(1)				5.1(2)	0	5.1(2)	0.011(59
40-Zr-91	11.23	5/2	8.8(1)	7.9(2)	10.1(2)	+/-	9.5(2)	0.15(4)	9.7(2)	1.17(10)
40-Zr-92	17.11	0	7.5(2)				6.9(4)	0	6.9(4)	0.22(6)
40-Zr-94	17.4	0	8.3(2)				8.4(4)	0	8.4(4)	0.0499(24)
40-Zr-96	2.8	0	5.5(1)				3.8(1)	0	3.8(1)	0.0229(10)
41-Nb-93	100	9/2	**7.054(3)**	7.06(4)	7.35(4)	+/-	**6.253(5)**	**0.0024(3)**	**6.255(5)**	**1.15(6)**
42-Mo			**6.715(20)**				**5.67(3)**	**0.04(5)**	**5.71(4)**	**2.48(4)**
42-Mo-92	15.48	0	6.93(8)				6.00(14)	0	6.00(14)	0.019(2)
42-Mo-94	9.1	0	6.82(7)				5.81(12)	0	5.81(12)	0.015(2)
42-Mo-95	15.72	5/2	6.93(7)				6.00(10)	0.5(5)*	6.5(5)	13.1(3)

1.1-12

ZSymbA	p or $T_{1/2}$	I	b_c	b_+	b_-	c	σ_{coh}	σ_{inc}	σ_{scatt}	σ_{abs}
42-Mo-96	16.53	0	6.22(6)				4.83(9)	0	4.83(9)	0.5(2)
42-Mo-97	9.5	5/2	7.26(8)				6.59(15)	0.5(5)*	7.1(5)	2.5(2)
42-Mo-98	23.78	0	6.60(7)				5.44(12)	0	5.44(12)	0.127(6)
42-Mo-100	9.6	0	6.75(7)				5.69(12)	0	5.69(12)	0.4(2)
43-Tc-99	**210000 Y**	**9/2**	**6.8(3)**				**5.8(5)**	**0.5(5)***	**6.3(7)**	**20.0(1.0)**
44-Ru			**7.02(2)**				**6.21(5)**	**0.4(1)**	**6.6(1)**	**2.56(13)**
44-Ru-96	5.8	0						0		0.28(2)
44-Ru-98	1.9	0						0		< 8.0
44-Ru-99	12.7	5/2								6.9(1.0)
44-Ru-100	12.6	0						0		4.8(6)
44-Ru-101	17.07	5/2								3.3(9)
44-Ru-102	31.61	0						0		1.17(7)
44-Ru-104	18.58	0						0		0.31(2)
45-Rh-103	**100**	**1/2**	**5.90(4)**	**8.15(6)**	**6.74(6)**		**4.34(6)**	**0.3(3)***	**4.6(3)**	**144.8(7)**
46-Pd			**5.91(6)**				**4.39(9)**	**0.093(9)**	**4.48(9)**	**6.9(4)**
46-Pd-102	1	0	7.7(7)*				7.5(1.4)	0	7.5(1.4)	3.4(3)
46-Pd-104	11	0	7.7(7)*				7.5(1.4)	0	7.5(1.4)	0.6(3)
46-Pd-105	22.33	5/2	5.5(3)			+/-	3.8(4)	0.8(1.0)	4.6(1.1)	20.0(3.0)
46-Pd-106	27.33	0	6.4(4)				5.1(6)	0	5.1(6)	0.304829)
46-Pd-108	26.71	0	4.1(3)				2.1(3)	0	2.1(3)	8.5(5)
46-Pd-110	11.8	0	7.7(7)*				7.5(1.4)	0	7.5(1.4)	0.226(31)
47-Ag			**5.922(7)**				**4.407(10)**	**0.58(3)**	**4.99(3)**	**63.3(4)**
47-Ag-107	51.8	1/2	7.555(11)	8.14(9)	5.8(3)	+/-	7.17(2)	0.13(3)	7.30(4)	37.6(1.2)
47-Ag-109	48.2	1/2	4.165(11)	3.24(8)	6.9(2)	+/-	2.18(1)	0.32(5)	2.50(5)	91.0(1.0)
48-Cd			**4.83(5)**			**E**	**3.04(6)**	**3.46(13)**	**6.50(12)**	**2520.0(50.0)**
48-Cd-106	1.2	0	5.0(2.0)*				3.1(2.5)	0	3.1(2.5)	1.0(2.0)
48-Cd-108	0.9	0	5.31(24)				3.7(1)	0	3.7(1)	1.1(3)
48-Cd-110	12.39	0	5.78(8)				4.4(1)	0	4.4(1)	11.0(1.0)
48-Cd-111	12.75	1/2	6.47(8)				5.3(2)	0.3(3)*	5.6(4)	24.0(5.0)
48-Cd-112	24.07	0	6.34(6)				5.1(2)	0	5.1(2)	2.2(5)
48-Cd-113	12.36	1/2	-8.0(1)			E	12.1(4)	0.3(3)*	12.4(5)	20600.0(400.0)
48-Cd-114	28.86	0	7.48(5)				7.1(2)	0	7.1(2)	0.34(2)
48-Cd-116	7.58	0	6.26(9)				5.0(2)	0	5.0(2)	0.075(13)
49-In			**4.065(20)**				**2.08(2)**	**0.54(11)**	**2.62(11)**	**193.8(1.5)**
49-In-113	4.28	9/2	5.39(6)				3.65(8)	0.000037(5)	3.65(8)	12.0(1.1)
49-In-115	95.72	9/2	4.00(3)	2.1(1)	6.4(4)		2.02(2)	0.55(11)	2.57(11)	202.0(2.0)
50-Sn			**6.225(2)**				**4.871(3)**	**0.022(5)**	**4.892(6)**	**0.626(9)**
50-Sn-112	1	0	6.0(1.0)*				4.5(1.5)	0	4.5(1.5)	1.00(11)

ZSymbA	p or $T_{1/2}$	I	b_c	b_+	b_-	c	σ_{coh}	σ_{inc}	σ_{scatt}	σ_{abs}
50-Sn-114	0.66	0	6.0(3)				4.8(5)	0	4.8(5)	0.114(30)
50-Sn-115	0.35	1/2	6.0(1.0)*				4.5(1.5)	0.3(3)*	4.8(1.5)	30.0(7.0)
50-Sn-116	14.3	0	6.10(1)				4.42(7)	0	4.42(7)	0.14(3)
50-Sn-117	7.61	1/2	6.59(8)	0.22(10)	-0.23(10)		5.28(8)	0.3(3)*	5.6(3)	2.3(5)
50-Sn-118	24.03	0	6.23(4)				4.63(8)	0	4.63(8)	0.22(5)
50-Sn-119	8.58	1/2	6.28(3)	0.14(10)	0.0(1)		4.71(8)	0.3(3)*	5.0(3)	2.2(5)
50-Sn-120	32.86	0	6.67(4)				5.29(8)	0	5.29(8)	0.14(3)
50-Sn-122	4.72	0	5.93(3)				4.14(7)	0	4.14(7)	0.18(2)
50-Sn-124	5.94	0	6.15(3)				4.48(8)	0	4.48(8)	0.133(5)
51-Sb			**5.57(3)**				**3.90(4)**	**0.00(7)**	**3.90(6)**	**4.91(5)**
51-Sb-121	57.25	5/2	5.71(6)	5.7(2)	5.8(2)		4.10(9)	0.0003(19)	4.10(19)	5.75(12)
51-Sb-123	42.75	7/2	5.38(7)	5.2(2)	5.4(2)		3.64(9)	0.001(4)	3.64(9)	3.8(2)
52-Te			**5.68(2)**				**4.23(4)**	**0.09(6)**	**4.32(5)**	**4.7(1)**
52-Te-120	0.09	0	5.3(5)				3.5(7)	0	3.5(7)	2.3(3)
52-Te-122	2.4	0	3.8(2)				1.8(2)	0	1.8(2)	3.4(5)
52-Te-123	0.87	1/2	-0.05(25)	-1.2(2)	3.5(2)		0.002(3)	0.52(5)	0.52(5)	418.0(30.0)
52-Te-124	4.61	0	7.95(10)				8.0(2)	0	8.0(2)	6.8(1.3)
52-Te-125	6.99	1/2	5.01(8)	4.9(2)	5.5(2)		3.17(10)	0.008(8)	3.18(10)	1.55(16)
52-Te-126	18.71	0	5.55(7)				3.88(10)	0	3.88(10)	1.04(15)
52-Te-128	31.79	0	5.88(8)				4.36(10)	0	4.36(10)	0.215(8)
52-Te-130	34.48	0	6.01(7)				4.55(11)	0	4.55(11)	0.29(6)
53-I-127	**100**	**5/2**	**5.28(2)**	**6.6(2)**	**3.4(2)**		**3.50(3)**	**0.31(6)**	**3.81(7)**	**6.15(6)**
54-Xe			**4.69(4)**				**3.04(4)**	**0**		**23.9(1.2)**
54-Xe-124	0.1	0						0		165.0(20.0)
54-Xe-126	0.09	0						0		3.5(8)
54-Xe-128	1.9	0						0		< 8.0
54-Xe-129	26.14	1/2								21.0(5.0)
54-Xe-130	3.3	0						0		< 26.0
54-Xe-131	21.18	3/2								85.0(10.0)
54-Xe-132	26.89	0						0		0.45(6)
54-Xe-134	10.4	0						0		0.265(20)
54-Xe-136	8.9	0						0		0.26(2)
55-Cs-133	**100**	**7/2**	**5.42(2)**			**+/-**	**3.69(15)**	**0.21(5)**	**3.90(6)**	**29.0(1.5)**
56-Ba			**5.07(3)**				**3.23(4)**	**0.15(11)**	**3.38(10)**	**1.1(1)**
56-Ba-130	0.1	0	-3.6(6)				1.6(5)	0	1.6(5)	30.0(5.0)
56-Ba-132	0.09	0	7.8(3)				7.6(6)	0	7.6(6)	7.0(8)
56-Ba-134	2.4	0	5.7(1)				4.08(14)	0	4.08(14)	2.0(1.6)
56-Ba-135	6.59	3/2	4.66(10)				2.74(12)	0.5(5)*	3.2(5)	5.8(9)

ZSymbA	p or T$_{1/2}$	I	b$_c$	b$_+$	b.	c	σ$_{coh}$	σ$_{inc}$	σ$_{scatt}$	σ$_{abs}$
56-Ba-136	7.81	0	4.90(8)				3.03(10)	0	3.03(10)	0.68(17)
56-Ba-137	11.32	3/2	6.82(10)				5.86(17)	0.5(5)*	6.4(5)	3.6(2)
56-Ba-138	71.66	0	4.83(8)				2.94(10)	0	2.94(19)	0.27(14)
57-La			**8.24(4)**				**8.53(8)**	**1.13(19)**	**9.66(17)**	**8.97(2)**
57-La-138	0.09	5	8.0(2.0)*				8.0(4.0)	0.5(5)*	8.5(4.0)	57.0(6.0)
57-La-139	99.91	7/2	8.24(4)	11.4(3)	4.5(4)	+/-	8.53(8)	1.15(15)	9.66(17)	8.93(4)
58-Ce			**4.84(2)**				**2.94(2)**	**0.00(10)**	**2.94(10)**	**0.63(4)**
58-Ce-136	0.19	0	5.76(9)				4.23(13)	0	4.23(13)	7.3(1.5)
58-Ce-138	0.26	0	6.65(9)				5.64(15)	0	5.64(15)	1.1(3)
58-Ce-140	88.48	0	4.81(9)				2.94(11)	0	2.94(11)	0.57(4)
58-Ce-142	11.07	0	4.72(9)				2.84(11)	0	2.84(11)	0.95(5)
59-Pr-141	**100**	**5/2**	**4.58(5)**			**+/-**	**2.64(6)**	**0.015(3)**	**2.66(6)**	**11.5(3)**
60-Nd			**7.69(5)**				**7.43(19)**	**9.2(8)**	**16.6(8)**	**50.5(1.2)**
60-Nd-142	27.11	0	7.7(3)				7.5(6)	0	7.5(6)	18.7(7)
60-Nd-143	12.17	7/2	14.0(2.0)*				25.0(7.0)	55.0(7.0)	80.0(2.0)	337.0(10.0)
60-Nd-144	23.85	0	2.8(3)				1.0(2)	0	1.0(2)	3.6(3)
60-Nd-145	8.5	7/2	14.0(2.0)*				25.0(7.0)	5.0(5.0)*	30.0(9.0)	42.0(2.0)
60-Nd-146	17.22	0	8.7(2)				9.5(4)	0	9.5(4)	1.4(1)
60-Nd-148	5.7	0	5.7(3)				4.1(4)	0	4.1(4)	2.5(2)
60-Nd-150	5.6	0	5.28(20)				3.5(3)	0	3.5(3)	1.2(2)
61-Pm-147	**2.62 Y**	**7/2**	**12.6(4)**				**20.0(1.3)**	**1.3(2.0)**	**21.3(1.5)**	**168.4(3.5)**
62-Sm			**0.00(5)**			**E**	**0.422(9)**	**39.0(3.0)**	**39.4(3.0)**	**5922.0(56.0)**
62-Sm-144	3.1	0	-3.0(4.0)*				1.0(3.0)	0	1.0(3.0)	0.7(3)
62-Sm-147	15	7/2	14.0(3.0)				25.0(11.0)	14.0(19.0)	39.0(16.0)	57.0(3.0)
62-Sm-148	11.2	0	-3.0(4.0)*				1.0(3.0)	0	1.0(3.0)	2.4(6)
62-Sm-149	13.8	7/2	18.7(28)			**E**	63.5(6)	137.0(5.0)	200.0(5.0)	42080.0(400.0)
62-Sm-150	7.4	0	14.0(3.0)				25.0(11.0)	0	25.0(11.0)	104.0(4.0)
62-Sm-152	26.7	0	-5.0(6)				3.1(8)	0	3.1(8)	206.0(6.0)
62-Sm-154	22.8	0	8.0(1.0)				11.0(2.0)	0	11.0(2.0)	8.4(5)
63-Eu			**5.3(3)**			**E**	**6.57(4)**	**2.5(4)**	**9.2(4)**	**4530.0(40.0)**
63-Eu-151	47.8	5/2				**E**	5.5(2)	3.1(4)	8.6(4)	9100.0(100.0)
63-Eu-153	52.8	5/2	8.22(12)				8.5(2)	1.3(7)	9.8(7)	312.0(7.0)
64-Gd			**9.5(2)**			**E**	**29.3(8)**	**151.0(2.0)**	**180.0(2.0)**	**49700.0(125.0)**
64-Gd-152	0.2	0	10.0(3.0)*				13.0(8.0)	0	13.0(8.0)	735.0(20.0)
64-Gd-154	2.2	0	10.0(3.0)*				13.0(8.0)	0	13.0(8.0)	85.0(12.0)
64-Gd-155	14.9	3/2	13.8(3)				40.8(4)	25.0(6.0)	66.0(6.0)	61100.0(400.0)
64-Gd-156	20.6	0	6.3(4)				5.0(6)	0	5.0(6)	1.5(1.2)
64-Gd-157	15.7	3/2	4.0(2.0)			**E**	650.0(4.0)	394.0(7.0)	1044.0(8.0)	259000.0(700.0)

ZSymbA	p or T$_{1/2}$	I	b$_c$	b$_+$	b$_-$	c	σcoh	σinc	σscatt	σabs
64-Gd-158	24.7	0	9.0(2.0)				10.0(5.0)		10.0(5.0)	2.2(2)
64-Gd-160	21.7	0	9.15(5)				10.52(11)		10.52(11)	0.77(2)
65-Tb-159	100	3/2	7.34(2)	6.8(2)	8.1(2)	+/-	6.84(6)	0.004(3)	6.84(6)	23.4(4)
66-Dy			16.9(3)				35.9(8)	54.4(1.2)	90.3(9)	994.0(13.0)
66-Dy-156	0.06	0	6.1(5)				4.7(8)		4.7(8)	33.0(3.0)
66-Dy-158	0.1	0	6.0(4.0)*				5.0(6.0)	0	5.(6.)	43.0(6.0)
66-Dy-160	2.3	0	6.7(4)				5.6(7)	0	5.6(7)	56.0(5.0)
66-Dy-161	18.9	5/2	10.3(4)				13.3(1.0)	3.0(1.0)	16.0(1.0)	600.0(25.0)
66-Dy-162	25.5	0	-1.4(5)				0.25(18)	0	0.25(18)	194.0(10.0)
66-Dy-163	24.9	5/2	5.0(4)	6.1(5)	3.5(5)		3.1(5)	0.21(19)	3.3(5)	124.0(7.0)
66-Dy-164	28.2	0	49.4(5)				307.0(3.0)	0	307.0(3.0)	2840.0(40.0)
67-Ho-165	100	7/2	8.44(3)	6.9(4)	10.3(4)	+/-	8.06(8)	0.36(3)	8.42(16)	64.7(1.2)
68-Er			7.79(2)				7.63(4)	1.1(3)	8.7(3)	159.0(4.0)
68-Er-162	0.14	0	9.01(11)				9.7(4)	0	9.7(4)	19.0(2.0)
68-Er-164	1.6	0	7.95(14)				8.4(4)	0	8.4(4)	13.0(2.0)
68-Er-166	33.4	0	10.51(19)				14.1(5)	0	14.1(5)	19.6(1.5)
68-Er-167	22.9	7/2	3.06(5)	5.3(3)	0.0(3)		1.1(2)	0.13(6)	1.2(2)	659.0(16.0)
68-Er-168	27	0	7.43(8)				6.9(7)	0	6.9(7)	2.74(8)
68-Er-170	15	0	9.6(6)				11.6(1.2)	0	11.6(1.2)	5.8(3)
69-Tm-169	100	1/2	7.07(3)			+/-	6.28(5)	0.10(7)	6.38(9)	100.0(2.0)
70-Yb			12.41(3)				19.42(9)	4.0(2)	23.4(2)	34.8(8)
70-Yb-168	0.14	0	-4.07(2)			E	2.13(2)	0	2.13(2)	2230.0(40.0)
70-Yb-170	3	0	6.8(1)				5.8(2)	0	5.8(2)	11.4(1.0)
70-Yb-171	14.3	1/2	9.7(1)	6.5(5)	19.4(4)		11.7(2)	3.9(2)	15.6(5)	48.6(2.5)
70-Yb-172	21.9	0	9.5(1)				11.2(2)	0	11.2(2)	0.8(4)
70-Yb-173	16.3	5/2	9.56(10)	2.5(2)	13.3(3)		11.5(2)	3.5	15	17.1(1.3)
70-Yb-174	31.8	0	19.2(1)				46.8(5)	0	46.8(5)	69.4(5.0)
70-Yb-176	12.7	0	8.7(1)				9.6(2)	0	9.6(2)	2.85(5)
71-Lu			7.21(3)				6.53(5)	0.7(4)	7.2(4)	74.0(2.0)
71-Lu-175	97.4	7/2	7.28(9)				6.59(5)	0.6(4)	7.2(4)	21.0(3.0)
71-Lu-176	2.6	7	6.1(2)				4.7(2)	1.2(3)	5.9	2065.(35.)
72-Hf			7.77(14)				7.6(3)	2.6(5)	10.2(4)	104.1(5)
72-Hf-174	0.184	0	10.9(1.1)				15.0(3.0)	0	15.0(3.0)	561.0(35.0)
72-Hf-176	5.2	0	6.61(18)				5.5(3)	0	5.5(3)	23.5(3.1)
72-Hf-177	18.5	0	0.8(1.0)*				0.1(2)	0.1(3)	0.2(2)	373.0(10.0)
72-Hf-178	27.2	0	5.9(2)				4.4(3)	0	4.4(3)	84.0(4.0)
72-Hf-179	13.8	9/2	7.46(16)				7.0(3)	0.14(2)	7.1(3)	41.0(3.0)
72-Hf-180	35.1	0	13.2(3)				21.9(1.0)	0	21.9(1.0)	13.04(7)

ZSymbA	p or T$_{1/2}$	I	b$_c$	b$_+$	b$_-$	c	σ coh	σ inc	σ scatt	σ abs
73-Ta			**6.91(7)**				**6.00(12)**	**0.01(17)**	**6.01(12)**	**20.6(5)**
73-Ta-180	0.012	9	7.0(2.0)*				6.2(3.5)	0.5(5)*	7.0(4.0)	563.0(60.0)
73-Ta-181	99.98	7/2	6.91(7)			+/-	6.00(12)	0.011(2)	6.01(12)	20.5(5)
74-W			**4.755(18)**				**2.97(2)**	**1.63(6)**	**4.60(6)**	**18.3(2)**
74-W-180	0.13	0	5.0(3.0)*				3.0(4.0)	0	3.0(4.0)	30.0(20.0)
74-W-182	26.3	1/2	7.04(4)				6.10(7)	0	6.10(7)	20.7(5)
74-W-183	14.3	1/2	6.59(4)	6.3(4)	7.0(4)		5.36(7)	0.3(3)*	5.7(3)	10.1(3)
74-W-184	30.7	0	7.55(6)				7.03(11)	0	7.03(11)	1.7(1)
74-W-186	28.6	0	-0.73(4)				0.065(7)	0	0.065(7)	37.9(6)
75-Re			**9.2(2)**				**10.6(5)**	**0.9(6)**	**11.5(3)**	**89.7(1.0)**
75-Re-185	37.5	5/2	9.0(3)				10.2(7)	0.5(9)	10.7(6)	112.0(2.0)
75-Re-187	62.5	5/2	9.3(3)				10.9(7)	0	10.9(4)	76.4(1.0)
76-Os			**10.7(2)**				**14.4(5)**	**0.3(8)**	**14.7(6)**	**16.0(4.0)**
76-Os-184	0.02	0	10.0(2.0)*				13.0(5.0)	0	13.0(5.0)	3000.0(150.0)
76-Os-186	1.6	0	12.0(1.7)				17.0(5.0)	0	17.0(5.0)	80.0(13.0)
76-Os-187	1.6	1/2	10.0(2.0)*				13.0(5.0)	0.3(3)*	13.0(5.0)	320.0(10.0)
76-Os-188	13.3	0	7.8(3)				7.3(6)	0	7.3(6)	4.7(5)
76-Os-189	16.1	3/2	11.0(3)				14.4(8)	0.5(5)*	14.9(9)	25.0(4.0)
76-Os-190	26.4	0	11.4(3)				15.2(8)	0	15.2(8)	13.1(3)
76-Os-192	41	0	11.9(4)				16.6(1.2)	0	16.6(1.2)	2.0(1)
77-Ir			**10.6(3)**				**14.1(8)**	**0.0(3.0)**	**14.0(3.0)**	**425.0(2.0)**
77-Ir-191	37.4	3/2								954.0(10.0)
77-Ir-193	62.6	3/2								111.0(5.0)
78-Pt			**9.60(1)**				**11.58(2)**	**0.13(11)**	**11.71(11)**	**10.3(3)**
78-Pt-190	0.01	0	9.0(1.0)				10.0(2.0)	0	10.0(2.0)	152.0(4.0)
78-Pt-192	1.78	0	9.9(5)				12.3(1.2)	0	12.3(1.2)	10.0(2.5)
78-Pt-194	32.9	0	10.55(8)				14.0(2)	0	14.0(2)	1.44(19)
78-Pt-195	33.8	1/2	8.91(9)	9.5(3)	7.2(3)	+/-	9.8(2)	0.13(4)	9.9(2)	27.5(1.2)
78-Pt-196	25.3	0	9.89(8)				12.3(2)	0	12.3(2)	0.72(4)
78-Pt-198	7.2	0	7.8(1)				7.6(2)	0	7.6(2)	3.66(19)
79-Au-197	**100**	**3/2**	**7.90(7)**	**6.26(10)**	**9.90(14)**	**+/-**	**7.32(12)**	**0.43(5)**	**7.75(13)**	**98.65(9)**
80-Hg			**12.595(45)**				**20.24(5)**	**6.6(1)**	**26.8(1)**	**372.3(4.0)**
80-Hg-196	0.15	0	30.3(1.0)			E	115.0(8.0)	0	115.0(8.0)	3080.0(180.0)
80-Hg-198	10.1	0								2.0(3)
80-Hg-199	16.9	0	16.9(4)			E	36.0(2.0)	30.0(3.0)	66.0(2.0)	2150.0(48.0)
80-Hg-200	23.1	0								< 60.0
80-Hg-201	13.2	3/2								7.8(2.0)
80-Hg-202	29.7	0	11.002(43)				15.2108(2)	0	15.2108(2)	4.89(5)

The Neutron and Its Fundamental Interactions

D. Dubbers

1. Introduction

Slow neutrons are used in a large number of experiments to study the physics of particles and their fundamental interactions, as well as their underlying symmetries. Some of these experiments search for manifestations of "new physics" in order to verify or exclude theories leading beyond the present Standard Model of particle physics. Other experiments provide high precision data for standard-model parameters on the first generation of elementary particles. They also serve as input for work in other fields like cosmology, astrophysics or neutrino physics. Finally, there is a larger number of experiments on the foundations of quantum mechanics, mostly in the field of neutron optics.

   The present compilation is limited to a listing of measured neutron observables, as well as a number of derived quantities. About two dozen different basic questions of physics require these numbers as input, as discussed in [1]. We exclusively list parameters involving *nucleons* (i.e. neutron, proton), but not the many neutron results on symmetry tests and basic interactions involving *nuclei*. For more details see also the compilation of the Particle Data Group, www-pdg.lbl.gov and [2], from which most of our data are taken, as well as the conference proceedings [3].

   In most cases we give the world-average value and, in parentheses, the one-sigma standard error; the error number given refers to the last digits of the value quoted, for instance $B = 0.983(4)$ stands for $B = 0.983 \pm 0.004$. In a few cases, more than one result is quoted, provided by different competing groups. When two error numbers are given, then the first is the statistical, the second the systematic error. In a few cases we give rounded values, for rule-of-thumb use. Upper or lower limits are quoted together with the confidence level (c.l.). The year when the last result was published appears in parentheses. *Only references not found in [2] are quoted.*

2. Gravitational Interaction

Mass $m_n = 1.008\ 664\ 915\ 78(55)$ atomic mass units   (1999)

           $m_n c^2 = 939.565\ 33(4)$ MeV   (1999)

Gravitational to inertial mass ratio [4]

           $\gamma = 1.000\ 11(17)$ (1989)

Gravitational force at sea level

           $m_n g = 102$ neV/m

Neutron-proton mass difference (= energy release in free-neutron ß-decay, see 4.)

$$(m_n - m_p)c^2 = 1.293\ 331\ 8(5)\ \text{MeV} \qquad (1998)$$

Neutron-antineutron mass difference

$$\frac{m_n - m_{\bar{n}}}{m_n} = (9 \pm 5) \cdot 10^{-5} \qquad (1986)$$

Planck's constant over neutron mass [5]

$$\frac{\hbar}{m_n} = 3.956\ 0333(3) \cdot 10^{-7}\ \text{m}^2\ \text{s}^{-1} \qquad (1995)$$

Derived quantity (using $\hbar/m_n$ and m_n/m_p from above):

Fine-structure constant α

$$\alpha^{-1} = 137.036\ 011(5) \qquad (1995)$$

3. Electromagnetic Interaction

Charge $\qquad q = (-0.4 \pm 1.1) \cdot 10^{-21}$ elementary charges e (1988)

Magnetic monopole moment [6]

$$g = (0.85 \pm 2.2) \cdot 10^{-20}\ \text{Dirac charges}\ e/2\alpha \qquad (1986)$$

Electric dipole moment (parity P and time reversal T-violating)

$$d = (-0.1 \pm 0.36) \cdot 10^{-25}\ e\ \text{cm} \qquad (1999)$$
$$d = (0.26 \pm 0.40 \pm 0.16) \cdot 10^{-25}\ e\ \text{cm} \qquad (1996)$$

Magnetic dipole moment

$$\mu = -1.913\ 042\ 7(5)\ \text{nuclear magnetons} \qquad (1982)$$
$$|\mu| = 60.31\ \text{neV/Tesla}$$

Larmor frequency ν_L

$$\nu_L/B = 29.16\ \text{MHz/Tesla}$$

Number of spin rotations in-flight at $v_o = 2200\ \text{ms}^{-1}$

$$n = 1.326 \cdot 10^4\ \text{m}^{-1}\ \text{Tesla}^{-1}$$

Electric polarisability

$$\alpha_n = (9.8(+1.9/-2.3))\ 10^{-4}\ \text{fm}^3 \qquad (1995)$$

Magnetic polarisability

$$\beta n = (1.2 \dots 7.6) \cdot 10^{-4}\ \text{fm}^3\ (1\ \text{sigma}) \qquad (2000)$$

Neutron-electron scattering length [7-9]

$$b_{ne} = (-1.32 \pm 0.03) \cdot 10^{-3} \text{fm} \qquad (1995)$$
$$b_{ne} = (-1.38 \pm 0.03 \pm 0.03) \cdot 10^{-3}\ \text{fm} \qquad (1997)$$
$$b_{ne} = (-1.59 \pm 0.04) \cdot 10^{-3} \text{fm} \qquad (1989)$$

Neutron mean square charge radius

$$<r_n^2> = (0.1161 \pm 0.0022)\ \text{fm}^2 \qquad (1997)$$

4. Weak Interaction

ß-decay: Endpoint energy $E_o = 781.567(17)$ keV

Mean life [2,10] $\tau_n = (885.8 \pm 0.9)$ s   (2000)

ß-asymmetry parameter (P-violating) [2,11]

    $A = -0.1170(13)$ (2002)

$\bar{\nu}$ asymmetry parameter (P-violating)

    $B = 0.983(4)$ (1998)

e-$\bar{\nu}$ angular correlation coefficient

    $a = -0.102(5)$ (1978)

Triple correlation coefficient (T-violating) [12]

    $D = (-0.6 \pm 1.0) \cdot 10^{-3}$ (2000)

Derived quantities:

Axial-vector to vector weak-coupling constants [24]

    $g_A/g_V = -1.2720(18)$ (2002)

CKM-quark-mixing matrix element [24]

    $V_{ud} = 0.9725(13)$ (2002)

Deviation from unitarity of CKM-matrix [24]:

$\Delta = 1 - (|V_{ud}|^2 + |V_{us}|^2 + |V_{ub}|^2) = (6.0 \pm 2.8) \cdot 10^{-3}$

Phase between g_A and g_V ($\varphi - 180^0$ is T-violating) [12]

    $\varphi = (180.08 \pm 0.10)^0$ (2002)

Mass of right-handed $m(W_R)$ boson [13]

    $m(W_R) > 281$ GeV/c^2 (90% c.l.)   (1995)

Mixing angle between right and left-handed coupling [14]

    $-0.20 < \zeta < 0.07$ (90% c.l.)   (1997)

Weak-interaction cross-sections, e.g. for neutrino-proton capture [15]

    $\sigma_o = 9.54 \cdot 10^{-44}$ cm^2

Number of neutrino families in universe [16]

    $N_\nu = 2.6 \pm 0.3$ (1989)

Polarised neutron capture on proton: γ-asymmetry (P-violating)

    $A_\gamma = (-1.5 \pm 4.7) \cdot 10^{-8}$ [17]   (1988)

Neutron-antineutron oscillation time

    $\tau_{n\bar{n}} > 0.86 \cdot 10^{-8}$ s (90% c.l.)   (1994)

5. Strong Interaction

Neutron-nucleon free scattering lengths [18]

    $a_{np} = (-23.5 \pm 0.8)$ fm   (1999)

    $a_{nn} = (-18.7 \pm 0.6)$ fm   (1999)

Neutron-proton bound coherent scattering length [19]

    $b_{np} = -3.7409(11)$ fm   (1975)

Neutron-proton spin-dependent scattering length difference [20]

$$b_{np}^+ - b_{np}^- = (58.24 \pm 0.02) \text{ fm} \qquad (1987)$$

Neutron-proton capture cross-section [21]

$$\sigma_c = 0.3326(7) \cdot 10^{-24} \text{ cm}^2 \qquad (1977)$$

Triplet to Singlet capture cross-sections [22]

$$\frac{\sigma_c^\tau}{\sigma_c^s} < 1.1 \cdot 10^{-3} \text{ (95\% c.l.)} \qquad (2000)$$

Polarised-neutron capture on proton: γ-circular polarisation [23]

$$P_\gamma = (-1.5 \pm 0.3) \cdot 10^{-3} \qquad (1992)$$

References:

[1]   D. Dubbers, Neutron News **5**, 21 (1994); Nucl. Phys. A **654**, 297C (1999)

[2]   K. Hagiwara et al. (Particle Data Group), Phys. Rev. D **66**, 010001 (2002)

[3]   International Workshop on Particle Physics with Slow Neutrons, O. Zimmer, J. Butterworth, V. Nesvizhevsky and E. Korobkina, eds., Nucl.Instr. Meth. A **440**, 471 (2000)

[4]   J. Schmiedmayer, Nucl. Instr. Meth. A **284**, 59 (1989)

[5]   E. Krüger, W. Nistler and W. Weirauch, Metrologia **32**, 117 (1995) and IEEE Trans. Instr. Meas. **44**, 514 (1995)

[6]   K.D. Finkelstein, C.G. Shull and A. Zeilinger, Physica **136B**, 131 (1986)

[7]   L. Koester et al., Phys. Rev. **C 51**, 3363 (1995)

[8]   S. Kopecky et al., Phys. Rev. C **56**, 2229 (1997)

[9]   Yu.A. Alexandrov, Nucl. Instr. Meth. A **284**, 134 (1989)

[10] S. Arzumanov et al., Phys. Lett. B **483**, 15 (2000)

[11] H. Abele et al., Phys.Rev. Lett. **88**, 211801 (2002)

[12] L.J. Lising et al., Phys. Rev. C **62**, 55501 (2000)

[13] I.A. Kuznetsov et al., Phys. Rev. Lett. **75**, 794 (1995)

[14] H. Abele et al., Phys. Lett. B **407**, 212 (1997)

[15] K. Schreckenbach and W. Mampe, J. Phys. G **18**, 1 (1992)

[16] D.N. Schramm and L. Kawano, Nucl. Instr. Meth. A **284**, 84 (1989)

[17] J. Alberi et al., Can. J. Phys. **66**, 542 (1988)

[18] D.E. Gonzalez Trotter et al., Phys. Rev. Lett. **83**, 3788 (1999)

[19] L. Koester and W. Nistler, Z. Physik A **272**, 189 (1975)

[20] H. Glättli and M. Goldmann, Methods of Experimental Physics, K. Sköld and D.L. Price, eds., Vol. 23, Part C, p. 266 (1987)

[21] D. Cokinos and E. Melkonian, Phys. Rev. C**15**, 1636 (1977)

[22] T.M. Müller et al., p. 736 in [3]

[23] A.N. Bazhenov et al., Phys. Lett. B **289**, 17 (1992)

[24] F.J. Gilman, K. Kleinknecht, B. Renk, Review on the CKM quark-mixing matrix, in [2]

Neutron Scattering

Small-Angle Scattering

R. P. May

Introduction

Small-angle scattering (SAS) deals with the deviation of electromagnetic or particle waves by heterogeneities in matter. Here, we shall treat the case of neutrons.

SAS allows one to study objects and structures in a size range of about 10 to 1000 Å at low resolution only, but on the other hand, it is not necessary to dispose of crystals. The samples can be considered as composed of elementary volumes with a linear dimension of a few Å, i.e. about the dimension of the neutron wavelengths used. The scattering then depends on the scattering length densities of the elementary volumes, which can readily be influenced for neutrons by modifying the isotopic composition of the sample. This technique is known as "contrast variation„ and has largely determined the success of small-angle neutron scattering (SANS) in the fields of soft condensed matter and biological structures. Other important reasons for using neutrons rather than X-rays are the natural differences in scattering length density for certain classes of matter, the ease with which one can use bulky sample environment and thick samples, and of course, the sensitivity of neutrons for nuclear spins.

Small-angle scattering principles

When a plane wave in z direction ($\Psi = e^{ikz}$) hits a sample, spherically symmetrical waves, $\Psi = -(b/L)\ e^{ikL}$ are emitted from the elementary scatterers in the sample, i.e. the nuclei; L is the distance of an observation point from the sample. The complex scattering amplitude b has the dimension of a length; it is called *scattering length*. The spherical waves interfere and create a pattern on the neutron detector. The scattering geometry is sketched in Fig. 1.
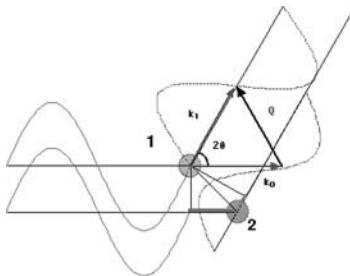
Figure 1. Scattering geometry:
An incoming plane wave (wave vector k0) hits two elementary volumes, 1 and 2. They emit spherical waves (scattering vector k1) that, at an angle 2θ, are dephased due to the different distances of the two volumes from the wave front. The momentum transfer Q is equal to Q = k1 - k0.

When the sample is disordered, as in the majority of the applications of SANS, the scattering pattern is isotropic, and the scattering can be expressed as a function of the modulus of $\mathbf{Q}$: $Q = |\mathbf{Q}| = (4\pi/\lambda) \sin \theta \approx 2\pi r/(\lambda L)$. λ is the wavelength of the neutrons, L the sample-to-detector distance, and r the distance of the spot of the scattered beam on the detector from that of the direct beam. The sample can be oriented by its preparation procedure or by external fields, in particular by a magnetic field, e.g. for studying flux lines, or by a shear gradient.

Scattering cross sections and absolute intensity
The number of neutrons scattered by a sample into a solid-angle element $\Delta\Omega$ of a detector during a time Δt at a momentum transfer Q can be expressed as

$$I_s(Q) = \Phi_o \Delta\Omega \, \Delta t \, \frac{T_s}{T_{ap}} a \, D_s \, \epsilon(\lambda) \frac{d\Sigma_V}{d\Omega}(Q) \tag{1}$$

Φ_o is the neutron flux (neutrons per cm^2 per second) on the sample. $\Phi_o \cdot \Delta t$ is proportional to the counts in the monitor counter used for determining the duration of

a scattering run. T_S/T_{ap} is the sample transmission, i.e. the ratio of the direct beam intensities behind and in front of the sample, respectively. a and D_S are the illuminated area and the thickness of the sample, respectively, $\varepsilon(\lambda)$ the detector efficiency for a given wavelength, and $d\Sigma_V/d\Omega$ is the differential scattering cross section *per unit volume*.

$d\Sigma_V/d\Omega$ can be expressed as

$$\frac{d\Sigma_V}{d\Omega}(Q) = \frac{1}{V}\sum_{i,j} b_i\, b_j\, e^{i\mathbf{Q}\left(\mathbf{r}_i - \mathbf{r}_j\right)} \tag{1a}$$

In the case of isotropic scattering, one averages all the possible configurations of the nuclei in the sample, expressed by $<...>$:

$$\frac{d\Sigma_V}{d\Omega}(Q) = \frac{1}{V}\sum_{i,j} b_i\, b_j\, e^{<i\mathbf{Q}\left(\mathbf{r}_i - \mathbf{r}_j\right)>} \tag{1b}$$

Using an attenuated beam intensity Φ_o' with known attenuation factor f_a, we obtain from equation 1

$$\frac{d\Sigma_V}{d\Omega}(Q) = \frac{K}{D_S T_S}\frac{I_s(Q)}{I_w(Q)} \tag{2}$$

for data that were divided by a background-corrected water run (see below) with

$$K = I_w(0)\frac{T_{ap}}{f_a \varepsilon(\lambda,0)\,\Phi_o'\, a\, \Delta\Omega\, \Delta t} \tag{2a}$$

A broad treatment of absolute scaling techniques in SANS can be found in Wignall and Bates (1987).

The differential scattering cross section *per unit mass* of the sample, $d\Sigma_V(Q)/d\Omega$, is

$$\frac{d\Sigma_m}{d\Omega}(Q) = \frac{1}{c_s}\frac{d\Sigma_V(Q)}{d\Omega} = \frac{K}{c_s\, D_s\, T_s}\frac{I_s(Q)}{I_w(Q)}, \tag{3}$$

with c_s, the sample concentration, in $g\cdot cm^{-3}$. Finally, the differential scattering cross section *per particle*, $d\Sigma_M(Q)/d\Omega$, is

$$\frac{d\Sigma_M}{d\Omega}(Q) = \frac{d\Sigma_m(Q)}{d\Omega}\frac{M}{N_a} = \frac{K}{c_s\, D_s\, T_s}\frac{M}{N_A}\frac{I_s(Q)}{I_w(Q)}, \tag{4}$$

when the molecular mass M is known; N_A is Avogadro's number.

Molecular mass

The molecular mass M can be obtained by considering

$$\frac{d\Sigma_M}{d\Omega}(Q=0) = \left(\sum_i b_i - \rho_p V_p\right)^2 = \left(\Delta\rho_p \bar{v}_p m_p\right)^2 = \left(\Delta\rho_p \bar{v}_p \frac{M}{N_A}\right)^2 \qquad (5)$$

as

$$M = \frac{d\Sigma_m(Q)}{d\Omega} \frac{N_a}{\left(\Delta\rho_p \bar{v}_p\right)^2}, \qquad (6)$$

with $\bar{v}_p$, the (dry) partial specific volume of the particle.

Background corrections

The background in a sample is composed of a transmission-dependent part (sample holder, e.g. a quartz cell, and matrix scattering, e.g. incoherent scattering from a proton-containing buffer solution) and a transmission independent, but also time-dependent part (electronic and neutron noise).

Of the former, the term that is proportional to the transmission (sample container scattering) is easy to treat, whereas the incoherent term (proportional to 1-T) is more complicated. Since the empty-cell contribution is weakened by the transmission of a water sample, the empty-cell and noise contributions are corrected by

$$\tilde{I}_w(Q) = M_o\left[\frac{I_w(Q)}{M_w} - T_w\frac{I_e(Q)}{M_e} - (1-T_w)\frac{I_{Cd}(Q)}{M_{Cd}}\right] \qquad (7)$$

M_w, M_e and M_{Cd} are the neutron monitor counts of the water sample, the container and the noise measurements (for identical geometry, wavelength etc.), and M_o is a reference monitor for scaling. T_w is the water transmission, i.e. the ratio of the intensity transmitted by the water sample and that of the empty cell.

In the more general case of subtracting a purely coherent container or reference background from a sample, we get

$$\tilde{I}_s(Q) = M_0\left[\frac{I_s(Q)}{M_s} - \frac{T_s}{T_b}\frac{I_b(Q)}{M_b} - \left(1 - \frac{T_s}{T_b}\right)\frac{I_{Cd}(Q)}{M_{Cd}}\right] \qquad (8)$$

T_s and T_b are defined according to T_w above.

Debye formula

If the scattering is produced by a dilute ensemble of particles of limited size, the scattering curve can be approximated by the first terms of a Taylor series.

According to Debye (1915), $\langle e^{iQr}\rangle = (\sin Qr)/Qr$ for randomly oriented particles. The scattering from N particles of volume V_p can be written as a sum of contributions from elementary volumes i, j with scattering densities ρ_i and ρ_j, separated by a distance r_{ij}:

$$\frac{d\Sigma_v}{d\Omega}(Q) = \frac{N}{V} \int_{v_p} \int \rho\left(r_i\right) \, \rho\left(r_j\right) \, \frac{\sin Qr_{ij}}{Qr_{ij}} \, dr_i \, dr_j \qquad (9)$$

Radius of gyration

Since $(\sin x)/x \approx 1 - x^2/6 + x^4/120 - x^6/5040 + \dots$, one can express $I(Q)$ near $Q = 0$ as

$$I(Q) = I(Q = 0)\left(1 - \frac{(QR_G)^2}{3} + \frac{(QR_G)^4}{60} - \dots\right), \qquad (10)$$

where in analogy to mechanics R_G is the radius of gyration of the particle or the weight average of the radii of gyration of a mixture of particles.

Eq. 10 is approximated again in two ways, the Zimm (1948) approximation for $1/(c_s \, I(Q))$

$$\frac{c_s}{I(Q)} \approx \frac{c_s}{I(Q = 0)}\left(1 + \frac{(QR_G)^2}{3} \dots\right) \qquad (10a)$$

and the Guinier (1955) approximation that uses the similarity of the first terms in eq. 10 with the expression $e^{-x} \approx 1 - x + x^2/2 - \dots$ to write

$$I(Q) \approx I(Q = 0) \, e^{-\frac{(QR_G)^2}{3}}. \qquad (10b)$$

Expression 10b was historically very useful, because it allowed one to extract R_G by plotting $I(Q)$ *vs.* Q^2 on logarithmic paper.

R_G can be obtained without the need of absolute calibration. In practice, equations 10a and 10b do not yield the same value of R_G, because the equations are not identical, and because the fit cannot start at $Q = 0$ due to the beam stop.

Table 1. Radii of gyration (R_G) of simple triaxial bodies (Mittelbach, 1964)

body	R_G
sphere (radius R)	$(3/5) \, R^2$
hollow sphere (radii R1 and R2)	$(3/5) \, (R_2^5 - R_1^5) / (R_2^3 - R_1^3)$
ellipsoid (semi-axes a, b, c)	$(a^2 + b^2 + c^2) / 5$
parallelepiped (edge lengths A, B, C)	$(A^2 + B^2 + C^2) / 12$
elliptic cylinder (semi-axes a, b; height h)	$(a^2 + b^2) / 4 + h^2 / 12 = Rc^2 + h^2 / 12$
hollow cylinder (radii R1 and R2; height h)	$(R_1^2 + R_2^2) / 2 + h^2 / 12$

Rc is the cross-sectional radius of gyration

Modelling

Frequently, scattering data are analysed by comparing the experimental data with that from models using least-squares fitting procedures, including polydisper-

sity treatment and instrumental smearing. The method and a catalogue of analytical and semi-analytical expressions is described in Pedersen (1997).

Some form factors for simple bodies are listed in table 2.

Table 2. Form factors for simple bodies

Sphere of radius R

$$P(Q) = A_S^2(Q,R) = \left(3 \frac{\sin(QR) - QR\cos(QR)}{(QR)^3}\right)^2$$

Two-shell sphere

$$P(Q) = \left(f_1 A_1(Q,R_1) + f_2 A_2(Q,R_2)\right)^2$$

where f_i and A_i are the relative scattering weights and amplitudes of the outer and inner shells, $f_1 = \rho V_1 / [\rho_1 V_1 + (\rho_2 - \rho_1) V_2]$, $f_2 = 1 - f_1$

cylinder/disk

$$P_d(Q) = \left(\int_0^{\pi/2} \sin\theta \frac{\sin(Q\, d\cos\theta)}{Q\, d\cos\theta} \frac{2 J_1(Q\, R\sin\theta)}{Q\, R\sin\theta} d\theta\right)^2$$

where 2d is the thickness, R the disk radius, J_1 the first order Bessel function, and θ is the angle between the disk normal and Q)

Membrane, thickness 2d $\qquad P_m(Q) = \frac{2}{Q^2}\left(1 - \cos(2Qd)e^{-(Qd)^2/2}\right)$

Pair-distance distribution function

Equation (9) can be rewritten to yield

$$\frac{d\Sigma_V}{d\Omega}(Q) = 4\pi \int_0^\infty r^2 V\gamma(r) \frac{\sin(Qr)}{Qr} dr \qquad (11)$$

$\gamma(r)$ is the correlation function (Debye and Bueche, 1949). Introducing p(r), the pair-distance distribution function, $p(r) = r^2 V\gamma(r)$, one gets

$$\frac{d\Sigma_V}{d\Omega}(Q) = 4\pi \int_0^\infty p(r) \frac{\sin(Qr)}{Qr} dr. \qquad (11a)$$

The Fourier inversion of 11a,

$$p(r) = \frac{1}{2\pi^2} \int_0^\infty \frac{d\Sigma_V}{d\Omega}(Q) Qr \sin(Qr) dr \qquad (12)$$

can, in general, not be solved, because the scattering function is neither known at $Q \to 0$, due to the beam stop, nor at $Q \to \infty$, due to the limited maximum scatter-

ing angle and bad statistics at high Q. Glatter (1981) has introduced an "indirect Fourier transformation,,, a least-square method that overcomes this problem for particles of limited size r_{max}.

The radius of gyration can be calculated as the second moment of p(r),

$$R_G^2 = \frac{\int_0^{r_{max}} p(r)\, r^2\, dr}{2 \int_0^{r_{max}} p(r)\, dr} \tag{13}$$

Size distributions

In the case of a dilute solution of monodisperse homogeneous particles with form factor P(Q),

$$\frac{d\Sigma_s}{d\Omega}(Q) = n \left(\Sigma\, b_i - \rho_b V \right)^2 P(Q) = n\, \Delta\rho_b^2 V^2\, P(Q) \tag{14}$$

n is the number concentration of the particles (number per unit volume), b_i are the scattering lengths of the nuclei of the particle, ρ_b is the scattering-length density of the bulk solvent, and V the volume which circumscribes the particle itself and its associated perturbed solvent (or matrix).

For a size distribution of homogeneous particles that differ only in their dimension, not in their shape, we can write

$$\frac{d\Sigma_s}{d\Omega}(Q) = \Delta\rho_b^2 \int_0^\infty D_n(R)\, V^2(R)\, P(Q,R)\, dR \tag{15}$$

where $D_n(R)$ is the number distribution of particles, i. e. the number of particles of size R per unit volume.

One can also define a volume distribution $D_V(R) \propto R^3 D_n(R)$, i.e. the sum of volumes occupied by particles of dimension R per sample unit volume, and an intensity distribution $D_i(R)$, i.e. the sum of intensity contributions per particle of dimension R per sample unit volume.

Porod's laws

Porod (1951) has shown that the total small-angle scattering from a sample, irrespective of the way its density is distributed, is a constant, called **Porod's invariant** C:

$$C = \int_0^\infty I(Q)\, Q^2 dQ = 2\pi^2 V \overline{\Delta\rho^2} \,. \tag{16}$$

In practice it is difficult to measure the data in all the Q range necessary to evaluate Porod's invariant, but in certain cases it is possible to approximate the low-Q (Guinier) and high-Q limits.

High-Q limit

Also to Porod, we owe an asymptotic law which is valid for high values of Q (Q >>

2.1-8

1/D), if there are sharp boundaries between the phases of the system. This is a condition that barely holds. The **specific surface** $O_S = S/V$, with S, the particle (or structure) surface, and V, the particle (or structure) volume, is given by

$$O_s = \frac{S}{V} = \pi \frac{\left[I(Q)Q^4 \right]_{Q \to \infty}}{C} . \tag{17}$$

Due to the usually very high incoherent scattering of neutrons at high Q, it is often very difficult, if not impossible, to determine O_S with sufficient precision. On the other hand, plotting IQ^4 versus Q^4 (**"Porod plot"**), which allows one to calculate O_S from the $Q^4 = 0$ intercept, can help us to determine a residual background, which shows up as a constant slope for large Q.

References

Debye, P. (1915) *Ann. Phys.* **28**, 809-823.

Guinier, A., and Fournet, G. (1955) "Small Angle Scattering of X-rays,,, New York: Wiley Interscience.

Mittelbach, P. (1964) *Acta Phys. Austriaca* **19**, 53-102.

Pedersen, J.S. (1997) *Adv. Coll. Interface Sci.* **70**, 171-210.

Wignall, G., and Bates, J. (1987) *J. Appl. Crystallogr.* **20**, 28-40.

Zimm, B.H. (1948) *J. Chem. Phys.* **16**, 1093.

General reading

"Small-Angle X-ray Scattering,,, Glatter, O., and Kratky, O., eds., London: Academic Press (1982).

"Neutron, X-ray and Light Scattering: Introduction to an Investigative Tool for Colloidal and Polymeric Systems,,, Lindner, P., and Zemb, Th., eds., Amsterdam: North Holland (1991).

Williams, C., May, R.P., and Guinier, A. (1994) "Small-Angle Scattering of X-rays and Neutrons" in "Characterisation of Materials,,, E. Lifshin ed., Vol. 2B of "Materials Science and Technology", Weinheim: VCH Verlagsgesellschaft, pp. 611-656.

Reflectometry

R. Cubitt

Introduction

Neutron reflectometry is a technique for the study of planar structures with a wide variety of materials from magnetic multi-layers to biological systems at a solid-liquid interface. The method not only permits the derivation of material structures perpendicular to the plane but also to ascertain the perfection of these layers at a boundary which maybe modified by roughness or inter-diffusion. Many problems such as the behaviour of lipid bi-layers in biological cells or the influence of magnetic impurities in superconductors can be greatly simplified by synthesising layers of the material on a substrate thus reducing the dimensionality of the system.

Reflectivity from a Thick Substrate

A beam of neutrons with its associated wave properties can behave in exactly the same way as light when impinging on a mirror like surface. Provided any deviation of the beam is far from satisfying the Bragg condition of the crystaline structure, the neutron can be considered to interact with a constant potential V_o simply related to the coherent scattering length by the relation

$$V_o = \frac{2\pi\hbar^2}{m_n}b\rho \qquad (1)$$

where m_n is the mass of the neutron, ρ is the number density of atoms in the material and b is the average coherent scattering length for these atoms. The product $b\rho$ is known as the scattering length density often denoted by N_b. Most materials have a positive b so in a positive potential a neutron has less kinetic energy and hence a longer wavelength (opposite to light where the wavelength shortens). We may now consider what happens to a beam approaching a surface with a bulk potential V_o, infinitely deep.

 With no structure within the surface the only potential gradient and hence force is perpendicular to the surface. Only the normal component of the incoming wave vector, k_i is altered by the barrier potential and it is the normal component of the kinetic energy $E_{i\perp}$ which determines whether the neutron is totally reflected from the barrier or not.

(a)

(b)
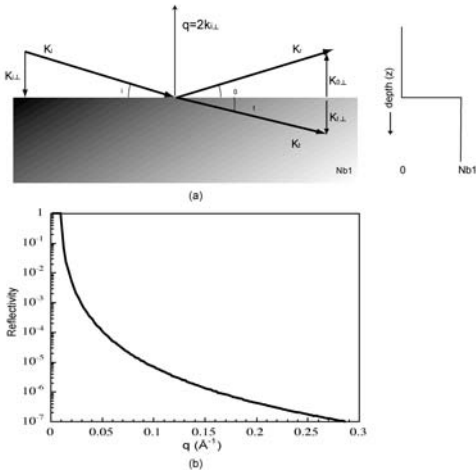
Figure 1: (a) Reflection of an incident beam from an ideally flat interface. k_i and k_r are the incident and scattered wave vectors, with angles $\theta_i = \theta_0 = \theta$ in the incidence plane; q is the wave vector transfer; Nb1 is the scattering length density of the semi-infinite substrate. On the right is the scattering length density profile as a function of depth; (b) Simulation of the specular neutron reflectivity as a function of q from a silicon/air interface (Nb1=2.07x10^{-6}Å^{-2}).

$$E_{i\perp} = \left(\frac{\left(\hbar k_i \sin\theta_i \right)^2}{2m_n} \right) \tag{2}$$

If $E_i\perp < V_o$ then there is total reflection and the critical value of wave vector transfer, q_c will be when $E_i\perp = V_o$ giving:

$$q_c = \sqrt{16\pi N_b} \quad \text{as} \quad q = 2k_i \sin\theta_i \tag{3}$$

Assuming the interaction is elastic then conservation of momentum means that i.e.

the reflection is specular provided the sample is static. Any off specular reflection must be a result of potential gradients within the xy plane of the surface.

If $E_{i\perp} > V_o$ then the reflection is not total the neutron can either be reflected or transmitted into the bulk of the material. The transmitted beam, k_t with its normal component of kinetic energy reduced by the potential must change direction i.e. it is refracted. The change in the normal wave vector is:

$$k_{t\perp}^2 = k_{i\perp}^2 - 4\pi N_b \qquad (4)$$

allowing us to define a relative refractive index n:

$$n^2 = \frac{k_t^2}{k_i^2} = \frac{k_{i//}^2 + (k_{i\perp}^2 - 4\pi N_b)}{k_i^2} = 1 - \frac{4\pi N_b}{k_i^2} = 1 - \frac{\lambda^2 N_b}{\pi} \qquad (5)$$

where λ is the neutron wavelength. For a material such as Si, N_b is $2.07\text{x}10^{-6}\text{Å}^{-2}$, much less than one, so for thermal neutron wavelengths we can make a good approximation for n with the well known result:

$$n \approx 1 - \frac{\lambda^2 N_b}{2\pi} \qquad (6)$$

This confirms the earlier statement about the wavelength change in the bulk being opposite to that of light (for positive b) as we see that n is less than one. The transmitted beam refracts towards the mirror plane and exactly at the point of total reflection, the refracted beam travels along the surface.

All of the above discussion (apart from treating neutrons as waves) can be derived from classical physics. In order to describe all the physical aspects of reflectometry we must use a quantum mechanical approach. The wavefunction describing the probability amplitude of a neutron near to the surface is

$$\frac{\partial^2 \Psi_z}{\delta z^z} + k_\perp^2 = 0 \qquad \text{where} \qquad k_\perp^2 = \frac{2m_n}{\hbar^2}(E_i - V) - k_{//}^2 \qquad (7)$$

Solutions for this above and below the surface are:

$$\Psi_z = e^{ik_{i\perp}z} + re^{-ik_{i\perp}z} \qquad \text{and} \qquad Y_z = te^{ik_{i\perp}z} \qquad (8)$$

where r and t are the probability amplitudes for reflection and transmission. Continuity of the wavefunction and its derivative give the expressions:

$$1 + r = t \qquad\qquad k_{i\perp}(1 - r) = t\,k_{t\perp} \qquad (9)$$

which leads directly to the classical Fresnel coefficients found in optics:

$$r = \frac{k_{i\perp} - k_{i\perp}}{k_{i\perp} + k_{i\perp}} \qquad \text{and} \qquad t = \frac{2k_{i\perp}}{k_{i\perp} + k_{i\perp}} \tag{10}$$

In reflectometry we measure the reflectivity as a function of wavevector transfer or q. Using the expressions (3), (4) and (10) we can relate the measured reflectivity R to q and q_c. Note that what we measure is an intensity and thus is a function of the quantum mechanical probability squared.

$$R = r^2 = \left| \frac{q - \left(q^2 - q_c^2\right)^{1/2}}{q + \left(\left(q^2 - q_c^2\right)^{1/2}\right)} \right|^2 \tag{11}$$

When q>>q_c this reduces to:

$$R \approx \frac{16\pi^2}{q^4} N_b^2 \tag{12}$$

which is the reflectivity used in the Born approximation [1]

Returning to the wavefunction within the surface (8) and using (4) we find that when E_I<V (or $k_{i\perp}$<$4\pi N_b$ or q<q_c) we have a real solution of the form:

$$Y_z = t e^{i\left(k_i^2 \perp - 4\pi N_b\right)^{1/2} z} = t e^{-\frac{1}{2}\left(q_c^2 - q^2\right)^{1/2} z} \tag{13}$$

This is a very important result as it shows that even when the potential barrier is higher than the particle energy normal to the surface it can still penetrate to a characteristic depth of $\left(q_c^2 - q^2\right)^{-1/2}$. This 'evanescent' wave travels along the surface with wave vector $k_{//}$ and after a very short time is ejected out of the bulk in the specular direction. Taking the value of N_b for Si again this penetration is of the order of 100Å at q=0 rising rapidly to infinity at q=q_c. No conservation laws are broken, as the reflectivity is still unity due to the fact that this wave represents no flux transmitted into the bulk. The result also explains why when a thin layer of material (<100Å) such as Ni, which has an N_b twice as large as Si, is put onto a Si substrate we find that q_c is still defined by the N_b of Si and not of Ni. The reason being in this case the layer is thinner than the characteristic penetration depth and the neutrons tunnel through the barrier.

Calculating the reflectivity from such a system or one with many layers requires a general technique such as the optical matrix method [2,3,4,5]. The transmission and reflection from one layer to the next can be described as a matrix multiplication product for each layer. The problem of inverting a reflectivity curve to extract N_b as a function of depth is complex and many profiles can produce the

(a)

(b)
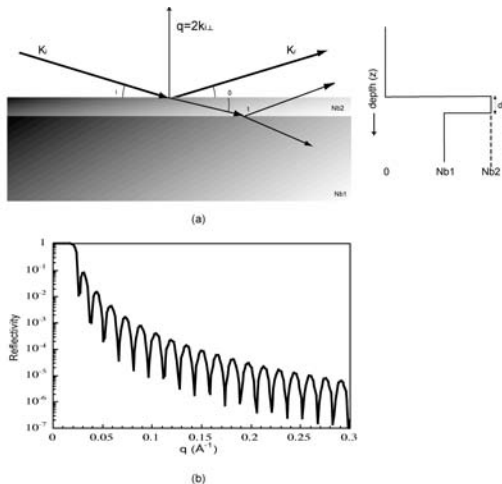
Figure 2 (a):As Figure 1a with an additional thin layer of scattering length density Nb2. (b) Simulation of the specular neutron reflectivity as a function of q from a 400 Å layer of nickel on a silicon substrate (Nb1=2.07x10^{-6}Å^{-2}, Nb2=9.04x10^{-6}Å^{-2}).

same reflectivity curve. A useful review of the various techniques for inversion can be found in [5].

Absorption

In reality many materials have a finite absorption cross-section. This is dealt with by adding an imaginary part to the coherent scattering length.

$$b_{total}=b_{coherent}+ib_{absorption} \qquad (14)$$

It can be seen then from (8) that the transmitted and the reflected intensity is exponentially reduced by the presence of absorption. Even in the regime of total

reflection, as the evanescent wave exists in a surface region of the material, absorption occurs reducing the total reflection amplitude to less than one. It should not be forgotten that even materials such as Cd and Gd that are very strong absorbers of neutrons can still have significant reflectivities.

Magnetic Materials

We have seen that a neutron in the bulk is affected by a mean potential related to the coherent scattering length. If the material is magnetised then there is an additional potential associated with the interaction of the magnetic dipole moment of the neutron and variations of magnetic flux density B. This potential has the value:

$$V_{mag} = -\mu \cdot B(r) \tag{15}$$

where μ is the magnetic dipole moment of the neutron and B(r) is the spatially varying magnetic field. If the incoming beam is polarized up or down with respect to the magnetisation of the sample then the magnetic potential switches sign. The magnetic potential can be expressed in the form of a coherent scattering length:

$$b_m = 1.913 \frac{e^2}{m_e} S \tag{16}$$

where S is the effective spin of the magnetic atom perpendicular to the momentum transfer of the reflection. The total coherent scattering length becomes polarization dependent with the plus sign corresponding to a beam polarised by a polarizer with a magnetisation in the same direction as the magnetisation of the sample:

$$b_{total} = b_{nuclear} \pm b_m \tag{17}$$

Assuming the sample is a saturated ferro-magnet, to extract the nuclear and magnetic parts of b two measurements must be made, one with the polarization parallel to the magnetisation, R_+ and the other with the polarization inverted, R_- by use of a flipper [6]. A very important point in polarised neutron reflectometry (PNR) is to remember that magnetic reflection is only going to occur at a potential boundary and from (15), that requires a step in B. If a sample has been magnetised within the plane of a magnetic layer then Maxwells equations tell us that the step in B is $\mu_o M$ at the surface, where M is the magnetisation density of the layer. If the sample is magnetised normal to the plane then B is continuous at the boundary and there is no potential step. Magnetic reflection can only occur in the presence of in-plane magnetisation components. Components of magnetisation normal to the plane do not reflect an in-plane polarized beam but can cause spin flip i.e. a completely polarized beam will have a certain fraction polarized in the opposite

direction after reflection. This can only be measured by the use of a second flipper and polarizer or analyser. Figure 3 shows the four combinations of the initial and final polarization states needed to measure the four reflectivities i.e. R_{++}, R_{--}, R_{+-}, R_{-+}. It should be noted that from the polarizer to the analyser there must be a small vertical guide field that maintains the polarization on a vertical axis. In addition to measuring these four cases the four cases should also be measured with a non-magnetic scatterer such as graphite to enable the imperfection of the flipper and polarizer efficiencies to be taken into account. A detailed description of neutron optics and magnetic effects can be found in ref [6,7].
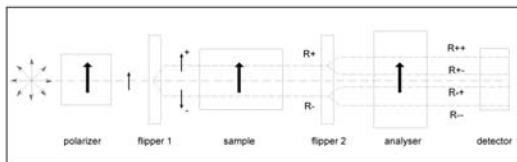
Figure 3: A schematic layout of a polarised neutron reflectivity experiment with analysis. The initially unpolarised beam is polarised vertically by the polariser mirror. Flipper 1, when activated, inverses the polarisation allowing the measurement of R+ and R-. The difference of these two data sets represents the magnetic contribution to the reflectivity. If in the process of reflection the neutron polarisation was changed (flipped) due to a magnetisation component out of the vertical plane this can be detected by the use of an analyser mirror and second flipper. Between the polariser and analyser a guide field (~20G) is required to maintain the polarisation in the vertical direction.

Roughness and Interdiffusion

There is a large field of interest in what happens between materials at an inter-material boundary. An interface may be rough with peaks and troughs over a large range of length scales with a fractal-like structure. It may also have magnetic roughness if the magnetisation does not sharply change at an interface. A boundary may be smooth but with one material diffused into the other. It turns out that in both the rough and diffuse case the specular reflectivity is reduced by a factor very much like the Debye-Waller factor reduces scattered intensity from a crystal. Expression (12) would be affected in the following manner:

$$R \approx \left(\frac{16\pi^2}{q^4} N_b^2 \right) e^{-q_z^2 \sigma^2} \tag{16}$$

where σ is a characteristic length scale of the layer imperfection. So what happens to the intensity lost by the exponential factor in (16)? In the case of the diffuse interface the lost intensity must go into the transmitted beam as there are no potential gradients in any other direction than normal to the surface. This is not the case for the rough interface where intensity is lost by local reflections in directions away from the specular direction or off-specular scattering. Information such as the height-height correlation function can be deduced from this off-specular scattering [2,3].
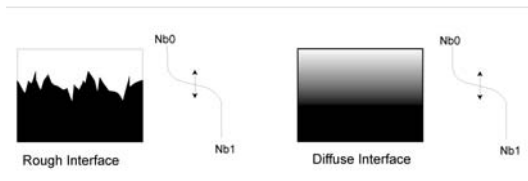
Figure 4: Two possible interfaces which can result in identical specular reflectivities. The data only differs in the case of the rough interface where off-specular scattering is observed.

Experimental Technique

The reflectivity can be measured as a function of q in two very different ways, each of which has advantages and disadvantages. The first method known as monochromatic involves making a θ-2θ scan with a well defined wavelength and storing the reflected intensity for each θ. The incoming intensity must also be measured either at the same time with the use of a monitor and then scaled up by the monitor efficiency or in the separate experiment. The reflectivity is simply the ratio of these two intensities for each θ which is converted to q by Braggs law:

$$q = 4\pi \sin(\vartheta)/\lambda \tag{17}$$

With a sample length of the order of a few cm and a starting θ of a fraction of a degree, the beam must be finely collimated to ensure the sample is under illuminated i.e. all the incoming beam strikes the reflection surface. The sample can

be over illuminated for very small samples but the data must be corrected for the varying flux on the sample as θ is increased.
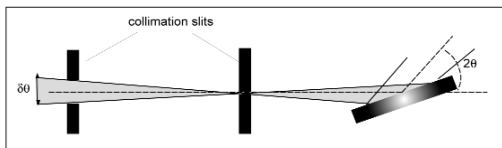
Figure 5: A typical collimation set-up within the reflection plane. When sample is under-illuminated (minimal background), the distance between the last slit and the sample should be as short as possible. In general the divergence out of the plane is defined only by the source.

As the reflectivity tends to drop quite fast with increasing q (see (12) where $R \propto 1/q^4$) in order to gain intensity (at the price of looser resolution) the collimation slits can be opened keeping $\delta\theta/\theta$ constant and equal to the fractional wavelength variation. The final curve in either case must have the resultant q resolution, δq, de-convolved from the data. The q resolution is related to θ and λ by the following relation:

$$\left(\frac{\delta q}{q}\right)^2 = \left(\frac{\delta\theta}{\theta}\right)^2 + \left(\frac{\delta\lambda}{\lambda}\right)^2 \tag{18}$$

This method has the advantage that the wavelength chosen can be that with the highest flux from the neutron source and therefore for a given resolution, is the most efficient method of using the flux available.

The alternative is to use time-of-flight (TOF). Here we keep θ constant and use all the available wavelengths in the beam. The wavelength and hence q is measured by pulsing the incoming beam and measuring the arrival time to the detector. The resolution is the same as (18) with $\delta\lambda/\lambda$ replaced by $\delta T/T$ where δT is the pulse time width and T is the time of -flight of the pulse. The resolution of the time binning at the detector in principle is also a factor but in practice this is chosen to be much smaller than δT. The range of q covered for a given θ depends on the useful wavelength range which is a factor of 10 for the ILL reflectometer D17. Over this range however, the flux at the minimum and maximum wavelengths compared to the peak flux may be more than 2 orders of magnitude smaller. The highest q (and lowest reflectivity) is measured by the shortest wavelength. For the

same resolution the TOF method is less efficient than the monochromatic technique as it will always require longer counting times to measure the same q-range to the same statistical accuracy. The reason the ILL reflectometer has both TOF and monochromatic options is that kinetic experiments cannot be done in the monochromatic mode. If one had a sample which the layer structure was changing as a function of time, only the TOF method can produce a unique R(q) for a given time range. The θ-2θ measurement is a sequential set of counts so each point in q is measured at a different time. In order to solve the problem of reduced flux in TOF, D17 has a chopper system that can continuously vary the time resolution. Provided the reflectivity curve does not have fine structure then low a resolution measurement can be completed in less than 1minute. The incoming beam intensity for TOF can be measured with a monitor in which case the data has to be re-binned in time before dividing as the monitor is not at the same distance from the pulsed source as the detector. In addition a separate measurement of the relative efficiencies of the detector to monitor is required as a function of wavelength. On D17 there is no monitor for this and the incoming beam is measured directly on the detector in a separate measurement. Care must be taken to avoid dead time losses where the local rate can be much higher than the mean count rate observed.

About the specular reflected beam in 2θ there is background that must be subtracted before dividing through by the direct beam. This background can be substantial for experiments involving a solid-liquid interface where the substrate can be pure water and limits the lowest reflectivity measurable to ~10^{-7}. With a two dimensional multi-detector a wide range of 2θ is captured which will include background and off-specular diffraction. Instruments with a single detector require a special measurement with the detector in an off-specular position to measure the background. In both cases care must be taken in deciding the 2θ range for background does not include diffracted intensity from the sample itself.

PNR experiments are complicated by the fact that the polarizers and flippers in the system are not perfect. With no sample and incoming beam directly on the analyser we would expect no flux on the detector in the condition -+ or +- for a perfect system. A measure of the efficiency of each flipper and the polarizers is the flipping ratio F defined as

$$F_1 = I_{++}/I_{-+} \qquad \text{and} \qquad F_2 = I_{++}/I_{+-} \qquad (19)$$

where F_1 and F_2 are the flipping ratios for the first and second flippers. The intensities are measured either with the direct beam for a single detector or with a non-magnetic scatterer for a multi-detector. The measured intensities, I correspond to the states of the two flippers as in figure 3. Acceptable flipping ratios are of the

order of 40. These must be taken into account when attempting to extract the magnetic and nuclear components of the reflectivity [6,7].

ILL instruments

At present there are three reflectometers at the ILL, two of which are externally funded (ADAM & EVA) and therefore have limited time for ILL experiments. They are both fixed wavelength resolution (1%) monochromatic instruments with ADAM
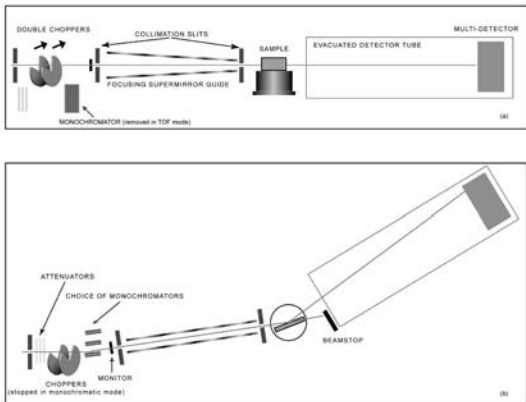
Figure 6: The dual mode instrument D17 at the ILL designed to take advantage of both TOF and monochromatic methods of measuring reflectivity. (a) A side view of the instrument in TOF mode. The monochromator is removed from the beam and a double chopper system defines the time resolution (1-20% δt/t). Between the collimation slits is a vertically focusing guide which increases the flux at the sample position at the price of increased vertical divergence of the beam. The slits define the beam in the horizontal direction. (b) A vertical view of the instrument in monochromatic mode. Here the collimation arm is rotated (~4 deg) to allow the beam reflected from the multi-layer monochromator system to pass through to the sample. The choice of monochromators involves high and low resolution (2-5%) plus polarising.

2.2-12

having a horizontal reflection plane and EVA vertical. EVA has been specially designed to measure scattering from the evanescent wave mentioned above.

D17 is an ILL instrument with both monochromatic and TOF modes. The wavelength resolution can be changed in the monochromatic mode and the time resolution in TOF is continuously variable. All three have polarized neutrons with polarization analysis. Unfortunately non of the three are capable of measuring reflection from a free liquid surface which requires a special instrument which hopefully will be built in the near future at the ILL. Further details about these instruments can be found in the ILL web pages at http://www.ill.fr/YellowBook/.

References

[1] Born and Wolf 'Principles of Optics', Permagon Press, Oxford (1970)

[2] Phys. Rev. B 'X-ray and Neutron scattering from rough surfaces' V38 N4 P2297

[3] J. Daillant A. Gibaud (Eds.) 'X-ray and Neutron Reflectometry: Principles and Applications', Springer (1999)

[4] V. F. Sears 'Neutron Optics', Oxford Press, Oxford (1989)

[5] X. Zhou S. Chen 'Theoretical foundation of X-ray and neutron reflectometry' Phys. Reports V257 p223 (1995)

[6] W. Williams 'Polarized Neutrons' , Oxford Press, Oxford (1989)

[7] A. Wildes 'Polarizer-analyser correction problem in neutron polarization analysis experiments' Rev. Sci. Inst. V70 p4241 (1999)

TIME-OF-FLIGHT NEUTRON DIFFRACTION

C. C Wilson

1. Introduction

The principal characteristic of instruments for diffraction on pulsed neutron sources is their use of time-of-flight (TOF) techniques to allow for optimal use of the white neutron beams produced by the source. These rely on the fact that neutrons with different energies, and hence different wavelengths, from de Broglie's relationship, travel at different velocities:

$$\lambda = h/mv \qquad (1)$$

where m is the neutron mass and v the neutron velocity.

Thus, since in the spallation process all neutrons in a given pulse are essentially created at the same time, t_0, the higher energy, shorter wavelength neutrons travel faster and hence arrive at sample and subsequently at detector, at an earlier time than the lower energy, longer wavelength, slower neutrons. By measuring the time of arrival of a neutron at the detector, and of course knowing its flight path, we can calculate its velocity and hence its wavelength (energy). This is the basis of TOF, which is a genuinely wavelength-sorted white beam technique of great use in a wide range of diffraction techniques.

The wavelength and time-of-flight are related by the following expression:

$$\lambda = ht/mL \qquad (2)$$

where t is the time-of-flight and L the total flight path.

And using Bragg's law $\lambda = 2d\sin\theta$, we get a relationship between TOF and d-spacing:

$$t = m.L.2d\sin\theta/h \qquad (3)$$
$$[=252.777.L.2d\sin\theta, \text{ with t in } \mu s, \text{ L in m, d in Å}]$$

We note here in passing that the commonly used unit for wavevector transfer in neutron scattering, $Q = 2\pi/d$.

The measured d-spacing at a given scattering angle is therefore given by:

$$d = t/(252.777.L.2\sin\theta) \qquad (4)$$

i.e. the measured d-spacing is directly proportional to TOF. This has important

consequences for the design of TOF diffraction instruments. For example, if we consider powder diffraction, Bragg's law for a monochromatic instrument is normally expressed in the form

$$\lambda = 2d_{hkl}\sin\theta_{hkl} \tag{5}$$

where λ is the chosen (fixed) wavelength and measurement of various Bragg reflections *hkl* is achieved (at d-spacing d_{hkl}) by scanning in angle (θ_{hkl}). However, in TOF techniques we have a range of wavelengths λ_{hkl} and we can rewrite the Bragg equation as

$$\lambda_{hkl} = 2d_{hkl}\sin\theta \tag{6}$$

i.e. we can measure a whole range of d-spacings (Bragg reflections) at a fixed scattering angle 2θ by scanning in wavelength ($\equiv$TOF). This is the basic principle of TOF diffraction as a fixed-angle, wavelength-dispersive technique (Figure 1).
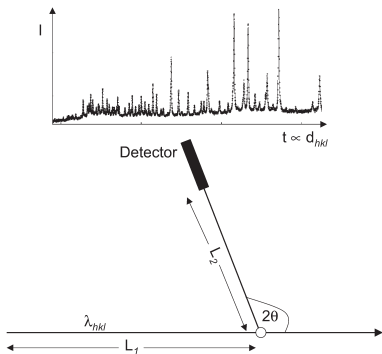
Figure 1: The basic principle of TOF diffraction. The time- (wavelength-) dispersive white beam is incident on the sample, and the diffraction pattern recorded at a fixed scattering angle 2θ. The total flight path, $L=L_1$ (source-sample distance)+L_2 (sample-detector distance). In this fixed geometry, the d-spacing d_{hkl} is directly proportional to the time-of-flight (Eq. 4) and the diffraction pattern is recorded as shown.

It is also, of course, possible to measure such TOF diffraction patterns simultaneously at many angles, in multi-detectors or in multiple detector banks. This can either lead to higher count-rates when the patterns measured in different detectors are summed and "focused,, (usually in the data processing software), or can lead to additional information being available in the diffraction pattern measured in the different detector banks. This is a trend very much in evidence on modern TOF diffractometers (Figure 2).
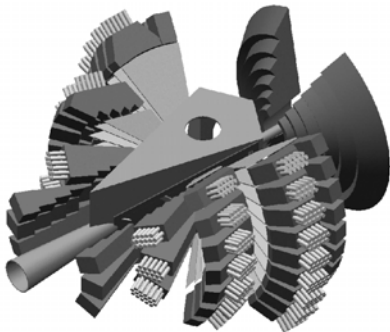
Figure 2: An example of a modern multi-detector bank TOF diffractometer, the GEM instrument at ISIS. The detectors are arranged in a series of banks around the sample tank, from low angles (lower left) to backscattering (upper right). GEM is used in the study of both crystalline (powder diffraction) and disordered materials (liquids and amorphous scattering).

2. Resolution

Among the important characteristics of a TOF diffraction instrument is that the resolution ($\Delta d/d$ or $\Delta Q/Q$) of a diffraction pattern measured at a given scattering angle (or, for example, in a given "focused,, detector bank)

(i)   is constant over the whole diffraction pattern (the angular term $\Delta\theta\cot\theta$ in the resolution being constant) and

(ii) can be improved linearly with the length of the instrument (by minimising the term $\Delta L/L$, where ΔL is a constant term reflecting the finite width of the moderator, and L is the length of the instrument).

As an example, the TOF powder diffractometer HRPD at the ISIS source has an overall flight path of around 100m, and an effective moderator width of around 3cm (the moderator is 5cm thick but has a poisoning layer which reduces this). Thus the $\Delta L/L$ term is of order 3×10^{-4}. With the main detector bank in the backscattering region (2θ close to $180°$, θ close to $90°$), the angular term in the resolution, linear in $\cot\theta$, is minimised and the overall resolution optimised. In the hi ghest resolution case, HRPD offers $\Delta d/d$ of around 4×10^{-4}. Of particular note is that this very high $\Delta d/d$ resolution is maintained over the whole diffraction pattern (Figure 3).
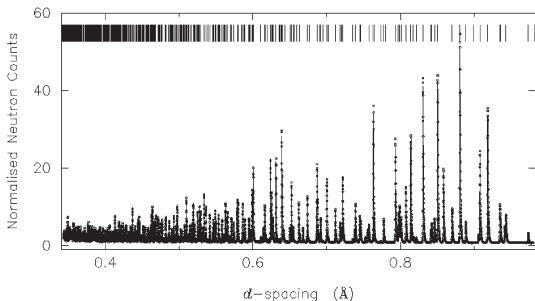
Figure 3: Powder diffraction pattern of Al_2O_3 measured on the high resolution diffractometer HRPD at ISIS. The excellent $\Delta d/d$ resolution is essentially constant over the whole pattern.

3. Q-Range

Another important aspect of a diffraction experiment is the Q-range (d-spacing range) accessed in a single measurement. As can simply be seen, to get to low values of d (high values of Q), one should measure at short TOF, i.e. with short

wavelength, high energy neutrons. Spallation sources are rich in such neutrons and so are well suited to short d/high Q measurements. For maximum Q-range it is also important to measure at a range of angles (in addition to measuring over a wide wavelength range), as lower angles give generally lower Q data, while higher angles give access to higher Q.

4. Powder Diffraction

The principles of TOF powder diffraction have been discussed above. High resolution diffractometers can allow the measurements of d-spacings of as low as 0.25 Å and refinement of structures of up to around 100 atoms.

5. Single Crystal Diffraction

Single crystal diffraction on a TOF instrument is by far most efficiently carried out using area detectors. White beam single crystal diffraction with an area detector (and a stationary crystal) is termed Laue diffraction, while adding wavelength discrimination
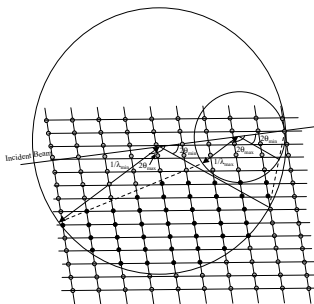
Figure 4: The geometry of TOF Laue diffraction. The two Ewald spheres are defined by the minimum and maximum wavelengths used – they have radii $1/\lambda_{min}$ and $1/\lambda_{max}$. The $2\theta_{min}$ and $2\theta_{max}$ values are defined by the angles sub-tended by the area detector. In this two-dimensional projection, all areas of reciprocal space between the Ewald sphere surfaces and the dotted lines are observed in a single measurement with a stationary crystal and detector; the reciprocal lattice points coloured in black (along with the spaces in between).

using TOF techniques leads to the TOF Laue diffraction used on such instruments. The particular feature of this technique is that it allows access to large volumes of reciprocal space simultaneously in a single measurement (Figure 4). These reciprocal space volumes, moreover, are completely resolved in three-dimensions.

This means that a single measurement accesses many Bragg reflections but also offers a wide survey of reciprocal space, ideally suited to the study of other features such as diffuse scattering which do not necessarily occur at the Bragg reflection positions. Routine determination of organic and other structures of 100 or more independent atoms is possible, with full anisotropic refinement of thermal parameters, and access to d-spacings of as low as 0.25 Å in simpler materials.

6. Diffraction From Disordered Materials

The important aspect of studies of materials which exhibit short range order, such as liquids, amorphous materials and highly disordered crystals, is to access a very wide Q-range in the measured pattern, S(Q). Only by so doing, along with very accurate determination of the instrument normalisation and background, can the pattern be reliably inverted (by Fourier transformation) to the pair distribution function g(r).

This g(r) function gives information about the relative distributions of the particles (e.g atoms or molecules) in the sample. While the principles of the method used for collecting TOF diffraction data from disordered materials are very similar to those for powder diffraction (Figure 1), in this case it is especially important to use a wide wavelength range at multiple angles (Figure 2; the GEM instrument is used to study both crystalline and disordered materials). However, it is also vital to keep the detectors well calibrated (both in terms of neutron detection performance and position) and very well shielded (to reduce background). Good secondary collimation (shielding between the sample and detector) is therefore usually employed, and the stationary detector arrangment is beneficial here. Q values of up to 50 Å^{-1} can be accessed.

7. Small Angle Neutron Scattering (SANS)

As its name implies, SANS is a forward scattering technique. Once again the strength of TOF SANS is in allowing simultaneous access to a very wide Q-range. By coupling the wavelength range allowed by the TOF technique with a fairly wide angle subtended by the area detector usually employed, TOF SANS typically accesses Q ranges of ~0.005 – 0.2 Å^{-1} in a single measurement without moving the detector. This has the benefit of allowing often complex 3D modelling to be carried out on the scattering patterns.

8. Neutron Reflectivity

Once again NR on a TOF source is a fixed angle technique. It is usually carried out on a horizontal sample as shown in Figure 5.
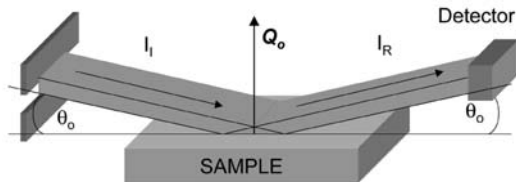
Figure 5: The geometry of TOF neutron reflectometry. The white beam (I) is incident upon a horizontal sample, and the reflectivity profile (R) is recorded as a function of TOF at a fixed angle, providing the $I_R(Q)$ used to analyse the characteristics of the sample perpendicular to the surface.

The use of a fixed horizontal sample in this way greatly simplifies the study of liquid surfaces.

The reflectivity patterns are recorded in total reflection geometry $\theta_i = \theta_r$, in the fixed detector (Figure 6), with the Q-range being provided by the wavelength scanning of the TOF method.

Interference fringes are observed in the reflectivity profile if there is a variation in the scattering length density perpendicular to the surface (see Chapter on Reflectometry). The determined variation in scattering length density can reflect changes in chemical composition, or the presence of, for example, a multilayer structure. Detailed modelling of the scattering length density can be carried out, most reliably if a wide range of reflectivity (and Q) have been measured – reflectivities of as low as 10^{-6} can be accessed. Accurate modelling of the composition of adsorbed chemical systems is often achieved, as in SANS, by the use of contrast variation. In this method selected components of the system are deuterated, the large variation in scattering lengths between H and D leading to substantial changes in the scattered intensities, thus offering extra information to assist in reliable model building. An effective "resolution" of around an Ångstrom in layer thickness is easily obtained in NR.
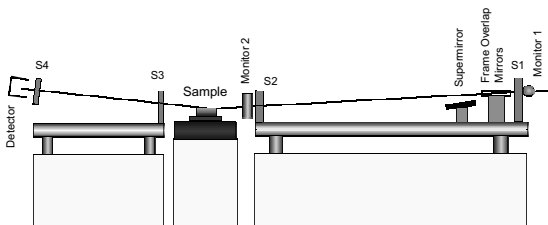
Figure 6: Schematic view of the CRISP reflectometer at ISIS, showing the horizontal geometry, the arrangement of apertures, the horizontal sample and the fixed detector.

Off-specular reflection can also be measured, usually using an area detector, and gives information on, for example, surface roughness or on local surface inhomogeneities.

9. Sample Environment

In common with all neutron scattering techniques, the use of sample environment in TOF diffraction is a major strength. There are specific advantages inherent in the TOF technique, however, related to the ability to measure the entire diffraction pattern at a single, fixed scattering angle. For complicated, bulky sample environment apparatus, it may therefore be possible to leave only small apertures, for the incoming beam and at limited fixed scattering angles, yet still measure the diffraction of interest (Figure 7).

Typical applications of this method include high pressure cells and thick-walled chemical reaction cells. The high degree of collimation means that extraneous scattering from these bulky items is minimised, and the signal from the (sometimes small) sample optimised.

10. Neutron Strain-Scanning

The neutron strain-scanning technique basically involves measuring diffraction
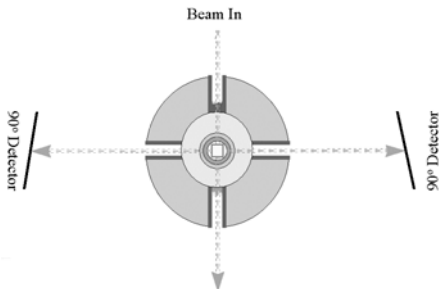
Figure 7: The TOF neutron diffraction technique is well suited to studying samples inside bulky sample environment apparatus, the ability to measure the whole diffraction pattern at a single scattering angle (Eq. 6; Figure 1) being an important factor in this. Here the sample is contained inside apparatus with only narrow apertures for incoming and outgoing beams and at very limited scattering angles necessary.

patterns from limited gauge volumes within a bulky engineering component, and characterises internal stresses and strains from the changes in position and shape of the measured Bragg peaks. The benefits of TOF for neutron strain-scanning follow from the above discussions of TOF powder diffraction and sample environment.

11. Further information

Further information on time-of-flight diffraction, instrumentation, techniques and applications can be found on the WWW site of the ISIS Pulsed Neutron and Muon Facility, Rutherford Appleton Laboratory, UK (http://www.isis.rl.ac.uk).

Polarised Neutron Scattering

E. Lelièvre-Berna, J.R. Stewart and F. Tasset

1 INTRODUCTION
1.1 The neutron spin and magnetic moment

The neutron carries a spin $\vec{s}$ which is an internal angular momentum with the quantum number $\frac{1}{2}$. The eigenvalue of the operator $\vec{s}^{\,2}$ is $s\,(s+1)\,\hbar^2 = \frac{3}{4}\hbar^2$ and the eigenvalues of the operator s_z are $m_s = \pm\frac{1}{2}\,\hbar$.

The neutron carries a magnetic moment $\vec{\mu} = \gamma_n \mu_s \vec{\sigma}$ where $\gamma_n = -1.913$ is the value of the neutron magnetic moment, μ_s is the nuclear Bohr magneton, and $\vec{\sigma} = \frac{2\vec{s}}{\hbar}$ is the angular momentum of the neutron. The gyromagnetic ratio of the neutron $\gamma_L = \frac{2}{\hbar}\gamma_n \mu_s$, which must not be confused with γ_n, is the ratio between the magnetic moment and the spin moment and is equal to: $\gamma_L = -1.8324\ 10^8\ rad\ s^{-1}\ T^{-1}$.

1.2 The polarisation of a neutron beam

It can be shown that the spin polarisation of a neutron beam is a classical vector in the space of the laboratory. In a particular direction $\vec{\alpha}$, the component P_α is defined as $P_\alpha = \frac{n_+ - n_-}{n_+ + n_-}$ where n_+ and n_- are the number of neutrons which fall in the $\left|+\frac{1}{2}\right\rangle$ and $\left|-\frac{1}{2}\right\rangle$ eigenstates of the angular momentum component.

1.3 The action of a magnetic field

In a magnetic field $\vec{H}$, the torque exerted on a magnetic moment $\vec{\mu}$ is $\Gamma = \vec{\mu} \wedge H$. The magnetic moment of the neutron precesses around the field. The corresponding Larmor frequency is determined by ω_L [rad/s] $= \gamma_L\ H = 18324\ H$ [Gauss]. For a moving neutron, the precession angle is given by $\Delta\varphi$ [°] $= 2.65\ \lambda[\text{Å}]\ H$ [Gauss] ℓ [cm]: the polarisation vector of a neutron beam with a 2 Å wavelength will precess by 53° in a 10 Gauss.cm field integral.

When the direction of the field is slow compared to the Larmor frequency ($\omega_H \langle\langle \omega_L$), the longitudinal component of the polarisation, i.e. the component which is parallel to the field, is adiabatically conserved and the transverse components keep rotating around the varying field. If the direction of the field changes abruptly from $\vec{H}$ to $\vec{H}'$ ($\omega_H \rangle \omega_L$), the polarisation vector replaces its rotation around $\vec{H}$ by a rotation around $\vec{H}'$.

2 THE FUNDAMENTAL EQUATIONS

2.1 The nuclear structure factor

For a non-Bravais single crystal, i.e. a crystal with more than one atom per unit cell, the nuclear structure factor at the reciprocal lattice point $\vec{Q}$ reads [1]:

$$N(\vec{Q}) = \sum_j \bar{b}_j \exp(i\vec{Q} \cdot \vec{r}_j) \exp(-W_j)$$

where $\bar{b}_j$ and W_j are the Fermi length and the Debye-Waller factor of the atom j located at the position $\vec{r}_j$ of the unit cell.

2.2 The magnetic interaction vector

For a non-Bravais single crystal, the magnetic interaction vector at the reciprocal lattice point $\vec{Q}$ is given by [1]:

$$\vec{M}_\perp(\vec{Q}) = \frac{\gamma e^2}{2 m_e c^2} \frac{\vec{Q} \wedge \vec{M}(\vec{Q}) \wedge \vec{Q}}{||\vec{Q}||^2}$$

where:

$$\frac{\gamma e^2}{2 m_e c^2} = 0.2695 \ 10^{-12} \ cm/\mu_B, \quad \vec{M}(\vec{Q}) = \sum_j f_j(\vec{Q}) \vec{m}_j^{\vec{k}} \exp(i\vec{Q} \cdot \vec{r}_j) \exp(-W_j).$$

$f_j(\vec{Q})$ is the form factor and $\vec{m}_j^{\vec{k}}$ is the Fourier component $\vec{k}$ of the magnetic moment of the atom j. One must notice that because of the dipolar nature of the magnetic interaction, the neutron is only sensitive to the projection of $\vec{M}(\vec{Q})$ on a plane perpendicular to the scattering vector $\vec{Q}$.

2.3 The scattering cross-section and the scattered polarisation

Using the density matrix formalism, Maleyev et al. [2,3] and Blume [4] could predict the scattering cross-section σ_i and the scattered polarisation vector $\vec{P}$ within the Born approximation. Both fundamental equations are the sum of four parts summarised in table 1 [8], where $\vec{k}_i$ and $\vec{k}_f$ are the incident and final wave vectors of the neutron beam, and $\mathcal{H}$ is the Van Hove correlation function:

$$\mathcal{H}(A,B) = \frac{1}{\pi\left(1-\exp\left(-\frac{\hbar\omega}{k_B T}\right)\right)} \langle A,B \rangle_\omega''$$

$$\mathcal{H}_\pm(N_{-\vec{Q}}, \vec{M}_{\perp,\vec{Q}}) = \mathcal{H}(N_{-\vec{Q}}, \vec{M}_{\perp,\vec{Q}}) \pm \mathcal{H}(\vec{M}_{\perp,-\vec{Q}}, N_{\vec{Q}})$$

Table 1: Scattering cross-section $\sigma_t = N_0 \dfrac{(2\pi)^3}{v_0} \sum_j \sigma_j$ and scattered polarisation vector $\left\{\vec{P}\sigma\right\}_t = N_0 \dfrac{(2\pi)^3}{v_0} \sum_j \left\{\vec{P}\sigma\right\}_j$

Contribution	Elastic scattering	Inelastic scattering
(n) Nuclear	$\sigma_n = NN^*$	$\sigma_n = \frac{k_f}{k_i}\mathcal{H}\left(N_{-\vec{Q}}, N_{\vec{Q}}\right)$
	$\{\vec{P}\sigma\}_n = \vec{P}_i\,\sigma_n$	$\{\vec{P}\sigma\}_n = \vec{P}_i\,\sigma_n$
(m) Magnetic non-chiral	$\sigma_m = \vec{M}_\perp \cdot \vec{M}_\perp^*$	$\sigma_m = \frac{k_f}{k_i}\,S_{\alpha\beta}\,\delta_{\alpha\beta}$
	$\{\vec{P}\sigma\}_m = -\,\vec{P}_i\,\sigma_m + \dots$	$\{\vec{P}_\alpha\sigma\}_m = \frac{k_f}{k_i}P_{i\beta}\dots$
	$\dots 2\Re\left(\vec{M}_\perp\left(\vec{P}_i\cdot\vec{M}_\perp^*\right)\right)$	$\dots\left[(S_{\alpha\beta}+S_{\beta\alpha})-\delta_{\alpha\beta}\delta_{\beta\alpha}\right]$
		$S_{\alpha\beta} = \mathcal{H}\left(M_{\perp-\vec{Q}}^\alpha, M_{\perp\vec{Q}}^\beta\right)$
(c) Magnetic chiral	$\sigma_c = \iota\vec{P}_i\cdot\left(\vec{M}_\perp^*\wedge\vec{M}_\perp\right)$	$\sigma_c = \frac{k_f}{k_i}\,\iota\,S_{\alpha\beta}\,\epsilon_{\alpha\beta\gamma}\,P_{i\gamma}$
	$\{\vec{P}\sigma\}_c = -\,\iota\left(\vec{M}_\perp^*\wedge\vec{M}_\perp\right)$	$\{\vec{P}_\alpha\sigma\}_c = -\frac{k_f}{k_i}\iota\epsilon_{\alpha\beta\gamma}S_{\beta\gamma}$
		$S_{\alpha\beta} = \mathcal{H}\left(M_{\perp-\vec{Q}}^\alpha, M_{\perp\vec{Q}}^\beta\right)$
(i) Nuclear–magnetic	$\sigma_i = 2\vec{P}_i\cdot\Re\left(N^*\vec{M}_\perp\right)$	$\sigma_i = \frac{k_f}{k_i}\,\iota\,\vec{S}_+\cdot\vec{P}_i$
	$\{\vec{P}\sigma\}_i = 2\Re\left(N^*\vec{M}_\perp\right) +$	$\{\vec{P}\sigma\}_i = \frac{k_f}{k_i}\left(\vec{S}_+ + i\vec{S}_-\wedge\vec{P}_i\right)$
	$\quad 2\vec{P}_i\wedge\Im\left(N^*\vec{M}_\perp\right)$	$\vec{S}_\pm = \mathcal{H}_\pm\left(N_{-\vec{Q}}, \vec{M}_{\perp\vec{Q}}\right)$

3 THE POLARISED NEUTRON TECHNIQUES

3.1 The spin-dependent diffraction technique

The polarised neutron diffraction technique takes advantage of the incident polarisation dependency of the cross-section σ_t to measure precise quantitative magnetisation distributions of single crystals. Its sensitivity to the distribution of unpaired electrons in the unit cell is greater than for the conventional method using unpolarised-beams (about 0.1 $m\mu_B$). This technique is mainly used for investigating single crystals that are ferro- or ferri-magnetically ordered in an applied magnetic field. It can also be applied to some antiferromagnetic materials where

$$\Re\left(N^*\vec{M}\right)\neq 0 \text{ or } \vec{M}_\perp^*\wedge\vec{M}_\perp\neq 0$$

If the beam is perfectly polarised parallel (+) or opposite (-) to the applied field ($P_i = \pm 1$), and if the sample is ferro- or para-magnetic and has a centre of symmetry, we get the simple expression for the flipping ratio:

$$R(\vec{Q}) = \frac{\sigma_t^+}{\sigma_t^-} = \left(\frac{N(\vec{Q}) + \sin(\alpha)\,M(\vec{Q})}{N(\vec{Q}) - \sin(\alpha)\,M(\vec{Q})}\right)^2$$

where α is the angle between the polarisation vector (i.e. the applied field) and the direction of the scattering vector $\vec{Q}$. From experimental values of $R(\vec{Q})$, the

preceding quadratic equation provides two solutions for the ratio $\gamma(\bar{Q}) = M(\bar{Q})/N(\bar{Q})$. The crystal structure having been measured by other techniques, the values of $N(\bar{Q})$ are known and it is normally easy to select the appropriate $M(\bar{Q})$.

3.2 The spin-flip and non-spin-flip cross sections

Following early experiments at Gatchina [5], Moon, Riste, and Koehler [6] looked at the scattered polarisation outside the direct beam and produced a subset of four spin-state indexed cross-sections from a simplified theory. The direction of the incident polarisation is set adiabatically in an arbitrary direction (usually $\vec{z}$ or $\vec{Q}$) using a strong enough magnetic guide-field at the sample position (see §1.3). The scattered polarisation may have any direction but it is only analysed in the longitudinal direction, i.e. the one parallel to the guide-field (the transverse components are not analysed). The four cross-sections they produced are deduced from the fundamental equations by keeping only the component parallel to the incident polarisation, e.g. $\vec{z}$:

$$\left\{\bar{P}\sigma\right\}_{l,z} = P_{l,z}\left(NN^* + M_{\perp,z}M^*_{\perp,z} - M_{\perp,x}M^*_{\perp,x} - M_{\perp,y}M^*_{\perp,y}\right)$$

$$+ N^*M_{\perp,z} + NM^*_{\perp,z} - iM^*_{\perp,x}M_{\perp,y} + iM_{\perp,x}M^*_{\perp,y}$$

For a perfectly polarised beam, one obtains the famous four cross-sections:

$$\sigma^{+,+}_{l,z} = N_0\frac{(2\pi)^3}{v_0}\left|N + M_{\perp,z}\right|^2 \qquad \sigma^{-,-}_{l,z} = N_0\frac{(2\pi)^3}{v_0}\left|N - M_{\perp,z}\right|^2$$

$$\sigma^{+,-}_{l,z} = N_0\frac{(2\pi)^3}{v_0}\left|M_{\perp,x} + iM_{\perp,y}\right|^2 \qquad \sigma^{-,+}_{l,z} = N_0\frac{(2\pi)^3}{v_0}\left|M_{\perp,x} - iM_{\perp,y}\right|^2$$

There is no nuclear contribution to the spin-flip cross-sections $\sigma^{+,-}_{l,z}$ and $\sigma^{-,+}_{l,z}$ and only the magnetic component $M_{\perp,z}$ parallel to the polarisation vector, i.e. the guide-field, contributes to the non-spin-flip cross-sections $\sigma^{+,+}_{l,z}$ and $\sigma^{-,-}_{l,z}$. Therefore, if the polarisation is parallel to the scattering vector $\bar{Q}$, only the nuclear part participates to the non-spin-flip cross-section.

3.3 XYZ–polarization analysis

The diffuse scattering that is found beneath the nuclear and magnetic Bragg peaks in a neutron diffraction pattern, and which is often considered as merely an annoying background contribution, can provide detailed information on magnetic disorder, and upon the interplay between such disorder and the local atomic defect structures. However magnetic disorder scattering is generally small in amplitude and often coexists with nuclear disorder scattering and nuclear spin incoherent

scattering. In order to separate each of these components it is necessary to use polarised neutron techniques. For example, in order to study spin correlations and magnetic defect structures in systems such as paramagnets, spin glasses and antiferromagnets, so called XYZ-polarisation analysis (XYZ–PA) is required [7].

In XYZ–PA, the longitudinal component of polarization of the scattered beam along the arbitrarily defined x- y- and z-directions is measured. Using this technique, and ensuring that the scattering vector is always in the x-y plane (defined with respect to the neutron polarization vector), one can separate the nuclear, magnetic and spin-incoherent structure factors unambiguously, *on a multi-detector spectrometer*, by combining the six measured cross-sections (x-, y- and z- directions, spin-flip and non-spin-flip) given below:

$$
\begin{vmatrix}
\sigma_x^{sf} = \frac{1}{2}\left(\cos^2\alpha + 1\right)\sigma_{mag} + \frac{2}{3}\,\sigma_{si} & \sigma_x^{nsf} = \frac{1}{2}\left(\sin^2\alpha + 1\right)\sigma_{mag} + \frac{1}{3}\,\sigma_{si} + \sigma_{nc} + \sigma_{ii} \\
\sigma_y^{sf} = \frac{1}{2}\left(\sin^2\alpha + 1\right)\sigma_{mag} + \frac{2}{3}\,\sigma_{si} & \sigma_y^{nsf} = \frac{1}{2}\left(\cos^2\alpha + 1\right)\sigma_{mag} + \frac{1}{3}\,\sigma_{si} + \sigma_{nc} + \sigma_{ii} \\
\sigma_z^{sf} = \frac{1}{2}\,\sigma_{mag} + \frac{2}{3}\,\sigma_{si} & \sigma_z^{nsf} = \frac{1}{2}\,\sigma_{mag} + \frac{1}{3}\,\sigma_{si} + \sigma_{nc} + \sigma_{ii}
\end{vmatrix}
$$

The subscripts *nc, mag, si,* and *ii* stand for "nuclear coherent," "magnetic," "spin incoherent," and "isotope incoherent," contributions respectively. These equations apply to systems with collinear magnetisation and a randomly oriented moment direction (i.e., a paramagnetic system or an antiferromagnetic powder in zero external field). In antiferromagnetically ordered single crystals, there will, in general, be a strong correlation between the x and y components of the sample magnetisation $\vec{M}$, i.e. the components of $\vec{M}$ in the scattering plane. Therefore, in order to separate the magnetic cross-section in an ordered antiferromagnetic single crystal, either the angle between $\vec{M}$ and $\vec{Q}$, or the magnetic structure factor of the sample must be known in advance. In practice, if neither of these quantities are known, then application of the equations will result merely in a possible change of sign of the magnetic intensity, depending on the moment direction. In the case of non-collinear systems, such as helical magnets, cross-terms appear in the magnetic interaction potential and the equations do not hold [2–4]. The XYZ–PA method cannot be applied to the study of ferromagnets since ferromagnetic domains and demagnetisation fields will in general depolarise the neutron beam.

3.4 Zero-field spherical neutron polarimetry

The only way to measure the three components of the scattered polarisation is to connect two independent magnetic guide-fields onto a zero-field sample chamber. Cryopad is presently the only device able to achieve full vectorial control of the neutron polarisation over a large $\vec{Q}$ range with a good precision [8]. The sample

chamber is maintained in a zero-field state, preventing any polarisation precession due to a parasitic field.

In the case of magnetic structures, spherical neutron polarimetry (SNP) allows the direct determination of the direction and phase of the magnetic interaction vector, and for $\bar{\tau} = 0$ antiferromagnetic structures, SNP is a powerful method for measuring precision form factors and magnetisation distributions [9].

Because transverse components contain information related to the nuclear–magnetic interference terms, SNP is clearly the best method to study antiferromagnetic compounds for which the magnetic and nuclear information are located at the same place in the reciprocal space. In the inelastic case, one should be able to observe the spin–lattice correlations expected in geometrically frustrated antiferromagnets or spin-Peierls systems like $CuGe0_3$.

Here are a few rules describing the polarisation behaviour when carrying out SNP experiments:

– The polarisation is conserved when the interaction is purely nuclear and coherent (e.g. an isolated phonon or a nuclear Bragg peak without nuclear spin polarisation).

– The polarisation precesses by π around $\bar{M}_\perp$ when the interaction is purely magnetic non-chiral (e.g. a magnetic satellite of a collinear arrangement or a magnon).

– In the case of a non-collinear magnetic structure, the intensity may depend on $\vec{P}_i$ and for an helix, $\bar{M}_\perp \wedge \bar{M}_\perp$ may create polarisation along the scattering vector $\vec{Q}$.

– When there are nuclear–magnetic interferences, the intensity depends on $\vec{P}_i$ when N and $\bar{M}_\perp$ are in phase. Polarisation is created along $\bar{M}_\perp$ when N and $\bar{M}_\perp$ are in phase (e.g. Fe_2O_3), and the polarisation rotates around $\bar{M}_\perp$ when N and $\bar{M}_\perp$ are in quadrature (e.g. Cr_2O_3).

References

1. G.L. Squires, "Thermal neutron scattering,,, Cambridge University Press.

2. S.V. Maleyev, *Physica B* **276-268** (1998) 236

3. S.V. Maleyev, V.G. Bar'yakhtar, R.A. Suris, *Fiz. Tv. Tela* **4** (1962) 3461 [*Sov. Phys. – Solid state* **4**(12) (1963) 2533]

4. M. Blume, *Phys. Rev.* **130** (1963) 1670

5. G.M. Drabkin et al., *Sov. Phys. JETP* **20** (1965) 1548

6. R.M. Moon, T. Riste and W. Koehler, *Phys. Rev.* **181** (1969) 2533

7. O. Schärpf and H. Capellmann, *Phys. Stat. Sol.* **A135** (1993) 359; O. Schärpf and

2.4-7

H Capellmann, *Z. Phys. B - Condens. Matter* **80** (1990) 253

8. F. Tasset, *Physica B* **156-157** (1989) 627; V. Nunez, P.J. Brown, J.B. Forsyth and F. Tasset: *Physica B* **174** (1991) 60; P.J. Brown, J.B. Forsyth and F. Tasset: *Proc. R. Soc. Lond. A* **442** (1993) 147; F. Tasset, *Physica B* **297** (2001) 1; P.J. Brown, *Physica B* **297** (2001) 198

9. P.J. Brown, J.B. Forsyth and F. Tasset: *Physica B* **267-268** (1999) 215; P.J. Brown, J.B. Forsyth, E. Lelièvre-Berna and F. Tasset: *J. Phys.: Condens. Matter* **14** (2002) 1

Magnetic Form Factors

P.J. Brown

The magnetic form factor $f(\mathbf{q})$ is obtained from the fourier transform of the magnetisation distribution of a single magnetic atom. Assuming that it has a unique magnetisation direction it can be written

$$\mathbf{M} \int m(\mathbf{r})e^{i\mathbf{q}\cdot\mathbf{r}}\,dr = \mathbf{M}f(\mathbf{q}) \qquad 1)$$

where $\mathbf{M}$ gives the magnitude and direction of the moment and $m(\mathbf{r})$ is a normalised scalar function which describes how the intensity of magnetisation varies over the volume of the atom. When the magnetisation arises from electrons in a single open shell the magnetic form factor can be calculated from the radial distribution of the electrons in that shell. The integrals from which the form factors are obtained have the form

$$\langle j_L(q)\rangle = \int U^2(r)j_L(qr)4\pi r^2\,dr \qquad 2)$$

The j_l are the spherical Bessel functions defined by\begin

$$j_l(x) = \sqrt{\frac{\pi}{2x}}J_{l+\frac{1}{2}}(x) \qquad 3)$$

If the open shell has orbital quantum number l the form factor for spin moment is

$$f_s(\mathbf{q}) = \frac{1}{M_S}\sum_{L=0}^{2l} i^L \langle j_L(q)\rangle \sum_{M=-L}^{L} S_{LM}Y_M^L(\hat{\mathbf{q}}) \qquad 4)$$

and that for orbital moment

$$f_o(\mathbf{q}) = \frac{1}{M_L}\sum_{L=0,2,\ldots}^{2l} (\langle j_L(q)\rangle + \langle j_{L+2}(q)\rangle) \sum_{M=-L}^{L} B_{LM}Y_M^L(\hat{\mathbf{q}}) \qquad 5)$$

The coefficients S_{LM}, B_{LM} have to be computed from the orbital wave-function [1]. The total spin moment M_s is given by S_{00} and the orbital moment M_L by B_{00}. For small q the dipole approximation

$$f(\mathbf{q}) = (L + 2S)\langle j_0(q)\rangle L\langle j_2(q)\rangle \qquad 6)$$

Tables 1-4 give coefficients of an analytic approximation to the $\langle j_0\rangle$ integrals for the d electrons in ions of the 3d and 4d series, and the f electrons of some rare earth and actinide ions. The approximation has the form

$$\langle j_0(s)\rangle = A\exp(-as^2) + B\exp(-bs^2) + C\exp(-cs^2) + D \qquad 7)$$

For these expansions $s = \sin\theta/\lambda$ in units of Å^{-1}.

The integrals $\langle j_l\rangle$ with $L \neq 0$ are zero when s = 0 and have been fitted with the form

$$\langle j_0(s)\rangle = (A\exp(-as^2) + B\exp(-bs^2) + C\exp(-cs^2) + D)\,s^2 \qquad 8)$$

2.5-2

Tables 5-13 give the coefficients obtained. For the transition metal series the fits were made withform factor integrals calculated from Hartree-Fock wave-functions [2]. For the rare-earth and actinide series the fits were with Dirac-Fock form factors [3, 4]. In the tables the number following the atom symbol indicates the ionisation state of the atom. Thus the coefficients following Fe0 are for a neutral iron atom and those following Fe2 are for Fe^{2+}

References

[1] Marshall W and Lovesey S W (1971) *Theory of thermal neutron scattering, Chapter 6*, Oxford University Press.
[2] Clementi E and Roetti C (1974) *Atomic Data and Nuclear Data Tables* **14**, 177-478.
[3] Freeman A J and Descleaux J P (1979) *J. Magn. Mag. Mater.* **12**, 11-21.
[4] Descleaux J P and Freeman A J (1978) *J. Magn. Mag. Mater.* **8**, 119-129.

Table 1: $\langle j_0 \rangle$ form factors for 3d transition elements and their ions

Ion	A	a	B	b	C	c	D
Sc0	0.2512	90.0296	0.3290	39.4021	0.4235	14.3222	−0.0043
Sc1	0.4889	51.1603	0.5203	14.0764	−0.0286	0.1792	0.0185
Sc2	0.5048	31.4035	0.5186	10.9897	−0.0241	1.1831	0.0000
Ti0	0.4657	33.5898	0.5490	9.8791	−0.0291	0.3232	0.0123
Ti1	0.5093	36.7033	0.5032	10.3713	−0.0263	0.3106	0.0116
Ti2	0.5091	24.9763	0.5162	8.7569	−0.0281	0.9160	0.0015
Ti3	0.3571	22.8413	0.6688	8.9306	−0.0354	0.4833	0.0099
V0	0.4086	28.8109	0.6077	8.5437	−0.0295	0.2768	0.0123
V1	0.4444	32.6479	0.5683	9.0971	−0.2285	0.0218	0.2150
V2	0.4085	23.8526	0.6091	8.2456	−0.1676	0.0415	0.1496
V3	0.3598	19.3364	0.6632	7.6172	−0.3064	0.0296	0.2835
V4	0.3106	16.8160	0.7198	7.0487	−0.0521	0.3020	0.0221
Cr0	0.1135	45.1990	0.3481	19.4931	0.5477	7.3542	−0.0092
Cr1	−0.0977	0.0470	0.4544	26.0054	0.5579	7.4892	0.0831
Cr2	1.2024	−0.0055	0.4158	20.5475	0.6032	6.9560	−1.2218
Cr3	−0.3094	0.0274	0.3680	17.0355	0.6559	6.5236	0.2856
Cr4	−0.2320	0.0433	0.3101	14.9518	0.7182	6.1726	0.2042
Mn0	0.2438	24.9629	0.1472	15.6728	0.6189	6.5403	−0.0105
Mn1	−0.0138	0.4213	0.4231	24.6680	0.5905	6.6545	−0.0010
Mn2	0.4220	17.6840	0.5948	6.0050	0.0043	−0.6090	−0.0219
Mn3	0.4198	14.2829	0.6054	5.4689	0.9241	−0.0088	−0.9498
Mn4	0.3760	12.5661	0.6602	5.1329	−0.0372	0.5630	0.0011
Fe0	0.0706	35.0085	0.3589	15.3583	0.5819	5.5606	−0.0114
Fe1	0.1251	34.9633	0.3629	15.5144	0.5223	5.5914	−0.0105
Fe2	0.0263	34.9597	0.3668	15.9435	0.6188	5.5935	−0.0119
Fe3	0.3972	13.2442	0.6295	4.9034	−0.0314	0.3496	0.0044
Fe4	0.3782	11.3800	0.6556	4.5920	−0.0346	0.4833	0.0005
Co0	0.4139	16.1616	0.6013	4.7805	−0.1518	0.0210	0.1345
Co1	0.0990	33.1252	0.3645	15.1768	0.5470	5.0081	−0.0109
Co2	0.4332	14.3553	0.5857	4.6077	−0.0382	0.1338	0.0179
Co3	0.3902	12.5078	0.6324	4.4574	−0.1500	0.0343	0.1272
Co4	0.3515	10.7785	0.6778	4.2343	−0.0389	0.2409	0.0098
Ni0	−0.0172	35.7392	0.3174	14.2689	0.7136	4.5661	−0.0143
Ni1	0.0705	35.8561	0.3984	13.8042	0.5427	4.3965	−0.0118
Ni2	0.0163	35.8826	0.3916	13.2233	0.6052	4.3388	−0.0133
Ni3	0.00118	34.99982	0.34682	11.98742	0.66670	4.25185	-0.01484
Ni4	−0.0090	35.8614	0.2776	11.7904	0.7474	4.2011	−0.0163
Cu0	0.0909	34.9838	0.4088	11.4432	0.5128	3.8248	−0.0124
Cu1	0.0749	34.9656	0.4147	11.7642	0.5238	3.8497	−0.0127
Cu2	0.0232	34.9686	0.4023	11.5640	0.5882	3.8428	−0.0137
Cu3	0.0031	34.9074	0.3582	10.9138	0.6531	3.8279	−0.0147
Cu4	−0.0132	30.6817	0.2801	11.1626	0.7490	3.8172	−0.0165

Table 2: $\langle j_0 \rangle$ form factors for 4d atoms and ions

Ion	A	a	B	b	C	c	D
Y0	0.5915	67.6081	1.5123	17.9004	−1.1130	14.1359	0.0080
Zr0	0.4106	59.9961	1.0543	18.6476	−0.4751	10.5400	0.0106
Zr1	0.4532	59.5948	0.7834	21.4357	−0.2451	9.0360	0.0098
Nb0	0.3946	49.2297	1.3197	14.8216	−0.7269	9.6156	0.0129
Nb1	0.4572	49.9182	1.0274	15.7256	−0.4962	9.1573	0.0118
Mo0	0.1806	49.0568	1.2306	14.7859	−0.4268	6.9866	0.0171
Mo1	0.3500	48.0354	1.0305	15.0604	−0.3929	7.4790	0.0139
Tc0	0.1298	49.6611	1.1656	14.1307	−0.3134	5.5129	0.0195
Tc1	0.2674	48.9566	0.9569	15.1413	−0.2387	5.4578	0.0160
Ru0	0.1069	49.4238	1.1912	12.7417	−0.3176	4.9125	0.0213
Ru1	0.4410	33.3086	1.4775	9.5531	−0.9361	6.7220	0.0176
Rh0	0.0976	49.8825	1.1601	11.8307	−0.2789	4.1266	0.0234
Rh1	0.3342	29.7564	1.2209	9.4384	−0.5755	5.3320	0.0210
Pd0	0.2003	29.3633	1.1446	9.5993	−0.3689	4.0423	0.0251
Pd1	0.5033	24.5037	1.9982	6.9082	−1.5240	5.5133	0.0213

Table 3: $\langle j_0 \rangle$ form factors for rare earth ions

Ion	A	a	B	b	C	c	D
Ce2	0.2953	17.6846	0.2923	6.7329	0.4313	5.3827	−0.0194
Nd2	0.1645	25.0453	0.2522	11.9782	0.6012	4.9461	−0.0180
Nd3	0.0540	25.0293	0.3101	12.1020	0.6575	4.7223	−0.0216
Sm2	0.0909	25.2032	0.3037	11.8562	0.6250	4.2366	−0.0200
Sm3	0.0288	25.2068	0.2973	11.8311	0.6954	4.2117	−0.0213
Eu2	0.0755	25.2960	0.3001	11.5993	0.6438	4.0252	−0.0196
Eu3	0.0204	25.3078	0.3010	11.4744	0.7005	3.9420	−0.0220
Gd2	0.0636	25.3823	0.3033	11.2125	0.6528	3.7877	−0.0199
Gd3	0.0186	25.3867	0.2895	11.1421	0.7135	3.7520	−0.0217
Tb2	0.0547	25.5086	0.3171	10.5911	0.6490	3.5171	−0.0212
Tb3	0.0177	25.5095	0.2921	10.5769	0.7133	3.5122	−0.0231
Dy2	0.1308	18.3155	0.3118	7.6645	0.5795	3.1469	−0.0226
Dy3	0.1157	15.0732	0.3270	6.7991	0.5821	3.0202	−0.0249
Ho2	0.0995	18.1761	0.3305	7.8556	0.5921	2.9799	−0.0230
Ho3	0.0566	18.3176	0.3365	7.6880	0.6317	2.9427	−0.0248
Er2	0.1122	18.1223	0.3462	6.9106	0.5649	2.7614	−0.0235
Er3	0.0586	17.9802	0.3540	7.0964	0.6126	2.7482	−0.0251
Tm2	0.0983	18.3236	0.3380	6.9178	0.5875	2.6622	−0.0241
Tm3	0.0581	15.0922	0.2787	7.8015	0.6854	2.7931	−0.0224
Yb2	0.0855	18.5123	0.2943	7.3734	0.6412	2.6777	−0.0213
Yb3	0.0416	16.0949	0.2849	7.8341	0.6961	2.6725	−0.0229
Pr3	0.0504	24.9989	0.2572	12.0377	0.7142	5.0039	−0.0219

Table 4: $\langle j_0 \rangle$ Form factors for actinide ions

Ion	A	a	B	b	C	c	D
U3	0.5058	23.2882	1.3464	7.0028	−0.8724	4.8683	0.0192
U4	0.3291	23.5475	1.0836	8.4540	−0.4340	4.1196	0.0214
U5	0.3650	19.8038	3.2199	6.2818	−2.6077	5.3010	0.0233
Np3	0.5157	20.8654	2.2784	5.8930	−1.8163	4.8457	0.0211
Np4	0.4206	19.8046	2.8004	5.9783	−2.2436	4.9848	0.0228
Np5	0.3692	18.1900	3.1510	5.8500	−2.5446	4.9164	0.0248
Np6	0.2929	17.5611	3.4866	5.7847	−2.8066	4.8707	0.0267
Pu3	0.3840	16.6793	3.1049	5.4210	−2.5148	4.5512	0.0263
Pu4	0.4934	16.8355	1.6394	5.6384	−1.1581	4.1399	0.0248
Pu5	0.3888	16.5592	2.0362	5.6567	−1.4515	4.2552	0.0267
Pu6	0.3172	16.0507	3.4654	5.3507	−2.8102	4.5133	0.0281
Am2	0.4743	21.7761	1.5800	5.6902	−1.0779	4.1451	0.0218
Am3	0.4239	19.5739	1.4573	5.8722	−0.9052	3.9682	0.0238
Am4	0.3737	17.8625	1.3521	6.0426	−0.7514	3.7199	0.0258
Am5	0.2956	17.3725	1.4525	6.0734	−0.7755	3.6619	0.0277
Am6	0.2302	16.9533	1.4864	6.1159	−0.7457	3.5426	0.0294
Am7	0.3601	12.7299	1.9640	5.1203	−1.3560	3.7142	0.0316

Table 5: $\langle j_2 \rangle$ form factors for 3d transition elements and their ions

Ion	A	a	B	b	C	c	D
Sc0	10.8172	54.3270	4.7353	14.8471	0.6071	4.2180	0.0011
Sc1	8.5021	34.2851	3.2116	10.9940	0.4244	3.6055	0.0009
Sc2	4.3683	28.6544	3.7231	10.8233	0.6074	3.6678	0.0014
Ti0	4.3583	36.0556	3.8230	11.1328	0.6855	3.4692	0.0020
Ti1	6.1567	27.2754	2.6833	8.9827	0.4070	3.0524	0.0011
Ti2	4.3107	18.3484	2.0960	6.7970	0.2984	2.5476	0.0007
Ti3	3.3717	14.4441	1.8258	5.7126	0.2470	2.2654	0.0005
V0	3.8099	21.3471	2.3295	7.4089	0.4333	2.6324	0.0015
V1	4.7474	23.3226	2.3609	7.8082	0.4105	2.7063	0.0014
V2	3.4386	16.5303	1.9638	6.1415	0.2997	2.2669	0.0009
V3	2.3005	14.6821	2.0364	6.1304	0.4099	2.3815	0.0014
V4	1.8377	12.2668	1.8247	5.4578	0.3979	2.2483	0.0012
Cr0	3.4085	20.1267	2.1006	6.8020	0.4266	2.3941	0.0019
Cr1	3.7768	20.3456	2.1028	6.8926	0.4010	2.4114	0.0017
Cr2	2.6422	16.0598	1.9198	6.2531	0.4446	2.3715	0.0020
Cr3	1.6262	15.0656	2.0618	6.2842	0.5281	2.3680	0.0023
Cr4	1.0293	13.9498	1.9933	6.0593	0.5974	2.3457	0.0027
Mn0	2.6681	16.0601	1.7561	5.6396	0.3675	2.0488	0.0017
Mn1	3.2953	18.6950	1.8792	6.2403	0.3927	2.2006	0.0022
Mn2	2.0515	15.5561	1.8841	6.0625	0.4787	2.2323	0.0027
Mn3	1.2427	14.9966	1.9567	6.1181	0.5732	2.2577	0.0031
Mn4	0.7879	13.8857	1.8717	5.7433	0.5981	2.1818	0.0034
Fe0	1.9405	18.4733	1.9566	6.3234	0.5166	2.1607	0.0036
Fe1	2.6290	18.6598	1.8704	6.3313	0.4690	2.1628	0.0031
Fe2	1.6490	16.5593	1.9064	6.1325	0.5206	2.1370	0.0035
Fe3	1.3602	11.9976	1.5188	5.0025	0.4705	1.9914	0.0038
Fe4	1.5582	8.2750	1.1863	3.2794	0.1366	1.1068	−0.0022
Co0	1.9678	14.1699	1.4911	4.9475	0.3844	1.7973	0.0027
Co1	2.4097	16.1608	1.5780	5.4604	0.4095	1.9141	0.0031
Co2	1.9049	11.6444	1.3159	4.3574	0.3146	1.6453	0.0017
Co3	1.7058	8.8595	1.1409	3.3086	0.1474	1.0899	−0.0025
Co4	1.3110	8.0252	1.1551	3.1792	0.1608	1.1301	−0.0011
Ni0	1.0302	12.2521	1.4669	4.7453	0.4521	1.7437	0.0036
Ni1	2.1040	14.8655	1.4302	5.0714	0.4031	1.7784	0.0034
Ni2	1.7080	11.0160	1.2147	4.1031	0.3150	1.5334	0.0018
Ni3	1.46828	8.67134	0.17943	1.10579	1.10681	3.25742	-0.00227
Ni4	1.1612	7.7000	1.0027	3.2628	0.2719	1.3780	0.0025
Cu0	0.9182	14.4904	1.3329	4.7301	0.3842	1.6394	0.0035
Cu1	1.8814	13.4333	1.2809	4.5446	0.3646	1.6022	0.0033
Cu2	1.5189	10.4779	1.1512	3.8132	0.2918	1.3979	0.0017
Cu3	1.2797	8.4502	1.0315	3.2796	0.2401	1.2498	0.0015
Cu4	0.9568	7.4481	0.9099	3.3964	0.3729	1.4936	0.0049

Table 6: $\langle j_2 \rangle$ form factors for 4d atoms and ions

Ion	A	a	B	b	C	c	D
Y0	14.4084	44.6577	5.1045	14.9043	−0.0535	3.3189	0.0028
Zr0	10.1378	35.3372	4.7734	12.5453	−0.0489	2.6721	0.0036
Zr1	11.8722	34.9200	4.0502	12.1266	−0.0632	2.8278	0.0034
Nb0	7.4796	33.1789	5.0884	11.5708	−0.0281	1.6353	0.0047
Nb1	8.7735	33.2848	4.6556	11.6046	−0.0268	1.5389	0.0044
Mo0	5.1180	23.4217	4.1809	9.2080	−0.0505	1.7434	0.0053
Mo1	7.2367	28.1282	4.0705	9.9228	−0.0317	1.4552	0.0049
Tc0	4.2441	21.3974	3.9439	8.3753	−0.0371	1.1870	0.0066
Tc1	6.4056	24.8243	3.5400	8.6112	−0.0366	1.4846	0.0044
Ru0	3.7445	18.6128	3.4749	7.4201	−0.0363	1.0068	0.0073
Ru1	5.2826	23.6832	3.5813	8.1521	−0.0257	0.4255	0.0131
Rh0	3.3651	17.3444	3.2121	6.8041	−0.0350	0.5031	0.0146
Rh1	4.0260	18.9497	3.1663	6.9998	−0.0296	0.4862	0.0127
Pd0	3.3105	14.7265	2.6332	5.8618	−0.0437	1.1303	0.0053
Pd1	4.2749	17.9002	2.7021	6.3541	−0.0258	0.6999	0.0071
Ce2	0.9809	18.0630	1.8413	7.7688	0.9905	2.8452	0.0120
Nd2	1.4530	18.3398	1.6196	7.2854	0.8752	2.6224	0.0126
Nd3	0.6751	18.3421	1.6272	7.2600	0.9644	2.6016	0.0150
Sm2	1.0360	18.4249	1.4769	7.0321	0.8810	2.4367	0.0152
Sm3	0.4707	18.4301	1.4261	7.0336	0.9574	2.4387	0.0182
Eu2	0.8970	18.4429	1.3769	7.0054	0.9060	2.4213	0.0190
Eu3	0.3985	18.4514	1.3307	6.9556	0.9603	2.3780	0.0197
Gd2	0.7756	18.4695	1.3124	6.8990	0.8956	2.3383	0.0199
Gd3	0.3347	18.4758	1.2465	6.8767	0.9537	2.3184	0.0217
Tb2	0.6688	18.4909	1.2487	6.8219	0.8888	2.2751	0.0215
Tb3	0.2892	18.4973	1.1678	6.7972	0.9437	2.2573	0.0232
Dy2	0.5917	18.5114	1.1828	6.7455	0.8801	2.2141	0.0229
Dy3	0.2523	18.5172	1.0914	6.7362	0.9345	2.2082	0.0250
Ho2	0.5094	18.5155	1.1234	6.7060	0.8727	2.1589	0.0242
Ho3	0.2188	18.5157	1.0240	6.7070	0.9251	2.1614	0.0268
Er2	0.4693	18.5278	1.0545	6.6493	0.8679	2.1201	0.0261
Er3	0.1710	18.5337	0.9879	6.6246	0.9044	2.1004	0.0278
Tm2	0.4198	18.5417	0.9959	6.6002	0.8593	2.0818	0.0284
Tm3	0.1760	18.5417	0.9105	6.5787	0.8970	2.0622	0.0294
Yb2	0.3852	18.5497	0.9415	6.5507	0.8492	2.0425	0.0301
Yb3	0.1570	18.5553	0.8484	6.5403	0.8880	2.0367	0.0318
Pr3	0.8734	18.9876	1.5594	6.0872	0.8142	2.4150	0.0111

Table 7: $\langle j_2 \rangle$ Form factors for actinide ions

Ion	A	a	B	b	C	c	D
U3	4.1582	16.5336	2.4675	5.9516	−0.0252	0.7646	0.0057
U4	3.7449	13.8944	2.6453	4.8634	−0.5218	3.1919	0.0009
U5	3.0724	12.5460	2.3076	5.2314	−0.0644	1.4738	0.0035
Np3	3.7170	15.1333	2.3216	5.5025	−0.0275	0.7996	0.0052
Np4	2.9203	14.6463	2.5979	5.5592	−0.0301	0.3669	0.0141
Np5	2.3308	13.6540	2.7219	5.4935	−0.1357	0.0493	0.1224
Np6	1.8245	13.1803	2.8508	5.4068	−0.1579	0.0444	0.1438
Pu3	2.0885	12.8712	2.5961	5.1896	−0.1465	0.0393	0.1343
Pu4	2.7244	12.9262	2.3387	5.1633	−0.1300	0.0457	0.1177
Pu5	2.1409	12.8319	2.5664	5.1522	−0.1338	0.0457	0.1210
Pu6	1.7262	12.3240	2.6652	5.0662	−0.1695	0.0406	0.1550
Am2	3.5237	15.9545	2.2855	5.1946	−0.0142	0.5853	0.0033
Am3	2.8622	14.7328	2.4099	5.1439	−0.1326	0.0309	0.1233
Am4	2.4141	12.9478	2.3687	4.9447	−0.2490	0.0215	0.2371
Am5	2.0109	12.0534	2.4155	4.8358	−0.2264	0.0275	0.2128
Am6	1.6778	11.3372	2.4531	4.7247	−0.2043	0.0337	0.1892
Am7	1.8845	9.1606	2.0746	4.0422	−0.1318	1.7227	0.0020

Table 8: $\langle j_4 \rangle$ form factors for 3d atoms and ions

Ion	A	a	B	b	C	c	D
Sc0	1.3420	10.2000	0.3837	3.0786	0.0468	0.1178	−0.0328
Sc1	7.1167	15.4872	−6.6671	18.2692	0.4900	2.9917	0.0047
Sc2	−1.6684	15.6475	1.7742	9.0624	0.4075	2.4116	0.0042
Ti0	−2.1515	11.2705	2.5149	8.8590	0.3555	2.1491	0.0045
Ti1	−1.0383	16.1899	1.4699	8.9239	0.3631	2.2834	0.0044
Ti2	−1.3242	15.3096	1.2042	7.8994	0.3976	2.1562	0.0051
Ti3	−1.1117	14.6349	0.7689	6.9267	0.4385	2.0886	0.0060
V0	−0.9633	15.2729	0.9274	7.7315	0.3891	2.0530	0.0063
V1	−0.9606	15.5451	1.1278	8.1182	0.3653	2.0973	0.0056
V2	−1.1729	14.9732	0.9092	7.6131	0.4105	2.0391	0.0067
V3	−0.9417	14.2045	0.5284	6.6071	0.4411	1.9672	0.0076
V4	−0.7654	13.0970	0.3071	5.6739	0.4476	1.8707	0.0081
Cr0	−0.6670	19.6128	0.5342	6.4779	0.3641	1.9045	0.0073
Cr1	−0.8309	18.0428	0.7252	7.5313	0.3828	2.0032	0.0073
Cr2	−0.8930	15.6641	0.5590	7.0333	0.4093	1.9237	0.0081
Cr3	−0.7327	14.0727	0.3268	5.6741	0.4114	1.8101	0.0085
Cr4	−0.6748	12.9462	0.1805	6.7527	0.4526	1.7999	0.0098
Mn0	−0.5452	15.4713	0.4406	4.9024	0.2884	1.5430	0.0059
Mn1	−0.7947	17.8673	0.6078	7.7044	0.3798	1.9045	0.0087
Mn2	−0.7416	15.2555	0.3831	6.4693	0.3935	1.7997	0.0093
Mn3	−0.6603	13.6066	0.2322	6.2175	0.4104	1.7404	0.0101
Mn4	−0.5127	13.4613	0.0313	7.7631	0.4282	1.7006	0.0113
Fe0	−0.5029	19.6768	0.2999	3.7762	0.2576	1.4241	0.0071
Fe1	−0.5109	19.2501	0.3896	4.8913	0.2810	1.5265	0.0069
Fe2	−0.5401	17.2268	0.2865	3.7422	0.2658	1.4238	0.0076
Fe3	−0.5507	11.4929	0.2153	4.9063	0.3468	1.5230	0.0095
Fe4	−0.5352	9.5068	0.1783	5.1750	0.3584	1.4689	0.0097
Co0	−0.4221	14.1952	0.2900	3.9786	0.2469	1.2859	0.0063
Co1	−0.4115	14.5615	0.3580	4.7170	0.2644	1.4183	0.0074
Co2	−0.4759	14.0462	0.2747	3.7306	0.2458	1.2504	0.0057
Co3	−0.4466	13.3912	0.1419	3.0110	0.2773	1.3351	0.0093
Co4	−0.4091	13.1937	−0.0194	3.4169	0.3534	1.4214	0.0112
Ni0	−0.4428	14.4850	0.0870	3.2345	0.2932	1.3305	0.0096
Ni1	−0.3836	13.4246	0.3116	4.4619	0.2471	1.3088	0.0079
Ni2	−0.3803	10.4033	0.2838	3.3780	0.2108	1.1036	0.0050
Ni3	-0.40139	9.04616	0.23144	3.07531	0.21916	1.08378	0.00597
Ni4	−0.3509	8.1572	0.2220	2.1063	0.1567	0.9253	0.0065
Cu0	−0.3204	15.1324	0.2335	4.0205	0.2312	1.1957	0.0068
Cu1	−0.3572	15.1251	0.2336	3.9662	0.2315	1.1967	0.0070
Cu2	−0.3914	14.7400	0.1275	3.3840	0.2548	1.2552	0.0103
Cu3	−0.3671	14.0816	−0.0078	3.3149	0.3154	1.3767	0.0132
Cu4	−0.2915	14.1243	−0.1065	4.2008	0.3247	1.3516	0.0148

Table 9: $\langle j_4 \rangle$ form factors for 4d atoms and ions

Ion	A	a	B	b	C	c	D
Y0	−8.0767	32.2014	7.9197	25.1563	1.4067	6.8268	−0.0001
Zr0	−5.2697	32.8680	4.1930	24.1833	1.5202	6.0481	−0.0002
Zr1	−5.6384	33.6071	4.6729	22.3383	1.3258	5.9245	−0.0003
Nb0	−3.1377	25.5948	2.3411	16.5686	1.2304	4.9903	−0.0005
Nb1	−3.3598	25.8202	2.8297	16.4273	1.1203	4.9824	−0.0005
Mo0	−2.8860	20.5717	1.8130	14.6281	1.1899	4.2638	−0.0008
Mo1	−3.2618	25.4862	2.3596	16.4622	1.1164	4.4913	−0.0007
Tc0	−2.7975	20.1589	1.6520	16.2609	1.1726	3.9427	−0.0008
Tc1	−2.0470	19.6830	1.6306	11.5925	0.8698	3.7689	−0.0010
Ru0	−1.5042	17.9489	0.6027	9.9608	0.9700	3.3927	−0.0010
Ru1	−1.6278	18.5063	1.1828	10.1886	0.8138	3.4180	−0.0009
Rh0	−1.3492	17.5766	0.4527	10.5066	0.9285	3.1555	−0.0009
Rh1	−1.4673	17.9572	0.7381	9.9444	0.8485	3.1263	−0.0012
Pd0	−1.1955	17.6282	0.3183	11.3094	0.8696	2.9089	−0.0008
Pd1	−1.4098	17.7650	0.7927	9.9991	0.7710	2.9297	−0.0006

Table 10: $\langle j_4 \rangle$ form factors for rare earth ions

Ion	A	a	B	b	C	c	D
Ce2	−0.6468	10.5331	0.4052	5.6243	0.3412	1.5346	0.0080
Nd2	−0.5744	10.9304	0.4210	6.1052	0.3124	1.4654	0.0081
Nd2	−0.5416	12.2043	0.3571	6.1695	0.3154	1.4847	0.0098
Nd3	−0.4053	14.0141	0.0329	7.0046	0.3759	1.7074	0.0209
Sm2	−0.4150	14.0570	0.1368	7.0317	0.3272	1.5825	0.0192
Sm3	−0.4288	10.0525	0.1782	5.0191	0.2833	1.2364	0.0088
Eu2	−0.4145	10.1930	0.2447	5.1644	0.2661	1.2054	0.0065
Eu3	−0.4095	10.2113	0.1485	5.1755	0.2720	1.2374	0.0131
Gd2	−0.3824	10.3436	0.1955	5.3057	0.2622	1.2032	0.0097
Gd3	−0.3621	10.3531	0.1016	5.3104	0.2649	1.2185	0.0147
Tb2	−0.3443	10.4686	0.1481	5.4156	0.2575	1.1824	0.0104
Tb3	−0.3228	10.4763	0.0638	5.4189	0.2566	1.1962	0.0159
Dy2	−0.3206	12.0714	0.0904	8.0264	0.2616	1.2296	0.0143
Dy3	−0.2829	9.5247	0.0565	4.4292	0.2437	1.0665	0.0092
Ho2	−0.2976	9.7190	0.1224	4.6345	0.2279	1.0052	0.0063
Ho3	−0.2717	9.7313	0.0474	4.6378	0.2292	1.0473	0.0124
Er2	−0.2975	9.8294	0.1189	4.7406	0.2116	1.0039	0.0117
Er3	−0.2568	9.8339	0.0356	4.7415	0.2172	1.0281	0.0148
Tm2	−0.2677	9.8883	0.0925	4.7838	0.2056	0.9896	0.0124
Tm3	−0.2292	9.8948	0.0124	4.7850	0.2108	1.0071	0.0151
Yb2	−0.2393	9.9469	0.0663	4.8231	0.2009	0.9651	0.0122
Yb3	−0.2121	8.1967	0.0325	3.1533	0.1975	0.8842	0.0093
Pr3	−0.3970	10.9919	0.0818	5.9897	0.3656	1.5021	0.0110

Table 11: $\langle j_4 \rangle$ Form factors for actinide ions

Ion	A	a	B	b	C	c	D
U3	−0.9859	16.6010	0.6116	6.5147	0.6020	2.5970	−0.0010
U4	−1.0540	16.6055	0.4339	6.5119	0.6746	2.5993	−0.0011
U5	−0.9588	16.4851	0.1576	6.4397	0.7785	2.6402	−0.0010
Np3	−0.9029	16.5858	0.4006	6.4699	0.6545	2.5631	−0.0004
Np4	−0.9887	12.4415	0.5918	5.2941	0.5306	2.2625	−0.0021
Np5	−0.8146	16.5809	−0.0055	6.4751	0.7956	2.5623	−0.0004
Np6	−0.6738	16.5531	−0.2297	6.5055	0.8513	2.5528	−0.0003
Pu3	−0.7014	16.3687	−0.1162	6.6971	0.7778	2.4502	0.0000
Pu4	−0.9160	12.2027	0.4891	5.1274	0.5290	2.1487	−0.0022
Pu5	−0.7035	16.3601	−0.0979	6.7057	0.7726	2.4475	0.0000
Pu6	−0.5560	16.3215	−0.3046	6.7685	0.8146	2.4259	0.0001
Am2	−0.7433	16.4163	0.3481	6.7884	0.6014	2.3465	0.0000
Am3	−0.8092	12.8542	0.4161	5.4592	0.5476	2.1721	−0.0011
Am4	−0.8548	12.2257	0.3037	5.9087	0.6173	2.1881	−0.0016
Am5	−0.6538	15.4625	−0.0948	5.9971	0.7295	2.2968	0.0000
Am6	−0.5390	15.4491	−0.2689	6.0169	0.7711	2.2970	0.0002
Am7	−0.4688	12.0193	−0.2692	7.0415	0.7297	2.1638	−0.0011

Table 12: $\langle j_6 \rangle$ form factors for rare earth ions

Ion	A	a	B	b	C	c	D
Ce2	−0.1212	7.9940	−0.0639	4.0244	0.1519	1.0957	0.0078
Nd2	−0.1600	8.0086	0.0272	4.0284	0.1104	1.0682	0.0139
Nd3	−0.0416	8.0136	−0.1261	4.0399	0.1400	1.0873	0.0102
Sm2	−0.1428	6.0407	0.0723	2.0329	0.0550	0.5134	0.0081
Sm3	−0.0944	6.0299	−0.0498	2.0743	0.1372	0.6451	−0.0132
Eu2	−0.1252	6.0485	0.0507	2.0852	0.0572	0.6460	0.0132
Eu3	−0.0817	6.0389	−0.0596	2.1198	0.1243	0.7639	−0.0001
Gd2	−0.1351	5.0298	0.0828	2.0248	0.0315	0.5034	0.0187
Gd3	−0.0662	6.0308	−0.0850	2.1542	0.1323	0.8910	0.0048
Tb2	−0.0758	6.0319	−0.0540	2.1583	0.1199	0.8895	0.0051
Tb3	−0.0559	6.0311	−0.1020	2.2365	0.1264	1.1066	0.0167
Dy2	−0.0568	6.0324	−0.1003	2.2396	0.1401	1.1062	0.0109
Dy3	−0.0423	6.0376	−0.1248	2.2437	0.1359	1.2002	0.0188
Ho2	−0.0725	6.0453	−0.0318	2.2428	0.0738	1.2018	0.0252
Ho3	−0.0289	6.0504	−0.1545	2.2305	0.1550	1.2605	0.0177
Er2	−0.0648	6.0559	−0.0515	2.2303	0.0825	1.2638	0.0250
Er3	−0.0110	6.0609	−0.1954	2.2242	0.1818	1.2958	0.0149
Tm2	−0.0842	4.0699	0.0807	0.8492	−0.2087	0.0386	0.2095
Tm3	−0.0727	4.0730	0.0243	0.6888	3.9459	0.0023	−3.9076
Yb2	−0.0739	5.0306	0.0140	2.0300	0.0351	0.5080	0.0174
Yb3	−0.0345	5.0073	−0.0677	2.0198	0.0985	0.5485	−0.0076
Pr3	−0.0224	7.9931	−0.1202	3.9406	0.1299	0.8938	0.0051

Table 13: $\langle j_6 \rangle$ Form factors for actinide ions

Ion	A	a	B	b	C	c	D
U3	-0.3797	9.9525	0.0459	5.0379	0.2748	1.6072	0.0016
U4	-0.1793	11.8961	-0.2269	5.4280	0.3291	1.7008	0.0030
U5	-0.0399	11.8909	-0.3458	5.5803	0.3340	1.6448	0.0029
Np3	-0.2427	11.8444	-0.1129	5.3774	0.2848	1.5676	0.0022
Np4	-0.2436	9.5988	-0.1317	4.1014	0.3029	1.5447	0.0019
Np5	-0.1157	9.5649	-0.2654	4.2599	0.3298	1.5494	0.0025
Np6	-0.0128	9.5692	-0.3611	4.3035	0.3419	1.5406	0.0032
Pu3	-0.0364	9.5721	-0.3181	4.3424	0.3210	1.5233	0.0041
Pu4	-0.2394	7.8367	-0.0785	4.0243	0.2643	1.3776	0.0012
Pu5	-0.1090	7.8188	-0.2243	4.1000	0.2947	1.4040	0.0015
Pu6	-0.0001	7.8196	-0.3354	4.1439	0.3097	1.4027	0.0020
Am2	-0.3176	7.8635	0.0771	4.1611	0.2194	1.3387	0.0018
Am3	-0.3159	6.9821	0.0682	3.9948	0.2141	1.1875	-0.0015
Am4	-0.1787	7.8805	-0.1274	4.0898	0.2565	1.3152	0.0017
Am5	-0.0927	6.0727	-0.2227	3.7840	0.2916	1.3723	0.0026
Am6	0.0152	6.0788	-0.3549	3.8610	0.3125	1.4031	0.0036
Am7	0.1292	6.0816	-0.4689	3.8791	0.3234	1.3934	0.0042

Time-of-Flight Inelastic Neutron Scattering

R. S. Eccleston

Introduction

In the inelastic neutron scattering experiment, the quantity we measure is the double differential cross section:

$$\frac{d^2\sigma}{d\Omega dE} = \frac{\mathbf{k}_f}{\mathbf{k}_i} b^2 S(\mathbf{Q}, \omega)$$

The velocity of thermal neutrons is of the order of km s^{-1}; consequently their energy can be determined by measuring their time-of-flight over a distance of a few metres. In the inelastic neutron experiment the parameters of interest are the energy and momentum transfer, $\hbar\omega$ and Q respectively.

Time-of-flight spectrometers may be divided into two classes:-

- **Direct geometry spectrometers**: in which the incident energy, E_i, is defined by a device such as a crystal or a chopper, and the final energy, E_f, is determined by time-of-flight.
- **Indirect (inverted) geometry spectrometers**: in which the sample is illuminated by a white incident beam and E_f is defined by a crystal or a filter and E_i is determined by time-of-flight.

At a pulsed source all spectrometers use the time-of-flight techniques. On steady state sources pulsing devices such as choppers are required.
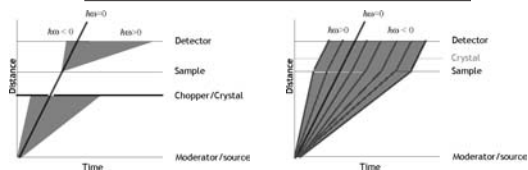
Figure 1: Distance-time plot for a direct geometry spectrometer (left) and an indirect geometry spectrometer (right).

2.6-2

The mode of operation of each type of spectrometer can be clearly understood if the distance-time plots are considered (figure 1).

Accessible regions of (Q,ω) space

To understand the trajectories traced out through (Q,ω), consider the scattering triangles. Clearly for direct geometry spectrometers k_i is fixed and k_f varies as a function of time whereas the reverse is true for indirect geometry instruments.
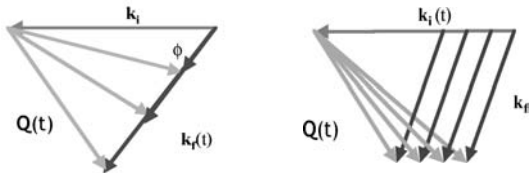
Figure 2: Scattering triangles for a direct geometry spectrometer (left) and an indirect geometry spectrometer (right).

Applying the cosine rule

$$\mathbf{Q}^2 = \mathbf{k}_i^2 + \mathbf{k}_f^2 - 2\mathbf{k}_i\mathbf{k}_f \cos\phi \qquad \frac{\hbar^2 Q^2}{2m} = E_i + E_f - 2\left(E_i E_f\right)^{1/2}\cos\phi$$

For direct geometry E_f can be eliminated leaving

$$\frac{\hbar^2 \mathbf{Q}^2}{2m} = 2E_i - \hbar\omega - 2\cos\phi\left[E_i\left(E_i - \hbar\omega\right)\right]^{1/2}$$

Each detector has a parabolic trajectory through (Q,ω) space.

To make optimum use of direct geometry spectrometers, they are equipped with large detector arrays, giving simultaneous access to a large area of (Q,ω) space.

Similarly for indirect geometry E_i can be eliminated giving

$$\frac{\hbar^2 \mathbf{Q}^2}{2m} = 2E_f + \hbar\omega - 2\cos\phi\left[E_f\left(E_f + \hbar\omega\right)\right]^{1/2}$$

The parabola are inverted. An important feature of the indirect geometry instrument is the access to a wide range of energy transfers for energy loss.
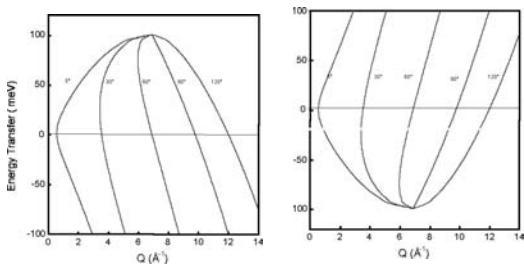
Figure 3: Trajectories through (Q,ω) space: a direct geometry spectrometer (left) and an indirect geometry spectrometer (right) for detector at the given scattering angles.

Generic instruments

The table (table 1) provides much simplified examples of direct and indirect geometry instruments. The critical differences between the two are the manner in which they cover (Q,ω) space and their resolution characteristics. On a steady state source, the moderator as it is shown in the table is replaced by a pulsing device such as a chopper.
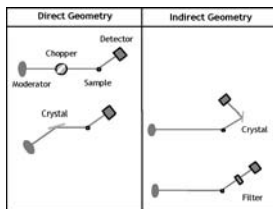
Table 1: Generic instrument types.

The chopper spectrometer

The chopper is a ubiquitous feature of direct geometry spectrometers for reasons given later in the chapter. Examples of chopper spectrometers include HET, MARI and MAPS at ISIS and IN4, IN5 and IN6 at the ILL. In the case of some time-of-flight spectrometers on steady state sources the chopper simply provides the pulsed structure of the beam and a crystal monochromator is used to select the incident energy, for example IN6. Other instruments such as IN5 use an array of choppers both to provide the pulsed structure and to monochromate the beam.

On a pulsed source the design of a chopper spectrometer is in general quite straightforward, with the key components arranged as indicated in the table. The

beam is monochromated using a Fermi chopper. A second chopper is usually installed effectively to close the beamline at the time at which the proton beam hits the spallation target, thereby preventing a large flux of epithermal neutrons entering the spectrometer where they will thermalise and produce a background signal. In all cases detector arrays tend to be as large as economically and physically possible to maximise the efficiency of the spectrometer.

Resolution

For the sake of simplicity the resolution function of a chopper spectrometer is considered. The energy resolution has two contributions: from the moderator pulse width and from the band width of the chopper pulse. Concisely the expression can be written:

$$\frac{\Delta \hbar \omega}{E_i} = \left(\left[\frac{2\Delta t_c}{t_c} \left(1 + \frac{L_1 + L_3}{L_2} \left(1 - \frac{\hbar \omega}{E_i} \right)^{3/2} \right) \right]^2 + \left[2\frac{\Delta t_m}{t_c} \left(1 + \frac{L_3}{L_2} \left(1 - \frac{\hbar \omega}{E_i} \right)^{3/2} \right) \right]^2 \right)^{1/2}$$

Where Δt_c is the chopper burst time width, t_c is the time of flight at the chopper and Δt_m is the moderator pulse width. L_1 is the moderator to chopper distance, L_2 the sample to detector distance and L_3 the chopper to sample distance.

Single crystal experiments on a chopper spectrometer

Direct geometry spectrometers have, in the past, been thought of as being well adapted for studying excitations in non-crystalline or polycrystalline samples, but not suitable for single crystals. However, the development of instrumentation and experimental techniques has shown that direct geometry spectrometers can be used very effectively for such studies allowing a broad survey of $(\mathbf{Q},\omega)$ space but also detailed, focussed studies.

From the scattering triangle we can see that an array of detectors will trace out a sector in reciprocal space, and as we have seen earlier, each detector has a parabolic trajectory through $(\mathbf{Q},\omega)$ space. Consequently a broad detector array produces a surface in $(\mathbf{Q}_\parallel, \mathbf{Q}_\perp, \omega)$ space.

Consider the example of a ferromagnetic spin wave in a three-dimensional magnetic system. As the dispersion intersects the surface traced out by the time-of-flight
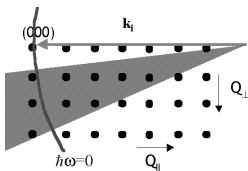
Figure 4. Use of a multidetector to cover a region in $(Q_{||}, Q_\perp)$ space.

trajectories for the detectors, scattering will be observed.

The development of large position sensitive detector (PSD) arrays provides greater flexibility for single crystal measurements. The MAPS spectrometer at the ISIS pulsed source has a detector area of $16m^2$ divided up into approximately 50000 pixels. For any given crystal orientation arbitrary cuts can be made across the surface of the detector, providing the ability to collect data along several crystallographic directions simultaneously. In essence, the spectrometer collects a large (0.5Gbytes) volume of data and the choice of scans is made in software after the experiment. For more information see reference (Perring).

Indirect geometry spectrometers

It is apparent from figure 2 that indirect geometry spectrometers offer access to a wide range of neutron energy loss values. They also offer high resolution at the elastic line and tend to offer broad coverage in terms of energy transfer with reasonable resolution.

A variety of spectrometer designs offer different capabilities:

- Crystal analyser spectrometer : molecular spectroscopy
- Back scattering spectrometer : high resolution
- Coherent excitations spectrometer : coherent excitations in single crystals.

Before discussing each of these in turn, it is useful briefly to consider the resolution characteristics of an indirect geometry spectrometer.

The resolution of indirect geometry spectrometers

For the indirect geometry spectrometer the energy resolution contains terms pertaining to the uncertainty in the angular spread of neutrons scattered from the analyser, $\Delta\theta_A$ and timing errors over the incident flight path, Δt. Timing errors arise from several contributions, including moderator thickness, sample size broadening, analyser thickness broadening, detector thickness and the finite width of data collection time channels. If Δt is expressed in terms of an equivalent distance $\delta=\hbar\kappa_i\Delta t/m$ the energy resolution can be concisely expressed as:

$$\frac{\Delta\hbar\omega}{E_i} = 2\left[\left(\frac{\delta}{L_1}\right)^2 + \left\{\frac{E_i}{E_f}\cot\theta_A\Delta\theta_A\left(1+\frac{L_2}{L_1}\left(\frac{E_i}{E_f}\right)^{3/2}\right)\right\}^2\right]^{1/2}$$

where L_1 is the moderator to sample distance, and L_2 the sample to detector distance. Clearly increasing θ_A or L_1 improves resolution but physical and instrumental limitations apply.

2.6-6

Back-scattering spectrometer

For a crystal analyser spectrometer, the resolution contains a $\cot\theta_A$ term which can be reduced to almost zero by using a back-scattering geometry, thereby optimising the definition of E_f. In a matched spectrometer, E_i should be determined to the same precision, hence L_1 tends to be long. IRIS at the ISIS Facility represents an excellent example of such an instrument. In the most frequently used mode of operation the 002 reflection from graphite analysers defines an E_f of 1.845 meV and provides resolution of 17μeV. The analysers are cooled to reduce thermal diffuse scattering (TDS), which broadens the elastic peak and gives rise to additional background.

Crystal analyser spectrometers

For molecular spectroscopy, energy information is often more important than Q information. Consequently, measuring energy transfer along a single trajectory provides an efficient method for measuring excitations across a broad spectral range. TOSCA at ISIS provides a good example. A graphite analyser defines an E_f of 3meV, a cooled beryllium filter is used to remove higher order reflections. The geometry of the secondary spectrometer is such that the sample, analyser and detectors are parallel; this effectively time-focuses the scattered neutrons, reducing uncertainty in the scattered neutron flight time.

Coherent excitations - PRISMA

One of the shortcomings of chopper spectrometers and the direct geometry spectrometers described above is their inability to perform scans uniquely along
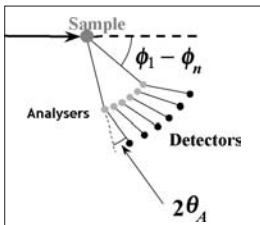
Figure 5: Schematic of the PRISMA spectrometer.
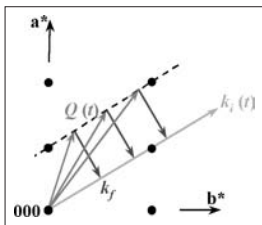
Figure 6: Time-of-flight scan with the PRISMA spectrometer.

high symmetry directions. By adopting a scattering geometry whereby the condition $\sin\phi \, / \sin\theta_A$ = constant is met (figure 5), time-of-flight scan scans for all detectors correspond to scans along a defined direction in Q space (figure 6).

The PRISMA spectrometer can operate in this mode. It is technically challenging because the movement of analysers is limited by the risk of clashing.

Monochromating devices

Choppers
As mentioned above, choppers are key components of a direct geometry spectrometer. For instruments using neutrons in the thermal to high energy ranges, Fermi choppers are most appropriate; for cold neutron instruments disk choppers offer inherent advantages.

Fermi choppers
A Fermi chopper is effectively a drum with a hole through the middle. The hole is filled with alternating sheets of neutron absorbing material (slats) and transparent material (slits). The slits and slats are curved, with the radius of curvature and the slit/slat ratio optimised for specific energy ranges. On the ISIS chopper spectrometers for example three slit packages are used to cover the incident energy range from 15meV to 2eV. An additional slit package with very broad slits is used to improve intensity by degrading resolution. The Fermi chopper can be rotated at frequencies of up to 600Hz. The incident energy is defined by the phase of the chopper relative to the incident neutron pulse. The resolution is dictated by the slit/slat ratio of the slit package and the chopper frequency. Fermi choppers allow continuous selection of E_i.

Disk choppers
Disk choppers are simply rotating disks with holes in them. They offer higher transmission than Fermi choppers with the same flexibility in the selection of E_i. Using two disks or a variable aperture chopper overcomes the need to change slit package. They are also compact. However their frequency is limited by engineering constraints, as is the thickness of the disks. Both these factors mean that disk choppers are often not practical for thermal to high-energy neutron instruments.

Crystal
The use of crystal monochromators for time-of-flight spectroscopy is limited, because they impose some geometrical constraints, and reflectivity falls as energy rises. The geometrical constraints can be lifted by using a double bounce

arrangement, but at the expense of additional losses arising from the second reflection. Focussing of the monochromator does offer the opportunity to trade resolution for additional flux.

As discussed above, the use of crystal analysers is widespread on indirect geometry spectrometers.

Filters

The Be filters effectively remove neutrons with an energy greater than the Bragg cut-off of 5.2meV. Incident neutrons are scattered in the beryllium and then absorbed in absorbing sheets within the filter. They are used to remove higher order contamination in indirect geometry instruments. Their efficiency can be improved by cooling, which reduces transmission of neutrons with energies above the cut-off that arise from up-scattering by thermally excited phonons.

Nuclear resonant absorption from a foil is used for very high-energy measurements. The eVS spectrometer at ISIS, for example, uses a filter difference technique using uranium or gold foils to measure atomic momentum distributions in the eV range.

Reference

"Neutron scattering (mostly) from low dimensional magnetic systems,, by T.G. Perring, in *Frontiers of Neutron Scattering*, edited by A. Furrer, (World Scientific, 2000)

Three-axis spectroscopy

R. Currat and J. Kulda

Principle of the technique

In order to obtain information on the excitation spectrum at a given point Q in reciprocal space, a more sophisticated procedure has to be adopted than just scanning the energy of the scattered neutrons. At each point of the scan the scattering triangle is modified, as indicated in Fig. 1, so that k_i and k_f will close at the same momentum transfer Q but the length of one of the wave vectors – preferably k_i – is varied to provide for the required energy transfer. As is clear from the Fig. 1, in addition to the k_i and k_f modification, also all the angles of the scattering triangle will change. Herein lies the price to be paid for the increased flexibility required for scans with Q = const.: the measurements have to be performed in a step-by-step mode, making multichannel data acquisition quite difficult.
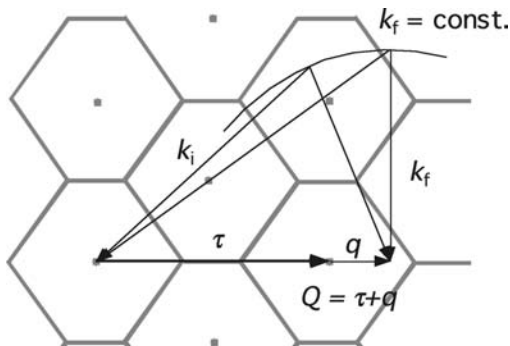
Figure 1: Scattering geometry for a Q = const. scan.

2.7-2

Compared to a direct-geometry TOF instrument, this disadvantage is, however, largely compensated by the high incident monochromatic flux due to the steady-state operation of the neutron source as opposed to a pulsed beam providing neutrons for only about 1/1000 of the total measurement time.

As a general rule, the TAS is the technique of choice whenever information on excitations in single crystals is sought [1] at a well defined point or along a given direction in the Q,ω space and when a detailed quantitative interpretation of the measured spectra is intended. On the contrary, if a global overview of the excitations in a broad Q,ω range is the goal, the TOF may be of advantage as soon as the number of useful detector channels can compensate the initial loss due to the time modulation of the incident beam with a low duty-cycle.

The neutron three-axis spectrometer (TAS)
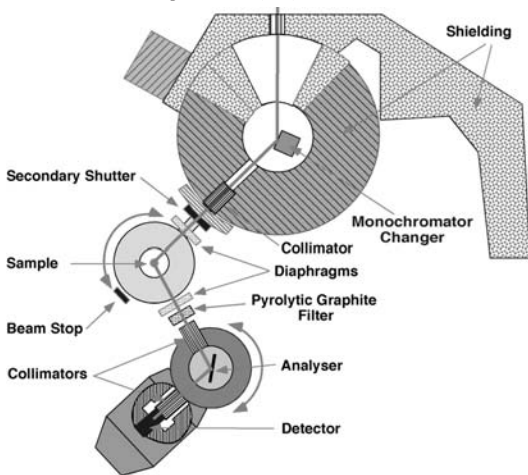
Figure 2: Schematic of a three-axis spectrometer.

A typical set-up of a three-axis spectrometer (TAS) is schematically displayed in Fig. 2. The incident and scattered neutron wave vectors, k_i and k_f, are selected by Bragg diffraction on the monochromator and analyser crystals, respectively. Traditionally, large crystals of Cu, Zn or pyrolitic graphite (PG) with mosaic width of 20 – 30 minutes have been used in combination with Soller collimators defining the beam divergence of the incident and diffracted beams. On present instruments the mosaic crystals are segmented into plates of a few centimeters size and mounted on mechanical devices (benders), which permit to control their individual orientations in order to act as curved mirrors and to focus the neutron beam horizontally and/or vertically on the sample and detector [2]. More recently, elastically bent perfect Si and Ge crystals, offering improved focusing properties thanks to the absence of random mosaic block misorientations, get employed for work requiring higher resolution [3]. The monochromatic neutron flux incident on the sample is monitored by a low-efficiency ($\approx 10^{-5}$ - 10^{-4}) detector ("monitor 1„), another similar "monitor 2„, is placed in the scattered beam to detect the eventual presence of strong Bragg diffraction peaks, which might give rise to spurious signals in the inelastic spectra. The detector is usually a single ^{3}He proportional gas tube.

The monochromator and analyser crystals diffract together with the nominal wavelength λ also its harmonics λ/2, λ/3 etc., which may be at the origin of spurious effects. Usually, the most dangerous one is λ/2, because it is most intense and its energy is closest to the nominal one. Harmonic contaminations may be suppressed by using appropriate filters. For hot neutrons absorption filters are available, using sharp absorption resonances of certain nuclei in the 0.1 - 1 eV range. For thermal neutrons pyrolithic graphite (PG) permits to suppress efficiently the second order for two "magic" wavelengths of λ = 1.53 Å and 2.36 Å, corresponding to k = 4.1 Å^{-1} and 2.66 Å^{-1}, respectively. For cold neutrons cooled polycrystalline beryllium permits to cut all wavelengths below 4 Å, ie. to transmit only neutrons with k < 1.57 Å^{-1}. Alternatively, silicon and germanium crystals, whose odd-*hkl* reflections are free from 2nd order contamination, can be used for certain applications.

The TAS resolution function

The resolution volume, i.e. the region of the Q,ω space which corresponds to the momentum and energy transfers of neutrons scattered and registered in a given spectrometer configuration, can be approximated by a rather anisotropic 4D ellipsoid. Its form is determined by the *convolution product* of the two reciprocal space distribution functions $p_i(k_i)$ and $p_f(k_f)$ which describe the transmission of the monochromator and analyser arms [4]. For a spectrometer configuration characterised by

2.7-4

nominal values $\mathbf{Q_0}, \omega_0$ of $\mathbf{Q}, \omega$ the measured intensity is given by

$$I(\mathbf{Q_0}, \omega_0) = N\, A(k_I) \int R(\mathbf{Q}\text{-}\mathbf{Q_0}, \omega\text{-}\omega_0)\, S(\mathbf{Q}, \omega)\, d\mathbf{Q}\, d\omega, \qquad (1)$$

where $A(k_I)$ and $S(\mathbf{Q}, \omega)$ describe the source spectrum and the sample scattering function, respectively. The norm of the resolution function is the product of the norms of the two distributions:

$$\int R(\mathbf{Q}\text{-}\mathbf{Q_0}, \omega\text{-}\omega_0)\, d\mathbf{Q}\, d\omega = \int p_i(\mathbf{k_i})\, p_f(\mathbf{k_f})\, d\mathbf{k_i}\, d\,\mathbf{k_f} = V_I\, V_F. \qquad (2)$$

In the gaussian approximation [4], [5] the TAS resolution function depends on the kinematic variables $\mathbf{k_i}$, $\mathbf{k_F}$, which define the energy and momentum transfer $\mathbf{Q}$, ω and on the collimation angles, mosaic widths and scattering senses. For a flat mosaic monochromator crystal (i.e. in the absence of focusing) one gets:

$$V_I = P_m(k_I) k_I^3 \cot\theta_M (2\pi)^3$$

$$\frac{\eta_m . \alpha_0 . \alpha_1}{\sqrt{4\,\eta_m^{\,2} + \alpha_0^{\,2} + \alpha_1^{\,2}}} \frac{\beta_0 \beta_1}{\sqrt{4 \sin^2(\theta_m)\, \eta'_m^{\,2} + \beta_0^{\,2} + \beta_1^{\,2}}}, \qquad (3)$$

where k_I is the average incident neutron wave vector, $\mathbf{k_I} = V_I^{-1} \int \mathbf{k_i}\, p_i(\mathbf{k_i})\, d\mathbf{k_i}$, and $\alpha_0, \beta_0, \alpha_1$ and β_1 are respectively, the horizontal and vertical beam collimations before and after the monochromator; η_m and η'_m are the horizontal and vertical mosaic widths of the monochromating crystal and $P_m(k_I)$ its the peak reflectivity. The expression for V_F is analogous.

Typical beam divergences are about $0.5 - 2$ degrees in both horizontal and vertical directions leading to relative momentum transfer resolution $\Delta Q/Q \approx 10^{-2}$. The overall energy resolution lies usually in the range of $5 - 10\%$, but can be improved in particular cases. Depending on the spectrum of the neutron source – hot, thermal or cold – the TAS can be employed for studies of excitations in the energy range from 50 µeV to 200 meV.

In reality the resolution volume has a more complicated shape, influenced by spatial variables (source size, slit widths, sample dimensions) and by the eventual use of composite crystals made up from platelike segments to obtain approximate horizontal and/or vertical focusing. Originally, the Gaussian approximation has been extended to enable a more realistic description of the TAS resolution function [6]. More recently, the RESTRAX [7] and McStas [8] computer packages became available, which provide a highly realistic Monte-Carlo ray-tracing simulation of the whole instruments including effects of neutron guides, slits etc. whose intrinsic transmission profiles are not necessarily represented by gaussian distributions.

Preparation and optimization of a TAS experiment

The first thing to be made in preparing a TAS experiment is to define the required neutron energy range matching the problem to be studied. Next a suitable instrument installed at a corresponding neutron source (cold, thermal or hot) is to be selected. Among the main factors influencing such a decision we may note

- the *kinematic constraints,* corresponding to the momentum conservation law ("closing the triangle,,), to be satisfied over all the required $\boldsymbol{Q}$, ω range; these constraints are particularly severe in studies of magnetic materials, where low-Q and large-ω often appear in combination

- the *resolution/intensity* conditions required for a given experiment; any improvement in resolution is paid for by a loss in countrate

- the *angular limitations* on the chosen instrument, notably the maximum value of the scattering angle q, which determines the maximum value of Q that may be reached for a given set of k_i, k_f values

- the risk of *spurious signals*; as a rule of thumb the final energy should be comparable to the energy transfer in the downscattering mode in order to minimise harmonic contaminations (see below) and the same applies to the incident energy in the upscattering mode

Table 1 indicates typical neutron energies and instrument parameters for a quick overview. Precise values depend on the detailed characteristics of each instrument, the fluxes correspond to the instruments at the High Flux Reactor at ILL Grenoble (France). The flux values available at smaller reactors may be 1-2 orders of magnitude lower. Optimising the experimental conditions also involves making choices and compromises with respect to the *d-spacing of the monochromator and*

Table 1: Typical neutron energies and instrument parameters for TAS spectrometers at the ILL.

TAS	cold	thermal	hot
Mono/analyser	PG002	PG002	Cu220
Flux [10^7 cm^{-2}s^{-1}]	1 - 3	3 - 30	1 - 3
k_i [Å^{-1}]	1 – 2.66	2.66 - 6	5 - 15
Q_{max} [Å^{-1}]	2	6	12
ΔQ [Å^{-1}]	0.003	0.01	0.03
E [meV]	0.1 - 10	5 - 60	50 - 200
ΔE [meV]	0.05 – 0.5	0.8 - 4	4 - 10

analyser crystals, collimations, the use of flat or focusing bent crystals, the scattering configurations. When carrying out this complex optimisation process one should use one of the simulation programs mentioned above.

Data treatment.

As a rule, the intensities measured in a constant-Q scan should be corrected *point by point* for the variation of the norm of the resolution function (*zeroth-order resolution correction*).

For a scan obtained in the *constant-k_f mode*, V_F is constant across the scan and the measured intensities should be corrected for the variation of $A(k_i) V_I$. Since the quantity $A(k_i) k_i V_I$ measures the neutron flux incident on the sample, it is sufficient to use a monitor with a $1/v_n$ characteristic in the incident beam to normalise the counting time per point. However the presence of higher-order harmonics ($\lambda/2, \lambda/3, \ldots$) in the incident beam requires, in general, additional corrections to be applied (see below).

For a scan obtained in the constant-k_i mode the measured intensities must be corrected for the variation of $P_a(k_F) k_F^3 \cot\theta_a$. Note that $P_a(k_F)$ may vary *rapidly* as a function of k_F due to parasitic multiple Bragg reflections.

Spurious signals.

An element, which may perturb the measurements, is the presence of the *harmonic* wavevectors $2k_i, 3k_i, \ldots$ in the primary beam or $2k_F, 3k_F \ldots$ in the scattered beam due to higher-order diffraction at the monochromator or analyser position. For instance, the contribution of the unfiltered $2k_i$ and $3k_i$ harmonics to the monitor count-rate (used to normalise the acquisition times in the constant-k_f mode) can be quite significant and lead to large scan profile distorsions unless corrected for.

Harmonics also lead to spurious signals for "commensurate,, values of k_i and k_f:
$$n k_i = m k_f \qquad \text{with } n,m = 1,2,3,4,..$$
due to elastic (coherent or incoherent) scattering on the sample (or its environment). To minimise the probability of such processes one should limit the magnitude of the energy transfer with respect to the incident neutron energy. A safe rule of thumb is given by $2/3 < k_i/k_f < 3/2$.

Spurious "inelastic,, peaks are observed for 3-axis configurations such that 2 crystals out of 3 (sample + monochromator or sample + analyser) satisfy a Bragg condition for a given neutron energy. These configurations are illustrated schematically in Figs. 3a and 3b.

The scattering process shown in Fig. 3a ("type I,,) can be described as follows: incident neutrons with the *nominal* wave vector k_i are Bragg scattered along the *nominal* scattered-beam direction (k_f - direction). These neutrons do not have the

proper energy to be Bragg-scattered by the analyser. Nevertheless some of them may be scattered into the detector via some other process (incoherent, diffuse or inelastic scattering) taking place at the analyser position. The low efficiency of such processes is offset by the high efficiency of Bragg scattering at the sample and thus, if in the course of a constant-Q or constant-ω scan a configuration such as the one shown in Fig. 3a is encountered, a significant increase in the detector counting rate may result. Such a process can be detected with the help of a monitor placed immediately before the analyser crystal, the so-called "monitor 2".
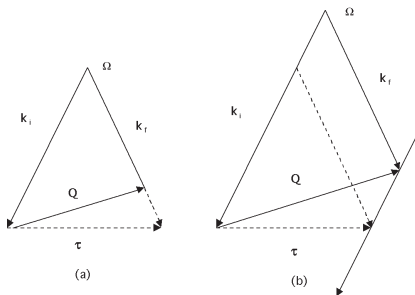
Figure 3: Configuration for spurious inelastic peaks.

Fig. 3(b) shows the reverse process ("type II") where the non-Bragg scattering occurs at the *monochromator* position. This latter type of event is not detected by "monitor 2".

Around any Bragg peak $\boldsymbol{\tau}_{hkl}$ there exist two directions in $\boldsymbol{Q}$-space for which spurious acoustic-like "inelastic" peaks will appear on the focused side of a constant-$\boldsymbol{Q}$ scan: these "dangerous directions" are those of $\boldsymbol{k}_i^B$ and $\boldsymbol{k}_i^B$, where $\boldsymbol{k}_i^B$ and $\boldsymbol{k}_i^B$ refer to the Bragg scattering configuration:

$$\boldsymbol{k}_i^B - \boldsymbol{k}_i^B = \boldsymbol{\tau}_{hkl}$$

When searching for long-wavelength excitations, i.e. when $\boldsymbol{Q} = \boldsymbol{\tau} + \boldsymbol{q}$ with $|\boldsymbol{q}| \ll |\boldsymbol{\tau}|$ the above picture must be extended, in such a way as to include the effect of sample mosaicity.

Effects related to sample mosaicity are significant when the ratio $|\boldsymbol{q}|/|\boldsymbol{\tau}|$ becomes

comparable to or smaller than the sample mosaic spread, expressed in radians.
Qualitatively, the effects are twofold:

- the spurious acoustic-like "branches,, are no longer restricted to special q-directions.
- the peaks occur symmetrically on both the focused and defocused sides of a constant-Q scan.

Quantitatively, the spurion "dispersion relation,, is found as

$$\nu_s(\mathbf{q})(\text{THz}) \approx \pm\, 2\, \frac{k_i^2}{\tau^2}\mathbf{q}\cdot\tau \tag{4}$$

where the - and + signs refer to type I and type II processes, respectively.
When the spectrometer is operated in the constant k_f mode, the value of k_i, at which the spurious peak should occur, is not known *a priori*. Since, however, eq.(1) above is only valid to *first order* in $|q|/|\tau|$ one may replace k_i by k_f.

References

[1] C. Stassis, *In:* Neutron Scattering (K. Skold, D.L. Price, eds.), Methods of Experimental Physics Vol. 23A, Academic Press, 1986, p.369.

W.G. Stirling, K.A. McEwen, *ibid* Vol. 23C, p.159.

[2] L. Pintschovius *In:* Proceeding of the Workshop on Focusing Bragg Optics, Braunschweig, Germany, 1993. Nucl. Instr. And Meth. In Phys. Res. A338 (1994) 136.

W. Buehrer, *ibid* p. 44.

[3] J.Kulda & J.Saroun, Nucl. Inst. Meth. A379 (1996) 155-166.

[4] M.J. Cooper, B. Nathans, Acta Cryst. 23 (1967) 357-367.

[5] B. Dorner, Acta Cryst. A28 (1972) 319-327.

[6] M.Popovici, A.D. Stoica, M. Ionita, J. Appl. Cryst. 20 (1987) 90.

[7] J. Saroun, J. Kulda, Physica B 234-236 (1997) 1102.

[8] K. Lefman, K. Nielsen, A. Tennant, B. Lake, Physica B 276-8 (2000) 152-3.

The basics of Neutron Spin Echo

B. Farago

Introduction

Until 1974 inelastic neutron scattering consisted of producing by some means a neutron beam of known speed and measuring the final speed of the neutrons after the scattering event. The smaller the energy change was, the better the neutron speed had to be defined. As the neutrons come form a reactor with an approximately Maxwell distribution, an infinitely good energy resolution can be achieved only at the expense of infinitely low count rate. This introduces a practical resolution limit around $0.1\mu eV$ on back-scattering instruments.

In 1972 F. Mezei discovered the method of Neutron Spin Echo. As we will see in the following, this method decouples the energy resolution from intensity loss.

Basics

It can be shown [1] that an ensemble of polarized particle with a magnetic moment and 1/2 spin behaves exactly like a classical magnetic moment. Entering a region with a magnetic field perpendicular to its magnetic moment it will undergo Larmor precession. In the case of neutrons:

$$\omega = \gamma B$$

where B is the magnetic field, ω is the frequency of rotation and $\gamma = 2.916 kHz/Oe$ is the gyromagnetic ratio of the neutron.

When the magnetic field changes its direction relative to the neutron trajectory, two limiting cases have to be distinguished:

1) Adiabatic change, when the change of the magnetic field direction (as seen by the neutron) is slow compared to the Larmor precession. In this case the component of the beam polarization which was parallel to the magnetic field will be maintained and it will follow the field direction.

2) Sudden change, is just the opposite limit. In that case the polarization will not follow the field direction. This limit is used to realize the static (Mezei) flippers.

Now let us consider a polarized neutron beam which enters a B magnetic field region of length l_1. The total precession angle of the neutron will be:

$$\varphi_1 = \frac{\gamma B_1 l_1}{v_1}$$

depending on the velocity (wavelength) of the neutrons. If v_1 has a finite distribution, after a short time (a few turns of the polarization) the beam will appear to be completely depolarized. If now the beam will go through an other region with opposite field B_2 and length l_2 the total precession angle is:

$$\varphi_{tot} = \frac{\gamma B_1 l_1}{v_1} - \frac{\gamma B_2 l_2}{v_2}$$

In the case of elastic scattering on the sample $v_1=v_2=$ v and if $B_1 l_1 = B_2 l_2$ then φ_{tot} will be zero independently of v and we recover the original beam polarization. Let us suppose now that a neutron is scattered with a small ω energy exchange between the B1 and B2 region. In that case in leading order in ω :

$$\varphi_{tot} = \frac{\hbar \gamma B l}{m v^3} \omega \quad \text{where m is the mass of the neutron}$$

If we put an analyzer after the second precession field and the angle between the polarization of a neutron and the analyzer direction is φ, then the probability that a neutron is transmitted is $\cos\varphi$. We have to take the expectation value of $\langle \cos\varphi \rangle$ over all the scattered neutrons. At a given q the probability of the scattering with ω energy exchange is by definition $S(q,\omega)$. Consequently the beam polarization measured is:

$$\langle \cos\varphi \rangle = \frac{\int \cos(\frac{\hbar \gamma B l}{m v^3} \omega) S(q,\omega) d\omega}{\int S(q,\omega) d\omega} = S(q,t)$$

So NSE directly measures the intermediate scattering function where:

$$t = \frac{\hbar \gamma B l}{m v^3}$$

It is important to notice that $t \propto \left(\frac{1}{v}\right)^3 \lambda^3$ so the resolution in t increases very rapidly with λ.

Implementation

In practice reversing the magnetic field is difficult as in the middle this would create a zero field point where the beam gets easily depolarized. Instead, a continuous horizontal field is used (conveniently produced by solenoids) and a $\pi/2$ flipper starts the precession by flipping the horizontal polarization perpendicular to the magnetic field. The field reversal is replaced by a π flipper which reverses the precession plane around an axis and at the end a second $\pi/2$ flipper stops the precession and turns the recovered polarization in the direction of the analyzer.
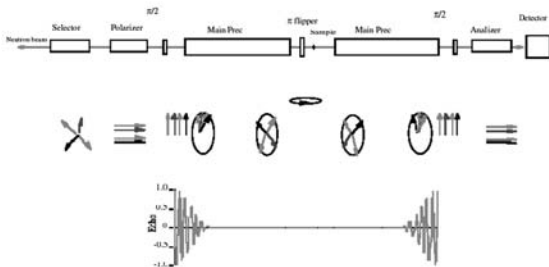
Figure 1: Sketch of a NSE spectrometer

Elements

Monochromatisation:

The biggest advantage of NSE is that it decouples monochromatisation from energy resolution. Whenever q resolution is not so important (or it is determined by the angular resolution rather than the wavelength distribution), a neutron velocity selector with high transmission (e.g. $\Delta\lambda/\lambda$=15% FWHM) is the best choice. If necessary the wavelength distribution can be reduced by installing the analyzer a crystal monochromator (graphite or mica) and the detector in Bragg geometry.

A further option is to use time of flight (TOF) as implemented on IN15. The fully polychromatic beam (Maxwell distribution from the reactor) can be pulsed by using rotating disk choppers relatively far (e.g. 20m) from the detector. By the time the neutrons reach the detector, the pulse will be completely spread and from the flight time we can calculate back that at any moment which wavelength at what monochromatization is detected. Collecting data in different time channels, a whole range of wavelengths can be used.

Polarizer:

This is a very essential part of the spectrometer, and generally supermirrors are used. There are two possible choices, reflection or transmission mode. As the polariser-sample distance is in the order of 2-3m the main danger in both cases is the unwanted increase of the incoming beam divergence from the polariser. Due to that relatively big distance here one can loose integer factors in the neutron flux on

the sample. Inherently the reflecting supermirrors are more susceptible to increase the beam divergence, and also have the inconvenience that the reflection angle might have to be adjusted to different wavelength if the useful range is large enough. On the other hand the supermirrors of this type were easier to obtain.

Recent progress allows the production of supermirrors on Si wafers with sufficiently good quality to make cavity like transmission devices.

As this is the most important part of the incoming beam it needs a closer examination. If we look at the trajectory **A** which comes parallel with the beam axis, we can see that it becomes very divergent after the polariser. Indeed if the
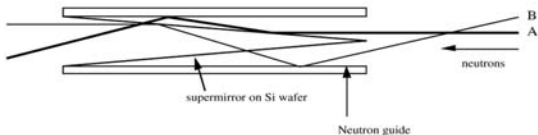
Figure 2: "Cavity" type transmission polariser

wavelength is sufficiently large, the first reflection on the supermirror is below the critical angle and the polarization happens only when the neutron is bounced back from the guide, but now with a larger incoming angle. However there is trajectory **B** arriving with the same large divergence and, as shown on Fig 2, will go out of the polariser parallel with the axis. If this very divergent neutron is missing, due to misalignement or cuts in the guide, trajectory **A** will not be replaced and effectively the center of the beam will be emptied.

π and π/2 flipper:

The flipper action is based on the nonadiabatic limit. Using a flat coil (≈5mm thick) perpendicular to the neutron beam with a relatively strong field inside and arranging such that the horizontal field is small, the polarized neutrons going through the (thin) winding do not have time to follow adiabatically the change in the field direction. All of a sudden the beam polarization is no more parallel to the magnetic field and it will start to precess around the field. With the appropriate choice of the field strength and direction, the neutrons will precess exactly π or π/2 by the time they fly through the flipper.

In the case of TOF, the flipper current has to be modulated in time to achieve the desired action for the wavelength which is just passing through.
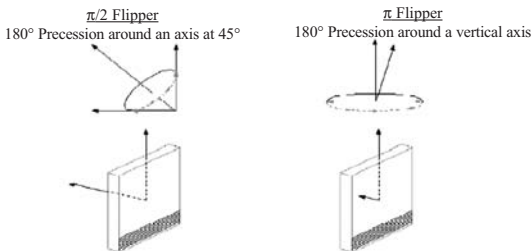
Figure 3: π/2 and π "Mezei" flippers simplified scheme

Main precession coils

We have seen that the Fourier time is proportional to the field integral. If we want a good resolution, we need high field and long integration path. Both will have a drawback. Even the most symmetric solution for the main precession coil, a solenoid, will produce an inhomogenous field for finite beam size. The underlying physical reason is that in the middle of the precession coil we have a strong field and at the flippers, as was explained above, we need a small horizontal component. Since Maxwell we know that div(B) is zero, consequently the transition region will introduce inhomogeneities.

Making long precession coils is not necessarily optimum because that increases the distance between the source (polariser exit) and the sample as well as the sample-detector distance. The counting rate will decrease with R^{-2}*R^{-2}.

Special attention has to be payed that at least the winding is as regular as possible to be able to calculate the necessary corrections. This is not always an evident task as for example on IN11, the coils consist of two layers of water cooled hollow conductor, with a total number of turns 400 and max current of 600 Amps.

"Fresnel coils"

How to correct the unavoidable inhomogeneities due to the finite size beam? Let us consider the field integral difference between the trajectory on the symmetry axis and one parallel at a distance r through the solenoid. In leading order this gives:

$$\Delta \int B dz \equiv \frac{r^2}{8} \int \frac{1}{B(z)} \left(\frac{\partial B(z)}{\partial z} \right)^2 dz$$

2.8-6

It can be shown also that a current loop placed in a strong field region changes the field integral by $4\pi I$, if the trajectory passes inside the loop and by zero if it passes outside. To correct the above calculated r^2 dependence we just have to place properly arranged current loops in the beam. The so called Fresnel coils just do that.[1]

They are usually made by printed circuit technology preparing two spirals where the radius changes as $r \propto \sqrt{\varphi}$, placed back to back with a thinnest possible insulator (30 micron kapton) to minimize neutron absorption.
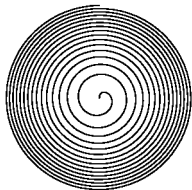
Figure 4: Fresnel coil

Resolution

Why field inhomogeneities are bad? In fact all we are interested in is the field integral. We have to use finite beam size if we want to have finite counting rates. With finite beam size we have different neutron trajectories arriving on the sample and coming to the detector. If the field integral for different trajectories are non equal then the final precession angle $\varphi_{tot} = \dfrac{\gamma B_1 l_1}{v_1} - \dfrac{\gamma B_2 l_2}{v_2}$ will be different for different trajectories and the detected

Figure 5: Echo response for an elastic scatterer (resolution) and sample.
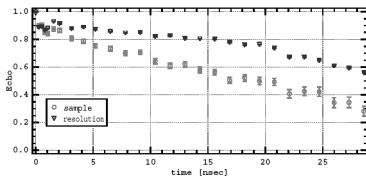
polarization even for an elastic scatterer will be reduced to $\langle cos\varphi \rangle$. The echo measured on the sample will be further reduced due to the energy exchange. Using an elastic scatterer we can measure the influence of the inhomogeneities and divide it out. (in other words while in energy space the instrumental response has to be deconvoluted from the measured curve to obtain the sample response, in the Fourier transformed space the deconvolution becomes a simple division)

Nevertheless if the field integral for different trajectories is too different, then $\langle cos\varphi \rangle$ quickly becomes zero and no matter how precisely we measure it, division by zero is usually problematic!
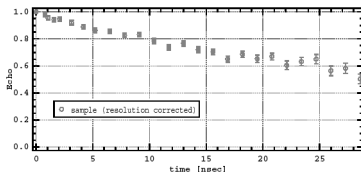
**Figure 6:
Resolution corrected sample response**

To put this into context lets have a look at some realistic numbers:
On IN11 we have a maximum field integral of ≈3*10⁵ Gauss·cm. With 8Å wavelength this gives a Fourier time of 28nsec. An exponential decrease with a time constant of 28nsec correspond in energy space to a Lorentzian line width of 23 neV. With the incoming neutron energy (8Å) this is a relative energy exchange of the order of 10^{-5}. The 360 degree phase difference between two trajectories corresponds to 17 Gauss·cm difference in field integral. This means a requested relative precision of better than $6*10^{-5}$ for all trajectories!

So what is the theoretical limit to the achievable resolution? There is no easy answer. In principle with sufficiently precise in-beam correction coils (like the Fresnels but including higher order term corrections) any resolution should be reachable. In practice we could certainly reached already an overall correction better than 10^{-4}.

If one changes the collimation conditions, the neutrons will explore different trajectories thus picking up different field inhomogeneities and the spectrometer resolution will change. When the resolution is pushed to its limits the number of important parameters which can give artifact increases rapidly and particular attention has to be paid to avoid them.

Measurement sequence
Now we will detail how an experiment is really done. Once the aims of the experiments are clear one has to decide what wavelength to use. Long wavelength gives better resolution but lower flux.

Then it has to be decided at which precession field (Fourier time) the echo points has to be measured. Depending on the problem studied, it can be adequate to take equidistant points on a logarithmic scale.

The field integral on the two side of the π flipper must be equal to a precision of 10^{-5}. This is done by using an additional winding on the first precession coil, the
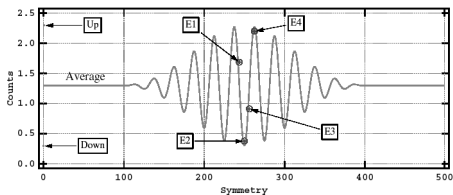
Figure 7: Measurement sequence

symmetry coil. Scanning the current in this coil will go through the exact symmetry point producing the typical echo group as shown in Fig. 7.

The periodicity of the damped oscillation is determined by the average wavelength and the envelope is the Fourier transform of the wavelength distribution. These depend only on the monochromator (velocity selector) so do not carry information on the sample. (With one notable exception, when the sample is crystalline and remonochromatize the beam. In that case the echo envelope becomes much more extended).

With the echo we measure how much of the initial polarization we recover. For elastic scatterer on an ideal instrument we recover it fully. During the scattering process the initial beam polarization can change. One reason for this can be when the sample contains hydrogen which has a high spin incoherent cross section. Spin incoherent scattering changes the initial polarization from P to -1/3P. The scattered intensity is thus composed of the sum of coherent and incoherent scattering decreasing the up/down ratio. The relative weight of these can, and will change as a function of scattering angle (or wave vector q). The measurement sequence thus starts with the measurement of spin-up and spin down for the given scattering angle and sample condition. This is accomplished by setting a guide field to maintain beam polarization and counting with π flipper on and π flipper off. This will give us two points marked as Up and Down on the figure 7. It would be inefficient to measure always the whole echo group as we are interested only in its maximum amplitude. At most it is equal to (Up-Down)/2. On an elastic scatterer we can quickly find where the center of the echo group is as a function of the current in the symmetry coil. As we also know the periodicity of the sinusoidal echo group it is more efficient to measure four points placed around the center with π/2 steps. This will give us:

$$E1 = Aver+Echo*\sin(\phi)$$
$$E2 = Aver-Echo*\cos(\phi)$$
$$E3 = Aver-Echo*\sin(\phi)$$
$$E4 = Aver+Echo*\cos(\phi)$$

From the four measurements Aver,Echo and ϕ (the phase) can be determined, and finally

$$I(q,t)/I(q,0) = 2*Echo/(Up-Down)$$

If we are sure that the phase is zero, then it is sufficient to measure E2 and E4. However in general to monitor any possible phase drift, (due to current instability, external perturbation, ... or accidental displacement of a coil.....) usually all the four points are measured but giving more weight to E2 and E4.

Signal and Background

No general recipe can be given, besides that both should be measured and the appropriate correction done! Nevertheless let us discuss a few typical cases and for the sake of simplicity let us take an ideal instrument (all flippers, polariser,analyzer having 100% efficiency, perfect field integrals).

Coherent, (spin) incoherent scattering:

As was mentioned, incoherent scattering changes the beam polarization to -1/3. Let's consider the case when the scattered intensity is composed of I= I*coh* + I*incoh*. Then we will have:

$$Up = Icoh+1/3Iincoh$$
$$Down = 2/3Iincoh$$
$$Echo = Icoh*fcoh(t) -1/3Iincoh*fincoh(t)$$

where f*coh*(t), f*incoh*(t) denotes the time dependence (dynamics) of each contribution and at t=0 both are equal to one.

Our usual data treatment will give

$$I(q,t)/I(q,0) = [Icoh*fcoh(t) -1/3Iincoh*fincoh(t)]/[Icoh-1/3Iincoh]$$

This means that from Up and Down we can determine the relative weight of each contribution but the separate time dependence is impossible to extract (except if suitable model exist and even then, it is hard to achieve the necessary statistical accuracy) . Fortunately in many cases it is possible to minimize the incoherent contribution by using deuterated samples. (Note the incoherent echo signal is further reduced by the factor 1/3) In other cases it is possible to suppose that the

2.8-10

dynamics of fcoh(t) and fincoh(t) is the same or nearly identical and then:

$$I(q,t)/I(q,0) = [Icoh*fcoh(t) -1/3Iincoh*fincoh(t)]/[Icoh-1/3Iincoh] = f(t)$$

There can be also some scattering from the sample holder, solvent, etc. Some cases can be treated in a simplified way. For example in polymer solution, scattering from deuterated solvent gives coherent scattering, but it is too inelastic to be seen by NSE, which means its relaxation time is out of the time window. In this case it will influence Up-Down but gives no echo. It is sufficient to measure Up and Down of the solvent. Similarly sample holders usually give only some elastic scattering. Again Up,Down and a few echo points in time are sufficient to establish its contribution.

NSE vs standard inelastic instruments

NSE not only has very high energy resolution but also has a very wide dynamical range. With some tricks (double echo) it can be as high as tmax/tmin = 1000 [2]. With the combination of several wavelength this can be further extended by a factor 10-100. We can measure energy exchanges up to $100\mu eV$ which not only overlaps with back scattering but also with Time-Of-Flight like IN5 or IN6. When to choose which instrument?

The fundamental difference is that NSE measures in Fourier time while TOF in omega space. Consider a sample which has a strong (95% of the intensity) elastic line, and well defined but weak (5%) excitations at finite energy. While this is well separated in omega space (Fig. 8), on NSE the Fourier transform will give a small (5%) cosine oscillation around 0.95. Statistically this is very unfavorable (Fig. 9). Furthermore the rough wavelength distribution (around 15% FWHM) of NSE will smear out the oscillations (t ~λ^3). For that type of experiments TOF is better suited.
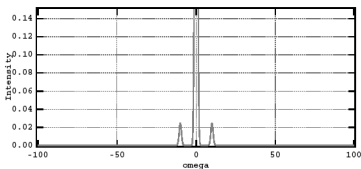
Figure 8: Spectrum in w space measured on a Time-Of-Flight spectrometer.

On the other hand when all (or most of) the intensity is quasielastic, NSE can give more precise information on the time dependence. The main reason is that the
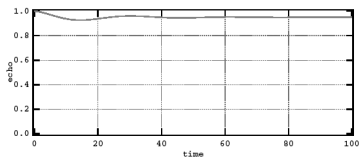
Figure 9: Same spectrum than Fig. 8 measured in the time domain by NSE.

deconvolution of the instrumental resolution is replaced by a simple division which leaves the data less influenced by numerical manipulation. Below is an example of the relaxation time measured on magnetic nanoparticles imbedded in an aluminium matrix (Fig. 10). With the combination of IN11 and IN15 (the NSE instrument optimized for long wavelength , long Fourier times) more than four decades in time could be covered.
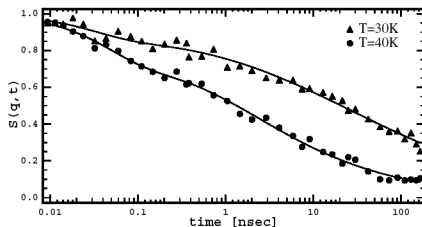
Figure 10: Relaxation spectrum of diluted magnetic nanoparticles measured by NSE.

Studying fully incoherent scatterers is also not very favorable for NSE. Already incoherent scattering in general gives rather weak intensity, secondly the - 1/3 factor in polarization decreases the statistical accuracy. These drawbacks are somewhat lifted by now on the multidetector spin echo instruments like IN11C and SPAN in Berlin. (see below)

Finally an interesting observation. If accidentally the incoherent contribution is about three times higher than the coherent one, then we end up with no

polarization of the scattered beam and if the dynamics of the two is the same, the experiment is unfeasible on NSE as the echo signal will be always zero.

Variants

Inelastic NSE

One could ask the question whether the method could be used in the case of well defined excitations? The answer is yes, but with some modification. By choosing $B_1 l_1 \neq B_2 l_2$ the same Fourier back-transformation happens but around the excitation energy ω_0 [1]:

$$\omega_0 = \frac{m}{2h} v_1^2 \left(1 - \left(\frac{B_1 l_1}{B_2 l_2}\right)^{\frac{3}{2}}\right) \quad ; \quad \frac{\int \cos(\frac{\hbar\gamma B_1 l_1}{m v_1^3}(\omega - \omega_0))S(q,\omega)d\omega}{\int S(q,(\omega-\omega_0))d\omega} = S(q,t)$$

v_1 is the velocity of the incoming neutron and v_2 is after the scattering

The problem here is that around $\omega=0$, $S(q,\omega)$ usually has a strong peak (either quasielastic scattering, diffuse elastic scattering and/or incoherent scattering or just instrumental background) The solution is to use a triple axis spectrometer geometry which acts as a filter, pre-cutting an interval around ω_0 with a coarse resolution compared to NSE. There is a further requirement when ω is q dependent (like a phonon branch). We have to make the spin precession dependent on the incoming and outgoing direction. Interested readers should look up the details in ref[1]. Here we just give an easy to understand picture. Quasielastic NSE measures the Fourier transform from ω to time space. This is a Fourier transform in the 1D space. Now we switch to the (at least) 2D q- ω space. If ω is q independent (at least in the
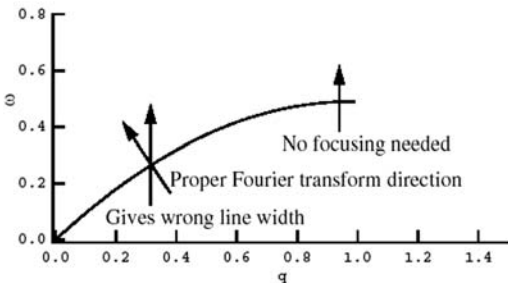
Figure 11: Principles for measuring linewidth on a dispersion curve by NSE.

vicinity we are measuring, e.g. close to the Brillouin zone boundary) with asymmetric field integral we make the Fourier transform around a finite ω_0 and we obtain the line width. Now if we do the same e.g. on an acoustical branch we will Fourier transform along a vertical line. To measure the real physical line width, we need to do the Fourier-transformation along a line perpendicular to the dispersion relation (Fig. 11). This refocalisation of the echo works if the spin precession becomes dependent on the neutron direction.

Magnetic scattering

The application of NSE to magnetic scattering has special features. One is that **ferromagnetic** samples can hardly be studied. The random orientation of magnetic domains introduces Larmor precessions around random axis and unknown precession angles normally resulting in depolarisation of the beam and the loss of the echo signal. In some cases the application of a strong external field to align all the domains in the same direction can help for one component of the polarization to survive [1]

The second case is **paramagnetic** scattering. If the scattering vector (q) is in the **y** direction, then in the sample only the spin components which are in the **xz** plane (perpendicular to q) will contribute to the magnetic scattering. As the precession plane of the neutrons in the usual NSE geometry is the **xy**, the neutrons which arrive spin parallel to q will undergo spin flip scattering, while those arriving perpendicular to q will have 50% probability of spin flip and 50% probability of non spin flip scattering. Accordingly the scattered beam polarization can be decomposed as:

$$\frac{1}{2}\begin{pmatrix} -P_x \\ -P_y \\ 0 \end{pmatrix} + \frac{1}{2}\begin{pmatrix} P_x \\ -P_y \\ 0 \end{pmatrix}$$

We can realize that the second term is equivalent to a π flipped beam around the **y** axis. Consequently without a π flipper the second term will give an echo with 50% amplitude of the magnetic scattering, while using a π flipper the first term results in a negative echo of 50% amplitude plus a full echo from the eventual nuclear scattering as well. This means that without π flipper *only* the magnetic scattering gives an echo signal, which eliminates the need of time consuming background measurements to separate the nuclear contribution.

Antiferromagnetic samples do not depolarize the beam, so in most cases they are identical to paramagnetic samples. However if we measure a single-crystal it might happen to be a single domain and depending on the spin direction one can have full echo without π flipper or we might need a π flipper to see any echo.

Resonance or Zero Field Neutron Spin Echo (ZFNSE)

This method was introduced by Gähler & Golub [3]. We will just give a quick explanation how to understand the basic principle. The method has clear advantages in the case of inelastic NSE. Whether the quasielastic NSE will or will not have better performance we will see when sufficient experience will be accumulated with ZFNSE.

The magnetic field profile along the axis of a classical NSE schematically is the following: Nearly zero horizontal field at the first $\pi/2$ flipper, strong (B_0) field in the first solenoid, nearly zero at the π flipper, again strong field in the second precession region, finally nearly zero again at the second $\pi/2$ flipper. In B_0 the neutron precesses with the Larmor frequency $\omega_0 = \gamma B_0$. Let us choose now a rotating frame reference which rotates with ω_0. In this frame the neutron seems not to precess in the solenoids which means it sees $B'_0 = 0$. However now in the originally low field region it will rotate with ω_0 which indicates the presence of a strong B_0 field. The small field of our static flipper will appear to rotate also with ω_0.

Let us realize this configuration now in the lab frame. Inside the π and $\pi/2$ flippers we must have a strong static field B_0 and perpendicular to that a small field which rotates with $\omega_0 = \gamma B_0$. We need a well localized strong magnetic field perpendicular to the neutron beam, and inside a smaller coil perpendicular both to the neutron beam and to the strong field. This small coil has to be driven by a radiofrequency generator which will produce the necessary (resonance) rotating field. In between these flippers a strictly zero field region has to be insured to avoid "spurious„ spin precession. The first prototype spectrometers all use mu-metal shielding + earth field compensation.

Multidetector variants

At the time of writing, four instruments are developed to extend the "classical„ NSE to use multidetectors, and thus reducing the data acquisition time. In all cases the problem is that useful information can be collected in all detectors only if the echo condition can be fulfilled simultaneously for all of them. This is not a straightforward exercise as the field integrals must be equal with a precision of 10^{-5}! This strict condition can be somewhat relaxed, if we can have enough information in each individual detector to make the phase correction on a one-by-one basis. This is not always possible if the scattering is weak. In that case, on an elastic scatterer, the relative phase differences between detectors can be measured and imposed during the data treatment.

The most straightforward implementation of such a multidetector is on the instrument IN15 at the ILL and a somewhat later construction in KFA Jülich. Here

simply the solenoid diameters were increased to allow the use of a small 32cm x 32cm multidetector. The difficulty is to make a sufficiently big Fresnel coil with the necessary precision, without absorbing a substantial fraction of the neutron beam. On IN11 an option has been constructed, to replace the secondary solenoid with a specially shaped sector magnet (Fig. 12). The expected field homogeneity is inherently lower, but in many cases in the high q region the best possible resolution is not needed anyway. The gain factor in total countrate is however 23 time higher. This gain is sufficient to measure even the very unfavorable incoherent scatterers.
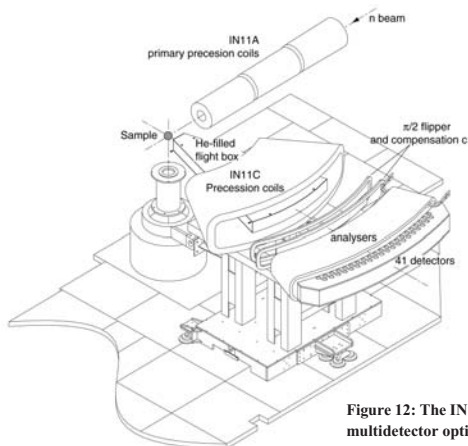
Figure 12: The IN11C multidetector option.

In Berlin a totally new approach was initiated. If one takes a Helmholtz like coil, but the two half generates a field opposite to each other, then in the equatorial plane the field is guaranteed to be rotationally symmetric. The neutron beam comes in along a radius and the detectors are placed all around. The practical problem here is a zero field point at the sample position which would depolarize the beam. The solution proposed is to move this zero point above the sample with the help of some additional coils.

Useful numbers

Some numbers from the ILL spin-echo instruments are given in the table.

Table 1:   **Fourier time covered in nsec**

	@ 4Å		@ 6Å		@ 8Å		@ 10Å		@15Å		@ 20Å	
-------	t_{min}	t_{max}	t_{min}	t_{max}	t_{min}	t_{max}	t_{min}	t_{max}	t_{min}	t_{max}	t_{min}	t_{max}
IN11	0.01	3.3	0.04	11.1	0.09	26.4	0.18	51.7				
In11C	0.01	0.5	0.04	1.83	0.09	3.1	0.18	4.2				
IN15					0.12	26.3	0.34	51.5	0.8	174	1.4	300

The miminum time can be shorter by a factor 3-5 if double echo [2] configuration is used. The maximum reachable Fourier times can be shorter as much as a factor two when the detector is positioned at high scattering angles.

References

[1] Mezei,F. (editor) Neutron Spin Echo Lecture Notes in Physics 128 Springer-Verlag 1979

[2] B. Farago Annual Report ILL 1988 p: 103

[3] R.Gähler, R.Golub Z.Phys, B65 (1987) 269.

Aknowledgement

Neutron Diffraction on Reactors

A.W. Hewat and G.J. McIntyre

1. Introduction

The efficiency of a neutron diffractometer, whether on a reactor or a spallation source, depends essentially on the time-averaged flux on the sample and the solid angle of the detector. Large new detectors and focusing neutron optics are increasingly being used to take advantage of the high flux on the sample that is obtained with a continuous neutron source. In this article, we consider the design of single-crystal and powder/liquids diffractometers, especially those using white beams and large area detectors, for different types of experiment. We give the essential formulae needed to extract structure amplitudes from the observed intensities.

2. The design of modern reactor-based diffractometers

The Shelter Island Workshop[1] proposed that the intensity of a neutron diffractometer, whether on a reactor or a pulsed neutron source, depended only on the time-averaged flux on the sample, the sample volume, and the solid angle of the detector:

$$I \sim flux*sample*detector$$

2.1. The time-averaged flux on the sample

On a reactor, the time-averaged flux on the sample can be greatly increased by using a wide band of wavelengths, without reducing the instrument resolution for a particular angle – the focussing angle – where the diffracted Bragg angle equals the monochromator Bragg angle (fig.1). For example, even on a high-resolution powder diffractometer such as D2B at ILL[2], the relative spread in wavelength $\Delta\lambda/\lambda$ can be 1% or more for a $\Delta d/d$ resolution of 0.1%.

An extreme case of the use of a wide band of wavelengths is the "quasi-Laue" diffractometer such as LADI[3] and VIVALDI[4] at the ILL. A very large position-sensitive detector (PSD), here a set of neutron-sensitive image plates, collects an almost "white" beam of neutrons falling on the sample, with the different wavelengths sorted out, not by time-of-flight (TOF) or by monochromator/analyser crystals, but by the diffraction conditions of the single-crystal sample itself (fig.3).

A continuous neutron intensity with a wide band of wavelengths, and the resulting high time-averaged flux on the sample, is the principal advantage of reactor diffractometers. On a TOF diffractometer, the flux on the sample is also rather constant
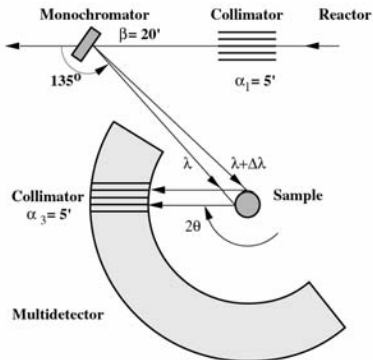
Figure 1. The focusing of a wide band of wavelengths on the D2B high-resolution diffractometer. A large detector collects many simultaneous reflections from the polycrystalline sample.

in time, since the sharp initial pulse is spread out at the sample such that the slowest neutrons arrive just before the fastest from the next pulse. But the time-averaged flux may be an order of magnitude lower; relatively long flight paths and a $\Delta\lambda/\lambda$ of 0.1% are needed to obtain a resolution $\Delta d/d$ of 0.1%. Fortunately, the solid angle of the TOF detector for high scattering angles (backscattering) can be large while still allowing high resolution, since $\Delta d/d \sim \Delta\theta.\cot\theta$ and $\cot\theta$ is small for large θ. This can compensate for the intrinsically lower flux on the sample of the TOF diffractometer, supposing that the sample volumes are similar.

2.2 The sample volume and resolution

The sample volume limits the resolution that can be obtained with a PSD, and must therefore be considered in the design of a diffractometer. For example, the D20 instrument at ILL uses a large PSD with an angular resolution of 0.1° at a distance of 1470 mm from the sample. The optimal 0.1° resolution would then require a sample of less than 2.57 mm diameter! Larger samples are normally measured on D20, with less than optimal resolution. Higher resolution could of course be obtained by increasing further the sample-detector distance, but then a very tall detector would be needed to conserve the solid angle.
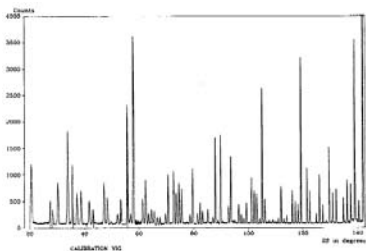
Figure 2. The first diffraction pattern (1984) from the D2B high-resolution powder diffractometer[2]. The peak intensity is rather constant over the entire d-spacing range, unlike with X-rays where scattering falls off with angle, or with time-of-flight techniques where intensity falls for shorter d-spacings or wavelengths.
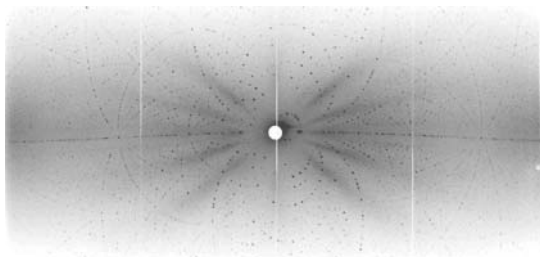
Figure 3. The dispersion of the "white" band of wavelengths on the quasi-Laue diffractometer VIVALDI. The large PSD collects many simultaneous reflections from the single-crystal sample, where each reflection corresponds to a different wavelength.

Alternatively, high resolution can be obtained with Söller collimators as fine as 5' as on D2B, and then much larger samples can be used, with sample volume

and neutron intensity increasing with the square of the diameter. Söller collimators also limit the detector solid angle, since even with 128x5' collimators, only 6.7% of the 158.5° scattering angle is covered, but a sample as large as 16 mm in diameter can be used, together with tall linear-wire detectors to increase the solid angle.

Until very large, high-resolution PSD's can be constructed, the D2B-type instrument is then more suitable for very high resolution, while the D20 instrument is more suitable for very high intensity. There is of course a degree of overlap in application, depending on the amount of sample actually available, and the particular problem.
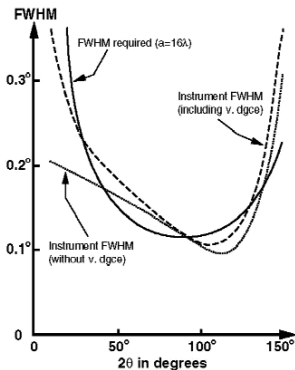
Figure 4. The resolution or Full Width at Half Maximum of peaks is best at the focussing angle (140°), which is high so as to match the FWHM required to resolve adjacent peaks for example, a 16Å cubic cell[2].

The resolution is worse at angles far from the focussing angle, but by choosing a large focussing angle the instrument resolution can be made to match the spacing between Bragg peaks (fig. 4). There are few peaks at very low or very high angles, and if necessary the neutron wavelength can be increased to ~6Å to move reflections with large d-spacings to higher angles for better resolution. This situation is different in the case of the backscattering TOF diffractometer, where the resolution is equally good for all d-spacings, but modern TOF instruments such as GEM at ISIS also use lower-angle detectors to increase efficiency and collect data with a variety of resolutions.
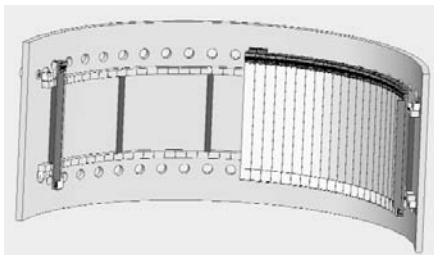
Figure 5. The new 30º x 120º 2D multi-wire PSD for D19 at ILL Grenoble. Such large detectors match the solid angle of the best pulsed-neutron source diffractometers, while also benefiting from the very high time-averaged neutron flux available on the sample at a reactor source.

2.3 The detector solid angle

When only small samples are available, as in pressure cells, or when medium resolution is sufficient, the PSD on a reactor can be as large or larger than that on a pulsed neutron source. Figure 5 shows the new 2D PSD being constructed at ILL for D19. This detector covers 30º vertically by 120º horizontally, covering a solid angle of $4\pi.\sin(15º)\times120/360=1.1$ steradians, a record for electronic detectors.

The D19 detector is being built for measurements on single crystals and fibres, but would also be good for fast powder or liquid diffraction, with an angular resolution of 11' (2.5 mm wide elements at 760 mm). Using a 160º detector, a Diffractometer for Rapid Acquisition over Ultra-Large Angles (DRACULA) might be constructed to compete with the fastest diffractometers on the future SNS pulsed source. (See table below.)

	ILL-D20	ILL-DRACULA	US-SNS
Time averaged sample flux	5×10^7	$\sim10^8$	$\sim2.5\times10^7$
Sample volume	1	1	1
Detector solid angle	0.27 sr	1.45 sr	3.0 sr

Table 1. A comparison of possible high-intensity powder diffractometers on the ILL reactor and US spallation source, showing that the high time-averaged flux at the sample, together with a D19-type PSD detector, should allow the reactor machine DRACULA to compete with the best pulsed source.
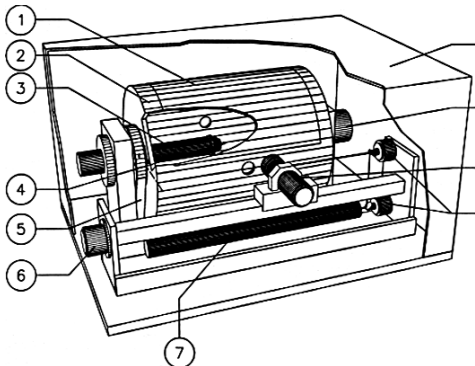
Figure 6. The first neutron image-plate diffractometer LADI, developed at EMBL-ILL Grenoble, showing the image plate (1) on a rotating drum (2) surrounding the crystal on its supporting rod (3). The neutron beam enters and exits through the small holes in the middle of the drum, and the remaining components allow the laser and photo-multiplier tube (7-9) to scan the surface of the image plate to read off the diffraction pattern.

Reactor sources look even more attractive when continuous white beams of neutrons can be used, as with the quasi-Laue technique on image-plate detectors such as those of LADI and VIVALDI at ILL (fig.6). Then the time-averaged flux on the sample is very much greater than can be obtained either with monochromatic or pulsed neutron techniques. As well, the image-plate detector covers a large solid angle (7.9 steradians); image plates can be curved over a cylinder around the sample, while still being read out electronically. These diffractometers are at present very new, and could be even further improved by using super-mirror optics to increase the flux on the sample.

3 The resolution function in diffractometry

The 3-D resolution function of a diffractometer depends on many factors, principally the incident-beam or incident-guide divergence, the monochromator mosaic, the sample size and mosaic, and the scattering geometry, and is

conveniently measured or calculated as an ellipsoid in terms of differential increments, $\Delta\gamma$, $\Delta\omega$ and $\Delta\nu$, in the observational variables, γ, ω and ν. Following (for the most part) the definitions of Busing & Levy[5], we describe the crystal orientation by the Euler angles ω, χ and ϕ. To allow for out-of-plane reflections we describe the direction of a particular diffracted ray by γ and ν, the in-plane and out-of-plane angles, respectively, on the surface of the Ewald sphere. 2θ remains the angle between the incident and diffracted beams, so that,

$$\cos 2\theta = \cos\gamma\cos\nu. \qquad (1)$$

In single-crystal diffraction the resolution in ω is usually considerably better than that in γ, which in turn is considerably better than that in ν.

The derivation of the full 3-D resolution function is straightforward but lengthy. Since the landmark papers by Nathans and Cooper[6], there have been many derivations for various instrumental geometries. These usually derive the function in terms of Gaussians, which facilitates the numerous convolutions particularly in three-axis geometry with its multitude of collimators, but can disguise the effect of individual parameters. For diffraction, Schoenborn[7] derived explicitly the direction in the multi-dimensional function of the contribution from each of the various instrumental parameters. The different contributions generally act along different directions, knowledge of which may indicate how to optimise a particular measurement.

$\Delta\gamma$, $\Delta\omega$ and $\Delta\nu$ can be converted to reciprocal-space coordinates over the range of interest for one reflection by a homogeneous affine transformation; for powder diffraction $\Delta\gamma$ ($\Delta 2\theta$) is then related to Δd^*. Going to shorter wavelength (λ) decreases the resolution in the reciprocal directions corresponding to $\Delta\gamma$ and $\Delta\nu$. The increasing use of PSD's with their capability to resolve single-crystal reflections in 3-D means that we can tolerate a shorter wavelength if this is needed to give better real-space resolution (d_{min} or Q_{max}). The principal rule, though, is to use as long a wavelength as possible to profit from the λ^4 dependence of the product of the reflectivities of the monochromator and the sample. Fig. 7 shows some resolution characteristics of the ILL single-crystal diffractometers for chemistry and physics.

3.1 'Conventional' crystallography

The aim of the experiment is to measure the integrated intensities of many reflections, even for incommensurate and magnetic structures. We are generally interested in nearly equal resolution in all directions of reciprocal space, so the choice of diffractometer is determined by which of $\Delta 2\theta$, $\Delta\omega$ and $\Delta\nu$ is largest, which is usually $\Delta\nu$. A corollary is that instruments intended for 'conventional' crystallography usually avoid the use of vertically focussing monochromators.
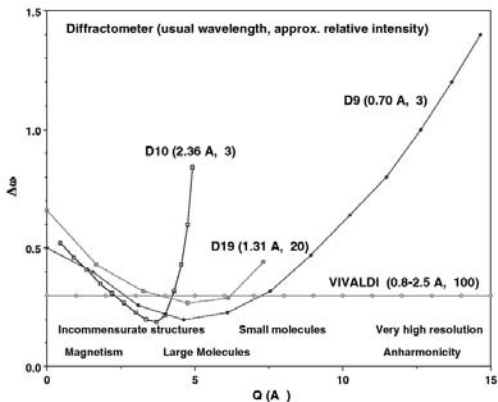
Figure 7. Different ILL single-crystal diffractometers optimised for different science: full-width at half-height ($\Delta\omega$) versus Q (= $4\sin\theta/\lambda$) for typical samples and choice of monochromators, and the approximate relative intensities. More intensity is available from other optional monochromators, at the expense of resolution.

3.2 Phase transitions and critical scattering

Here the aim is often just to scan repeatedly a few reflections or a limited region of reciprocal space while varying the temperature, magnetic field or pressure. Concentration of the time-averaged flux into a small wavelength band clearly gives the advantage to the monochromatic single-crystal diffractometer. The adaptability of monochromatic diffractometers means that we can usually orient the sample to put the reciprocal-space direction of interest most nearly along $\Delta\omega$, and we can even accept a large $\Delta\nu$ if the flux on the sample is increased by a vertically focussing monochromator. One important consequence of the affine transformation between $\Delta\gamma$, $\Delta\omega$ and $\Delta\nu$, and orthogonal reciprocal-space coordinates is that there is one orientation (up or down) of a given reciprocal-lattice plane that gives best resolution along a given line in that plane [8]. The orientation is usually that which gives the larger $|\Delta\omega + \Delta\phi \cos\chi|$ between q steps along the line of interest.

3.3 Laue diffraction

The spatial resolution of the reflections is given by the projection of the crystal shape onto the image plate, convoluted with the divergence of the incident beam, the mosaic spread of the crystal (negligible for a crystal of good quality), and the point spread function of the image-plate and scanner. The divergence of the incident beam in a curved thermal guide is typically 3.5λ mrad Å full width at half height, which gives ~0.25° at $\lambda = 1.5$ Å, a typical wavelength of maximum flux on a thermal guide. In terms of the angle between reciprocal-lattice directions $\mathbf{Q}_1$ and $\mathbf{Q}_2$ the spatial resolution becomes,

$$\angle\mathbf{Q}_1\mathbf{Q}_2 = w/(2R) * \alpha * \eta * p \qquad (2)$$

where w is the cross-section of the crystal perpendicular to the diffracted beam, R is the sample-to-detector distance, α is the beam divergence, η is the mosaic spread, and p is the point spread function. (The factor 1/2 is due to the relation $\theta{:}2\theta$ between the angle between scattering vectors and the angle between the corresponding diffracted beams.) The spatial point-spread function of an image-plate detector is usually negligibly small (~150 µm). Thus for a detector of radius 160 mm and a typical crystal dimension of 2 mm, the spot diameter is about 0.6° in reciprocal space. The resolution is dominated by the crystal size, and for a spherical sample is constant over the whole Laue diffraction pattern, and over all orientations of the crystal. Allowing for twice the spot diameter between reflection centres (to allow confident estimation of the background) we can resolve reflections up to order 25 for a primitive cubic unit cell. A reflection of order 25 at $2\theta = 180°$ at a wavelength of 1.5 Å corresponds to a unit-cell edge of 20 Å.

4 Structure amplitudes from integrated intensities

The reduction of the observed integrated intensities to structure amplitudes (F_{hkl}^2) is the same as for X-ray diffraction, except that no polarisation factor is required for unpolarised neutron beams. For the three diffraction methods that we discuss here, the total integrated intensity of one reflection is related to the structure amplitude by [9]:

a) powder sample in a monochromatic beam

$$I_{hkl} = m\, I_o(\lambda_o)\, \Delta\lambda_o\, V\, N^2\, |F_{hkl}|^2\, \lambda_o{}^3\, [1/(4\sin\theta)]\, A^*\, T\, E \ \ n\, s^{-1} \qquad (3)$$

b) rotating single crystal in a monochromatic beam

$$I_{hkl} = I_o(\lambda_o)\, \Delta\lambda_o\, V\, N^2\, |F_{hkl}|^2\, \lambda_o{}^3\, (1/\varpi)\, L\, A^*\, T\, E \ \ n\, s^{-1} \qquad (4)$$

c) fixed single crystal in a polychromatic beam (Laue technique)

$$I_{hkl} = I_o(\lambda)\, V\, N^2\, |F_{hkl}|^2\, \lambda^4/2\sin^2\theta\, A^*\, T\, E \ n\, s^{-1} \qquad (5)$$

where m is the multiplicity factor for the powder reflection, λ the wavelength, V the sample volume, N the number of unit cells per unit volume, ϖ the angular scanning velocity, L the Lorentz factor which is related to the time-of-reflection opportunity, A* the absorption correction, T the correction for inelastic phonon or thermal-diffuse scattering, and E the correction for extinction and multiple diffraction. To obtain $|F_{hkl}|$ involves measurement of I_{hkl} as accurately and as efficiently as possible, followed by application of the various correction factors. For most powder experiments, the corrections for absorption, thermal-diffuse scattering, extinction and multiple scattering can be ignored.

The principal disadvantage of the steady-state Laue technique is that it integrates over all wavelengths, which gives a particularly high background if the sample contains elements that give significant incoherent scattering. The incoherently scattered neutron background is,

$$\overline{I_{inc}} = I_o\,(\lambda)\Sigma\sigma_{inc}\,\Delta\lambda\,(V_s/V_c)\,(1/4\pi)\ \text{n s}^{-1}\ \text{sterad}^{-1}, \qquad (6)$$

where $\Delta\lambda$ is the wavelength band-pass and $\Sigma\sigma_{inc}$ is the total incoherent cross-section of the atoms in one unit cell, arising principally from hydrogen, which often constitutes 50% of organic samples and inorganic hydrates. Here, $I_o\,(\lambda)\Sigma\sigma_{inc}$ is averaged over the band-pass. The different units for I_{hkl} and I_{inc} emphasize the advantage of small guide divergence to reduce the point-by-point signal-to-noise ratio of the Laue diffraction pattern.

4.1 The generalised Lorentz factor

The expressions for I_{hkl} differ principally in the Lorentz factors. The Lorentz corrections for monochromatic powder diffraction and for single-crystal Laue diffraction are relatively simple since the sample does not rotate. Buras & Gerward [9] show how the Lorentz factors for the three techniques are related when the monochromatic single-crystal measurement is made by an ω rotation in the equatorial plane. With a large PSD, reflections may also be observed out of the equatorial plane, for which the Lorentz factor for an ω rotation becomes:

$$L = 1/(\sin\gamma\cos v). \qquad (7)$$

For some crystal structures, particularly those that are incommensurate in their nuclear or magnetic structures, it might be preferable to perform linear scans in reciprocal space rather than pure rotational scans. Here *linear* refers to the trajectory of the *detector aperture* through reciprocal space; for a particular reflection observed in such a scan the motion of the corresponding reciprocal-lattice point through the Ewald sphere is still along an angular trajectory. The

Lorentz factor is conventionally the inverse of the wavelength-independent part of the term dz/ds that relates the scan variable s to the normal z to the Ewald sphere in the integral of the observed counts over s:

$$|Fhkl|2 \; \alpha \int I_i(z) \, dz = \int I_i(s) \, (dz/ds) \, ds = \Sigma_i \, (dz/ds) \, \Delta s_i \, I_i(s_i). \qquad (8)$$

Since the interval in s over which I_i is non-zero is usually small, (dz/ds) is usually evaluated at the peak maximum and taken outside the integral. However for linear scans, rather than evaluate dz/ds and then perform the integration over s, it is computationally more convenient to evaluate the (ds/dz)Δs_i directly in terms of the incremental angular shifts, $\Delta\omega_i$, $\Delta\chi_i$ and $\Delta\phi_i$, that effect the steps Δs_i. If the reflection diffracts at the setting ω, χ, and ϕ [10],

$$\lambda(ds/dz)\Delta s_i = -[\Delta\omega_i \sin\gamma\cos v \; + \Delta\chi_i \sin\omega\sin v$$
$$+ \Delta\phi_i(\cos\chi\sin\gamma\cos v - \cos\omega\sin\chi\sin v)]. \qquad (9)$$

Although this expression does not in general permit a separation of (ds/dz)Δsi into an incremental scan step and a Lorentz factor, it does correct quite generally for the different velocities of different reciprocal-lattice points through the Ewald sphere whatever the scan mode. $|Fhkl|2$ for reflections observed in linear reciprocal-space scans are thus brought to the same scale as $|Fhkl|2$ for reflections observed by rotational scans.

4.2 Absorption correction

When a monochromatic beam of neutrons with incident intensity Io passes through a homogenous plate of uniform thickness t the intensity is reduced to,

$$I = I_o \exp(-\mu t), \qquad (10)$$

which defines μ, the total linear absorption coefficient. To a reasonable approximation the mass absorption coefficient μ/ρ, where ρ is the density of the absorber, is independent of the physical state of the absorber, and μ/ρ for a compound is additive with respect to the μ/ρ of its elements. This gives the practical working expression [11]:

$$\mu = (n/Vc) \; \Sigma_i \sigma_i \qquad (11)$$

where n is the number of molecules in the unit cell, Vc is the unit-cell volume, σi is the atomic absorption coefficient of atom i, defined as $(\mu/\rho)i$ (A/N) where A is the atomic weight and N is Avogadro's number, and the summation is over all atoms in one molecule.

For neutrons in the wavelength range of interest, σ is the sum of two terms: i) true absorption, which is due to nuclear capture processes; and ii) apparent

absorption due to scattering, both coherent and incoherent. For single crystals the absorption due to coherent scattering is usually considered separately as extinction and multiple diffraction. Nuclear capture absorption varies as λ, while the incoherent apparent absorption is independent of wavelength for most elements. A notable exception is hydrogen, for which the dependence of σ_{inc} on wavelength is roughly linear [12],

$$\sigma_{inc} = 19.2(5)\lambda + 20.6(9), \tag{12}$$

and is usually the dominant contribution to μ for hydrogenous materials. Sears [13] lists the values of the true absorption (σ_{abs}) and incoherent absorption (σ_{inc}) cross-sections required to calculate σ (= $\sigma_{abs} \lambda/1.798 + \sigma_{inc}$) for neutron experiments (reproduced and updated in the first article in this booklet). For measurements near nuclear resonances, it is prudent to determine the absorption coefficient experimentally.

For diffraction from a crystal bathed entirely in the beam, eq. (10) applies to each infinitesimal volume element with t being the total path length of the incident and diffracted beams within the crystal for that volume element. The absorption for the whole crystal is then obtained by integration over all volume elements

$$I = Io\,(1/V)\int V \exp(-\mu t)dV = Io\,A \tag{13}$$

to give the transmission coefficient A, which is the inverse of the absorption correction A*. Analytical integration is feasible for crystals of very regular shape such as spheres and cylinders [11]. For faceted crystals numerical integration is the usual technique [14]. These equations and methods also apply to the Laue technique, with the wavelength different for each reflection, and to very well compacted powder samples.

There is further absorption along the incident and diffracted beam paths outside the crystal, the absorption in each substance, be it air, sample-capillary walls, cryostat walls etc. also given by eq. (10). If the path length through any of these varies significantly with crystal orientation or detector position a correction for that absorption may need to be applied as well.

4.3 Extinction

Correction for extinction is made as in X-ray crystallography, usually following the formulae of Becker & Coppens [15], who include the crystal form via the mean absorption-weighted path length:

$$T = (1/VA)\int V\, t \exp(-\mu t)dV \tag{14}$$

which is calculated in a similar manner to the transmission factor. To check the

(a)   (b)
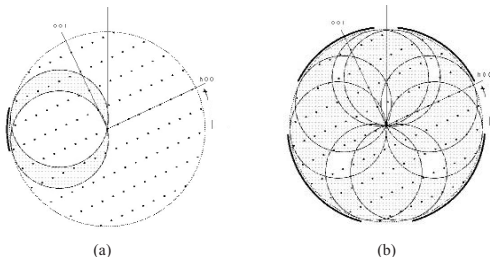
Figure 8. Reciprocal-space constructions to find the accessible regions for: (a) a vertical cryomagnet with a single 25º blind arc; and (b) one of the ILL horizontal cryomagnets which has restricted openings of 15º, 32º, 30º and 32º in the equatorial plane. The heavy outer arcs denote the blind angles of the cryomagnets, the open areas the accessible regions of reciprocal space, the shaded areas the inaccessible regions, and the black dots represent a possible reciprocal lattice plane.

corrections for absorption and extinction, it is recommended to make integrated intensity measurements of one or two reflections over a wide range of azimuthal angle (rotation around the scattering vector). After correction for absorption and extinction, the observed |Fhkl|2 for each reflection should be independent of the azimuthal angle.

5 Accessible regions of reciprocal space in extreme sample environments
The accessible region of reciprocal space for single-crystals in sample environments with limited access is found by drawing the Ewald sphere when the limit of each accessible window is in the incident beam. For the vertical and horizontal cryomagnets often used for diffraction experiments at the ILL, the accessible regions are as shown in Fig. 8. For a sample environment with very restricted access the wavelength can often be varied to bring the reflection(s) of interest into an accessible zone.

References
1. Jorgensen, J.D., Cox, D.E., Hewat, A.W., Yelon, W.B. (1985) Nuc.Inst.Meth. **B12**, 525-561.

2. Hewat, A.W. (1986) Mat.Sci.Forum **9**, 69-79.

3. Cipriani, F., Castagna, J.-C., Wilkinson, C. Oleinek, P., Lehmann, M.S (1996)

J. Neutron Res. **4**, 79-85.

4. Wilkinson,C., Cowan,J.A., Myles,D.A. A., Cipriani,F., McIntyre,G.J. (2002) *Neutron News* **13,** 37-41.

5. Busing, W.R., Levy, H.A. (1967) *Acta Cryst.* **22**, 457-464.

6. Cooper, M.J., Nathans, R. (1968) *Acta Cryst.* A**24**, 619-624, 624-627.

7. Schoenborn, B.P. (1983) *Acta Cryst.* A**39**, 315-321.

8. McIntyre, G.J., Renault, A. (1989) *Physica* B **156 & 157**, 880-883.

9. Buras, B. Gerward, L. (1975) *Acta Cryst.* **A31**, 372-374.

10. McIntyre, G.J., Stansfield, R.F.D. (1988) *Acta Cryst.* **A44**, 257-262.

11. *International Tables for X-ray Crystallography, Volume III* (1968), pp 157-200.

12. Howard, J.A.K., Johnson, O., Schultz, A.J., Stringer, A. (1987) *J.Appl.Cryst.* **20,** 120-122.

13. Sears, V.F. (1992) *Neutron News* **3**, 26-37.

14. Coppens, P., Leiserowitz, L., Rabinovich, D. (1965) *Acta Cryst.* **18**, 1035-1038.

15. Becker, P.J., Coppens, P. (1974) *Acta Cryst*. A**30**, 129-147.

TECHNIQUES

The Production of Neutrons

C. J. Carlile

1. THE PRODUCTION OF NEUTRONS

1.1 Natural Radioactive Sources

Neutrons can be produced by fusion processes in stars, by spallation processes of cosmic rays in the atmosphere and by the process of spontaneous fission. Other than that there is no natural source of neutrons. **The (α,n) reaction** however, with which Chadwick was first able to isolate and identify the neutron in 1932, is the nearest. In certain light isotopes the 'last' neutron in the nucleus is weakly bound and is released when the compound nucleus formed following α-particle bombardment decays. Chadwick made use of the naturally occurring α-emitter polonium-210 which
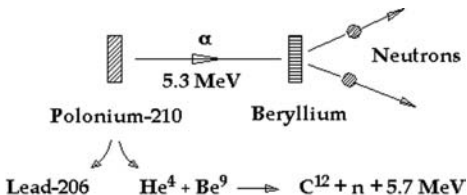
Figure 1: The discovery of the neutron in 1932 by Chadwick followed experiments of α particle bombardment of beryllium.

3.1-2
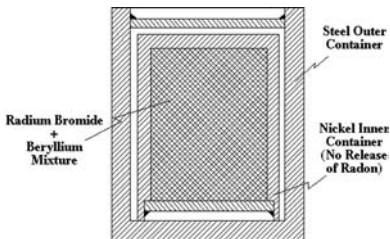
Figure 2: The cross-section through a portable laboratory neutron source containing radium and beryllium. A typical source is about 1cm in diameter.

decays to lead-206 with the emission of a 5.3 MeV α-particle. The bombardment of beryllium by α-particles leads to the production of neutrons by the following exothermic reaction which is illustrated schematically in Figure 1

$$He^4 + Be^9 \rightarrow C^{12} + n + 5.7 \text{ MeV}$$
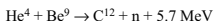
This reaction yields a weak source of neutrons with an energy spectrum resembling that from a fission source and is used nowadays in portable neutron sources of the kind commonly used for setting up neutron detectors. Radium or americium is normally the α-emitter in the typical design shown in Figure 2.

(γ,n) sources can also be used for the same purpose. In this type of source, because of the greater range of the γ-ray, the two physical
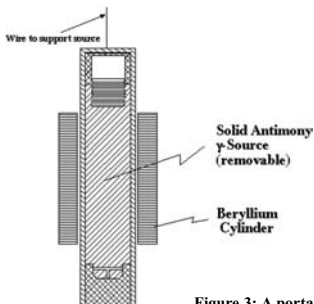
Figure 3: A portable neutron source using a γ emitter which by removal of the γ source can be switched off.
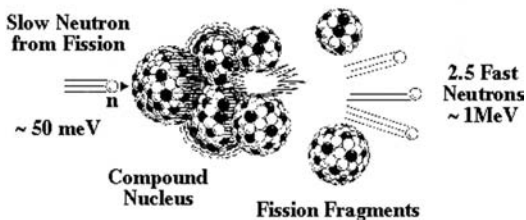
Figure 4: A schematic representation of the fission reaction.

components of the source can be separated making it possible to 'switch off' the reaction if so required by removing the radioactive source from the beryllium. The source illustrated in Figure 3 uses antimony-124 as the γ-emitter in the following endothermic reaction.

$$Sb^{124} \rightarrow Te^{124} + \beta^- + \gamma$$

$$\gamma + Be^9 \rightarrow Be^8 + n - 1.66 \text{ MeV}$$
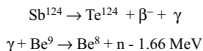
1.2 Fission

Uranium-235 which exists as 0.7% of naturally occurring uranium undergoes fission with thermal neutrons with the production of, on average, 2.5 fast neutrons and the release of ~ 180 MeV of energy per fission. In a critical assembly the fission reaction becomes self-sustaining with 1 neutron required to trigger a further fission, 0.5 neutrons being absorbed in other material and 1 neutron able to leave the surface of the core and be available for use. The reaction is shown schematically in Figure 4.

$$n_{thermal} + U^{235} \rightarrow 2 \text{ fission fragments} + 2.5 \ n_{fast} + 180 \text{ MeV}$$
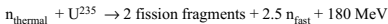
If we take the example of a 10 MW research reactor then 10^7 joules/sec are released which is 3.3×10^{17} fissions/sec at 180 MeV/fission which gives 8.5×10^{17} neutrons/sec released in the whole reactor volume. The resultant neutron energy spectrum of a reactor source is shown schematically in Figure 5.

The spectrum is composed of three distinct regions:

The first is **the fast neutron region** where the neutrons are produced. This is referred to as a Lamb distribution with the peak intensity occurring between 1 and 2

3.1-4
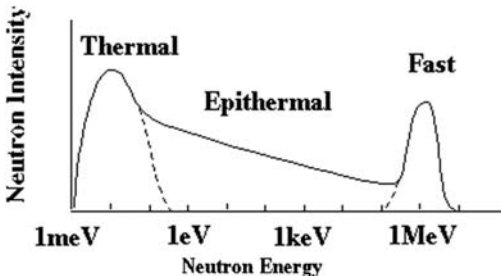
Figure 5: The various components in a thermal reactor spectrum (intensities not to scale).

MeV which can be described mathematically by the expression

$$\Phi(E)dE = \Phi_f \exp(-E \sinh\sqrt{2E})\, dE \qquad E > 0.5 \text{MeV}$$

The **intermediate energy region** is known as the slowing down or epithermal region and is characterised by a 1/E intensity distribution. Thus

$$\Phi(E)dE = \frac{\Phi_{epi}}{E}\, dE \qquad 200 \text{ meV} < E < 0.5 \text{ MeV}$$

describes the spectrum in this region where the source neutrons are losing energy in the moderation process.

At low energies the neutron spectrum tends towards thermodynamic equilibrium with the moderator as the neutrons, acting like a gas, both lose energy and gain energy in collisions with nuclei in the moderator. The resultant spectrum is described by a Maxwell-Boltzmann distribution with an effective temperature $T_n \sim 300$ K, always somewhat higher than the physical moderator temperature since full equilibrium is never achieved in a finite sized moderator.

$$\Phi(E)dE = \Phi_{th} \frac{E}{kT_n} \exp\left(-\frac{E}{kT_n}\right) dE \qquad E < 200 \text{ meV}$$

The Maxwellian peaks in intensity at an energy of about 25 meV for a room temperature moderator.

A stylised representation of the basic components of a research reactor, a swimming pool reactor, is shown in Figure 6. The uranium fuel is normally contained
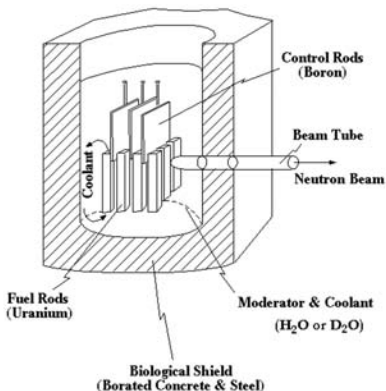
Figure 6: A schematic view of a research reactor showing the essential components.

	Thermal Flux Φ_{th} n/cm²/sec	Epithermal Flux Φ_{epi} n/cm²/sec	Fast Flux Φ_f n/cm²/sec	Gamma Flux γ/cm²/sec
Natural Uranium + D₂O	6.10^{13}	2.10^{12}	4.10^{12}	2.10^{12}
Enriched Uranium + H₂O	2.10^{14}	2.10^{13}	2.10^{14}	1.10^{13}

Table 1: Typical values of neutron and gamma fluxes for the two most common fuel/moderator combinations in a 20 MW reactor.

3.1-6

(a)

THE HIGH FLUX REACTOR

Power : 58.3 Megawatts
Operation : 4.5 cycles of 50 days per year
Availability : 98 - 99%
Fuel element : 9.5 Kg 93% enriched uranium
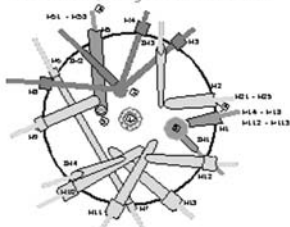
1 - reactor core
2 - hot source
3 - cold source
4 - neutron guides
5 - horizontal cold source
— Cold neutrons
  Thermal neutrons
— Hot neutrons
H - horizontal tube
IH - inclined tube

(b)
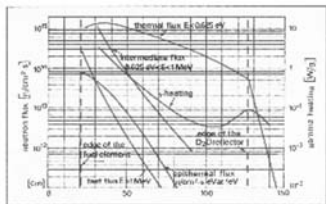
Figure 7: (a) view of the beam tubes and the cold and hot moderators of the ILL reactor. (b) The fluxes as a function of distance from the centre of the core are shown in the lower graph.

in a number of fuel rods (although there is only one at ILL) and the critical reaction is controlled by neutron absorbing control rods (normally boron loaded). The moderator, which can be H_2O or D_2O depending on the enrichment of the fuel, is often also employed as the reactor coolant. A massive radiation shield of borated concrete and steel surrounds the reactor which protects both experimenters and instruments.

The use of natural uranium fuel with its inherently low fissile isotope content requires the use of heavy water D_2O as the moderator since its absorption cross section is low compared to light water H_2O. When fuel enriched in the U^{235} isotope is used, then the more highly absorbing H_2O moderator can be used. Typical values of the flux components for a 20 MW research reactor are shown in table I for both combinations of fuel and moderator.
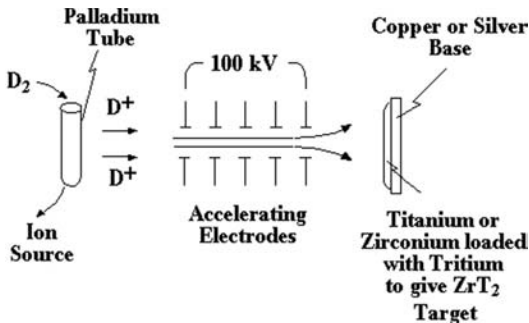
Figure 8: The principle behind a laboratory source of neutrons using accelerated deuterons onto a tritium loaded target.

Clearly, whilst the source strength of both reactors illustrated in the above table is the same (1.7×10^{18} n/sec), the flux is considerably higher in the enriched uranium/H_2O case. This arises simply because of the smaller core and consequent higher power density of this combination of fuel and moderator. The use of enriched uranium as the fuel presents its own special problems for reactor operation however from the political point of view.

The principal object in designing a neutron beam reactor is to deliver the maximum neutron flux at the required energy at the neutron scattering instrument. Accordingly the noses of beam tubes are located in the region of maximum neutron intensity which can be designed to occur just outside the reactor core.

This is achieved by "under-moderating" the core which delivers a high fast neutron distribution to the surrounding reflector, where the process of moderation raises the thermal flux to a maximum. This can also be achieved for other neutron energies by locally inserting blocks of moderating material at higher or lower temperatures. This is most notable in the case of liquid hydrogen or deuterium cold sources. The distribution of beam tubes and the various components of the neutron spectra around the high flux reactor at the Institut Laue Langevin in Grenoble is shown in Figure 7 as an illustration. The thermal flux peaks at ~15 cm from the edge of the reactor core.

Figure 9: A schematic representation of an electron linear accelerator which produces pulsed neutron beams.

1.3 Particle Accelerator Sources

Neutrons can be generated by bombarding a target with high energy particles produced with an accelerator. Depending on the type of accelerator the neutrons will be produced continuously or in bursts. A number of types of reaction have been employed, of which the following are typical:

(D,T) Fusion

Neutrons are produced in the fusion of deuterium and tritium in the following exothermic reaction.

$$D^2 + T^3 \rightarrow He^4 + n + 17.6 \text{ MeV}$$

The neutron is produced with a kinetic energy of 14.1 MeV. This can be achieved on a small scale in the laboratory with a modest 100 kV accelerator for deuterium atoms bombarding a tritium target. Monatomic or nascent deuterium is produced by bleeding D_2 gas through a heated palladium tube. The accelerated D^+ ions bombard a titanium or zirconium target loaded with tritium in the form of the hydride TiT_2 or ZrT_2 as shown in Figure 8. Before target heating becomes a problem, continuous neutron sources of $\sim 10^{11}$ neutrons/second can be achieved relatively simply. This type of neutron source is often used in reactor physics simulation experiments in the laboratory, for example to measure neutron thermalisation in graphite.

Note that this reaction is the same as that which is being exploited in the development of thermonuclear fusion reactors such as JET. In this case the energy to initiate the binding of the deuterium and tritium atoms is derived from the required high temperature of the plasma.

Bremsstrahlung from Electron Accelerators

Energetic electrons when slowed down rapidly in a heavy target emit intense γ-radiation during the deceleration process. This is known as Bremsstrahlung or braking radiation. The interaction of the γ-radiation with the target produces neutrons via the (γ,n) reaction, or the (γ,fission) reaction when a fissile target is used.

$$e^- \rightarrow Pb \rightarrow \gamma \rightarrow Pb \rightarrow (\gamma,n) \text{ and } (\gamma,\text{fission})$$
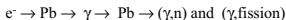
The Bremsstrahlung γ energy exceeds the binding energy of the "last" neutron in the target. This reaction is comparable to the (γ,n) reaction in Sb^{124} referred to above. A neutron source such as this is achieved with a moderately large purpose-built electron linear accelerator or "linac" which produces electrons in bursts at frequencies of between 25 Hz to 250 Hz at energies ~150 MeV. Examples of target materials are tungsten, lead or depleted uranium. Such a source is illustrated in Figure 9.

A source strength of 10^{13} neutrons/second produced in short (i.e. < 5 μs) pulses can be readily realised. This source strength is adequate for specialised neutron scattering measurements as for example was done at the Harwell, Toronto and Hokkaido linacs, and also at the Frascati cyclotron source LISONE.

Spallation from Energetic Protons

The process of spallation is a common nuclear reaction occurring for high energy particles bombarding heavy atoms. The reaction occurs above a certain energy threshold for the incident particle, which is typically 5 - 15 MeV. The
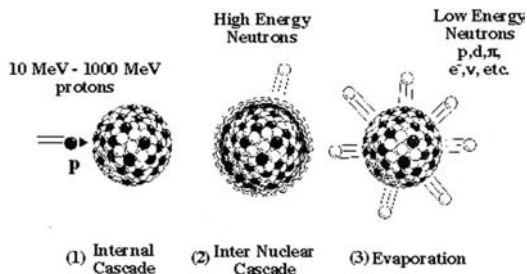
Figure 10: A schematic representation of the spallation reaction.

EVAPORATION 97%

CASCADE 3% (but dominates shielding requirements)
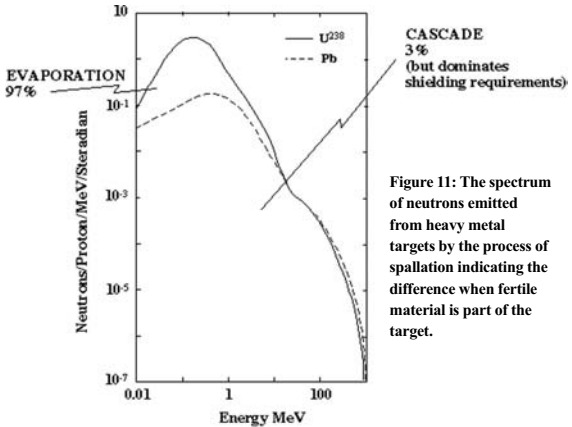
Figure 11: The spectrum of neutrons emitted from heavy metal targets by the process of spallation indicating the difference when fertile material is part of the target.

reaction, illustrated in Figure 10 is a sequential one involving the incorporation of the incident particle (say a proton) by the target nucleus followed by an internal nucleon cascade, an internuclear cascade where high energy neutrons are ejected, and an evaporation process where the target nuclei de-excite by the emission of several low energy neutrons and a variety of nucleons, photons and neutrinos.

The reaction is multifarious and in general involves several different target nuclei. It is often likened to a cannon ball careering through a wooden-hulled ship although it is a geological term representing the splitting of rocks. In the spallation reaction 20 to 30 neutrons per incident particle can typically be generated. The energy released per neutron produced is quite low being ~55 MeV again dependent upon the incident particle energy and the target nucleus, and whether or not fission processes play a part. The neutron source strength can be significantly increased by using a fissile target, normally depleted uranium. The source spectrum from an 800 MeV proton spallation reaction on both a lead target (with no fission) and a uranium-238 target (where fast fission contributes to the neutron intensity) is shown in Figure 11.

The cascade processes account for only ~3% of the source neutrons but since

they are produced at energies up to the energy of the incident protons these extremely penetrating neutrons dominate the shielding requirements of the source.

In practice a spallation source is usually realised with accelerated protons. These can be produced in a number of ways, for example:

1. Linear Accelerators such as LAMPF at Los Alamos which are high current, high duty cycle accelerators resulting in either long pulses or at frequencies too high to be utilised effectively in neutron scattering instruments. Accordingly particle storage rings, which compress the long pulses, are needed.

2. Cyclotrons such as SINQ at PSI near Zurich which produce a continuous beam of neutrons via the spallation reaction, and

3. Synchrotrons such as ISIS in the UK. Synchrotrons have operated with low currents until relatively recent times with the implementation of rapid cycling techniques and weak focusing magnets. Narrow neutron pulses ($< 1 \, \mu s$) can be produced, due to the single turn proton beam extraction method, at a modest duty cycle (50 Hz) which is well-suited to the neutron scattering instrumentation. A typical schematic layout of a synchrotron-based pulsed spallation neutron source is shown in Figure 12. Multi-turn-injection into the synchrotron is achieved using more modest linear accelerators for negative H^- ions. At the point of injection the beam passes through a thin electron stripper foil such as alumina and the resultant protons enter the synchrotron for further acceleration. A neutron source strength of $\sim 5 \; 10^{16}$ fast neutrons/second can be produced in a pulsed manner by this method.
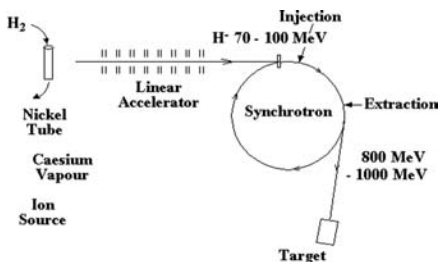
Figure 12: The principle of operation of a spallation neutron source using a combination of linear accelerator and synchrotron accelerator.

2. MODERN NEUTRON SOURCES

2.1 The Quest for Higher Intensities

Neutron scattering techniques suffer from low data rates particularly in comparison with x-ray diffraction or infra-red spectroscopy. Accordingly much effort has been concentrated on improving the available intensities of neutron sources. In Figure 13, originally due to Carpenter, the effective thermal neutron flux of various neutron sources has been plotted chronologically. The precise positions of various points on this graph and the use of average flux for continuous sources and peak flux for pulsed sources has been and still is the subject of debate, without even mentioning the multitude of questionable assumptions made in attempting to compare such complex facilities using only one variable.

Nevertheless the visible trends are genuine and quite clearly fission reactors, having improved rapidly in the five years following the success of the first critical assembly at Chicago in 1942, have reached a slowly increasing quasi-asymptote around $2 \ 10^{15}$ n/cm^2 sec. Technical advances in instrumentation, for example neutron guides, focusing monochromators and area detectors have however ensured a steady rise in data acquisition rates. Pulsed sources on the other hand have not yet reached saturation of the source flux and much potential remains to be realised with this type of neutron source before such limits are approached. The most advanced spallation source currently under construction is the 1MW SNS
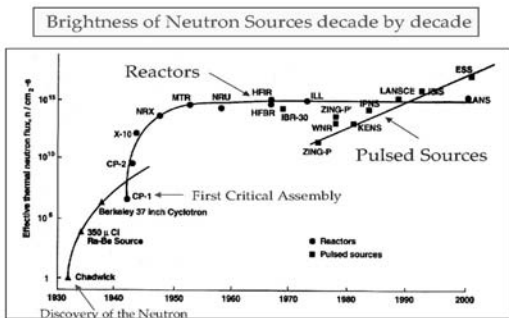
Figure 13: The effective neutron flux of various neutron sources from the discovery of the neutron in 1932 until the present day.
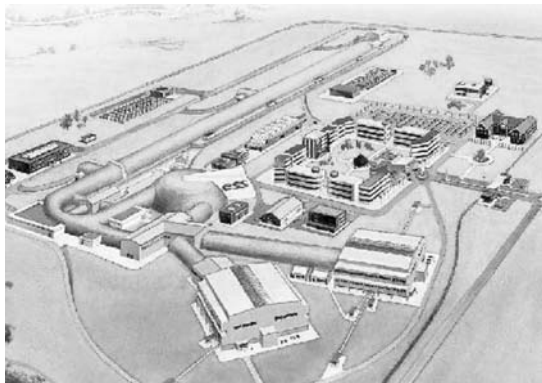
Figure 14: A representation of the layout of the proposed European Spallation Source with two shared pulse targets. The current design includes a long pulse target fed directly from the Linac.

(spallation neutron source) at Oak Ridge in Tennessee which is scheduled to generate its first neutrons in 2006. A design study has just been completed for a 10 MW European Spallation Source which promises source fluxes 30 times those of the 160 kW ISIS source near Oxford. The layout of the ESS is shown in Figure 14.

An important limiting factor in determining the maximum neutron output of a particular type of source is the rate of removal of the heat deposited in the target by the nuclear reaction. Table II shows the energy released per useful neutron in the various reactions discussed earlier. Spallation releases 3 times less energy than fission which in turn releases 10 times less energy than photoneutron reactions (Bremsstrahlung). Controlled thermonuclear fusion reactors offer a future promise of neutrons for yet lower releases of energy, and consequently the potential for higher intensities.

If additionally the neutron generating reaction is pulsed in nature, the heat deposited in the target can be substantially reduced (perhaps by a factor of 20) compared with a continuous source of the same equivalent source strength.

Process	Example	Neutron Yield	Energy Released MeV / neutron
1. (α,n) reaction	Radium-beryllium Laboratory source	$8 \cdot 10^{-5}$ / alpha	6,600,000
2. (D,T) fusion	400 keV deuterons on tritium-loaded titanium	$4 \cdot 10^{-5}$/deuteron	10,000
3. Electron Bremsstrahlung & photofission	100 MeV electrons on uranium	$5 \cdot 10^{-2}$/electron	2,000
4. Fission	U^{235} (n, fission) in nuclear reactor	1 / fission	180
5. Spallation	800 MeV protons on uranium	30 / proton	55
6. (D,T) fusion	Laser fusion in controlled thermonuclear reactor	1 / fusion	18

Table 2: The neutron yield and heat released per useful neutron from the various reactions used to generate neutrons.
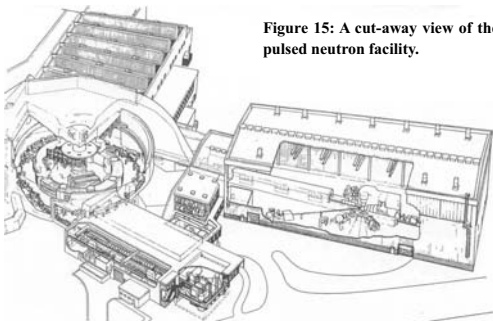
Figure 15: A cut-away view of the ISIS pulsed neutron facility.
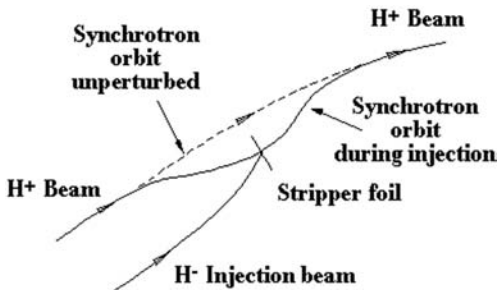
Figure 16: The principle of injection of an H⁻ beam into a closed orbit synchrotron.

Provided that the peak flux of the pulsed source can be utilised for a high proportion of the time frame between pulses this substantial gain can be achieved with no decrease in data rate at the neutron scattering instrument. Conversely for the same rate of heat deposition in the target a pulsed source will, in general, achieve a higher data rate than the continuous source.

2.2 ISIS at the Rutherford Appleton Laboratory

A cut-away view of the pulsed neutron source ISIS at the Rutherford Appleton Laboratory in the UK is shown in Figure 15. It comprises a series of accelerators which produce an intense 800 MeV pulsed beam of protons which is incident on a tantalum target, producing fast neutrons by the spallation process.

We can divide the facility into nine sections for the purpose of describing it.

1. A **pre-injector** high voltage generator of the Cockcroft-Walton potential divider type. This produces pulsed voltages at 665 kV and 50 Hz, delivering a current of 40 mA in 500 μs bursts to ....

2. ... an **H⁻ ion source**. The ion source produces negative hydrogen ions H⁻ in a caesium vapour discharge fed with monatomic hydrogen atoms generated by passing hydrogen gas through a heated nickel tube. The H⁻ ions sitting at the 665 kV potential of the pre-injector are driven towards the first element of ....

3. ... a **linear accelerator injector** of the Alvarez type consisting of a series of potential gaps increasing in length along the linac as the H⁻ ions gain energy.

3.1-16

The linac accelerates the H⁻ ions to 70 MeV producing a current of 20 mA in 500 μs bursts every 20 ms (i.e. at 50 Hz). The H⁻ ion beam enters the synchrotron via....

4. ... an **injection straight** where a 0.25 μm thick foil of alumina Al_2O_3 strips the electrons from the H⁻ ions and the resulting protons are trapped in the magnetic field of the synchrotron and join the acceleration process. The use of H⁻ ions and multi-turn injection allows the current in the synchrotron to be increased up to the space-charge limit. Thus H⁻ ions and protons from earlier on in the injection process pass through the same magnetic field at the stripper foil but with equal and opposite curvatures, as shown in Figure16.

5. The **synchrotron** is 52 metres in diameter in the shape of a ten-sided polygon. Each of the ten sides has common magnet elements for focusing the proton beam and for bending it by 36° into the next straight section.

   Each straight has an individual purpose. The first straight is used for injection as we have seen above. Six straights are used for acceleration purposes, each containing a radio frequency ferrite-cored accelerating cavity which feeds energy, appropriately phased, into the proton beam. As the beam gains energy so the frequency of the RF cavities is increased to give the proton beam a slight increase in energy on each pass. The six RF cavities accelerate the beam to 800 MeV at which stage the protons are circulating in two bunches on opposite sides of the synchrotron. Each bunch is 90 nsec wide and separated from the second bunch by 210 nsec. There are 2.5×10^{13} protons per pulse in the accelerated beam which is equivalent to an average current of 200 μA. Two straights of the synchrotron are for vacuum pumping ports - the ring is held at a vacuum of 5×10^{-8} mbar - and the final straight is ....

6. ... the **extraction straight** which contains a set of fast acting kicker magnets. These magnets are powered at the end of the acceleration process and the two bunches of protons in the ring are extracted simultaneously from the synchrotron into ....

7. ... the **extracted proton beamline**. The proton pulse is then guided by quadrupole magnets along an 80 metre vacuum tank to...

8. ... the **target station** where it strikes the tantalum target thus producing a burst of fast neutrons by the spallation process. The target is surrounded by four moderators – two are ambient water, one is liquid methane at 110 K, and one is supercritical hydrogen vapour at 25 K - and a beryllium reflector to concentrate the neutron flux in the region of the moderators. The moderated neutrons pass through shutters and beam lines to reach ....
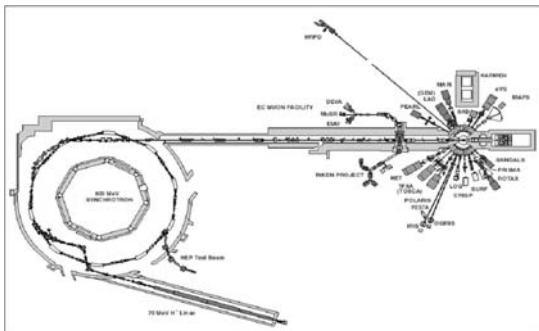
Figure 17: A plan view of the components of the ISIS pulsed neutron source with the instruments arranged around the tantalum target. Upstream is the muon target with its instrument suite.

9.   ... the **neutron scattering instruments**. There are 18 beam holes on ISIS, nine on either side of the target station. The present (March 2002) layout of instruments is shown in Figure 17.

2.3 The High Flux Reactor at the Institut Laue Langevin

A plan view of the high flux reactor at the ILL in Grenoble and the associated neutron instruments is shown in Figure 18. A short discussion of the reactor core and the coolant system has taken place earlier in the paper.

The reactor core consists of a single fuel element made from highly enriched (93%) uranium-235 with a mass of ~ 8.57 kg. The core has a diameter of 40 cm and is controlled by a single, central control rod. A power of 58 MW is generated which is removed by pumping water through the fins of the fuel element. At equilibrium the temperature of the fuel element is 50 °C. The core is surrounded by a D_2O reflector vessel of diameter 2.5 m and outside the reflector is a tank of H_2O and a concrete radiation shield. There are also three purpose-built moderators at different temperatures to provide a wide range of neutron spectra for the various instruments. These are a hot moderator, which is a graphite block at 2500°C providing peak flux at 200 meV, and two cold moderators, one being a spherical 25
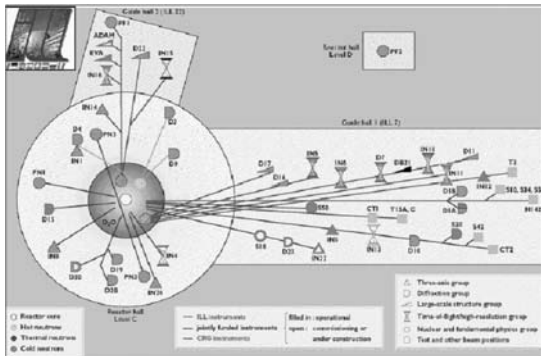
Figure 18: A schematic layout of the instruments at the ILL showing the two guide halls.

litre vessel containing liquid deuterium at 20 K with its peak intensity at 5 meV. In addition there is an ultra cold neutron source which generates neutrons at wavelengths of 1000 Angstroms.

The neutron beam tubes pass through the biological radiation shield of the reactor into the region of highest thermal flux in the D_2O reflector arrayed around the core of the reactor. Some of the beam tubes are radial and thus view the core itself whilst others are tangential to the core. The former have a more intense neutron flux than the latter but with the disadvantage of a higher gamma flux also. There are also three bunches of neutron conducting tubes, or guides, which view respectively the ambient reflector and transmit a thermal neutron spectrum, and the two cold sources and transmit a low energy or cold neutron spectrum. These guides transmit the neutrons without a significant loss in intensity to regions distant from the reactor (40 m to 140 m) where backgrounds are low and space is available to more than treble the neutron instrumentation which can be installed close to the reactor.

2.4 A brief Comparison of Pulsed Sources and Reactor Sources

To hazard a comparison of different neutron sources is perhaps unwise given the large number of committed individuals and vested interests. Nevertheless my

Pulsed Sources	Reactors
1. More high energy neutrons	1. More low energy neutrons
2. Produce neutrons in bursts & measure when source is off. Lower backgrounds!	2. Easier to shield against fission neutrons. Lower backgrounds!
3. Pulsed Operation	3. Continuous Operation
If peak ~ $_\phi$average then data rates are "equal"	
4. Higher $_\phi$peak possible	4. Higher $_\phi$average difficult
5. Sharp pulses give high resolution	5. Resolution can be adapted to problem
6. Pulse shape asymmetric, resolution function asymmetric	6. Resolution function symmetric, normally gaussian
7. Must use Time of Flight methods constrained to source frequency	7. Complete flexibility
8. Horizons still to be explored.	8. Mainly tried & tested techniques
9. Seen as environmentally friendly	9. Seen as environmentally unfriendly

Table 3: Frequently stated advantages of pulsed sources and reactors. Many of those advantages are subjective and therefore the table makes no claim to be consistent.

personal list is given in table III. In the end it is the science which is done on the different instruments at the various sources which is important and this is dependent upon many other issues than a simple comparison will provide.

3. Further Reading

Neutron Physics by K H Beckurts & K Wirtz, Springer Verlag, 1964.

The Elements of Nuclear Reactor Theory S Glasstone & M C Edlund, Van Nostrand, 1952.

Pulsed Spallation Neutron Sources for Slow Neutrons J M Carpenter, Nuclear Instruments and Methods, (1977), **145**, 91-113.

Spallation Neutron Sources for Neutron Beam Research G Manning, Contemporary Physics, (1978), **19**, 505-529.

The Neutron & the Bomb Andrew Brown 1998 Oxford University Press

Neutron Optics

Ian S. Anderson

1. Introduction

Owing to the low primary flux of neutrons, the beam definition devices that play the role of defining the beam conditions (direction, divergence, energy, polarisation, etc.) have to be highly efficient. The following sections give a (non-exhaustive) review of commonly used beam definition devices. A more detailed review may be found in [1].

2. Collimators

A collimator is perhaps the simplest neutron optical device and is used to define the direction and divergence of a neutron beam. The most rudimentary collimator consists of just two slits or pinholes cut into an absorbing material and placed one at the beginning and one at the end of a collimating distance L. The maximum beam divergence that is transmitted with this configuration is

$$\alpha_{max} = (a_1 + a_2)/L , \qquad (1)$$

where a_1 and a_2 are the widths of the slits or pinholes.

Such a device is normally used for small-angle scattering and reflectometry. To avoid parasitic scattering by reflection from slit edges, very thin sheets of a highly absorbing material (e.g., gd or cd foils) are used as the slit material. In cases where a very precise edge is required, cleaved single-crystalline absorbers such as gadolinium gallium garnet (GGG) can be employed.

As can be seen from eqn. 1, the divergence from a simple slit or pinhole collimator depends on the aperture size. To collimate (in one dimension) a beam of large cross section within a reasonable distance L, Soller collimators, composed of a number of equidistant neutron-absorbing blades separated by spaces, are used. The transmission, τ, of such a collimator depends on the thickness of the blades t compared with the width of the transmission (spaces) channels s:

$$\tau = \frac{s}{s+t}$$

Blades must be as thin and as flat as possible. If their surfaces do not reflect neutrons, the angular dependence transmission of the function is close to the ideal triangular form, and transmissions of 96% of the theoretical value can be obtained

with 10´ collimation. Alternatively, thin single-crystal silicon (sapphire or quartz are also suitable) wafers, coated with an absorbing layer (e.g., gd), can also be used to construct microcollimators. The transmission losses through silicon can be minimized by choosing very thin silicon wafers ($\approx$200 μm) coated with a few microns of gd. The principal potential gain of this design, however, is the possibility to build collimators with reflecting walls. If the blades of the Soller collimator are coated with a material whose critical angle of reflection is equal to $\alpha_{max}/2$ (for one particular wavelength), then a square angular transmission function is obtained instead of the normal triangular function, doubling the theoretical transmission.

Soller collimators are often used in combination with single-crystal mono-chromators to define the wavelength resolution of an instrument. The Soller geometry is only useful for one-dimensional collimation. For small-angle scattering applications where two-dimensional collimation is required, a converging "pepper pot" collimator can be used. [2]

Cylindrical collimators with radial blades are sometimes used to reduce background scattering from the sample environment. This type of collimator is particularly useful for use with position-sensitive detectors and may be oscillated about the cylinder axis to reduce the shadowing effect of the blades. [3]

3. Crystal Monochromators

Bragg reflection from crystals is the most widely used method for selecting a well-defined wavelength band from a white neutron beam.

To obtain reasonable reflected intensities and to match typical neutron beam divergences, crystals that reflect over an angular range of 0.2 to 0.5 degrees are typically employed. Traditionally, mosaic crystals are preferred over perfect crystals, although reflection from a mosaic crystal gives rise to an increase in beam divergence with a concomitant broadening of the selected wavelength band. Thus, collimators are often used together with mosaic monochromators to define the initial and final divergences and therefore the wavelength spread.

Because of the beam broadening produced by mosaic crystals, elastically deformed perfect crystals and crystals with gradients in lattice spacings may be more suitable candidates for focusing applications since the deformation can be modified to optimise focusing for different experimental conditions [4]. Perfect crystals are used commonly in high-energy-resolution backscattering instruments, interferometry, and in Bonse-Hart cameras for ultrasmall-angle scattering [5].

Mosaic crystals show a much broader diffraction profile compared with perfect crystals with a lower peak reflectivity. An ideal mosaic crystal is assumed to

comprise an agglomerate of independently scattering domains or mosaic blocks that are more or less perfect but small enough that primary extinction does not come into play. Additionally, the intensity reflected by each block can be calculated using the kinematic theory of Zachariasen. [6]

One assumes that the mosaic blocks are oriented almost parallel to the crystal surface (for Bragg case) following a distribution $W(\theta - \theta_B)$, with θ being the angle formed by the incident beam and the Bragg planes and θ_B being the Bragg angle. The full-width-at-half-maximum η of this distribution is called the mosaic spread or mosaicity. The multiple Bragg reflections in a mosaic crystal and the concept of secondary extinction are summarised by the Darwin equations. An exact and very general solution of these equations has been given by Sears [7]. The physical quantities that govern diffraction by a mosaic crystal are the absorption coefficient, μ, and the scattering coefficient $\sigma = Q[W(\theta - \theta_B)]$. The Q factor is given by $Q = \lambda^3 F_{hkl}^2 / (V_0^2 \sin 2\theta_B)$, where λ is the wavelength, F_{hkl} is the structure factor, and V_0 is the unit cell volume. If we define $a = \mu d / \sin \varphi$ and $b = \sigma d / \sin \varphi$, with d as the crystal thickness and φ as the angle formed by the incident beam and the surface, the Sears' equations for the reflected and transmitted beam in symmetric Laue (transmission) and Bragg (reflection) geometries are

$$R_{Laue\ symm} = \frac{1}{2} e^{-a} \left(1 - e^{-2b}\right) \tag{2}$$

$$T_{Laue\ symm} = \frac{1}{2} e^{-a} \left(1 + e^{-2b}\right) \tag{3}$$

$$R_{Bragg\ symm} = \frac{b}{\sqrt{a(a+2b)} \coth \sqrt{a(a+2b)} + (a+b)} \tag{4}$$

$$T_{Bragg\ symm} = \frac{\sqrt{a(a+2b)}}{\sqrt{a(a+2b)} \cosh \sqrt{a(a+2b)} + (a+b)\sinh \sqrt{a(a+2b)}} \tag{5}$$

The ideal monochromator material should have a large scattering length density, low absorption, incoherent and inelastic crosssections, and should be available as large single crystals with a suitable defect concentration. Relevant parameters for some typical neutron monochromator crystals are given in Table 1.

Because of the higher reflectivities that can be obtained, neutron monochromators are usually designed to operate in reflection geometry rather than transmission geometry, for which the optimisation of crystal thickness is only achieved for a small wavelength range. The maximum peak reflectivities and the optimum thicknesses for

Table 1: Some important properties of materials used for neutron monochromator crystals (in order of increasing unit-cell volume).

Material	Structure	Lattice constant(s) at 300 K a, c (Å)	Unit-cell volume V_c (10^{-24} cm³)	Coherent scattering length b (10^{-12} cm)	Square of scattering length density 10^{-2} cm⁻¹	Ratio of incoherent to total scattering crosssection σ_{inc}/σ_t	Absorption cross section σ_{abs} (barns)* at $\lambda = 1.8$ Å	Atomic mass A	Debye temperature θ_D (K)	$A\bar{u}^2$ (10^3 K)
Beryllium	h.c.p.	a: 2.2856 c: 3.5832	16.2	0.779(1)	9.25	6.5×10^{-4}	0.0076(8)	9.013	1188	12.7
Iron	b.c.c.	a: 2.8664	23.5	0.954(6)	6.59	0.033	2.56(3)	55.85	411	9.4
Zinc	h.c.p.	a: 2.6649 c: 4.9468	30.4	0.5680(5)	1.40	0.019	1.11(2)	65.38	253	4.2
Pyrolytic graphite	layer hexag.	a: 2.461 c: 6.708	35.2	0.66484(13)	5.71	$<2 \times 10^{-4}$	0.00350(7)	12.01	800	7.7
Niobium	b.c.c.	3.3006	35.9	0.7054(3)	1.54	4×10^{-4}	1.15(5)	92.91	284	7.5
Nickel (⁵⁸Ni)	f.c.c.	3.5241	43.8	1.44(1)	17.3	0	4.6(3)	58.71	417	9.9
Copper	f.c.c.	3.6147	47.2	0.7718(4)	4.28	0.065	3.78(2)	63.54	307	6.0
Aluminium	f.c.c.	4.0495	66.4	0.3449(5)	0.43	5.6×10^{-3}	0.231(3)	26.98	402	4.4
Lead	f.c.c.	4.9502	121	0.9400(3)(14)	0.97	2.7×10^{-4}	0.171(2)	207.21	87	1.6
Silicon	diamond	5.4309	160	0.41491(10)	0.43	6.9×10^{-3}	0.171(3)	28.09	543	8.3
Germanium	diamond	5.6575	181	0.8192(7)	1.31	0.020	2.3(2)	72.60	290	6.1

*1 barn= 100 fm².
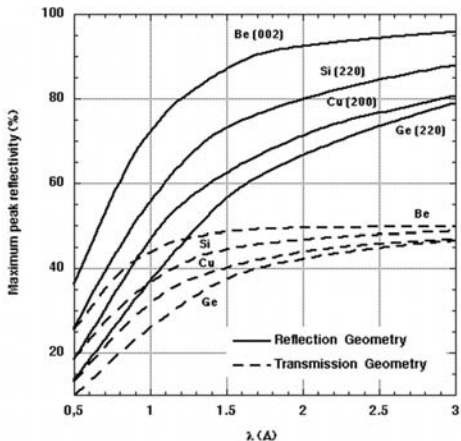
Figure 1: Peak reflectivity for some typical monochromator crystals calculated using an intrinsic mosaic of 0.1°.

some selected reflections are shown in Figs. 1 and 2, respectively.

The reflection from a mosaic crystal in reciprocal space is visualised in Fig. 3. An incident beam with small divergence is transformed into a broad exit beam. The range of **k** vectors, Δk, selected in this process depends on the mosaic spread, η, and the incoming and outgoing beam divergences α_1 and α_2:

$$\Delta k/k = \Delta\tau/\tau + \cot(\theta)\alpha \qquad (6)$$

where τ is the crystal reciprocal-lattice vector ($\tau = 2\pi/d$) and α is given by:

$$\alpha = \sqrt{\frac{\alpha_1^2\alpha_2^2 + \alpha_1^2\eta^2 + \alpha_2^2\eta^2}{\alpha_1^2 + \alpha_2^2 + 4\eta^2}} \qquad (7)$$

The resolution can therefore be defined by collimators, and the highest resolution is obtained in backscattering, where the wavevector spread depends only on the intrinsic $\Delta d/d$ of the crystal.
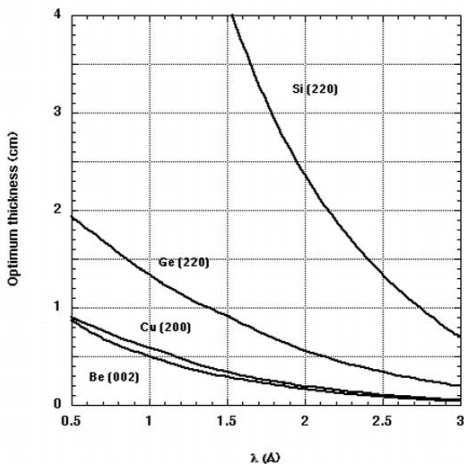
Figure 2: Wavelength dependence of the optimum thickness for various monochromator reflections.

In some applications, the beam broadening produced by mosaic crystals can be detrimental to the instrument performance. An interesting alternative is a gradient crystal, that is, single crystals with a smooth variation of the interplanar lattice spacing along a defined crystallographic direction. As shown in Figure 3, the diffracted phase space element has a different shape from that obtained from a mosaic crystal. Gradients in d-spacing can be produced in various ways: thermal gradients [8], vibrating crystals by piezoelectric excitation [9], and mixed crystals with concentration gradients (e.g., Cu-Ge [10] and Si-Ge. [11]).

Both vertically and horizontally focusing assemblies of mosaic crystals are employed to make better use of the neutron flux when making measurements on small samples. Vertical focusing can lead to intensity gain factors between 2 and 5 without affecting resolution (real-space focusing) [12]. Horizontal focusing changes the k-

3.2-7

(a) ideal crystal

(b) mosaic crystal

(c) gradient crystal
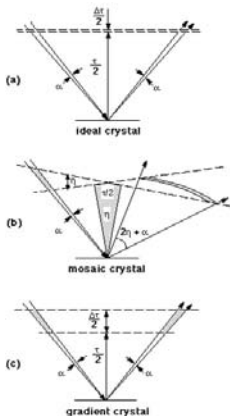
Figure 3: Reciprocal-lattice representation of the effect of a monochromator with reciprocal-lattice vector t on the reciprocal-space element of a beam with divergence a. (a) For an ideal crystal with a lattice constant width $\Delta\tau$; (b) for a mosaic crystal with mosaicity h, showing that a beam with small divergence, a, is transformed into a broad exit beam with divergence 2h + a; (c) for a gradient crystal with interplanar lattice spacing changing over $\Delta\tau$, showing that the divergence is not changed in this case.

garland reflection $\theta < \theta^*$
zig-zag reflection $\theta > \theta^*$
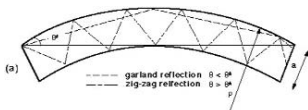
Figure 4: In a curved neutron guide, the transmission becomes λ dependent: (a) the possible types of reflection (garland and zigzag), the direct line-of-sight length, the critical angle θ^*, which is related to the characteristic wavelength $\lambda^* = \theta^* \sqrt{\pi / Nb_{coh}}$.

(b) Transmission across the exit of the guide for different wavelengths, normalized to unity at the outside edge. (c) Total transmission of the guide as a function of λ.
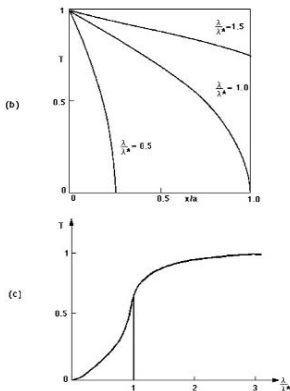
space volume that is selected by the monochromator through the variation in Bragg angle across the monochromator surface (k-space focusing) [13]. The orientation of the diffracted k-space volume can be modified by variation of the horizontal curvature so that the resolution of the monochromator may be optimised with respect to a particular sample or experiment without loss of illumination. Monochromatic focusing can be achieved. Furthermore, asymmetrically cut crystals can be used, allowing focusing effects in real space and k-space to be decoupled. [14]

4. Mirror Reflection Devices

The refractive index, n, for neutrons of wavelength λ propagating in a nonmagnetic material of atomic density N is given by the expression

$$\eta = 1 - \partial - i\beta \quad = 1 - \frac{\lambda^2 N.b_{coh}}{2\pi} - i\left(\frac{\lambda}{4\pi}\right)\mu \quad , \tag{8}$$

where b_{coh} is the mean coherent scattering length, and m is the linear absorption coefficient. Values of the scattering-length density $N.b_{coh}$ for some common materials are reported in Table 2. The refractive index for most materials is slightly less than unity so that total external reflection can take place. Thus, neutrons can be reflected from a smooth surface, but the critical angle of reflection, γ_c, given by:

$$\gamma_c = \lambda \sqrt{\frac{Nb_{coh}}{\pi}} \tag{9}$$

is small so that reflection can take place only at grazing incidence. The critical angle for nickel for example is $0.1°$ $Å^{-1}$.

Because of the shallowness of the critical angle, reflective optics are traditionally bulky, and focusing devices tend to have long focal lengths. In some cases however, depending on the beam divergence, a long mirror can be replaced by an equivalent stack of shorter mirrors.

Neutron Guides

The principle of mirror reflection is the basis of neutron guides that are used to transmit neutron beams to instruments situated up to 100 m away from the source [15].

A standard neutron guide is constructed from boron glass plates assembled into a rectangular cross section, the dimensions of which may be up to 200 mm high by 50 mm wide. The inner, reflecting surface of the guide is coated with approximately 1200 Å of nickel, ^{58}Ni ($\gamma_c = 0.12$ $Å^{-1}$), or a "supermirror" (described subsequently). The guide is usually evacuated to reduce losses from absorption and scattering of neutrons in air.
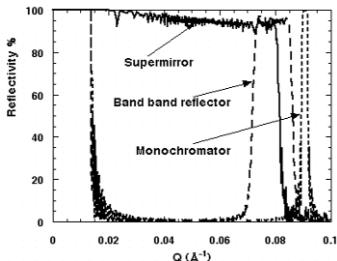
Figure 5: Illustration of how a variation in the bilayer period can be used to produce a monochromator, a broad-band device, or a supermirror.

Theoretically, a neutron guide that is fully illuminated by the source will transmit a beam with a square divergence of full width $2\gamma_c$, in both the horizontal and vertical directions so that the transmitted solid angle is proportional to λ^2. In practice, because of imperfections in the assembly of the guide system, the divergence profile is closer to Gaussian at the end of a long guide.

Because neutrons could undergo a large number of reflections in the guide, it is important to achieve a high reflectivity. The specular reflectivity is determined by the surface roughness and, typically, values in the range 98.5 to 99% are achieved. Further transmission losses occur because of imperfections in the alignment of the sections that make up the guide.

The great advantage of neutron guides, in addition to the transport of neutrons to areas of low background, is that they can be multiplexed, that is, one guide can serve many instruments. This is achieved either by deflecting only a part of the total crosssection to a given instrument or by selecting a small wavelength range from the guide spectrum. In the latter case, the selection device (usually a

Material	Nb_{coh} (10^{-6} Å^{-2})
^{58}Ni	13.31
Diamond	11.71
Nickel	9.4
Quartz	3.64
Germanium	3.64
Silver	3.50
Aluminum	2.08
Silicon	2.08
Vanadium	-0.27
Titanium	-1.95
Manganese	-2.95

Table 2: Scattering length densities for some common materials typically used in neutron optics.

crystal monochromator) must have a high transmission at other wavelengths.

It the neutron guide is curved, the transmission becomes wavelength dependent. The characteristic wavelength, λ^*, at which the theoretical transmission drops to 67% is related to the characteristic angle $\theta^* = \sqrt{\frac{2a}{\rho}}$ in the following way:

$$\lambda^* = \sqrt{\frac{\pi}{Nb_{coh}}} \quad \theta^*, \qquad (10)$$

where a is the guide width, and ρ is the radius of curvature. For wavelengths less than λ^*, neutrons can be transmitted only by "garland" reflections along the concave wall of the curved guide. Thus, the guide acts as a low-pass energy filter as long as its length is longer than the direct line-of-sight length $L_1 = \sqrt{8.a.\rho}$. The line-of-sight length can be reduced by subdividing the guide into a number of narrower channels, each of which acts as a mini-guide. The resulting device, often referred to as a neutron bender since deviation of the beam is achieved more rapidly, is used in beam deviators

Multilayers

Schoenborn and coworkers [16] first pointed out that multilayers, comprising alternating thin films of different scattering-length densities ($N.b_{coh}$), act like two-dimensional crystals with a d-spacing given by the bilayer period. With modern deposition techniques (usually sputtering), uniform films of thickness ranging from ~ 20 Å to a few 100 Å can be deposited over large surface areas of the order of 1 m². Owing to the rather large d-spacings involved, the Bragg reflection from multilayers is generally at grazing incidence so that long devices are required to cover a typical beam width. Alternatively, a stacked device must be used. However, with judicious choice of the scattering-length contrast, the surface and interface roughness, and the number of layers, reflectivities of close to 100% can be reached.

Fig. 5 illustrates how variation in the bilayer period can be used to produce a
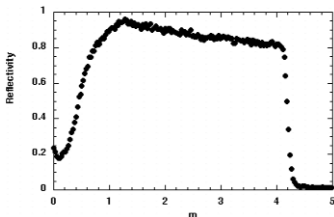
Figure 6: Measured reflectivity of an m = 4 supermirror. The reduction in reflectivity at low values of m is an artifact caused by underillumination of the sample during the measurement.

monochromator (the minimum $\Delta\lambda/\lambda$ that can be achieved is of the order of 1%), a broad band device or a "supermirror," so called because it is composed of a particular sequence of bilayer thicknesses that in effect extends the region of total mirror reflection beyond the ordinary critical angle. [17] Nowadays supermirrors can be produced which extend the critical angle of nickel by a factor, m, between 3 and 4 with reflectivities better than 90% (Fig. 6). Such high reflectivities enable supermirror neutron guides to be constructed with flux gains compared with nickel guides close to the theoretical value of m^2.

The choice of the layer pairs depends on the application. For non-polarising supermirrors and broad band devices, the nickel/titanium pair is commonly used due to the high contrast in scattering density, while for narrow band monochromators a low contrast pair such as tungsten/silicon is more suitable.

Capillary optics
Capillary neutron optics, in which hollow glass capillaries act as waveguides are also based on the concept of total external reflection of neutrons from a smooth surface. The advantage of capillaries, compared with neutron guides, is that the channel sizes are of the order of a few tens of micrometers, so that the radius of curvature can be significantly decreased for a given characteristic wavelength (see eqn. 10). Thus, neutrons can be efficiently deflected through large angles resulting in a more compact optical system.

Two basic types of capillary optics exist, and the choice depends on the beam characteristics required. Polycapillary fibers are manufactured from hollow glass tubes several centimetres in diameter, which are heated, fused, and drawn multiple times until bundles of thousands of micrometer-sized channels are formed having an open area of up to 70% of the crosssection. Fiber outer diameters range from 300 to 600 mm and contain hundreds or thousands of individual channels with inner diameters between 3 and 50 μm. The channel cross section is usually hexagonal, though square channels have been produced, and the inner channel wall surface roughness is typically less than 10 Å rms, giving rise to very high reflectivities. The principal limitations on transmission efficiency are the open area, the acceptable divergence (note that the critical angle for glass is 1 mrad/Å), and reflection losses from absorption and scattering. A typical optical device will comprise hundreds or thousands of fibers threaded through thin screens to produce the required shape.

The second type of capillary optic is a monolithic configuration. The individual capillaries in monolithic optics are tapered and fused together so that no external frame assembly is necessary. Unlike the multifiber devices, the inner

diameters of the channels that make up the monolithic optics vary along the length of the component, resulting in a smaller, more compact design. Capillary optics can be used in lenses to focus or collimate a neutron beam [18] or simply as a beam bender.

Filters

Neutron filters are used to remove unwanted radiation from the beam while maintaining as high a transmission as possible for neutrons of the required energy. Two major applications can be identified: removal of fast neutrons and γ-rays from the primary beam and reduction of higher-order contributions (λ/n) in the secondary beam reflected from crystal monochromators. In this section, we consider nonpolarising filters, that is, those whose transmission and removal cross sections are independent of the neutron spin. Polarising filters are dealt with in the section concerning polarizers.

Filter action relies on a strong variation of the neutron cross section with energy, usually either the wavelength-dependent scattering cross section of polycrystals or a resonant absorption cross section. Following Freund [19], the total cross section determining the attenuation of neutrons by a crystalline solid can be written as a sum of three terms

$$\sigma = \sigma_{abs} + \sigma_{tds} + \sigma_{bragg} \tag{11}$$

Here, σ_{abs} is the true absorption cross section, which at low energy, away from resonances, is proportional to $E^{-1/2}$. The temperature-dependent thermal diffuse cross section, σ_{tds}, describing the attenuation caused by inelastic processes can be split into two parts depending on the neutron energy. At low energy, $E \leq k_b \Theta_D$, where k_b is Boltzman's constant and Θ_D is the Debye temperature, single phonon processes dominate, giving rise to a cross section σ_{sph}, which is also proportional to $E^{-1/2}$. The single-phonon cross section is proportional to $T^{7/2}$ at low temperatures and to T at higher temperature T.

At higher energies $E \geq k_b \Theta_D$, multiphonon and multiple-scattering processes come into play, leading to a cross section σ_{mph}, which increases with energy and temperature.

The third contribution, σ_{bragg}, arises from Bragg scattering in single- or polycrystalline material. At low energies, below the Bragg cutoff ($\lambda > 2d_{max}$), σ_{bragg} is zero. In polycrystalline materials the cross section rises steeply above the Bragg cutoff and oscillates with increasing energy as more reflections come into play. At higher energies, σ_{bragg} decreases to zero.

In single-crystalline material above the Bragg cutoff, σ_{bragg} is characterized by

Element or isotope	Resonance (eV)	σ_s (resonance) (barns)	λ (Å)	$\sigma_s(\lambda)$ (barns)	$\dfrac{\sigma_s(\lambda/2)}{\sigma_s(\lambda)}$
In	1.45	30000	0.48	94	319
Rh	1.27	4500	0.51	76	59.2
Hf	1.10	5000	0.55	58	86.2
^{240}Pu	1.06	115000	9.55	145	793
Ir	0.66	4950	0.70	183	27.0
^{229}Th	0.61	6200	0.73	< 100	> 62.0
Er	0.58	1500	0.75	127	11.8
Er	0.46	2300	0.84	125	18.4
Eu	0.46	10100	0.84	1050	9.6
^{231}Pa	0.39	4900	0.92	116	42.2
^{239}Pu	0.29	5200	1.06	700	7.4

Table 3: Characteristics of some typical elements and isotopes used as neutron filters.

a discrete spectrum of peaks whose heights and widths depend on the beam collimation, energy resolution, and the perfection and orientation of the crystal. Hence, a monocrystalline filter has to be tuned by careful orientation. Figures 7-11 show the total cross sections for common filter materials as a function of energy, while Fig. 12 shows the transmission of a pyrolitic graphite filter as a function of incident wavelength.

Cooled, polycrystalline beryllium is frequently used as a filter for neutrons with energy less than 5 meV since there is an increase of nearly two orders of magnitude in the attenuation cross section for higher energies. BeO, with a Bragg cutoff at approximately 4 meV, is also commonly used.

Pyrolitic graphite, being a layered material with good crystalline properties along the c-direction but with random orientation perpendicular to it, lies somewhere between a polycrystal and a single crystal as far as its attenuation cross section is concerned. Pyrolitic graphite serves as an efficient second- or third-order filter [20] and can be "tuned" by slight misorientation away from the c-axis.

Resonant absorption filters show a large increase in their attenuation cross sections at the resonant energy and are therefore used as selective filters for that energy. A list of typical filter materials and their resonance energies is given in Table 3.
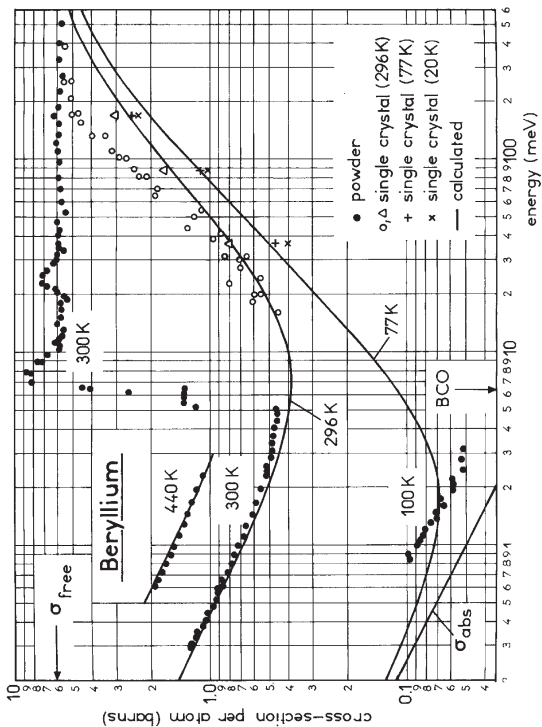
Figure 7: Total cross section for beryllium in an energy range where it can be used as a filter [19].
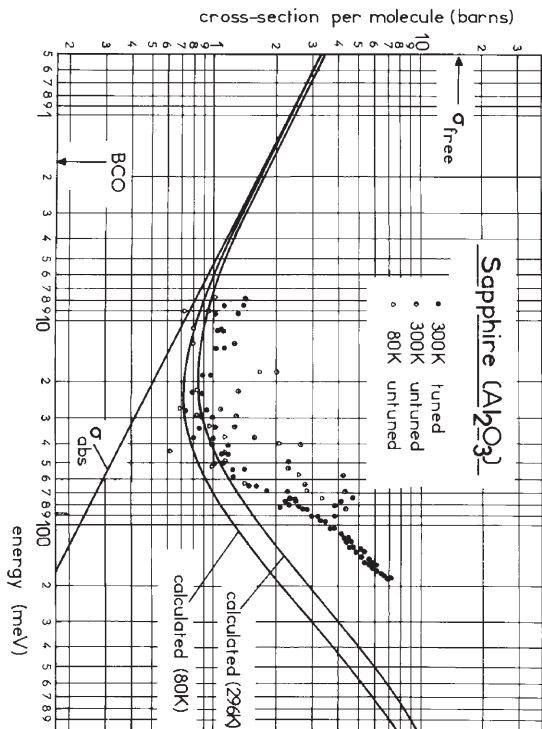
Figure 8: Total cross section for sapphire in an energy range where it can be used as a filter [19].
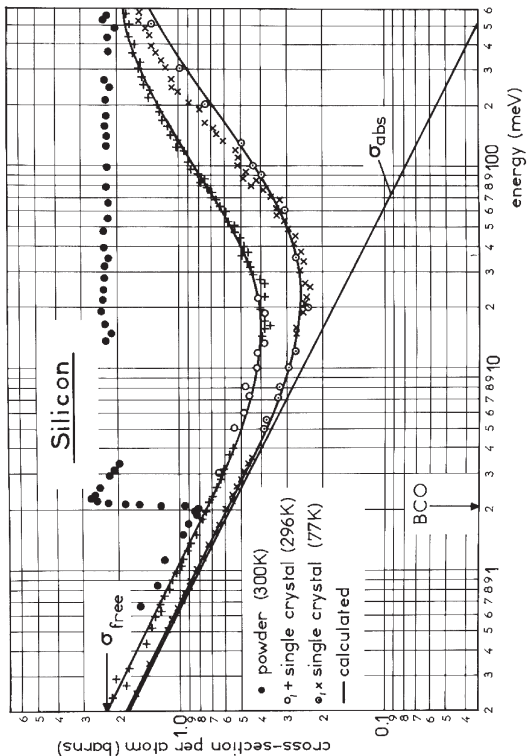
Figure 9: Total cross section for silicon in an energy range where it can be used as a filter [19].
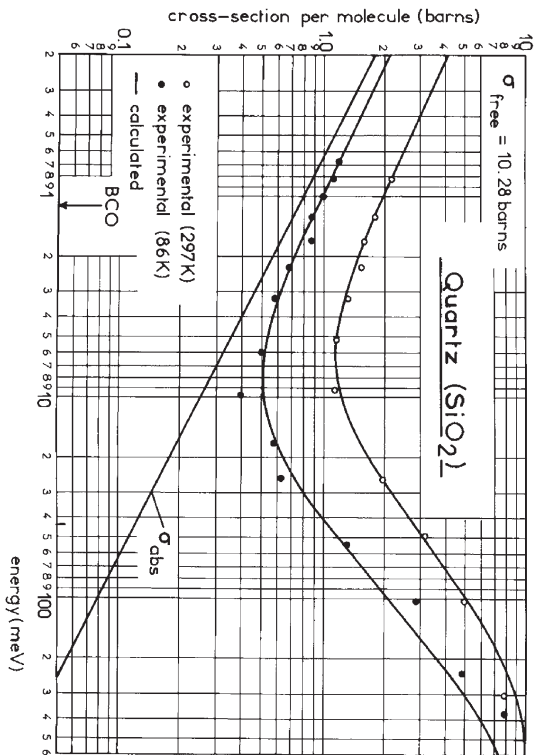
Figure 10: Total cross section for quartz in an energy range where it can be used as a filter [19].
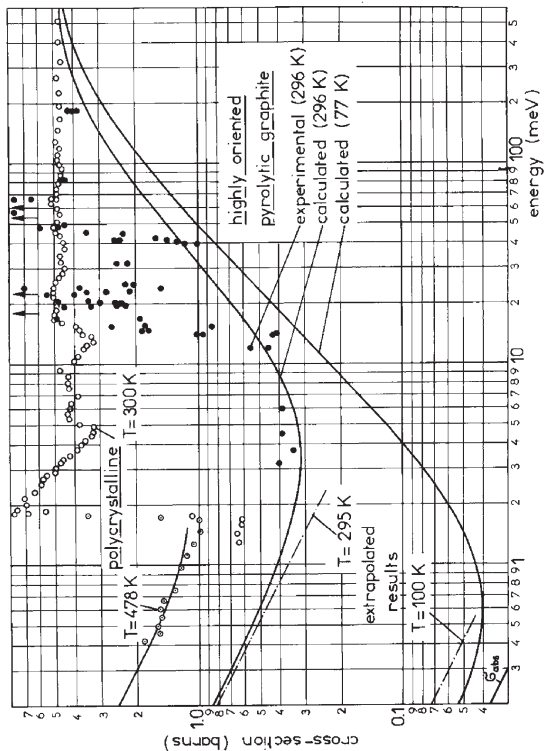
Figure 11: Total cross section for pyrolitic graphite in an energy range where it can be used as a filter [19].

3.2-19

Refractive lenses

The real part of the decrement $\partial = \frac{\lambda^2}{2\pi} N . b_{coh}$ of the refractive index given by $n = 1 - \partial - i\beta$ is small and positive for most materials. Hence, concave lenses must be generally used to focus neutron beams, and the focal lengths $f = \frac{R}{2\delta}$, where R is the on-axis radius of curvature, are prohibitively long. Reducing R, to reduce the focal length to practical values, would severely limit the lens aperture.

A series of N-aligned lenses with a negligible distance between each lens has a focal length $f = \frac{R}{2N\delta}$.

The factor $\frac{1}{N}$ reduction in focal length of a compound refractive lens allows for a reasonable value for the radius, R, of each element. Spherical surfaces make imperfect lenses, and only the central paraxial region of these approximate the paraboloid of revolution surface of ideal lenses. For lenses with paraboloid surfaces, R is the radius of curvature on axis at the apex of the paraboloid.

A suitable lens material should have a large value of δ and a small value of the linear attenuation coefficient, μ. The figure of merit, $\frac{\delta}{\mu}$, is listed for several materials in Table 4.

material	density [g/cm³]	μ [m⁻¹]	δ	δ/μ [m]
O	1.14	0.00425	1.28E-06	0.000302
CO_2	2.15	0.0191	1.60E-06	8.4E-05
C	2.26	0.051	3.88E-06	7.62E-05
Be	1.85	0.116	4.95E-06	4.27E-05
F	1.11	0.0365	1.02E-06	2.80E-05
Bi	9.73	0.118	1.23E-06	1.04E-05
MgO	3.58	1.28	3.62E-06	2.83E-06
Pb	11.3	0.573	1.6E-06	2.78E-06
MgF	3.18	0.471	1.24E-06	2.62E-06
SiO_2	2.2	0.441	1.05E-06	2.37E-06
ZrO_2	5.89	0.812	1.6E-06	1.98E-06
Mg	1.74	0.615	1.19E-06	1.94E-06
Si	2.32	0.796	1.06E-06	1.34E-06
Zr	6.49	1.2	1.55E-06	1.29E-06
Al	2.69	1.38	1.06E-06	7.73E-07

Table 4: Density, linear absorption coefficient, and figure of merit of selected materials at a wavelength of 1.8 Å.
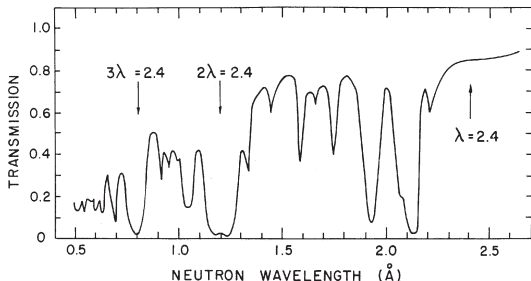
Figure 12: Measured transmission of a typical pyrolytic graphite filter, 4 cm thick, as a function of neutron wavelength, for neutrons traveling approximately normal to the (0002) graphite planes. The filter orientation is "tuned" to achieve minimum transmission of unwanted higher-order neutrons.

Polarizers

Methods used to polarise a neutron beam are varied, and the choice of the best technique depends on the instrument and the experiment to be performed. The main parameter that has to be considered when describing the effectiveness of a given polariser is the polarising efficiency, defined as

$$P = (N_+ - N_-)/(N_+ + N_-), \qquad (12)$$

where N_+ and N_- are the numbers of neutrons with spin parallel (+) or antiparallel (-) to the guide field in the outgoing beam. The second important factor, transmission of the wanted spin state, depends on various factors such as acceptance angles, reflection, and absorption.

Single-crystal polarizers

The principle by which ferromagnetic single crystals are used to polarize and monochromate a neutron beam simultaneously is shown in Fig. 13. A field **B,** applied perpendicular to the scattering vector **κ**, saturates the atomic moments **M** along the field direction **B**. The cross section for Bragg reflection in this geometry is

$$(d\sigma/d\Omega) = F_N(\mathbf{\kappa})^2 + 2 F_N(\mathbf{\kappa}) F_M(\mathbf{\kappa})(\mathbf{P} \cdot \mathbf{\mu}) + F_M(\mathbf{\kappa})^2, \qquad (13)$$
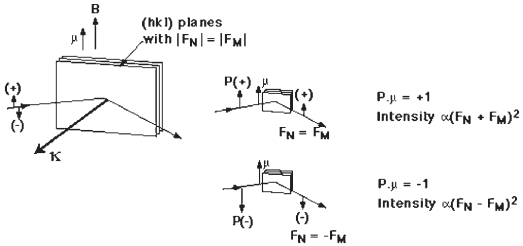
Figure 13: Geometry of a polarizing monochromator showing the lattice planes (hkl) with $|F_N| = |F_M|$, the direction of P and μ, the expected spin direction and intensity.

where $F_N(\mathbf{\kappa})$ and $F_M(\mathbf{\kappa})$ are the nuclear and magnetic structure factors, respectively. The vector **P** describes the polarization of the incoming neutron with respect to **B**; **P** = 1 for (+) spins, **P** = -1 for (-) spins, and **μ** is a unit vector in the direction of the atomic magnetic moments.

Hence, for neutrons polarized parallel to **B** (**P•μ** = 1), the diffracted intensity is proportional to $[F_N(\kappa)+F_M(\kappa)]^2$, while, for neutrons polarized antiparallel to **B** (**P•μ** = -1), the diffracted intensity is proportional to $[F_N(\kappa) - F_M(\kappa)]^2$. The polarising efficiency of the diffracted beam is then:

$$P = \pm 2 \, F_N(\kappa) \, F_M(\kappa) \, / \, [F_N(\kappa)^2 - F_M(\kappa)]^2, \qquad (14)$$

which can be either positive or negative and has a maximum value for $|F_N(\mathbf{\kappa})| = |F_M(\mathbf{\kappa})|$.

Thus, a good single-crystal polariser, in addition to possessing a convenient crystallographic structure, must be ferromagnetic at room temperature and should contain atoms with large magnetic moments. Furthermore, large single crystals with "controllable" mosaic should be available. Finally, the structure factor for the required reflection should be high, while those for higher-order reflections should be low.

None of the three naturally occurring ferromagnetic elements (Fe, Ni, and Co) makes efficient single-crystal polarizers. Cobolt is strongly absorbing, and the nuclear scattering lengths of iron and nickel are too large to be balanced by their weak magnetic moments. An exception is ^{57}Fe, which has a rather low nuclear scattering length, and structure-factor matching can be achieved by mixing ^{57}Fe with Fe and 3% Si [21].

	$Co_{0.92}Fe_{0.08}$	Cu_2MnAl	Fe_3Si	$^{57}Fe{:}Fe$	$HoFe_2$
Matched reflection $|F_N| \sim |F_M|$	(200)	(111)	(111)	(110)	(620)
d-spacing (Å)	1.76	3.43	3.27	2.03	1.16
Take-off angle $2\theta_B$ at 1 Å (deg)	33.1	16.7	17.6	28.6	50.9
Cut-off wavelength, λ_{max} (Å)	3.5	6.9	6.5	4.1	2.3

Table 5: Properties of polarizing crystal monochromators.

In general, to facilitate structure factor matching, alloys are used rather than elements. The characteristics of some alloys used as polarizing monochromators are presented in Table 5. At short wavelengths, the 200 reflection of $Co_{0.92}Fe_{0.08}$ is used to give a positively polarized beam [$F_N(\kappa)$ and $F_M(\kappa)$ both positive], but the absorption from cobalt is high. At longer wavelengths, the (111) reflection of the Heusler alloy Cu_2MnAl [22] is commonly used since it has a higher reflectivity (Fig. 14) and a larger d-spacing than $Co_{0.92}Fe_{0.08}$. Since, for the (111) reflection, $F_N \sim -F_M$, the

Figure 14: Calculated and measured reflectivity from the (111) reflection of a Heusler crystal with an intrinsic mosaic of 0.045°.

diffracted beam is negatively polarized. Unfortunately, the structure factor of the (222) reflection is higher than that of the (111) reflection, leading to significant higher-order contamination of the beam.

3.2-23

Polarizing mirrors

For a ferromagnetic material, the neutron refractive index is given by

$$n_{\pm} = 1 - \lambda^2 N(b_{coh} \pm p)/2\pi \,, \tag{15}$$

where, the magnetic scattering length, p, is defined by

$$p = 2\mu(B - H) \, m\pi/h^2 N \,, \tag{16}$$

where, m and μ are the neutron mass and magnetic moment, B is the magnetic induction in an applied field H, and h is Planck's constant.

The - and + signs refer, respectively, to neutrons whose moments are aligned parallel and antiparallel to **B**. The refractive index depends on the orientation of the neutron spin with respect to the film magnetization, thus giving rise to two critical angles of total reflection, γ_- and γ_+. Thus, reflection in an angular range between these two critical angles gives rise to polarized beams in reflection and in transmission. The polarization efficiency, P, is defined in terms of the reflectivity r_+ and r_- of the two spin states:

$$P = (r_+ - r_-)/(r_+ + r_-) \,. \tag{17}$$

For optimum reflectivity, polarizing mirrors are usually made by depositing thin films of ferromagnetic materials onto substrates of low surface roughness (e.g., float glass or polished silicon). The reflection from the substrate can be reduced by including an antireflecting layer made from, for example, gadolirium/titanium alloys.

The major limitation of such polarizers is that grazing-incidence angles must be used and the angular range of polarization is small. This limitation can be partially overcome by using multilayers, as described previously, in which one of the layer materials is ferromagnetic. In this case the refractive index of the ferromagnetic material is matched for one spin state to that of the nonmagnetic material so that reflection does not occur. A polarizing supermirror made in this way has an extended angular range of polarization (Figs. 15 and 16).

Note that modern deposition techniques allow the refractive index to be adjusted readily so that matching is easily achieved. The scattering-length densities of some commonly used layer pairs are given in Table 6.

Polarizing multilayers are also used in monochromators and broadband devices. Depending on the application, various layer pairs can be used: Co/Ti, Fe/Ag, Fe/Si, Fe/Ge, Fe/W, $Fe_{50}Co_{48}V_2$/TiN, FeCoV/TiZr, and $^{63}Ni_{0.66}{}^{54}Fe_{0.34}$/V, and the range of fields used to achieve saturation varies from about 10 to 500 Gs.

Polarizing mirrors can be used in reflection or transmission with polarization
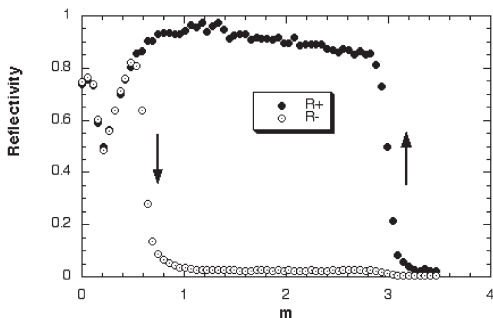
Figure 15: Measured performance of an m = 3 Fe/Si polarizing supermirror in reflection geometry. The reduction in reflectivity at low values of m is an artefact due to underillumination of the sample during the measurement.
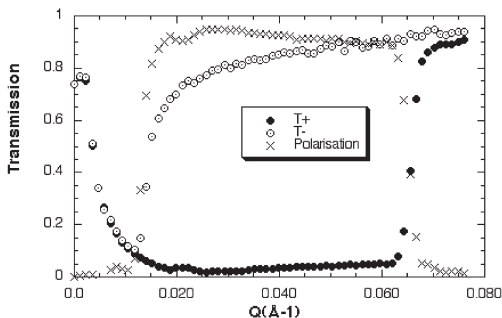
Figure 16: Measured performance of an m = 3 Fe/Si polarizing supermirror in transmission geometry. The increase in transmission at low values of m is an artifact caused by underillumination of the sample during the measurement.

Magnetic layer	N(b+p) (10^{-6} Å^{-2})	N(b-p) (10^{-6} Å^{-2})	Nonmagnetic layer	Nb (10^{-6} Å^{-2})
Fe	13.04	3.08	Ge	3.64
			Ag	3.50
			W	3.02
			Si	2.08
			Al	2.08
Fe:Co (50:50)	10.98	-0.52	V	-0.27
			Ti	-1.95
Ni	10.86	7.94		
Fe:Co:V (49:49:2)	10.75	-0.63	V	-0.27
			Ti	-1.95
Fe:Co:V (50:48:2)	10.66	-0.64	V	-0.27
			Ti	-1.95
Fe:Ni (50:50)	10.53	6.65		
Co	6.55	-2.00	Ti	-1.95
Fe:Co:V (52:38:10)	6.27	2.12	Si	2.08
			Al	2.08

Table 6: Scattering-length densities for some typical materials used for polarizing multilayers. For the nonmagnetic layer, we have listed only the simple elements that give a close match to the N(b-p) value of the corresponding magnetic layer. In practice, excellent matching can be achieved by using alloys (e.g., TixZry alloys allow niobium b values between -1.95 and 3.03 x 10-6 Å-2 to be selected) or reactive sputtering (e.g. TiNx).

efficiencies reaching 97%, although because of the low incidence angles, their use is generally restricted to wavelengths above 2 Å. Various devices can be constructed using mirror polarizers including simple reflecting mirrors, V-shaped transmission polarizers [23], cavity polarizers [24], and benders [25].

Polarizing Filters

Polarizing filters operate by selectively removing one of the neutron spin states from an incident beam, allowing the other spin state to be transmitted with only

moderate attenuation. The spin selection is obtained by preferential absorption or scattering, so the polarizing efficiency usually increases with the thickness of the filter, whereas the transmission decreases. A compromise must therefore be made between polarization, P, and transmission, T. The "quality factor" often used is $P \cdot \sqrt{T}$ [26].

The total cross sections for a generalized filter may be written as

$$\sigma_\pm = \sigma_0 \pm \sigma_p , \qquad (18)$$

where σ_0 is a spin-independent cross section and $\sigma_p = (\sigma_+ + \sigma_-)/2$ is the polarization cross section. It can be shown [27] that the ratio σ_p/σ_0 must be ≥ 0.65 to achieve $|P| > 0.95$ and $T > 0.2$.

Magnetized iron was the first polarizing filter to be used. The method relies on spin-dependent Bragg scattering from a magnetized polycrystalline block for which σ_p approaches 10 barns near the iron cutoff at 4 Å. For wavelengths in the range 3.6 to 4 Å, the ratio σ_p/σ_0 is ~ 0.59, resulting in the polarizing efficiency of 0.8 for a transmittance of ~ 0.3. In practice, however, since iron cannot be fully saturated, depolarization occurs, and values of P ~ 0.5 with T ~ 0.25 are more typical.

Resonance absorption polarization filters rely on the spin-dependence of the absorption cross section of polarized nuclei at their nuclear resonance energy and can produce efficient polarization over a wide energy range. The nuclear polarization is normally achieved by cooling in a magnetic field, and filters based on ^{149}Sm ($E_r = 0.097$ eV) and ^{151}Eu ($E_r = 0.32$ eV and 0.46 eV) have been tested successfully [28]. The ^{149}Sm filter has a polarizing efficiency close to 1 within a small-wavelength range (0.85 to 1.1 Å), while the transmittance is about 0.15.

Broadband polarizing filters, based on spin-dependent scattering or absorption, provide an interesting alternative to polarizing mirrors or monochromators because of the wider range of energy and scattering angle that can be accepted. The most promising such filter is polarized ^{3}He, which operates through the huge spin-dependent neutron capture cross section that is totally dominated by the resonance capture of neutrons with antiparallel spin. The polarization efficiency of a ^{3}He neutron spin filter of length, l, can be written as

$$P_n(\lambda) = \tanh[O(\lambda)P_{He}] , \qquad (19)$$

where P_{He} is the ^{3}He nuclear polarization and $O(\lambda) = [^3He] \, l \, \sigma_0(\lambda)$ is the dimensionless effective absorption coefficient, also called the opacity [29]. For gaseous ^{3}He, the opacity can be written in more convenient units by

$$O' = p[bar] \times l[cm] \times \lambda[\text{Å}] , \qquad (20)$$

where p is the ^{3}He pressure and O =7.33 x 10^{-2} O.'

Similarly, the residual transmission of the spin filter is given by:

$$T_n(\lambda) = \exp[-O(\lambda)]\cosh[O(\lambda)\cdot P_{He}]$$ (21)

It can be seen from Fig. 17, that even at low ^{3}He polarization, full neutron polarization can be achieved in the limit of large absorption at the cost of the transmission.

^{3}He can be polarised either by spin exchange with optically pumped Rb [30] or by pumping of metastable ^{3}He* atoms followed by metastable exchange collisions [31]. In the former method, the ^{3}He gas is polarized at the required high pressure whereas ^{3}He* pumping takes place at a pressure of about 1 mbar, followed by a polarization conserving compression by a factor of nearly 10,000. Although the polarization time constant for Rb pumping is of the order of several hours, compared with fractions of a second for ^{3}He*, pumping the latter requires several "fills" of the filter cell to achieve the required pressure. Typically, nuclear polarizations P_{He} of 55% are achieved.

Zeeman Polarizer

The reflection width of perfect silicon crystals for thermal neutrons and the Zeeman splitting ($\Delta E = 2\mu B$) at a field of about 10 kG are comparable and therefore can be used to polarize a neutron beam. For a monochromatic beam (energy E_0) in a strong magnetic field region, the result of the Zeeman splitting will be a separation into two polarized subbeams, one polarized along B with energy $E_0 + \mu B$ and the other polarized antiparallel to B with energy $E_0 - \mu B$. The two polarized beams can be selected by rocking a perfect crystal in the field region B [32].

Spin-orientation devices

Polarization is the state of spin orientation of an assembly of particles in a target or beam. The beam polarization vector **P** is defined as the vector average of this spin state of the assembly in the beam, often described by the density matrix $\rho = \frac{1}{2}(1+\boldsymbol{\sigma}\mathbf{P})$. The polarization is then defined as $\mathbf{P} = \mathbf{Tr}(\boldsymbol{\rho\sigma})$. If the polarization vector is inclined to the field direction in a homogenous magnetic field, **B**, the polarization vector will precess with the classical Larmor frequency $\omega_L = |\gamma|B$. This results in a precessing vector and a precessing spin polarization. For most experiments, it is sufficient to consider the linear polarisation vector in the direction of an applied magnetic field. If, however, the magnetic field direction changes along the path of the neutron, it is also possible that the direction of **P** will change. If the frequency, Ω, with which the magnetic field changes is such that

$$\Omega = d(\mathbf{B}/|\mathbf{B}|)/dt \ll \omega_L ,$$ (22)
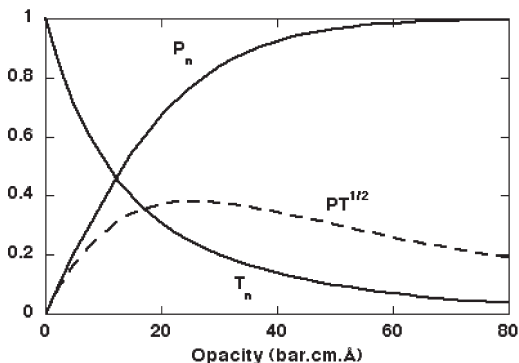
Figure 17: Neutron polarization and transmission of a 3He filter with 55% nuclear polarization. Also shown is the quality factor $P\sqrt{T}$.

then the polarization vector follows the field rotation adiabatically. Alternatively, when $\Omega \gg \omega_L$, the magnetic field changes so rapidly that **P** cannot follow and the condition is known as nonadiabatic fast passage. All spin-orientation devices are based on these concepts.

Maintaining the direction of polarization
A polarised beam will tend to become depolarized during passage through a region of zero field since the field direction is ill defined over the beam cross section. Thus, to keep the polarization direction aligned along a defined quantization axis, special precautions must be taken.

The simplest way of maintaining the polarization of neutrons is to use a guide field to produce a well-defined field **B** over the whole flight path of the beam. If the field changes direction, it has to fulfill the adiabatic condition $\Omega \ll \omega_L$, that is the field changes must take place over a time interval that is long compared with the Larmor period. In this case, the polarization adiabatically follows the field direction with a maximum angle of deviation, $\Delta\Theta \leq 2 \ \tan^{-1}(\omega/\omega_L)$ [33].

3.2-29

Rotation of the polarization direction

The polarization direction can be changed by the adiabatic change of the guide field direction so that the direction of the polarization follows it. Such a rotation is performed by a spin turner or spin rotator [34].

Alternatively, the direction of polarization can be rotated relative to the guide field by using the property of precession described previously. If a polarized beam enters a region where the field is inclined to the polarization axis, then the polarization vector **P** will precess about the new field direction. The precession angle will depend on the magnitude of the field and the time spent in the field region. By adjustment of these two parameters together with the field direction, a defined, though wavelength-dependent, rotation of **P** can be achieved. A simple device uses the nonadiabatic fast passage through the windings of two rectangular solenoids wound orthogonally on top of each other [35]. In this way the mechanical rotation can be replaced by two currents the ratio of which defines the direction of the precession field axis and the size of the fields determines the angle ϕ of the precession. The orientation of the polarization vector can therefore be defined in any direction.

In order to produce a continuous rotation of the polarization (i.e., a well-defined precession), as required in neutron spin echo applications, precession coils are used. In the simplest case these are long solenoids for which the change of the field integral over the cross section can be corrected by Fresnel coils [36]. Zeyen and coworkers have developed and implemented optimal field shape coils (ofs) [37]. The field in these coils follows a $\cos^2$ shape that results from the optimization of the line integral homogeneity. The OFS coils can be wound over a very small diameter, drastically reducing stray fields.

Flipping of the polarization direction

The term "flipping" was originally applied to the situation where the beam polarization direction is reversed with respect to a guide field; that is. it describes a transition of the polarization direction from parallel to antiparallel to the guide field and vice versa. A device that produces this 180° rotation is called a π-flipper. A π/2 flipper, as the name suggests, produces a 90° rotation and is normally used to initiate precession by turning the polarization at 90° to the guide field.

The most direct, wavelength-independent way of producing such a transition is again a nonadiabatic fast passage from the region of one field direction to the region of the other field direction. This can be realized by a current sheet like the Dabbs foil [38], a Kjeller eight [39], or a cryoflipper [40].

Alternatively, a spin flip can be produced using a precession coil, as described

previously, in which the polarization direction makes a precession of just π about a direction orthogonal to the guide field direction. Normally, two orthogonally wound coils are used, where the second, correction coil, serves to compensate the guide field in the interior of the precession coil. Such a flipper is wavelength dependent and can be easily tuned by varying the current in the coils.

Mechanical Choppers and Selectors

In this section we deal with devices that take advantage of the neutron flight time to make a selection of some sort. To put things into perspective, we should mention that a 4-Å neutron has a reciprocal velocity of approximately 1,000 μs m^{-1} so that accurate neutron energy determinations can be made with flight paths of only a few meters.

Disc choppers rotating at speeds up to 20,000 rpm about an axis that is parallel to the neutron beam are used to produce a well-defined pulse of neutrons. The discs are made from absorbing material (at least where the beam passes) and comprise one or more neutron-transparent apertures or slits. For polarized neutrons these transparent slits should not be metallic, as the eddy currents in the metal moving in even a weak guide field will strongly depolarize the beam. The pulse frequency is determined by the number of apertures and the rotation frequency, while the duty cycle is given by the ratio of open to closed time in one rotation. Two such choppers rotating in phase can be used to monochromate and pulse a beam simultaneously [41]. In practice, more than two choppers are generally used to avoid frame overlap of the incident and scattered beams. The time resolution of disc choppers (and hence the energy resolution of the instrument) is determined by the beam size, the aperture size, and the rotation speed. For a realistic beam size the rotation speed limits the resolution.

Therefore, in modern instruments it is normal to replace a single chopper with two counter-rotating choppers [42]. The low duty cycle of a simple disk chopper can be improved by replacing the single slit with a series of slits either in a regular sequence (Fourier chopper) [43] or a pseudostatistical sequence (pseudostatistical chopper) [44] with duty cycles of 50% and 30%, respectively.

The Fermi chopper is an alternative form of neutron chopper that simultaneously pulses and monochromates the incoming beam. It consists of a slit package, essentially a collimator, rotating about an axis that is perpendicular to the beam direction [45]. For optimum transmission at the required wavelength, the slits are usually curved to provide a straight collimator in the neutron frame of reference. The curvature also eliminates the "reverse burst," that is. is a pulse of neutrons that passes when the chopper has rotated by 180°.

A Fermi chopper with straight slits in combination with a monochromator

assembly of wide horizontal divergence can be used to time focus a polychromatic beam, hence maintaining the energy resolution while improving the intensity [46].

Velocity selectors are used where a continuous beam is required with coarse energy resolution. They exist in either multiple disc configurations or helical channels rotating about an axis parallel to the beam direction [47]. Modern helical channel selectors are made up of lightweight absorbing blades slotted into helical grooves on the rotation axis [48]. At higher energies, where no suitable absorbing material is available, highly scattering polymers (polymethyl metacrylate) can be used for the blades, although in this case adequate shielding must be provided. The neutron wavelength is determined by the rotation speed and resolutions, $\Delta\lambda/\lambda$; range from 5 to practically 100% ($\lambda/2$ filter) can be achieved. The resolution is fixed by the geometry of the device but can be slightly improved by tilting the rotation axis or can be relaxed by rotating in the reverse direction for shorter wavelengths. Nowadays transmissions of up to 94% are obtainable.

References

[1] Anderson, I. S., Brown, P.J., Carpenter, J.M., Lander, G., Pynn, R., Rowe, J.M., Schärpf, O., Sears, V.F., and Willis, B.T.M., Intern. Tables for Crystallography C, 2nd Edition, Kluwer Academic Publish. (1999) 426

[2] Nunes, A. C., *NIM* **119** (1974) 291; Glinka, C. J., Rowe, J. M., and LaRock, J. G., J. Appl. Cryst. **19** (1986) 427

[3] Wright, A. F., Berneron, M., and Heathman, S. P., *NIM* **180** (1981) 655-658

[4] Maier-Leibnitz, H., Summer School on Neutron Physics, Alushta Joint Insitute of Nuclear Physics (Russia) (1969)

[5] Bonse, U., and Hart M., *Appl. Phys. Lett.* **7** (1965) 238-240

[6] Zachariasen, W. H., "Theory of X-ray Diffraction in Crystals," Dover, New York (1945)

[7] Sears, V. F., *Acta Cryst.* **A53** (1997) 35-36

[8] Alefed, B., *Kerntechnik* **14** (1972) 15-17

[9] Hock, R., Vogt, T., Kulda, J., Mursic, Z., Fuess, H., and Magerl A., *Z. Phys B* **90** (1993) 143.

[10] Freund, A. K., Guinet, P., Mareschal, J., Rustichelli, F., and Vanoni, F., *J. Cryst. Growth* **13-14** (1972) 726

[11] Magerl, A., Liss, K. D., Doll, C., Madar R., and Steichele, E., *NIM A* **338** (1994) 83-89

[12] Riste, T., *NIM* **86** (1970) 1-4; Currat, R., *NIM* **107** (1973) 21-28

[13] Scherm, R., Dolling, G., Ritter, R., Schedler, E., Teuchert, W., and Wagner, V., *NIM* **143** (1977) 77-85

[14] Scherm, R. H., and Kruger, E., *NIM A* **338** (1994) 1

[15] Christ, J., and Spinger, T., *Nukleonik* **4** (1962) 23-25

[16] Schoenborn, B. P., Caspar, D. L. D., and Kammerer, O. F., *J. Appl. Cryst.* **7** (1974) 508-510

[17] Mezei, F., *Commun. Phys.* **1** (1976) 81-85; Hayter J. B. and Mook H. A., *J. Appl. Cryst.* **22** (1989) 35-41

[18] Mildner, D.F.R., Chen-Mayer, H.H., and Downing, R.G., *J. Phys. Soc. Jpn* **65** (1996) Suppl. A, 308-311

[19] Freund, A. K., *NIM* **213** (1983) 495-501

[20] Shapiro, S. M., and Chesser, N. J., *NIM* **101** (1972) 183-186

[21] Reed, R. E., Bolling, E. D., and Harmon, H. E., Solid State Division Report. Oak Ridge National Laboratory, USA (1973) 129

[22] Delapalme, A., Schweizer, J., Couderchon, G., and Perrier de la Bathie, R., *NIM* **95** (1971) 589-594; Freund, A., Pynn, R., Stirling, W. G., and Zeyen, C. M. E., *Physica B* **120** (1983) 86-90

[23] Majkrzak, C. F., Nunez, V., Copley, J. R. D., Ankner, J. F., and Greene, G. C. in "Neutron optical devices and applications," edited by C. F. Majkrzak and J. L. Wood., *SPIE Proc.* **1738** (1992) 90-106

[24] Mezei, F. in "Thin film neutron optical devices: mirrors, supermirrors, multiplayer monochromators, polarizers and beam guides," edited by C. F. Majkrzak., *SPIE Proc.* **983** (1988) 10-17

[25] Schärpf, O., *Physica (Utrecht) B* **156 & 157** (1989) 639-646

[26] Tassel, F. and Resouche, E., *NIM A* **359** (1995) 537-541

[27] Williams, W. G, "Polarized Neutrons," Claredon Press, Oxford (1988)

[28] Freeman, F. F., and Williams, W. G., J. Phys. E. **11** (1978) 459-467

[29] Surkau, R., Becker, J., Ebert, M., Grossman, T., Heil, W., Hofmann, D., Humblot, H., Leduc, M., Otten, E. W., Rohe, D., Siemensmeyer, K., Steiner, M., Tasset, F., and Trautmann N., *NIM A* **384** (1997) 444-450

[30] Bouchiat, M., A., Carver, T., R., and Varnum, C., M., Phys. Rev. Lett. **5** (1960) 373-375; Chupp, T., E., Coulter, K., P., Hwang, S., R., Smith, T., B., and Welsh, R., C., J., *J. Neutron Res.* **5** (1996) 11-24

[31] Colgrove, F., D., Schearer, L., D., and Walters, K., *Phys. Rev.* **132** (1963) 2561-2572

[32] Forte M. and Zeyen C. M. E., *NIM A* **284** (1989) 147-150

[33] Schärpf, O., in "Neutron spin echo," *Lecture notes in physics,* vol. **128**, edited by F. Mezei, Springer-Verlag (1980) 27-52

[34] Schärpf, O., and Capellman, H., *Phys. Status Solidi A* **135** (1993) 359-379

[35] Jones, T. J. L., and Williams, W. G., Rutherford Laboratory Report RL-77-O79/A (1977)

[36] Mezei, F., *Z. Phys.* **255** (1972) 146-160

[37] Zeyen, C. M. E., and Rem, P. C., *Meas. Sci. Tech.* **7** (1996) 782

[38] Dabbs, J. W. T., Roberts, L. D., and Bernstein, S., Report ORNL-CF-55-5-126. Oak Ridge National Laoratory, USA (1955)

[39] Abrahams, K., Steinsvoll, O., Bongaarts, P. J. M., and De Lange, P. W., Rev. Sci. Instrum. **33** (1962) 524-529

[40] Forsyth, J. B., *At. Energy Rev.* **17** (1979) 345-412

[41] Egelstaff, P. A., Cocking, S. J., and Alexander, T. K., Inelastic Scattering of neutrons in solids and liquids. IAEA, Vienna (1961) 165-177

[42] Hautecler, S., Legrande, E., Vansteelandt, L., d'Hooghe, P., Rooms, G., Seeger, A., Schalt, W., and Gobert, G., Proccedings of the Conference on "Neutron Scattering in the Nineties," Jülich. IAEA, (1985) 211-215; Copley J. R. D., *NIM A* **303** (1991) 332-341

[43] Colwell, J. F., Miller, P. H., and Whittemore, W. L., "Neutron Inelastic Scattering", Vol. **II**, IAEA, Vienna (1968) 429-437

[44] Hossfeld, F., Amadori, R., and Scherm, R., "Instrumentation for Neutron Inelastic Scattering," IAEA, Vienna (1970) 117

[45] Turchin, V. F., "Slow neutrons," Israel Programme for Scientific Translation (1965)

[46] Blanc, Y., "Le spectrometre à temps de vol IN6: characteristiques, techniques et performances." ILL internal Report No **82BL21G**, Institut Laue-Langevin, Grenoble (1983)

[47] Dash, J. G., and Sommers, H. S., *Rev. Sci. Instrum.* **24** (1953) 91-96

[48] Wagner, V., Friedrich, H., Wille, P., *Physica B* **180&181** (1992) 938-940

Detectors for Thermal Neutrons

A.Oed

Introduction

The particle- or radiation-detection is based on the measurement of electric currents. Thermal neutrons with their low velocity and without an electric charge can only be measured subsequent to a nuclear reaction with target atoms which emit either ionizing radiations or ionizing particles. The target isotopes commonly used for thermal neutron detection are indicated in Tab (1). Except for Gd, all the other reactions are fission processes where two fission particles are ejected in opposite directions randomly oriented in space.

The Maxwell distributions of thermal neutrons are shown in Fig (1).
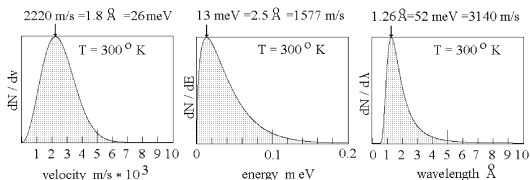
Figure 1: Velocity-, energy- and wave-length-distribution for neutrons at 300 º K.

reaction	energy	particle	energy	particle	energy
n (^{3}He, p) ^{3}H	+0.77 MeV	p	0.57 MeV	^{3}H	0.19 MeV
n (^{6}Li, α) ^{3}H	+4.79 MeV	α	2.05 MeV	^{3}H	2.74 MeV
$^{93\%}$ n (^{10}B, α)^{7}Li	+2.3 MeV + γ (0.48MeV)	α	1.47 MeV	^{7}Li	0.83 MeV
$^{7\%}$ n (^{10}B, α) ^{7}Li	+2.79 MeV	α	1.77 MeV	^{7}Li	1.01 MeV
n (^{235}U, Lfi) Hfi	+ ~ 100 MeV	Lfi	< ~ 80 MeV	Hfi	< ~ 60 MeV
n (^{157} Gd, Gd) e$^-$	+ < = 0.182 MeV	conversion electron	0.07 to 0.182 MeV		

Table 1: Commonly used isotopes for thermal neutron detection, reaction products and their kinetic energies.

3.3-2

Absorption law

A neutron flux J_o [1/s] after having passed the length of x [cm] in an absorber with the absorption length μ [cm], is reduced to the value

$$J= J_o \, e^{-(x/\mu)}$$

0r the relative amount of the flux which disappears in the absorber is

$$(J_o\text{-}J) / J_o = 1\text{-} e^{-(x/\mu)}$$

Expressed in percentage, this leads to the efficiency of the detector or absorber

$$Eff = (1\text{-} e^{-(x/\mu)})* 100$$

The absorption length μ [cm] is inversely proportional to the product of the cross section σ[cm²] and the atomic density A_d [atom/cm³] of the absorber

$$\mu = 1/(\ \sigma * A_d)$$

The absorption law expressed with the cross-section therefore is

$$J= J_o \, e^{-(\sigma*\ x* Ad)}$$

Target-material		density g / cm³	cross-section σ barn	abs. length μ cm	mass abs. dens. γ g / cm
³He	gas 1bar	1.27 10⁻⁴	5.33 10³	7.36	9.34 10⁻⁴
⁶Li	metal	4.70 10⁻¹	9.45 10²	2.24 10⁻²	1.05 10⁻²
Li nat	metal	5.43 10⁻¹	6.62 10¹	3.20 10⁻¹	1.74 10⁻¹
⁶LiF	crystal	2.55	1.21 10³	1.56 10⁻²	3.98 10⁻²
¹⁰BF₃	gas 1bar	2.82 10⁻³	4.01 10³	9.80	2.77 10⁻²
¹⁰B	crystal	2.16	4.01 10³	1.92 10⁻³	4.14 10⁻³
B nat	crystal	2.34	7.50 10²	1.2 10⁻²	2.81 10⁻²
Mg	metal	1.74	6.23 10⁻²	3.67 10²	6.39 10²
Al	metal	2.70	2.38 10⁻¹	6.96 10¹	1.88 10²
Fe	metal	7.86	2.59	4.55	3.57 10¹
Cd	metal	8.64	2.51 10¹	8.56 10⁻³	7.40 10⁻²
Gd nat	metal	7.89	4.61 10⁴	7.16 10⁻⁴	5.65 10⁻³
¹⁵⁷Gd	metal	7.89	2.51 10⁵	1.31 10⁻⁴	1.03 10⁻³
Hg	metal	1.35 10¹	3.70 10²	6.68 10⁻²	9.02 10⁻¹
²³⁵U	metal	1.89 10¹	5.77 10²	3.58 10⁻²	6.77 10⁻¹
U nat	metal	1.91 10¹	7.60	2.72	5.20 10¹

Table 2: Cross-section, absorption length and mass-absorption–density for thermal neutrons. (v = 2224 m/s; λ = 1.78 Å ; E_{kin}= 26 m eV ; T = 300 °K). Isotopes with high cross-section and therefore used in neutron detection are marked in bold type.

For gases at 1 bar, the atomic density A_d is $2.7 \cdot 10^{19}$ [$1/cm^3$] and for solids and liquids its value is about 1000 times higher. In general, the atomic density is given by

$$A_d = \rho * N_a / M_v \quad [1/cm^3] \text{ where}$$

ρ is the volumetric weight [g/cm^3], $N_a = 6.25 \cdot 10^{23}$ the Avogadro number [atom/ mol] and M_v the molar weight of the absorber-material [g /mol].

Sometimes the absorption is also expressed in terms of the mass-absorption-coefficient $\gamma = \mu * \rho$ [g / cm^2]. With the surface mass density $M_d = x*\rho$ [g/cm^2] of an absorber of x [cm] in thickness, the law reads:

$$J = J_o \, e^{-(Md/\gamma)}$$

The absorption length, cross section and mass absorption-coefficient for thermal neutrons for some materials used in neutron experiments are indicated in Tab (2)

The cross-section σ for thermal neutrons is inversely proportional to their velocity v.

$$\sigma \sim 1/v \quad \text{or} \quad \sigma \sim 1/\sqrt{E} \text{ where E is kinetic energy}$$
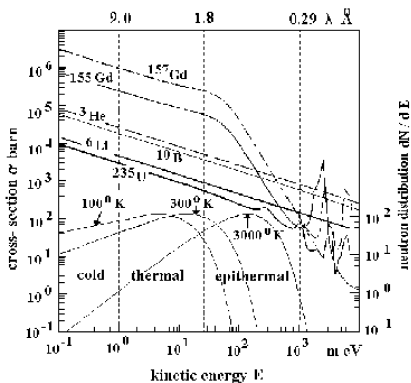
Figure 2: Neutron cross-section as function of the kinetic energy for the isotopes commonly used in thermal neutron detection.

3.3-4

As the Broglie wavelength λ = h / (m_n • v) with h = Planck–constant and m_n= neutron mass is also inversely proportional to the velocity v, the cross-section increases linearly with the neutron wavelength λ: σ ~ λ.
^{157}Gd and ^{235}U have resonances at higher energies, as shown in Fig (2)

Neutron detectors
The following list is a survey of all possible neutron detectors subdivided into integrating and counting devices. Its characteristics are indicated as advantages and disadvantages.

Without taking into account the importance of the different qualities and especially the costs, it seems that counting detectors have more advantages than the integrating ones. Integrating detectors are more suitable for beam monitoring, beam alignment and neutronography whereas the counting devices are appropriate in interference pattern recordings for structure analysis and time-depending changes inside the samples.

INTEGRATING
Converter foil with

photogr. film;
A1,A2,A8, **D3,D4,D5,D6,D7**

image plate;
A1,A2,A5,A8, **D3,D4,D6,D7**

CCD camera;
A1,A2,A5, **D3,D4,D6,D7,D8**

n-Scintillator with

CCD camera*;*
A1,A2,A5, D3,D4,D7

Thomson tube;
A*1,A2,A5,*A6,*A8,* **D3,D4,D7**

Image amplifier;
*A1,***D2,D3,D5,D6,D7,D8**

Internal converter

ionization chamber;
A1,A4,A5,A8, **D2,D3**

Gd loaded image plate;
A1,A2,A5,A8, **D3, D4,D7**

COUNTING
Converter foil with

pixel semiconductor;
A1,A2,A3,A4,A5, **D6,D8**

pos. sensitive. gas counter;
A3,A4A5,A6,A8, **D1,D2**

n-Scintillator with

pos. sensitive PM;
A1,A2,A3,A4,A5,A6, A7,**D8**

pos. sensitive gas counter;
A3,A4,A5,A6,A7, A8, **D1,D2**

Internal converter

gas-counter, -array;
A3,A4,A5,A6,A7,A8, **D1,D2**

multi wire prop. counter.;
A3,A4,A5,A6,A7,A8, **D1,D2**

micro pattern gas counter;
A1,A3,A4,A5,A6,A7, A8, **D2**

boron diode;
A1,A2,A3,A4,A5,A6,A7, **D8**

Advantages	**Disadvantages**
A1) high intensity capability	D1) limited counting capacity < 1 kHz/mm²
A2) high position resolution	D2) limited position resolution > 100 μcr.
A3) gamma discrimination	D3) gamma sensitivity
A4) on-line read-out, short time slices	D4) long read-out time > 1ms /frame
A5) high dynamic	D5) low dynamic < 1/100
A6) high n-efficiency	D6) low n-efficiency < 20 %
A7) low noise	D7) high noise > 1 count / pixel
A8) large sensitive area	D8) small sensitive area < 100 cm²

Some useful constants:		
k= 1.384 10^{-23}	Joule/ °K = kg(m/s)²/ °K	Boltzmann constant
h= 6.6252 10^{-34}	VAs = Joule*s= kg (m/s)² s	Planck constant
e= 1.62 10^{-19}	As	elementary charge
v= 2.998 10^{8}	m/s	velocity of light
m_e= 9.108 10^{-31}	kg	electron mass
m_p= 1.6723 10^{-27}	kg	proton mass
m_n= 1.6747 10^{-27}	kg	neutron mass
N_a= 6.25 10^{23}	atom/Mol	Avogadro number

Gas-detectors

Ionization chamber

The simplest neutron gas detector is the ionization chamber: a condenser consisting of two metallic plates and the gap in between filled with ^{3}He or ^{10}BF$_3$ gas.

The two particles emitted by the nuclear reaction are slowed down in the gas. Along their trace they produce electron-ion pairs, and with an electric field strength of about 100 V/(cm · bar) these charges are collected on the corresponding plates where the current can be measured. To generate one electron-ion pair in a gas, the ionizing particle loses about 30 eV of its energy. This is why in the n (^{3}He, p) ^{3}H +0.77 MeV reaction for one neutron about 22 000 electron-ion pairs are produced and a charge of 4.1 10^{-15} [As] is collected. Usually ionization chambers are used as beam monitors.

The triton range is about 1/3 of the proton range as can be seen in Fig (4). This means that there exists a systematic deviation between the centre of gravity of the
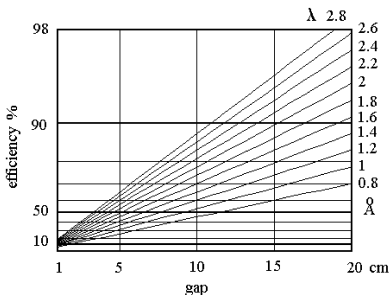
Figure 3: Neutron detection efficiency as a function of the detection gap filled with 1 bar ^{3}He.

charges and the location where the reaction takes place.

This deviation can be reduced be adding other gases with higher molecular weight, preferably composed of light atoms like C, H and F in order to be less sensitive to x- rays and gammas. For some gases, the mean energy loss of a particle to produce one electron-ion pair, the particle range and the mean deviation from the reaction point are indicated in Tab (3).

Proportional counter

The small amount of charges in an ionization chamber (see above) produced by a single neutron is difficult to measure, whereas this is easy to do with a Geiger counter {2}. A very thin wire of several microns in diameter , which serves as anode, is located in the axe of a cylindrical tube. This condenser is filled with gas. The electrons produced by the ionizing particles of the nuclear reaction drift towards the positive wire where they will experience an avalanche amplification at the very high field strength surrounding the wire. This gas amplification is noiseless and proportional to the amount of primarily produced charges. The gas gain reaches factors up to 10^5. Single neutrons are easily detectable. A typical pulse height spectrum of a ^{3}He +Ar +CH$_4$ counter is shown in Fig (5).

As a matter of fact, at 770 keV only one line would be expected, corresponding to the total reaction energy. But some of the particle traces enter into the housing and the charges are lost. At the point of 192 keV the reaction has taken
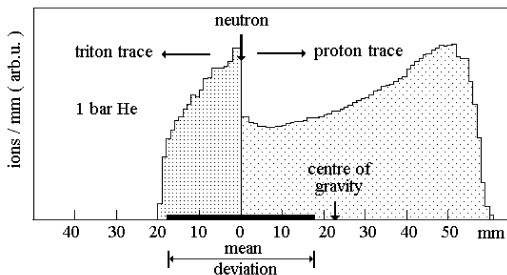
Figure 4: Ionization /mm in He of the particles emitted by the reaction n (^{3}He, p) ^{3}H +0.77 MeV. Ionization and Range are calculated with the Program :TRIM86 {1}.

place directly on the inner surface of the cylinder and the proton is stopped in the metal. Only the triton, emitted in the opposite direction, releases its complete energy into the gas. With a higher gas pressure the amount of counts in the tail will be smaller as the range of the particles will be shorter. Between the neutron signals and the gamma background there is a large gap which allows a very good gamma discrimination. Unfortunately the local counting capacity is limited to about 1 kHz / mm^2. The ions generated in the gas amplification very slowly drift towards

Gas 1 bar	Mean ionisation energy eV	Trace length mm proton	Trace length mm triton	Mean deviation mm
He	41.3	61	20	36
Ar	26.4	12	4	7.4
Xe	22.1	6.17	1.85	3.94
C_4H_{10}	23	3.38	.93	2.3
CF_4	~27	4.4	1.6	2.5
		α	^{7}Li	
BF_3	35.3	4.3	2.1	1.4

Table 3: Mean ionization energy, particle range and deviation in some gases
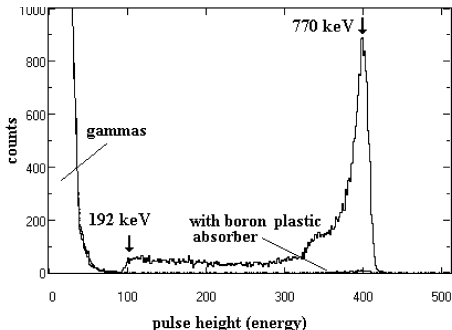
Figure 5: Pulse height spectrum of a ^{3}He neutron counter irradiated with a lab. Am–Be source. In order to distinguish between gamma background and neutron signal, a boron loaded plastic absorber was installed between source and counter in a second measurement.

the cylinder walls. At high rates their space charge reduces the applied electric field on the wire and hence the gas gain. For a good energy resolution, which allows a good gamma discrimination, all the primary charges of one event must be collected. As the ionizing particles are emitted in random directions with respect to the wire orientation, the drift time of the electrons towards the wire varies considerably due to the inhomogeneous cylindrical field. The drift time depends on the gas mixture and on the local electric field strength. In general, up to 10 μs are necessary for a good charge collection. The maximal count rate of the whole counter therefore is of about 30 kHz with a pileup of 30% of the signals. The drift velocity of electrons in a CF_4– He mixture is shown in Tab (4). With He the highest drift velocity is reached by adding CF_4

As shown recently {4}, a counter filled with N_2 +CF_4 is an excellent neutron beam monitor. For a 1 cm gap filled with 1 bar N_2 the neutron efficiency is 9.05 10^{-5} at a wavelength of 1.8 Å. In the reaction n (^{14}N, ^{14}C) H + 627 keV, with a cross-section of 1.8 barn , the proton is emitted with an energy of 585 keV and delivers a charge signal which is very well separated from the gamma background.

Gas mixture	velocity cm / μ s
CF₄ 100%	11.2
CF₄ 50% + He 50%	6.2
He 100 %	1.1

Table 4: Drift velocity of electrons in an electric field of 1.14 V/ (cm · mb) in a gas mixture {3}.

Multi wire proportional chamber (MWPC)

The position sensitive variant of the Geiger counter is the MWPC invented by Charpak{5}.

It consists of a great number of thin anode wires assembled in a plane and mounted between two plates which are composed of separated cathode strips. The orientation of the strips is orthogonally to each other. As with Geiger counters, the gas amplification takes place on the wires. After the separation of the electron-ion pairs in the avalanche by the electric field, the ion cloud influences signals on the cathode strips which allows to determine the position of the event. The achievable position resolution perpendicular to the wires depends on the wire spacing.

With a wire spacing smaller than one millimeter the operation of this device is extremely difficult. As the electric field between the anode frame and the cathodes is homogeneous, the distribution of the drift time of the primary charges is more uniform compared to a cylindrical counter and therefore the time for the charge-collection is reduced to about 1 μs. As the counting capacity only depends on this collection time, the rate limit for a two-dimensional detector increases to about 300 kHz for the whole sensitive surface, with a position error of 30 % at this rate. To record a higher rate, the detector has to be segmented. A one dimensional detector with individual read-out presents such a segmentation. Each cell is able to record the rate of 300 kHz. In any case the local counting capacity is limited to about 1 kHz/ mm² just as for the counter tube.

Micro Pattern Gas Counter (MPGC)

To improve the counting capacity, the cathode distance has to be reduced for a faster evacuation of the avalanche ions; for a better position resolution, the structure pitch of the electrodes has to be smaller. This aim has been reached with the recently developed Micro Pattern Gas Counters. Their very small electrode structures are manufactured by means of the photolithographic technique, a common procedure to fabricate integrated circuits.

The first type was the Micro Strip Gas Chamber (MSGC) {6} which will be shortly described. Its arrangement corresponds to an ionization chamber but the anode plate is made of a glass plate on the surface of which very thin conductor-strips are

fixed. Small strips, with a width of several microns, are located between two larger strips in a distance of several ten microns. The applied electric potential alternates between each strip. The smaller strips are the anodes, the larger ones the cathodes. This micro strip plate operates just like a proportional counter. An electron produced anywhere in the gas volume drifts towards the positive strip where it will experience an avalanche amplification. But now more than 90 % of the ions produced in the avalanche are neutralised on the very close cathode strips and therefore the space charge is significantly reduced. A local rate limit in neutron detection of 20 kHz / mm^2 was reached , 20 times higher than in a wire counter. The overall rate limit is the same as in a MWPC, as it only depends on the charge collection time. In neutron detection the smaller pitch of such a structure does not automatically lead to a better localisation because the precision also depends on the intrinsic deviation between the reaction point and the centre of gravity of the charges. The spatial resolution is only improved if the particle range is reduced to the size of the structure pitch.

A very recent development is the Gas Electron Multiplier (GEM) {7}. Its amplifying part consists of a Polyimide foil metallized on both sides with small holes drilled through. A potential difference between the two surfaces generates the necessary field strength for the avalanche amplification. This device is inexpensive and can be produced in large sizes up to 30 cm x 30 cm. A survey of the recent MPGC developments can be found in {8} and {9}.

The general characteristics of gaseous neutron detectors are:

1) high and noiseless internal amplification
2) very good gamma discrimination
3) large sensitive areas
4) radiation hard
5) max local rate: <= 1 kHz/ mm^2 respectively < = 20 kHz/ mm^2
6) total rate per cell or per sensitive surface < = 300 kHz
7) position resolution > = 1 mm

Scintillator detectors

In Fig (6) the pulse height spectra of two neutron scintillators, directly coupled to a photomultiplier, are shown. Only the glass scintillator leads to a tolerable separation between neutron- and gamma-signals. The photon output of the lithium loaded ZnS- powder is higher but this is also true for its gamma sensitivity.

The characteristics of some neutron scintillators are indicated in Tab (5).

As a result of the higher density of the scintillator material, the range of the ionizing particles is reduced to a few microns which can result in a better spatial resolution. The light emitted from the scintillator is either directly recorded by a
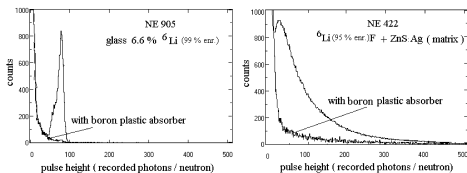
Figure 6: Pulse height spectra of the scintillators NE 905 and NE 422 (Nuclear Enterprises) irradiated with a lab. Am-Be neutron source (reaction: n (^{6}Li , α) ^{3}H + 4.79 MeV) and measured with a photo multiplier at the same amplification. In a second measurement a boron loaded plastic absorber was installed between source and scintillator in order to distinguish between gamma background and neutron signal.

light sensitive detector or collected by different optical means as there are lenses, mirrors or fibres towards such a detector. This can be a photographic film, a CCD camera, a photo multiplier (PM) or a photo-sensitive gaseous counter. But all the integrating light-devices also record the light generated by the gammas.

On a continuous neutron beam the lithium loaded ZnS scintillator NE422 is applicable only for measurements where its gamma sensitivity is of little importance for the result: in beam- monitoring or neutronography. The gamma background can only be discriminated on a pulsed neutron beam and with a counting light detector, taking advantage of the time of flight difference between neutrons and gammas.

Owing to the short decay time of the glass-scintillator NE 905, a local rate up to several MHz / mm^2 can be recorded with a directly connected PM. This is also valid for a position sensitive PM. The combination of the latter with this scintillator is the neutron detector with the highest rate capability and with a spatial resolution of about

scintillator :doping	Decay time ns	Peak wave length nm	Photons / neutron
^{6} Li –glass : Ce	18 and 98	395	~ 6 000
^{6} Li F/ Zn S : Ag	>1000	450	~ 160 000
^{6} Li I crystal : Eu	~ 1400	470	~ 48 000

Table 5: Characteristics of the most useful scintillators for thermal neutrons {12}.

200 microns. The maximum sensitive area though is still limited to 8 x 8 cm^2 and the costs for this arrangement are rather high. Unfortunately the light output of the NE 905 scintillator is too low for single neutron detection with a CCD.

The Anger camera {10} is the combination of a scintillator and a light disperser coupled to a bundle of photomultipliers. The localisation of the neutron event is achieved by determining the centroid between the different PM signals. Its sensitive area is up to several hundred cm^2 and its position resolution is of several mm.

The commercially available Thomson tube looks like an inverse cathode ray tube. The screen is replaced by a Gd Oxide–scintillator, covered with a photocathode. The light produced by the Gd-conversion electron in the scintillator releases an electron from the photocathode into the vacuum where it is accelerated and focused, by an electrostatic optic, onto an output screen. There it produces a huge amount of photons. This spot can be recorded by all the light sensitive devices mentioned above. The sensitive area has a diameter of 215 mm and a spatial resolution of 200 to 300 microns.

For beam monitoring, a so-called "Handmonitor" {11} combines the lithium loaded ZnS scintillator with a commercially available image amplifier. A neutron beam profile can be directly seen on the screen of the device.

Photographic films have a dynamic of 1:100 at the most. A spatial resolution of some hundred microns can be achieved depending on the optic and the thickness of the scintillator. But as this is an integrating device, the light of the gamma background is also recorded.

At present, R&D work is done for inorganic scintillators with a higher light output for the future spallation neutron sources. A summary is published by Carel W.E. van Eijk {12}

Foil detectors

Fig (7) shows the calculated pulse height spectra of the charged particles escaped from a boron foil after the n (^{10}B, α) ^{7}Li reaction. The spectrum is always extended down to the lowest channels. As the charged particles are emitted randomly in space, their energy losses during the travelling through the material can be as high as their complete kinetic energy, that is why only some of them escape from the foil.

The absorption length for neutrons with a wavelength of 1.8 Å in a metallic ^{10}B-foil is 19.2 microns, whereas the ranges of the particles of the reaction n (^{10}B,α) ^{7}Li amount to 3.9 microns respectively 1.7 microns only. This means that the particle range is much shorter than the absorption length. Particles produced deeper than this range cannot escape from the foil. The situation is similar for all
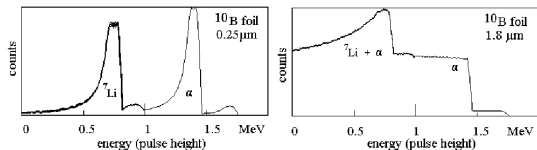
Figure 7: Calculated spectra of the charged particles escaped on the backside from frontally irradiated ^{10}B foils and produced in the reactions n (^{10}B, α) ^{7}Li + 2.3 MeV + γ(0.48 MeV) and n (^{10}B, α) ^{7}Li + 2.79 MeV. The efficiency for 1.8 Å neutrons with the indicated foil thickness would be 1.0 %, respectively 5.5 %.

the other neutron converter foils. Therefore any combination of a particle detector with a foil leads to an arrangement with low detection efficiency. At a foil thickness which is about 10% smaller than the range of the particle with the higher kinetic energy, the escape probability reaches a maximum as shown in Fig. (8). The foil thickness for a maximum neutron detection for commonly used converters is indicated in Tab (6).

Foil detectors are preferably used in neutronography and beam monitoring. For the latter a very thin layer of the absorbing material is evaporated onto the cathode inside a gas counter or ionization chamber. For special applications, foil detectors are constructed in combination with photographic films, image plates, CCD's and channel plates; in most cases Gd foils are used because of their higher neutron efficiency and an easier handling but the disadvantage is a high gamma sensitivity.
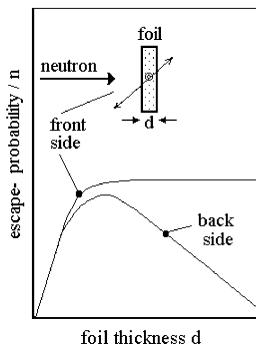
Figure 8: Escape probability of the particles produced by a neutron reaction in a foil as function of its thickness.

3.3-14

foil material	n detection efficiency %	optimal foil thickness d µm
^{6}Li	13.6	112
^{6}LiF	5.8	29
^{10}B	6.4	3.4
Gd nat	< 11	~ 3.5
^{235}U	0.7	6.4

Table 6: Foil thickness and maximum detection efficiency for neutrons with a wavelength of 1.8 Å for frontal irradiation and backside detection.

Other internal detectors

In a special image plate for neutron detection the storage phosphor is mixed with Gd_2O_3 {11,13}. By this means the efficiency can be increased: the conversion electron does not have to escape from a foil but is stopped in the phosphor whereby the latter will be excited. Such image plates are available in a size of 20 x 20 cm^2. The dynamic of an image plate amounts to 1: 10^5. The spatial resolution of a neutron detector is of about 100 to 200 microns. For these reasons the device finds favour in protein crystallography with its huge amount of interference spots. But like all the integrating detectors and particularly because of the incorporated Gd with its higher atomic number, such a plate is rather gamma sensitive.

An excellent neutron detector which has not yet been constructed will be proposed here: The boron-diode. Boron is, like silicon or germanium, a semiconductor with a band gap of 1.4 eV. In the thirties, photographs used boron photocells just as silicon cells are used today. With a surface barrier diode of boron or a boron diode doped with silicon, a high signal of each neutron could be measured. An energy of about 6 eV is necessary to produce one electron–hole pair in a semiconductor. 2.3 MeV are available in the n (^{10}B, α) ^{7}Li reaction , and therefore a charge of 6 10^{14} [As] is generated. With an integrating operation amplifier and a capacitor of 1 pF in its loop an output signal of 60 mV could be measured. With a boron crystal thickness of only 60 microns, the neutron (1.8 Å) detection efficiency is of 97 %.

A position sensitive detector would be a CCD or a pixel device made of a boron crystal. and a position resolution of less than 10 microns would be achieved as the range of the α particle is only 3.9 microns. Moreover the gamma sensitivity would be rather low as boron has a low atomic number.

FAQ

find their answer in the textbook of Glenn F. Knoll {14}.

References

[1] The stopping and range of ions in solids: J.F. Ziegler, J.P. Biersack and U. Littmark; Pergamon Press Inc., New York, USA (1985)

[2] H. Geiger, E. Rutherford and J.J. Thomson; Phil. Mag .XIII (1896) 392

[3] M.K. Kopp et al NIM 201 (1982) 395

[4] D. Feltin and B. Guérard, ILL NEWS 34 (2000) 8; Edit. G. Cicognani

http://www.ill.fr/News/34/034_NEWS.HTM

[5] G. Charpak ; NIM 62 (1968) 262

[6] A. Oed ; NIM A 263 (1988) 35

[7] F. Sauli ; NIM A 386 (1997) 531

[8] F. Sauli and A. Sharma ; Annual Rev. of Nucl. and Particle Sci. 49 (1999) 341

[9] A. Oed ; NIM A471 (2001) 109

[10] H. O. Anger ; Rev Sci. Instrum. 29 (1958) 27

[11] Ch. Rausch et al; SPIE Proc. 1737 (1992) 255

[12] Carel W.E. van Eijk ; NIM A 460 (2001) 1

[13] D.A.A. Myles et al; Physica B 241 - 243 (1998) 1122

[14] Radiation detection and measurement: Glenn F. Knoll; 3rd ed.1999;John Wiley & Sons, Inc, New York

ACTIVATION AND SHIELDING

Activation Table of the Elements

M. Johnson, S. A. Mason and R. B. Von Dreele

The best way to determine the activation of a sample is to measure it in situ with appropriate instruments. However in planning neutron experiments it may be useful to know whether activation is likely to be significant. Properly estimating activation of a sample by a neutron beam requires knowledge of the neutron spectrum, time of exposure, mass, isotopic composition, etc. The Table below allows you to calculate roughly the activation of a sample after it has been in a neutron beam for one day and the amount of time for it to decay to 74Bq/g (i.e. 2nCi/g) or less, which is a typical limit for shipping a sample as "nonradioactive". It also displays the anticipated exposure you may receive when removing the sample from the instrument. The entries in this table are derived from an approximate calculation (by M. Johnson) for decay times to 10^5 and to 10^4Bq/cm^3 for 5cm^3 pure solid samples of the elements exposed to a neutron beam for 1day at an intensity comparable to that found on HIPD with LANSCE operating at 100μA. These calculations were made for pulsed sources and may somewhat overestimate activation for reactors for some elements (no epithermal neutrons). They are augmented by calculations from NIST of the activation from a 1 day exposure to a 10^7n/s-cm^2 reactor thermal beam (marked [†]). *Storage time* is the time required for a sample of the pure solid element exposed to this "standard" neutron beam to decay to 74Bq/g or less. *Prompt activation* gives the anticipated activation for the pure solid elements 2 min after the neutron exposure ceases. *Contact dose* is that expected from a 1g sample of the pure element from the prompt activation. Elements with a dash for the entries in all three columns do not show any activation. Those marked with a single asterisk are radioactive before exposure to the neutron beam; apart from Tc and Pm, they are all α-particle emitters. Bismuth is a special case; it is stable before exposure to the

beam, but the activation product is an α-emitter. A typical sample activation calculation may be found in the Web version of the table.

NB: The current Web version of this Table may be found on the ILL Web site:
(http://www.ill.fr/YellowBook/D19/help/act_table.htm).

The original Table first appeared in the LANSCE Newsletter 12/1/92. We thank R. Pynn and V. T. Forsyth, for their cooperation. Comments to the present authors are very welcome *(m.w.johnson@rl.ac.uk, mason@ill.fr, vondreele@lanl.gov)*.

Symbol/Name		Mass	Storage Time	Prompt activation 1 unit=37Bq/g (= 1nCi/g)	Contact dose at 2.54cm 1 unit=10µGy/hr/g (=1mr/hr/g, at 1 inch)
Ac	actinium	227	*	*	*
Al	aluminium	26.982	21m	1900	2.0
Am	americium	243	*	*	*
Sb	antimony	121.75	520d	800	0.7
Ar	argon	39.948	19h	3500	3.0
As	arsenic	74.922	18d	8.4×10^4	7.3
At	astatine	210	*	*	*
Ba	barium	137.34	<150h	<80	<0.1
Bk	berkelium	247	*	*	*
Be	beryllium	9.012	-	-	-
Bi	bismuth	208.980	**	**	**
B	boron	10.811	-	-	-
Br	bromine	79.909	18d	1.4×10^4	12[†]
Cd	cadmium	112.40	190d	370	0.3
Ca	calcium	40.08	-	-	-
Cf	californium	249	*	*	*
C	carbon	12.011	-	-	-
Ce	cerium	140.12	<86h	<40	<0.1
Cs	cesium	132.905	54h	4.6×10^5	400
Cl	chlorine	35.453	<2.8h	<80	<0.1
Cr	chromium	51.996	<61d	<40	<0.1
Co	cobalt	58.933	24y	5.2×10^4	45[†]
Cu	copper	63.54	7.4d	1.0×10^4	8.5
Cm	curium	247	*	*	*
Dy	dysprosium	162.50	52h	5.0×10^5	430[†]

Symbol/Name		Mass	Storage Time	Prompt activation 1 unit=37Bq/g (= 1nCi/g)	Contact dose at 2.54cm 1 unit=10µGy/hr/g (=1mr/hr/g, at 1 inch)
D	deuterium	2.015	-	-	-
Es	einsteinium	254	*	*	*
Er	erbium	167.26	78d	600	0.5
Eu	europium	151.96	50y	2200	1.9†
Fm	fermium	253	*	*	*
F	fluorine	18.998	-	-	-
Fr	francium	223	*	*	*
Gd	gadolinium	157.25	11d	7400	6.4
Ga	gallium	69.72	8d	3.2×10^4	27†
Ge	germanium	72.59	<6d	1100	1.0†
Au	gold	196.967	29d	3000	2.5
Hf	hafnium	178.49	1.6y	620	0.5
He	helium	4.003	-	-	-
Ho	holmium	164.930	20d	2.8×10^4	24†
H	hydrogen	1.008	-	-	-
In	indium	114.82	12d	1.1×10^4	9.5†
I	iodine	126.904	7h	1.2×10^5	100
Ir	iridium	192.2	4.2y	5.0×10^4	43†
Fe	iron	55.847	-	-	-
Kr	krypton	83.80	42h	3200	2.8†
La	lanthanum	138.91	22d	1.9×10^4	16
Pb	lead	207.19	-	-	-
Li	lithium	6.939	-	-	-
Lu	lutetium	174.97	1.8y	1.4×10^4	12†
Mg	magnesium	24.312	-	-	-
Mn	manganese	54.938	38h	1.1×10^5	95
Md	mendelevium	256	*	*	*
Hg	mercury	200.59	24d	700	0.6
Mo	molybdenum	95.94	30d	430	0.4
Nd	neodymium	144.24	15h	1200	1.0
Ne	neon	20.183	-	-	-
Np	neptunium	237	*	*	*
Ni	nickel	58.71	<5.5h	<30	<0.1
Nb	niobium	92.906	80m	2.0×10^4	17
N	nitrogen	14.007	-	-	-

Symbol/Name		Mass	Storage Time	Prompt activation 1 unit=37Bq/g (= 1nCi/g)	Contact dose at 2.54cm 1 unit=10µGy/hr/g (=1mr/hr/g, at 1 inch)
Os	osmium	190.2	41d	2300	2.0[†]
O	oxygen	15.999	-	-	-
Pd	palladium	106.4	9d	7.1x10⁴	60
P	phosphorus	30.974	-	-	-
Pt	platinum	195.09	20d	230	0.2
Pu	plutonium	242	*	*	*
Po	polonium	210	*	*	*
K	potassium	39.102	<38h	<300	<0.3
Pr	praseodymium	140.907	11d	2.0x10⁴	17
Pm	promethium	147	*	*	*
Pa	proctactinium	231	*	*	*
Ra	radium	226	*	*	*
Rn	radon	222	*	*	*
Re	rhenium	186.2	53d	4.9x10⁴	42
Rh	rhodium	102.905	2h	2.6x10⁴	22[†]
Rb	rubidium	85.47	56d	1800	1.6
Ru	ruthenium	101.07	106d	230	0.2
Sm	samarium	150.35	35d	6200	5.4
Sc	scandium	44.956	<1.8y	<90	<0.1
Se	selenium	78.96	10h	4900	4.2[†]
Si	silicon	28.086	-	-	-
Ag	silver	107.870	7.4y	1.6x10⁴	14[†]
Na	sodium	22.991	5.5d	5700	5.0
Sr	strontium	87.62	<25h	<100	<0.1
S	sulphur	32.064	-	-	-
Ta	tantalum	180.948	3y	1600	1.4
Tc	technetium	98	*	*	*
Te	tellurium	127.60	96h	2600	2.2
Tb	terbium	158.924	2.1y	3300	2.8
Tl	thallium	204.37	41m	460	0.4
Th	thorium	232.038	*	*	*
Tm	thulium	168.934	3.7y	7700	6.7[†]
Sn	tin	118.69	<50d	<40	<0.1
Ti	titanium	47.90	-	-	-

Symbol/Name		Mass	Storage Time	Prompt activation 1 unit=37Bq/g (= 1nCi/g)	Contact dose at 2.54cm 1 unit=10μGy/hr/g (=1mr/hr/g, at 1 inch)
W	tungsten	183.85	15d	3.7×10^4	32
U	uranium	238.03	*	*	*
V	vanadium	50.942	48m	4.7×10^5	41
Xe	xenon	131.30	7d	3200	2.8
Yb	ytterbium	173.04	275d	780	0.7
Y	yttrium	88.905	24d	1000	0.9
Zn	zinc	65.37	5d	1600	1.4
Zr	zirconium	91.22	79h	<40	<0.1

SHIELDING OF RADIATIONS

H.G. Börner and J. Tribolet

Shielding of photons

The decrease in intensity of a parallel beam of photons traversing an absorber of thickness d is given by

$$\Phi = \Phi_0 \, e^{-\Sigma d}$$

where Φ_0 and Φ are the beam intensity before and after passing through the absorber, Σ is the attenuation coefficient for photons of energy E and for a given material. It should be noted that the attenuation calculated by the above formula gives only the decrease in intensity of the original beam. The total radiation downstream of the absorber is larger, due to the presence of scattered photons, and to the creation of secondary photons by a variety of processes, including fluorescence and positron annihilation radiation.

The graphs in Figure 1 give values for the attenuation coefficient Σ (expressed in cm^{-1}) for some commonly used materials like iron, lead, aluminium and concrete. One can deduce that one needs roughly 5 cm of lead or 50 cm of concrete, respectively, to attenuate a 10 MeV photon beam (a typical primary gamma ray energy produced in neutron capture) by an order of magnitude.

Shielding of neutrons

Concerning the attenuation of neutrons one has to distinguish between two categories: Thermal and subthermal neutrons on one hand and epithermal and fast neutrons on the other one.

Thermal and subthermal neutrons can easily be stopped by capture in materials with high neutron capture cross sections like cadmium, gadolinium, boron and lithium. Generally a rather thin layer of absorbant material is sufficient to stop such neutron beams. However, in the case of cadmium and gadolinium the absorption of neutrons is accompanied by strong emission of capture gamma rays. Therefore additional shielding is necessary to attenuate the gamma rays (see above). This phenomenon does not exist for lithium and is much less pronounced for boron. Consequently the latter materials are preferably used, especially on the outside of heavy shielding in experimental areas.
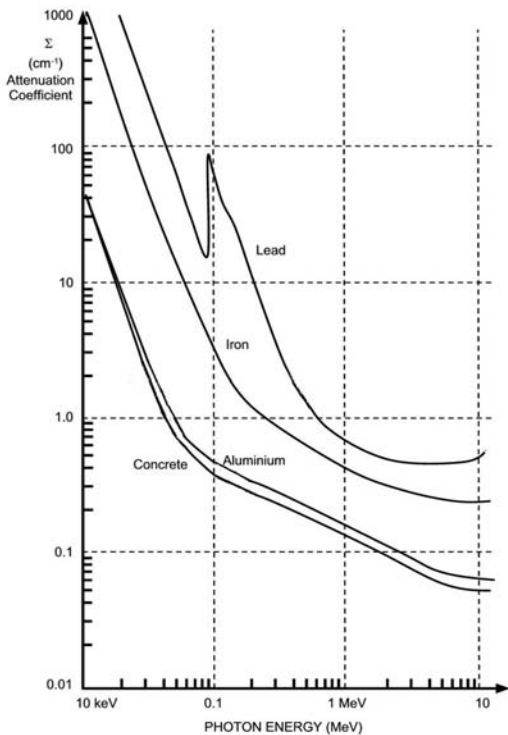
Figure 1: Attenuation of photons.

4.2-3

To attenuate neutrons of higher energies is by far more complex because they cannot be stopped directly via capture and have first to be slowed down. A precise determination of a specific protection demands generally more complicated calculations using Monte Carlo methods. For neutrons in the MeV region, three types of materials are generally added together: dense materials (inelastic collisions), hydrogenated materials (moderation), and absorbing materials (capture). An example is "heavy concrete" in which one finds iron, hydrogen and boron.
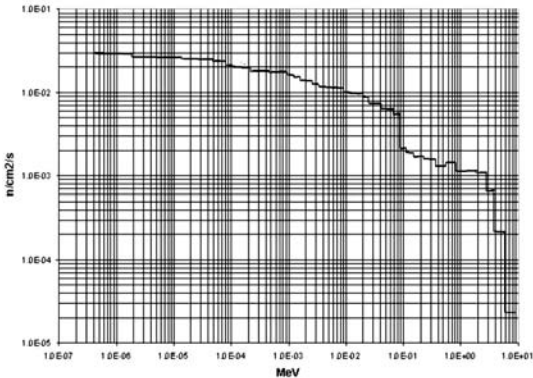
Figure 2: High energy part of the spectral distribution of neutrons emerging from a standard thermal beam tube.

Specific examples:

a) *Neutron guides*: In the parts which are sufficiently distant from the reactor neutrons are stopped by one to two layers (concerning ILL standards) of B_4C.

b) P*rimary casemates*: Typically 80 to 90 cm of heavy concrete are used (at ILL). This insures simultaneous protection against neutrons and gamma rays.

c) T*hermal neutron beam tubes*: An example for the high energy part of the spectral distribution of neutrons in a standard 'thermal beam tube' of ILL is shown in Figure 2. Optimized shielding against neutrons with such spectral distribution depends on the space available:

• If 10 cm: Best attenuation is obtained by using borated polyethylene (attenuation by factor 25)

• If 20 cm: Best attenuation is obtained by using 2 cm of iron, followed by 18 cm of borated polyethylene (attenuation by factor 310). However, the use of 20 cm of borated polyethylene is only about 10 percent less efficient.

• If 30 cm: Best attenuation is obtained by using 12 cm of iron, followed by 18 cm of borated polyethylene (attenuation by factor 3400).

MISCELLANEOUS

Radioactivity and Radiation Protection

The International Commission on Radiation Units and Measurements (ICRU) recommends the use of SI units. Therefore, we list SI units first, followed by cgs (or other common) units in parentheses, where they differ.

A. DEFINITIONS

Unit of activity = becquerel (curie):
    1 Bq = 1 disintegration s^{-1} [= 1/(3.7 × 10^{10}) Ci]
Unit of absorbed dose = gray (rad):
    1 Gy = 1 J kg^{-1} (= 10^4 erg g^{-1} = 100 rad)
        = 6.24 × 10^{12} MeV kg^{-1} deposited energy
Unit of exposure, the quantity of x- or γ-radiation at a point in space integrated over time, in terms of charge of either sign produced by showering electrons in a small volume of air about the point:
        = 1 C kg^{-1} of air (roentgen; 1 R = 2.58 × 10^{-4} C kg^{-1})
        = 1 esu cm^{-3} (= 87.8 erg released energy per g of air)
    Implicit in the definition is the assumption that the small test volume is embedded in a sufficiently large uniformly irradiated volume that the number of secondary electrons entering the volume equals the number leaving.
Unit of equivalent dose for biological damage = sievert. 1 Sv = 100 rem (roentgen *e*quivalent for *m*an). The equivalent dose in Sv = absorbed dose in grays × w_R, where w_R is the radiation weighting factor (formerly the quality factor Q), which depends upon the type of radiation and other factors, as shown in Table 5-1. The equivalent dose expresses the long-term risk (primarily due to cancer and leukemia) from low-level chronic exposure.

B. RADIATION LEVELS

Natural annual background from all sources. In most of the world, the whole-body equivalent dose rate ≈ 0.4–4 mSv (40–400 mrem). It can range up to 50 mSv (5 rem) in certain areas. The U.S. average ≈ 3.6 mSv, including about 2 mSv (≈ 200 mrem) from inhaled natural radioactivity, mostly radon and radon daughters. This radon exposure value is for a typical house; radon exposure varies by more than an order of magnitude.
Cosmic ray background in counters (Earth̄s surface): ~1 min^{-1}cm^{-2} sr^{-1}.
Man-made radiation dose: The greatest contribution to man-made radiation dose has been from irradiation from x-ray diagnostics in medicine, which accounts for about 20% of the average natural radiation dose.

Table 5.1 *Radiation weighting factors.*

Type of radiation	w_R
X- and γ-rays, all energies	1
Electrons and muons, all energies	1
Neutrons:	
< 10 keV	5
10–100 keV	10
0.1–2 MeV	20
2–20 MeV	10
> 20 MeV	5
Protons (other than recoils), > 2 MeV	5
Alphas, fission fragments, and heavy nuclei	20

Fluxes (per cm^2) to deposit one Gy, assuming uniform irradiation:

For photons:

$\approx 6.24 \times 10^9 \, l \, / Ef$, for photons of energy E [MeV], attenuation length l (g cm^{-2}), and fraction $f \leq 1$ expressing the fraction of the photon s energy deposited in a small volume of thickness $\ll l$ but large enough to contain the secondary electrons.

$\approx 2 \times 10^{11}$ photons cm^{-2} for 1-MeV photons on carbon ($f \approx 0.5$).

For charged particles:

$\approx 6.24 \times 10^9/(dE/dx)$, where dE/dx [MeV g^{-1} cm^2], the energy loss per unit length, may be obtained from range-energy figures.

$\approx 3.5 \times 10^9$ cm^{-2} for minimum-ionizing singly-charged particles in carbon.

Quoted fluxes are good to about a factor of two for all materials.

Recommended exposure limits for radiation workers (whole-body dose):

ICRP: 20 mSv yr^{-1} averaged over 5 years, with the dose in any one year $\leq$ 50 mSv.

U.S.: 50 mSv yr^{-1} (5 rem yr^{-1}). Many laboratories in the U.S. and elsewhere set lower limits.

Lethal dose: Whole-body dose from penetrating ionizing radiation resulting in 50% mortality in 30 days (assuming no medical treatment), about 5 Gy (500 rads) as measured internally on body longitudinal center line. Surface dose varies owing to variable body attenuation and may be a strong function of energy.

This section is reprinted, with permission, from the 2001 web edition of the *X-Ray Data Booklet (http://xdb.lbl.gov).* For further information, see ICRP Publication 60, *1990 Recommendation of the International Commission on Radiological Protection* (Pergamon Press, New York, 1991) and E. Pochin, *Nuclear Radiation: Risks and Benefits* (Clarendon Press, Oxford,1983).

Physical Constants

Table 5.2 *Physical constants.*

Quantity	Symbol, equation	Value	Uncert. (ppb)
speed of light	c (see note *)	$2.997\,924\,58{\times}10^{8}$ m s^{-1} $(10^{10}$ cm s$^{-1})$	exact
Planck constant	h	$6.626\,068\,76(52){\times}10^{-34}$ J s $(10^{-27}$ erg s$)$	78
Planck constant, reduced	$\hbar = h/2\pi$	$1.054\,571\,596(82){\times}10^{-34}$ J s $= 6.582\,118\,89(26){\times}10^{-22}$ MeV s	78, 39
electron charge magnitude	e	$4.803\,204\,20(19){\times}10^{-10}$ esu $= 1.602\,176\,462(63){\times}10^{-19}$ C	39, 59
conversion constant	$\hbar c$	$197.326\,960\,1(78)$ MeV fm $(=$eV nm$)$	39
electron mass	m_e	$0.510\,998\,902(21)$ MeV/$c^2 = 9.109\,381\,88(72){\times}10^{-31}$ kg	40, 79
proton mass	m_p	$938.271\,998(38)$ MeV/$c^2 = 1.672\,621\,58(13){\times}10^{-27}$ kg	40, 79
neutron mass	m_n	$1.674\,95{\times}10^{-27}$ kg	-
deuteron mass	m_d	$1875.612\,762(75)$ MeV/c^2	40
unified atomic mass unit (u)	(mass ^{12}C atom)$/12 = (1$ g)/(N_A mol)	$931.494\,013(37)$ MeV/$c^2 = 1.660\,538\,73(13){\times}10^{-27}$ kg	40, 79
permittivity of free space	$\varepsilon_0 = 1/(\mu_0 c^2)$	$8.854\,187\,817...{\times}10^{-12}$ F m^{-1}	exact
permeability of free space	μ_0	$4\pi{\times}10^{-7}$ N A$^{-2} = 12.566\,370\,614...{\times}10^{-7}$ N A^{-2}	exact
fine-structure constant	$\alpha = e^2/4\pi\varepsilon_0 \hbar c$	$1/137.035\,999\,76(50)$	3.7
classical electron radius	$r_e = e^2/4\pi\varepsilon_0 m_e c^2$	$2.817\,940\,285(31){\times}10^{-15}$ m	11
Bohr radius ($m_{\text{nucleus}} = \infty$)	$a_0 = 4\pi\varepsilon_0 \hbar^2/m_e e^2 = r_e \alpha^{-2}$	$0.529\,177\,208\,3(19){\times}10^{-10}$ m $(10^{-8}$ cm$)$	3.7
Rydberg energy	$hcR_\infty = m_e e^4/2(4\pi\varepsilon_0)^2 \hbar^2$ $= m_e c^2 \alpha^2/2$	$13.605\,691\,72(53)$ eV	39
Thomson cross section	$\sigma_T = 8\pi r_e^2/3$	$0.665\,245\,854(15)$ barn $(10^{-28}$ m$^2)$	22
Bohr magneton	$\mu_B = e\hbar/2m_e$	$5.788\,381\,749(43){\times}10^{-11}$ MeV T^{-1}	7.3
nuclear magneton	$\mu_N = e\hbar/2m_p$	$3.152\,451\,238(24){\times}10^{-14}$ MeV T^{-1}	7.6
electron cyclotron freq./field	$\omega^e_{cycl}/B = e/m_e$	$1.758\,820\,174(71){\times}10^{11}$ rad s^{-1} T^{-1}	40
proton cyclotron freq./field	$\omega^p_{cycl}/B = e/m_p$	$9.578\,834\,08(38){\times}10^{7}$ rad s^{-1} T^{-1}	40

Table 5-2. Physical constants (continued).

Quantity	Symbol, equation	Value	Uncert. (ppm)
Avogadro constant	N_A	$6.022\ 141\ 99(47) \times 10^{23}\ \text{mol}^{-1}$	79
Boltzman constant	k	$1.380\ 650\ 3(24) \times 10^{-23}\ \text{J K}^{-1} = 8.617\ 342(15) \times 10^{-5}\ \text{eV K}^{-1}$	1700
molar volume, ideal gas at STP	$N_A k\ (273.15\ \text{K})/(101\ 325\ \text{Pa})$	$22.413\ 996(39) \times 10^{-3}\ \text{m}^3\ \text{mol}^{-1}$	1700

$\pi = 3.141\ 592\ 653\ 589\ 793\ 238$ $e = 2.718\ 281\ 828\ 459\ 045\ 235$ $\gamma = 0.577\ 215\ 664\ 901\ 532\ 861$

*The meter is the length of the path traveled by light in vacuum during a time interval of 1/299 792 458 of a second.

1 in. = 2.54 cm	1 newton = 10^5 dyne	$1\ \text{eV}/c^2$ = $1.782\ 662 \times 10^{-33}$ g	1 coulomb = $2.997\ 924\ 58 \times 10^9$ esu
1 Å = 10^{-8} cm	1 joule = 10^7 erg	$hc/(1\ \text{eV})$ = 1239.842 μm	1 tesla = 10^4 gauss
1 fm = 10^{-13} cm	1 cal = 4.184 joule	$1\ \text{eV}/h$ = $2.417\ 9894 \times 10^{14}$ Hz	1 atm = $1.013\ 25 \times 10^6$ dyne/cm²
1 barn = 10^{-24} cm²	1 eV = $1.602\ 176\ 5 \times 10^{-12}$ erg	$1\ \text{eV}/k$ = 11 604.5 K	0°C = 273.15 K
		1 meV = 8.0668 cm⁻¹	

The table is adapted with permission from the 2001 web edition of the X-Ray Data Booklet (http://xdb.lbl.gov).
It was drawn from the recommendations of CODATA (the Committee on Data for Science and Technology).
The full 1998 CODATA set of constants may be found at http://physics.nist.gov/cuu/Constants/index.html.

Physical Properties of the Elements

Table 5.3 lists several important properties of the elements.

Data were taken mostly from D. R. Lide, Ed., CRC Handbook of Chemistry and Physics, 80th ed. (CRC Press, Boca Raton, Florida, 1999). Atomic weights apply to elements as they exist naturally on earth; values in parentheses are the mass numbers for the longest-lived isotopes. Some uncertainty exists in the last digit of each atomic weight. Specific heats are given for the elements at 25°C and a pressure of 100 kPa. Densities for solids and liquids are given as specific gravities at 20°C unless otherwise indicated by a superscript temperature (in°C); densities for the gaseous elements are given in g/cm^3 for the liquids at their boiling points.

Table 5.3 *Properties of the elements.*

Z	Element	Atomic weight	Density	Melting point (°C)	Boiling point (°C)	Specific heat (J/g·K)
1	Hydrogen	1.00794	0.0708	−259.34	−252.87	14.304
2	Helium	4.002602	0.122	—	−268.93	5.193
3	Lithium	6.941	0.534	180.50	1342	3.582
4	Beryllium	9.012182	1.848	1287	2471	1.825
5	Boron	10.811	2.34	2075	4000	1.026
6	Carbon	12.0107	1.9–2.3 (graph)	4492[10.3 MPa]	3825[b]	0.709
7	Nitrogen	14.00674	0.808	−210.00	−195.79	1.040
8	Oxygen	15.9994	1.14	−218.79	−182.95	0.918
9	Fluorine	18.9984032	1.50	−219.62	−188.12	0.824
10	Neon	20.1797	1.207	−248.59	−246.08	1.030
11	Sodium	22.989770	0.971	97.80	883	1.228
12	Magnesium	24.3050	1.738	650	1090	1.023
13	Aluminum	26.981538	2.6989	660.32	2519	0.897
14	Silicon	28.0855	2.33[25]	1414	3265	0.705
15	Phosphorus	30.973761	1.82	44.15	280.5	0.769
16	Sulfur	32.066	2.07	119.6	444.60	0.710
17	Chlorine	35.4527	1.56[−33.6]	−101.5	−34.04	0.479
18	Argon	39.948	1.40	−189.35	−185.85	0.520
19	Potassium	39.0983	0.862	63.5	759	0.757
20	Calcium	40.078	1.55	842	1484	0.647
21	Scandium	44.955910	2.989[25]	1541	2836	0.568
22	Titanium	47.867	4.54	1668	3287	0.523
23	Vanadium	50.9415	6.11[18.7]	1910	3407	0.489
24	Chromium	51.9961	7.18–7.20	1907	2671	0.449
25	Manganese	54.938049	7.21–7.44	1246	2061	0.479
26	Iron	55.845	7.874	1538	2861	0.449

Table 5.3 Properties of the elements (continued).

Z	Element	Atomic weight	Density	Melting point (°C)	Boiling point (°C)	Specific heat (J/g·K)
27	Cobalt	58.933200	8.9	1495	2927	0.421
28	Nickel	58.6934	8.902[25]	1455	2913	0.444
29	Copper	63.546	8.96	1084.62	2562	0.385
30	Zinc	65.39	7.133[25]	419.53	907	0.388
31	Gallium	69.723	5.904[29.6]	29.76	2204	0.371
32	Germanium	72.61	5.323[25]	938.25	2833	0.320
33	Arsenic	74.92160	5.73	817[3.7 MPa]	603[b]	0.329
34	Selenium	78.96	4.79	220.5	685	0.321
35	Bromine	79.904	3.12	−7.2	58.8	0.226
36	Krypton	83.80	2.16	157.38[73.2 kPa]	−153.22	0.248
37	Rubidium	85.4678	1.532	39.30	688	0.363
38	Strontium	87.62	2.54	777	1382	0.301
39	Yttrium	88.90585	4.469[25]	1522	3345	0.298
40	Zirconium	91.224	6.506	1855	4409	0.278
41	Niobium	92.90638	8.57	2477	4744	0.265
42	Molybdenum	95.94	10.22	2623	4639	0.251
43	Technetium	(98)	11.50[a]	2157	4265	—
44	Ruthenium	101.07	12.41	2334	4150	0.238
45	Rhodium	102.90550	12.41	1964	3695	0.243
46	Palladium	106.42	12.02	1554.9	2963	0.246
47	Silver	107.8682	10.50	961.78	2162	0.235
48	Cadmium	112.411	8.65	321.07	767	0.232
49	Indium	114.818	7.31	156.60	2072	0.233
50	Tin	118.710	7.31	231.93	2602	0.228
51	Antimony	121.760	6.691	630.73	1587	0.207
52	Tellurium	127.60	6.24	449.51	988	0.202
53	Iodine	126.90447	4.93	113.7	184.4	0.145
54	Xenon	131.29	3.52	−111.79[81.6 kPa]	−108.12	0.158

Table 5.3 Properties of the elements (continued).

Z	Element	Atomic weight	Density	Melting point (°C)	Boiling point (°C)	Specific heat (J/g·K)
55	Cesium	132.90545	1.873	28.5	671	0.242
56	Barium	137.327	3.5	727	1897	0.204
57	Lanthanum	138.9055	6.145^{25}	918	3464	0.195
58	Cerium	140.116	6.770^{25}	798	3443	0.192
59	Praseodymium	140.90765	6.773	931	3520	0.193
60	Neodymium	144.24	7.008^{25}	1021	3074	0.190
61	Promethium	(145)	7.264^{25}	1042	3000	—
62	Samarium	150.36	7.520^{25}	1074	1794	0.197
63	Europium	151.964	5.244^{25}	822	1529	0.182
64	Gadolinium	157.25	7.901^{25}	1313	3273	0.236
65	Terbium	158.92534	8.230	1356	3230	0.182
66	Dysprosium	162.50	8.551^{25}	1412	2567	0.170
67	Holmium	164.93032	8.795^{25}	1474	2700	0.165
68	Erbium	167.26	9.066^{25}	1529	2868	0.168
69	Thulium	168.93421	9.321^{25}	1545	1950	0.160
70	Ytterbium	173.04	6.966	819	1196	0.155
71	Lutetium	174.967	9.841^{25}	1663	3402	0.154
72	Hafnium	178.49	13.31	2233	4603	0.144
73	Tantalum	180.9479	16.654	3017	5458	0.140
74	Tungsten	183.84	19.3	3422	5555	0.132
75	Rhenium	186.207	21.02	3186	5596	0.137
76	Osmium	190.23	22.57	3033	5012	0.130
77	Iridium	192.217	22.42^{17}	2446	4428	0.131
78	Platinum	195.078	21.45	1768.4	3825	0.133
79	Gold	196.96655	~19.3	1064.18	2856	0.129
80	Mercury	200.59	13.546	–38.83	356.73	0.140
81	Thallium	204.3833	11.85	304	1473	0.129
82	Lead	207.2	11.35	327.46	1749	0.129

Table 5.3 *Properties of the elements (continued).*

Z	Element	Atomic weight	Density	Melting point (°C)	Boiling point (°C)	Specific heat (J/g·K)
83	Bismuth	208.98038	9.747	271.40	1564	0.122
84	Polonium	(209)	9.32	254	962	—
85	Astatine	(210)	—	302	—	—
86	Radon	(222)	—	−71	−61.7	0.094
87	Francium	(223)	—	27	—	—
88	Radium	(226)	—	700	—	—
89	Actinium	(227)	—	1051	3198	0.120
90	Thorium	232.0381	11.72	1750	4788	0.113
91	Protactinium	231.03588	15.37[a]	1572	—	—
92	Uranium	238.0289	~18.95	1135	4131	0.116
93	Neptunium	(237)	20.25	644	—	—
94	Plutonium	(244)	19.84[25]	640	3228	—
95	Americium	(243)	13.67	1176	2011	—
96	Curium	(247)	13.51[a]	1345	3100	—
97	Berkelium	(247)	14 (est.)	1050	—	—
98	Californium	(251)	—	900	—	—
99	Einsteinium	(252)	—	860	—	—
100	Fermium	(257)	—	1527	—	—
101	Mendelevium	(258)	—	827	—	—
102	Nobelium	(259)	—	827	—	—
103	Lawrencium	(262)	—	1627	—	—
104	Rutherfordium	(261)	—	—	—	—

This table is adapted with permission from the 2001 web edition of the *X-Ray Data Booklet* (http://xdb.lbl.gov).

PERIODIC TABLE OF THE ELEMENTS

Key:

6	atomic number
C	
12.011	atomic mass

s-block

1	2
1 H 1.0079	
3 Li 6.941	4 Be 9.0122
11 Na 22.9898	12 Mg 24.3050
19 K 39.0983	20 Ca 40.078
37 Rb 85.4678	38 Sr 87.62
55 Cs 132.905	56 Ba 137.327
87 Fr (223)	88 Ra (226)

d-block

3	4	5	6	7	8	9	10	11	12
21 Sc 44.9559	22 Ti 47.88	23 V 50.9415	24 Cr 51.9961	25 Mn 54.9381	26 Fe 55.847	27 Co 58.9332	28 Ni 58.69	29 Cu 63.546	30 Zn 65.39
39 Y 88.9059	40 Zr 91.224	41 Nb 92.9064	42 Mo 95.94	43 Tc (99)	44 Ru 101.07	45 Rh 102.905	46 Pd 106.42	47 Ag 107.868	48 Cd 112.411
57 La 138.905	72 Hf 178.49	73 Ta 180.947	74 W 183.85	75 Re 186.207	76 Os 190.2	77 Ir 192.22	78 Pt 195.08	79 Au 196.966	80 Hg 200.59
89 Ac (227)	104	105	106	107	108	109			

p-block

13	14	15	16	17	18
					2 He 4.0026
5 B 10.811	6 C 12.011	7 N 14.0067	8 O 15.9994	9 F 18.9984	10 Ne 20.1797
13 Al 26.9815	14 Si 28.0855	15 P 30.9738	16 S 32.066	17 Cl 35.4527	18 Ar 39.948
31 Ga 69.723	32 Ge 72.61	33 As 74.9216	34 Se 78.96	35 Br 79.904	36 Kr 83.80
49 In 114.82	50 Sn 118.710	51 Sb 121.75	52 Te 127.60	53 I 126.904	54 Xe 131.29
81 Tl 204.383	82 Pb 207.2	83 Bi 208.980	84 Po (210)	85 At (210)	86 Rn (222)

f-block

Lanthanides

| 58 Ce 140.115 | 59 Pr 140.907 | 60 Nd 144.24 | 61 Pm (147) | 62 Sm 150.36 | 63 Eu 151.965 | 64 Gd 157.25 | 65 Tb 158.925 | 66 Dy 162.50 | 67 Ho 164.930 | 68 Er 167.26 | 69 Tm 168.934 | 70 Yb 173.04 | 71 Lu 174.967 |

Actinides

| 90 Th 231.038 | 91 Pa (231) | 92 U 238.028 | 93 Np (237) | 94 Pu (242) | 95 Am (243) | 96 Cm (247) | 97 Bk (247) | 98 Cf (249) | 99 Es (254) | 100 Fm (253) | 101 Md (256) | 102 No (253) | 103 Lw (257) |

Parenthesis indicates the most stable isotope

Disclaimer

Neither ILL nor any of its employees, nor any of the contributors to the present document makes any warranty, express or implied, or assumes any legal liability or responsibility for the accuracy, completeness, or usefulness of any information, apparatus, product or process disclosed, or represents that its use would not infringe privately owned rights.

The user accepts sole responsibility and any risks associated with the use and results of material in this booklet, irrespective of the purpose to which such use or results are applied.